Roma Tre

Scienze della Terra – Curriculum “Geodinamica e Vulcanologia”

CORSO DI DOTTORATO DI RICERCA IN

XXXVIII Cycle

CICLO DEL CORSO DI DOTTORATO

# The depth-to-surface dynamics of silicic peralkaline magmas from Pantelleria Island

Titolo della tesi

Carmine Magri

Nome e Cognome del dottorando

Claudia Romano

Docente Guida/Tutor: Prof.

Valerio Acocella

Coordinatore: Prof.

**Abstract**: “The depth-to-surface dynamics of silicic peralkaline magmas from Pantelleria Island”

Silicic peralkaline magmas are characterized by unusually low viscosity and responsible for a wide spectrum of eruptive styles, ranging from effusive to highly explosive Plinian eruptions. This apparent paradox challenges classical models of magma fragmentation and eruption dynamics. This thesis investigates the physical and chemical processes controlling magma ascent, degassing, fragmentation dynamics and eruptive behaviour in peralkaline silicic systems, using Pantelleria Island (Italy) as a natural laboratory. The study integrates textural analyses of juvenile products, anhydrous glass viscosity measurements, Raman spectroscopy, melt inclusion analyses and simultaneous thermal and evolved gas analyses (STA-EGA-MS) on products from four eruptions with similar bulk compositions but different eruptive styles: Cinque Denti (caldera-forming-eruption), Green Tuff (caldera-forming-eruption), Zinedi (Sub-Plinian eruption) and Cuddia Mida (low-energy-Strombolian eruption). Integrated laboratory analyses are further used to perform numerical simulation of conduit dynamics. The results show that variations in eruptive style are primarily controlled by differences in ascent dynamics, volatile content and conduit geometry rather than bulk composition alone. Despite their low viscosities, peralkaline magmas can fragment due to their high water content concentration. Overall, this work provides new constraints on the mechanisms governing fragmentation and eruption dynamics of peralkaline magmas and contributes to improving rheological models for these compositions, with implications for volcanic hazard assessment in peralkaline volcanic regions.

## INDEX

## Thesis outline

This thesis is organized into six main chapters, each addressing a specific aspect of the study and collectively contributing to a comprehensive understanding of the physical, textural, rheological and eruptive dynamics of peralkaline magmas from Pantelleria Island.

### Chapter 1 - Introduction

This chapter provides the general framework of the study, introducing the geological setting of Pantelleria Island and the petrological and volcanological characteristics of peralkaline magmas. It summarizes the current state of knowledge on the generation, evolution and eruption dynamics of peralkaline systems, highlighting the main open questions that motivated this research. The final part of the chapter outlines the aims, scope, and methodological approach of the study.

### Chapter 2 - Methods

This chapter details the analytical and experimental procedures employed in this work. It describes the sampling strategy, grain size distribution (GSD) and density measurements, textural and vesicularity analyses through image processing and rheological experiments performed using concentric cylinder viscometry, differential scanning calorimetry (DSC) and micropenetration (MP) techniques, Micropobe analysis, Raman spectroscopy measurements, melt inclusions analysis and simultaneous thermal analysis (STA) and evolved gas analysis by mass spectrometry (EGA-MS).

### Chapter 3 - Results

The results chapter presents the main outcomes of the laboratory and analytical work. It includes the grain size, density and porosity distributions for all studied eruptions, the quantitative textural parameters derived from image analysis, the chemical compositions of both natural and synthesized glasses. Vesicle size and number density distributions are described and compared among the different eruptions. Rheological data obtained from the experimental measurements are also reported as well as Raman spectroscopy measurements for detecting structural changes post-viscosity measurements. Melt inclusion and STA-EGA-MS results are also reported.

## Chapter 4 - Discussion

This chapter interprets the results in the context of magmatic and eruptive processes. It discusses the relationships between vesicle textures, vesicle number densities and eruptive styles, providing insights into the conduit dynamics of the studied eruptions. Special emphasis is given to the peculiar features of the Green Tuff eruption and the role of post-fragmentation processes such as relaxation, welding, and rheomorphism. The discussion also compares the Pantelleria eruptions viscosity results with available viscosity model pointing out the need for an updated model for predicting magma viscosity in peralkaline field. A new model for predicting peralkaline magma viscosity is present in this part of the thesis.

## Chapter 5 - Simulations

Chapter 5 presents the numerical simulations of magma ascent performed with the MAMMA model. The governing equations, constitutive relationships and boundary conditions are briefly introduced, followed by the input parameters used for each eruption. In this chapter, the influence of conduit geometry, volatile content, temperature, VND, magmatic chamber depth and chemical composition on eruptive dynamics are shown. The comparison between natural data and modeled behaviour provides a quantitative framework for interpreting the observed eruptive variability.

## Chapter 6 - Conclusions

The final chapter summarizes the main findings of the thesis and integrates the experimental, analytical and modelling results into a unified conceptual model of peralkaline magma dynamics. It emphasizes the dominant role of rheology, controlled by alkali content, volatile concentration, and temperature, in governing eruptive style and transitions between explosive and effusive activity. The chapter concludes by outlining the broader implications of the study for volcanic hazard assessment and by suggesting directions for future research, particularly concerning the role of halogens and the development of improved rheological models for peralkaline melts.

# 1. Introduction

Peralkaline silicic magmas and rocks play important roles in many aspects of volcanology, petrology, geochemistry, economic geology and volcanic hazards. Peralkaline magmas and rocks are relevant for a number of different reasons, as described here below:

1. Peralkaline volcanic systems can produce vast quantities of eruptive products, substantially contributing to the growth of the continental crust. For instance, the Oligocene peralkaline ignimbrites of Ethiopia's western plateau are estimated to have a dense-rock-equivalent volume exceeding 60,000 $km^3$ (Ayalew et al., 2002). Within the Main Ethiopian Rift, peralkaline rhyolites make up around 90% of the volcanic output (Trua et al., 1999). A pantelleritic phase that occurred in central Kenya between 6.36 and 8.13 Ma originally covered roughly 40,000 $km^2$ (Claessens et al., 2016). The Deccan flood basalts in India preserve an estimated volume of $1.5 \times 10^6$ $km^3$, while the associated peralkaline rhyolites have volumes ranging from 500 to 1000 $km^3$ (Lightfoot et al., 1987).
2. Ongoing volcanological and petrological investigations of peralkaline volcanic rocks are uncovering the intricate evolutionary pathways of peralkaline silicic centres, each of which exhibits distinct characteristics. These include variations in petrogenetic interactions, lithological diversity, magma chamber dynamics and the precise P–T–X conditions governing magmatic evolution. Such research also enhances our understanding of magmatic phase relationships and stability conditions within the corresponding intrusive systems, where secondary alterations often obscure primary features.
3. Numerous peralkaline volcanoes pose potential eruptive hazards, carrying significant implications for human populations and infrastructure. Recent geophysical observations indicate unrest at several Ethiopian Rift volcanoes, including Corbetti, Aluto, Bora and Haledebi (Biggs et al., 2011; Hutchison et al., 2016a,b). In the Kenya Rift, Longonot and Menengai calderas (Biggs et al., 2009) and the Olkaria volcanic complex (Clarke et al., 1990) are likewise considered capable of future eruptions. The AD 946 eruption of Changbaishan–Tianchi volcano on the China-North Korea border (Pan et al., 2020), also called the "Millennium Eruption", ranks among the two most voluminous Holocene eruptions, comparable only to the 1815 CE Tambora event in Indonesia.

4. Awareness is growing that peralkaline volcanic eruptions can exert substantial environmental impacts through sulphur release, potentially inducing short-term global cooling (Scaillet & Macdonald, 2006a). Consequently, understanding the processes controlling these emissions and developing predictive models for their magnitude are crucial research objectives..
5. Peralkaline granitic systems often serve as hosts for rare-metal mineralization, as seen at Strange Lake (Canada; Salvi & Williams-Jones, 2006), the Ambohimirahavavy complex (Madagascar; Estrade et al., 2014), Khan Bogd (Mongolia; Kynicky et al., 2011), the Haldzan Buragtag massif (Mongolian Altai; Kovalenko et al., 2009), and the Siwana peralkaline granite (India; Mondal et al., 2021). Their extrusive counterparts record crucial information on rare-metal enrichment during magmatic differentiation and offer insights into subsequent hydrothermal modification. Moreover, peralkaline volcanic rocks themselves can exhibit high concentrations of critical metals; when exposed at the surface, these deposits may be economically exploitable and warrant further exploration.

Although the generation of peralkaline magmas involves complex petrological and geochemical processes related to mantle source characteristics, crustal interactions and magma differentiation, these aspects are beyond the scope of the present study. Here, the focus is instead on the volcanological implications of peralkaline magmatism, including eruption dynamics, products and associated hazards.

## Fluids and degassing

Water values in the literature peralkaline magmas are in the range 3.5–5.8 wt% except for a value of 7.9 ± 0.5 wt% for a comenditic trachyte pumice from Puy Chopine, Massif Central, France (Martel et al., 2013). Levels of $CO_2$ are usually low, <150 ppm (Lowenstern and Mahood, 1991; Gioncada and Landi, 2010; Field et al., 2012; Neave et al., 2012; Lanzo et al., 2013). Such low values strongly suggest that most of the $CO_2$ is lost from the magmatic system during the pre-pantellerite evolutionary stages. Lowenstern (1994) suggested that the low $CO_2$ contents of Pantescan pantellerites (<100 ppm) are consistent with saturation with a mixed $H_2O$–$CO_2$ vapour at 50–100 MPa. Neave et al.(2012) used the $H_2O$ and $CO_2$ contents to estimate a maximum equilibration pressure of 1.5 kbar (150 MPa). Fluorine abundances in peralkaline rhyolites can be very high, e.g., ≤ 2.2

wt% in the pantelleritic Gold Flat ignimbrite in Nevada (Macdonald et al., 2019), or very low, e.g., ≤ 0.13 wt% in the Green Tuff, Pantelleria (Liszewska et al., 2018). The high values are in part made possible by the tendency of F to partition into the melt during magma evolution (Webster et al., 1993; Barclay et al., 1996). In peralkaline silicic magmas, Cl partitions between melt, vapour, and saline liquids. How it partitions determines, inter alia, when it is degassed from the melt. For example, high and constant levels of Cl (up to 1 wt%) in pantellerites are because they are saturated with $H_2O$–NaCl fluids at low pressures (Metrich and Rutherford, 1992; Lowenstern, 1994). As an example of degassing, White et al. (2009) showed that a Cl-rich aqueous phase exsolved in the transition pantelleritic trachyte to pantellerite on Pantelleria. Neave et al. (2012) noted that Cl abundances in melt inclusions in the pantellerites are consistent with partitioning of Cl into a subcritical hypersaline fluid at low pressures, while Lanzo et al. (2013) used combined $H_2O$ and Cl data to estimate a confining pressure of ~50 MPa for Pantescan pantellerites. From determination of volatiles, mainly $H_2O$ and $CO_2$, in melt inclusions in phenocrysts, saturation pressures can be calculated using solubility models, such as those of Di Matteo et al. (2004) and Papale et al. (2006). The pressure estimates are then converted to depth. The method relies on the magmas having been volatile-saturated prior to eruption and suitable crustal density models being available. el. Neave et al. (2012) also used $H_2O$ and $CO_2$ data to estimate equilibration pressure for Pantescan pantellerites of up to 1.5 kbar. For the Green Tuff ignimbrite, Pantelleria, which is virtually $CO_2$-free, Lanzo et al. (2013) found a pressure interval of 45-65 MPa. Considering the possibility that some water may have been lost by degassing of the melt inclusions, they preferred a storage depth of 2.5 km.

## Volcanic hazard

Several peralkaline silicic volcanoes have the potential to erupt in the near future. One of the most spectacular is the Changbaishan-Tianchi volcano, China/North Korea. When it erupted around 946 CE, it deposited ~100 $km^3$ of comendite–trachyte ejecta which spread as far as northern Japan, a distance of some 1000 km, where some 4-5 cm of ash were deposited (Horn and Schmincke, 2000; Wei et al., 2013; Pan et al., 2017). With a Volcanic Explosivity Index (VEI) of 7, the eruption is one of the two largest Holocene eruptions on Earth. From 2002-2005, there were marked increases in seismicity, deformation and the hydrogen and

helium contents of spring waters, causing regional concern. The unrest did not result in an eruption, but it stressed the need for complete and continuous monitoring, especially since millions of people live close to the volcano (Wei et al., 2013). The magmas of the Millennium Eruption may have been stored in the crust for 10,000-20,000 years before eruption (Zou et al., 2010; Wei et al.,2013); future eruptions may not be imminent. Throughout the East African Rift System, it appears that shallow magmatic processes are currently operating on a decadal timescale (Biggs et al., 2011). In the Kenya sector, three centres (Paka, Menengai and Longonot) showed signs of inflation or deflation over the period 1997–2008, as determined by InSAR (Biggs et al., 2009). The Olkaria volcano complex, associated with the caldera centres, is a multi-centred comenditic dome field which last erupted at 180 ± 50 yBP (Clarke et al., 1990). Menengai, Olkaria and Longonot are located in densely populated areas and present important hazards to life and property. Further north, in the Main Ethiopian Rift, four volcanic centres (Aluto, Corbetti, Bora and Haledebi) experienced deformation from 1993 to 2010 (Biggs et al., 2011; Gleeson et al., 2017; see also Fontijn et al., 2018). As in Kenya, the hazard implications are significant; for example, 6.8 million people live within 100 km of Aluto. On the basis of a newly developed probabilistic volcanic hazard assessment methodology, Clarke et al. (2020) argued that numerous settlements, amenities and economically valuable geothermal infrastructure lie within the most hazardous regions of the Aluto caldera. More than 250,000 people could be endangered by an even modest-scale eruption (0.5 $km^3$ of magma) from the Corbetti Volcanic system (Rapprich et al., 2016). In an earlier phase of magmatic activity, layers of tephra 15-20 cm thick and compositionally similar to the Oligocene Ethiopian plateau ignimbrites have been found in the central Indian Ocean ~2600 km away from the ignimbrites. Ayalew et al. (2002) speculated that the tephra layers represent distal fallout from the Ethiopian ignimbrite-forming eruptions. On Pantelleria, ash from the eruption of the Green Tuff ignimbrite (45.7 ± 1.0 Ma; Scaillet et al., 2013) reached as far as the Dodecanese, 1300 km away (Margari et al., 2007). As noted above, there is much uncertainty about the volcano's future eruptive potential, but careful monitoring is necessary. Mayor Island is the emergent portion of a compound lava shield built predominantly of peralkaline rhyolites. A caldera formed during two or three collapse periods some 6300 years ago. The most recent eruption is thought to have occurred 500-1000 years ago (Houghton et al.,1992). Ash from the caldera-forming event produced

tephra deposits up to 70 cm thick on mainland North Island, New Zealand. Nemrut volcano, adjacent to Lake Van in Turkey, is the country's most active volcano. Magmatism for ~570,000 years has been dominated by peralkaline trachytes and rhyolites (Macdonald et al.,2015), the most recent eruption, ~500 years ago, being of comenditic lava flows in a rift valley on the northern flank of the volcano (Peretyazhko et al., 2015). The active Furnas central volcano on São Miguel, Azores, is considered to be one of the most hazardous in the archipelago. There have been ten young (<5 ka) sub-Plinian eruptions of comenditic trachyte (Jeffery et al., 2016), the latest occurring in 1761 CE (Pimentel et al., 2016).Pimentel et al. (2021) describe the potentially devastating effects on the 55,000 inhabitants of a future ignimbrite-forming eruption of Pico Alto volcano, Terceira. A further, and perhaps underestimated, hazard is the emission of CO2 and radon from active systems. For example, D'Alessandro et al. (2018) have estimated that the total $CO_2$ output of the volcanic/geothermal system of Pantelleria is 24.2 tons per day and have pointed to areas on the island which are at high risk to human health from indoor concentrations exceeding European Union threshold values. It is perhaps inevitable that such high concentrations also characterize other systems and detailed monitoring is required.

## Ore deposit potential

Critical elements and/or materials are defined as those elements for which a marked increase in usage has emerged, relative to past consumption. These elements or materials are usually listed as strategic based on assessed risks to their supply and/or impact to potential supply restrictions. Although the particular element list varies as a function of assessor, country, or economic union, they have many things in common. The critical elements include two general groups: (1) traditional commodities that have either very limited occurrences or supply such as Co and Sn and/or are involved in new technologies such as Mn and Sb, (2) and elements such as REE, Y, Nb, Ta that are used in new technologies such as electric vehicles, smartphones, wind power generation, and superalloys for jet engines and turbine blades. The magmatic processes that yield peralkaline magmas enrich the final products in incompatible elements such as REE, HFSE, etc. (e.g., Mahood and Stimac, 1990). The concentration of these elements can be further enhanced by late-stage magmatic and hydrothermal fluids, and supergene processes. Peralkaline intrusives have been explored and

mined for these elements for many decades (e.g., Bokan Mountain, Alaska, USA, Strange Lake, Canada, Lovozero, Russia, Siwana Complex, India, and Norra Kärr, Sweden). With the rapidly increasing use of REE in modern technology, current REE deposit exploration considers all potential sources. Mungall and Martin (1996) described a peralkaline rhyolite, Terceira, Azores, with extreme enrichment of HFSE in the glass and suggest that this occurrence is analogous to the Strange Lake, CA intrusive; however, mining in the Azores is improbable. Chandler and Spandler (2020) report active exploration in a peralkaline rhyolite complex in the Peak Range volcanics in central Queensland, Australia that is extremely enriched in REE and HFSE. Uranium is included in some critical element lists due to military, medical isotope and energy production, and satellite-energy uses. The Streltsovka caldera hosts the largest U mine and reserves in Russia. The ore developed through an extensive hydrothermal system that mobilized U from both the Late Jurassic peralkaline volcanics as well as from the Hercynian subalkaline granitic basement (Chabiron et al., 2003). Castor and Henry (2000) describe exploration of large U deposits in Tertiary volcanics in Nevada and Oregon, USA. The peralkaline McDermitt and Virgin Valley calderas host rhyolites with U contents up to 15 ppm; much of the ore is hydrothermal with high Zr contents. Also of considerable importance, the largest Li deposit in the USA (~2 Mt) occurs in basins adjacent to the McDermitt caldera. The Li has been leached from peralkaline rhyolite lavas and ash by hydrothermal and meteoric fluids (Benson et al., 2017) and is bound in clay in ash-rich sediments. The Cumberland Hill (New Brunswick, CA) peralkaline rhyolite is highly enriched in incompatible elements including U (up to ~20 ppm). Gray et al. (2010) suggest that the combination of a high U content and the probable supergene remobilization into the host sedimentary basin would create an area with high U ore potential. The interplay of various factors makes a mineral deposit economic, such as tonnage and grade, amenability to mining and processing, acceptable low values of deleterious components, the impact on the environment, and market demand and price. Peralkaline extrusives with the requisite tonnage and grade, would be good candidates for mining mainly due to their surficial position conducive to open pit mining and their relative ease of beneficiation. Exploration targets should also observe the potential for hydrothermal and/or meteoric fluid element mobilization to nearby sedimentary hosts.

Peralkaline magmas and rocks, and in particular pantellerites, play a key role in various fields of the geosciences. They contribute to continental crustal growth, serve as natural models for studying magmatic evolution and represent potentially explosive volcanic systems of great relevance for assessing volcanic hazards and global environmental impacts. At the same time, their distinctive chemical composition leads to enrichment in rare and critical elements, giving them notable economic importance. Given their multidisciplinary significance and distinctive eruptive behavior, pantellerites provide an ideal case study for investigating vulcanological aspects, with particular focus on the processes of magma ascent, degassing, and eruption in peralkaline silicic systems.

## 1.2 Aim of the work

Peralkaline rhyolite viscosities are so low that it has been postulated (Di Genova et al., 2013) that the fragmentation threshold for brittle failure (Papale, 1999) should never be reached during magma ascent and degassing unless disequilibrium conditions or microlites/nanolites crystallization takes place, though numerical modelling has suggested that changes in initial temperature may induce brittle fragmentation even for these peculiar magmas (Campagnola et al., 2016). Peralkaline magmas are associated with a large range of eruptive styles (Houghton et al., 1985, 1987, 1992; Mahood and Hildreth, 1986; Stevenson and Wilson, 1997). On the island of Pantelleria, Italy, magmas with near-identical major element compositions have produced domes, lava flows (including fountain fed agglutinates), pumice cones, thick tephra fall deposits and pyroclastic flow deposits (Villari, 1974; Mahood and Hildreth, 1986; Civetta et al., 1988, 1998; Stevenson and Wilson, 1997; White et al., 2009; Neave et al., 2012). The widespread welding and rheomorphism of the ignimbrites and fall deposits (Schmincke, 1974; Wolff and Wright, 1981; Mahood, 1984) are a consequence of the low viscosity and correspondingly low glass transition temperature ($T_g$) of peralkaline melts, which can allow deformation to continue for many days after emplacement (Di Genova et al., 2013, Scarani et al., 2023). Understanding the mechanisms that allows the fragmentation of these low viscosity magmas and that can cause the shift between large-scale explosive and mild effusive eruptions, as evidenced by the wide spectrum of eruptive styles and intensities, as well as the extended welding and large-scale rheomorphic structures commonly associated with silica-rich peralkaline magmas, represents a

fascinating and intriguing question in volcanology. In this study, we use textural observations made on juvenile products, together with viscosity measurements and observations of the glass structure by Raman spectroscopy, initial and residual volatile content estimation by melt inclusion and Simultaneous thermal analysis (STA) and evolved gas analysis by mass spectrometry (EGA-MS) for four different eruptions from Pantelleria Island expressive of different eruptive styles (from strombolian to sub-Plinian to Plinian) with the aim of reconstructing the eruptive dynamics of peralkaline melts and to unravel the role of different physical and chemical parameters in producing eruptions with different energetics and styles. We discuss the conditions upon which peralkaline magmas can and do fragment giving rise to very explosive caldera forming eruptions such as the Green Tuff. Variation in temperature, volatile content and composition, geometry of the conduit, VNDs and depth of magmatic chamber are held responsible for the great variety of eruptive style encountered on Pantelleria island, from highly energetic Plinian eruption (Cinque Denti and Green Tuff) to sub-Plinian eruption (Zinedi) to effusive eruption (Cuddia Mida), as well as for the welding and rheomorphism associated to those low viscosity peralkaline melts.

## 1.3 Pantelleria Island: geological and volcanological background

Pantelleria is a pear-shaped volcanic island, approximately 80 $km^2$, and it represents the emerged part of a large volcanic complex that lies on a submerged NW-SE trending continental rift between Sicily and Tunisia (Civile et al., 2008; Lodolo and Civile 2010; Rotolo et al., 2006), in the foreland of the Africa-Europe collision zone. The Sicily Channel Rift Zone (SCRZ) is developed within the Pelagian Block, in the northest part of the African plate, which underwent a tectonic stretching since the Late Miocene – Early Pliocene (Civile et al., 2008). The island of Pantelleria is completely of volcanic nature and the beginning of emerged activity is dated at 324.2±10.5 ka (Mahood & Hildreth, 1986). The structural setting of the island is defined by faults and fractures following the regional northwest-southeast and northeast-southwest trends (Civetta et al., 1988). The landscape is dominated by two nested calderas: La Vecchia caldera (140–145 ka old; Rotolo et al., 2013) and the Cinque Denti caldera (45–50 ka old; Mahood & Hildreth, 1983, 1986). The latter is considered associated with the caldera-forming Plinian eruption of the Green Tuff (GT; Orsi & Sheridan, 1984),

although Williams (2010) questioned this point, supposing that a large part of the Cinque Denti caldera might be older than the GT eruption. The volcanological evolution of Pantelleria appears to be extremely complicated and was recently reviewed by Rotolo et al. (2021). They summarized the Pantelleria activity as a sequence of nine ignimbrite eruptions, interspersed with inter-ignimbrite activity during which several local centers were active (Jordan et al., 2018), with at least two caldera collapses (but likely up to five). After the emplacement of the last ignimbrite, the Green Tuff, volcanism resumed with numerous (>40) low explosivity to effusive eruptions produced from several spatially and temporally close eruptive vents (local centers). The island is characterized by a bimodal suite of basaltic and trachytic to rhyolitic lavas and pyroclastic deposits (Civetta et al., 1984). The majority of the exposed eruptive products are felsic, ranging from metaluminous trachyte to peralkaline rhyolite, whereas basaltic magmatism has also occurred at several stages in the island's history (Mahood & Hildreth, 1986; Rotolo et al., 2013; Rotolo et al., 2019). No eruption has been recorded in historic times, though a small basaltic submarine eruption was witnessed, offshore, in 1891 (Washington, 1909; Coltelli et al., 2016). The volcanological history of Pantelleria can be divided in three main cycles (Rotolo et al., 2013):

. The first cycle of activity (324-180 ka) is characterized by effusive and explosive activity (Mahood & Hildreth, 1986). A reliable estimate of the volume of magma erupted during this period is precluded because most of the eruptive units are buried by younger deposits.

2. The second cycle (190-45 ka) consist of a series of ignimbrite forming eruption, alternated to >20 local effusive/strombolian eruptions, the last one being the Green Tuff which mantles all older stratigraphy (Wolff and Wright, 1981; Mahood and Hildreth, 1986; Scaillet et al., 2013; Williams et al., 2014). At least 9 ignimbrite events occurred during this period, ranging in composition from trachyte to comendite/pantellerite. These are, in a chronological order: Zinedi fm., Pozzolana fm., Polacca fm., Arco fm., Capre fm., Cinque Denti fm., Acqua fm., Mordomo fm. and Green Tuff (Jordan et al., 2018). Among these, two eruptions have been linked, based on geomorphological observation, to the formation of two main caldera collapse: the first, originated La Vecchia Caldera (140 ka), and then the Cinque Denti caldera (46 ka), nested in the first one. The latter is related to the Green Tuff eruption and marks the last caldera collapse and the end of the second cycle of activity (Civetta et al., 1984; Mahood and Hildreth,

1986; Rotolo et al., 2013). Volumes of onshore erupted magma were estimated to be 2.32 $km^3$ DRE, cumulative of all nine ignimbrites, including the Green Tuff, with individual volumes ranging from 0.003 to 0.64 $km^3$ DRE (Jordan et al., 2021; Jordan et al., 2018). The presence of lithic breccias in 5 ignimbrites (Green Tuff, Mordomo, Bagno dell'Acqua, Capre e Polacca) suggests that, although there are only two evident caldera collapses, there were actually at least five, the remains of which would have been covered by more recent products (Jordan et al., 2014; Jordan et al., 2018).

3. The third cycle of activity (45-8 ka) consists of more than 50 low energy eruptions (strombolian eruptions, lava flows or lava domes), predominantly of pantelleritic composition, that followed the Cinque Denti caldera collapse (post-Green Tuff) (Rotolo et al., 2007, Scaillet et al., 2011). During this phase, volcanism develops primarily within the most recent caldera with much lower erupted volumes. Th post Green Tuff activity started with the eruption of Mt. Gibele – Montagna Grande trachyte lava, immediately following the Cinque Denti caldera collapse, with estimated erupted volumes of 3 $km^3$ (Mahood & Hildreth, 1986). The end of the last cycle is marked with the eruption of extra caldera basalts (scoria cones and lava flows) confined in the northwest sector of the island (Rotolo et al., 2021 et references therein).

### 1.3.1 Targeted eruptions

In order to understand which is or which are the parameters that govern the transition from a low-energy to a high-energy eruption, we selected four different eruptions similar in chemical composition but different in eruptive style. The selected eruptions are:

1. **Cinque Denti eruptive unit (125 ka)**: it comprises a pumice-fall deposit at the top and a welded ignimbrite at the bottom (Jordan et al., 2018). The bulk of the ignimbrite is grey, poorly sorted, matrix-supported, crystal-rich and lithic poor with subtle fiamme (Jordan et al., 2018). The top fall member is a ~0.6–1 m thick layer is made by white to yellow to orange clast-supported well-sorted pumices and subordinate black glassy lithic lapilli (Jordan et al., 2018). The colour grades from yellow-white at the base to bright orange-red at the top (Jordan et al., 2018). This eruption has been classified as a Plinian eruption (Jordan et al., 2018). For our purposes we collected pumices from Cinque Denti basal fall (Fig. 1.1). Geographic coordinates of the sampling sites: 36°49'8.36"N 11°59'42.73"E.

*Fig. 1.1* Basal fall from Cinque Denti eruptive unit.

2. **Green Tuff eruptive unit (50 ka)**: the Green Tuff eruptive unit consists of a 1 m thick pumice fall at the bottom and the Green Tuff ignimbrite, on average 5 m thick, interpreted as a low aspect-ratio ignimbrite, as described by Williams (2010) and Williams et al. (2014). There is no clear evidence for a single caldera-forming phase during the eruption but some of the breccia lenses may record reactivation of existing caldera scarps (Jordan et al., 2018). This eruption has been classified as a Plinian eruption (Jordan et al., 2018). The Green Tuff eruption represents the most studied eruptive event in Pantelleria history (eg., Villari, 1974; Wolff and Wright, 1981; Orsi and Sheridan, 1984; Mahood and Hildreth, 1986; Williams, 2010; Lanzo et al., 2013; Scaillet et al., 2013; Williams; 2010; Williams et al., 2014; Jordan et al., 2018; Liszewska et al., 2018; Romano et al., 2019). For our purposes we collected pumices from Green Tuff basal fall (Fig. 1.2). Geographic coordinates of the sampling sites: 36°49'08.4"N 11°59'42.7"E.

*Fig. 1.2* Basal fall from Green Tuff eruptive unit.

3. **Zinedi eruptive unit (189 ka)**: it consists of a lava overlain by a mostly massive non-welded ignimbrite (Jordan et al., 2018). Zinedi formation is a ~15 m thick grey non-welded clast-supported pumice-rich ash-lapilli deposit interpreted as an ignimbrite and it's the only non-welded ignimbrite among the nine recognized on the island (Jordan et al., 2018). For our purposes we collected pumices from the non-welded ignimbrite (Fig. 1.3). Geographic coordinates of the sampling sites: 36°49'26.62"N 11°59'2.24"E.


*Fig. 1.3* Zinedi non-welded ignimbrite. Unfortunately, no more detailed photo has been taken.

4. **Cuddia Mida eruptive unit (9.7 ka)**: it consists of a monogenetic cone derived from a Strombolian eruption (Hughes et al., 2017). The lowermost layer of the sequence is an explosion breccia (1m thick) and is overlain by a poorly-sorted fallout layer, which has an increasing ash content towards the top (0.3 m). Above this is an ashy bed (0.08 m) overlain by a much thicker, massive, poorly-sorted fall deposit (1.2 m) (Orsi et al., 1991 ). For our purposes we collected pumices from the upper fall deposit (Fig. 1.4). Geographic coordinates of the sampling sites: 36°47'15.40"N 11°59'33.10"E.

*Fig. 1.4* Cuddia Mida eruptive unit.

Juvenile products, pumices, from the four targeted eruptions were sampled and used as a proxy to investigate magma fragmentation processes. All analyses presented in this study were conducted on these samples.

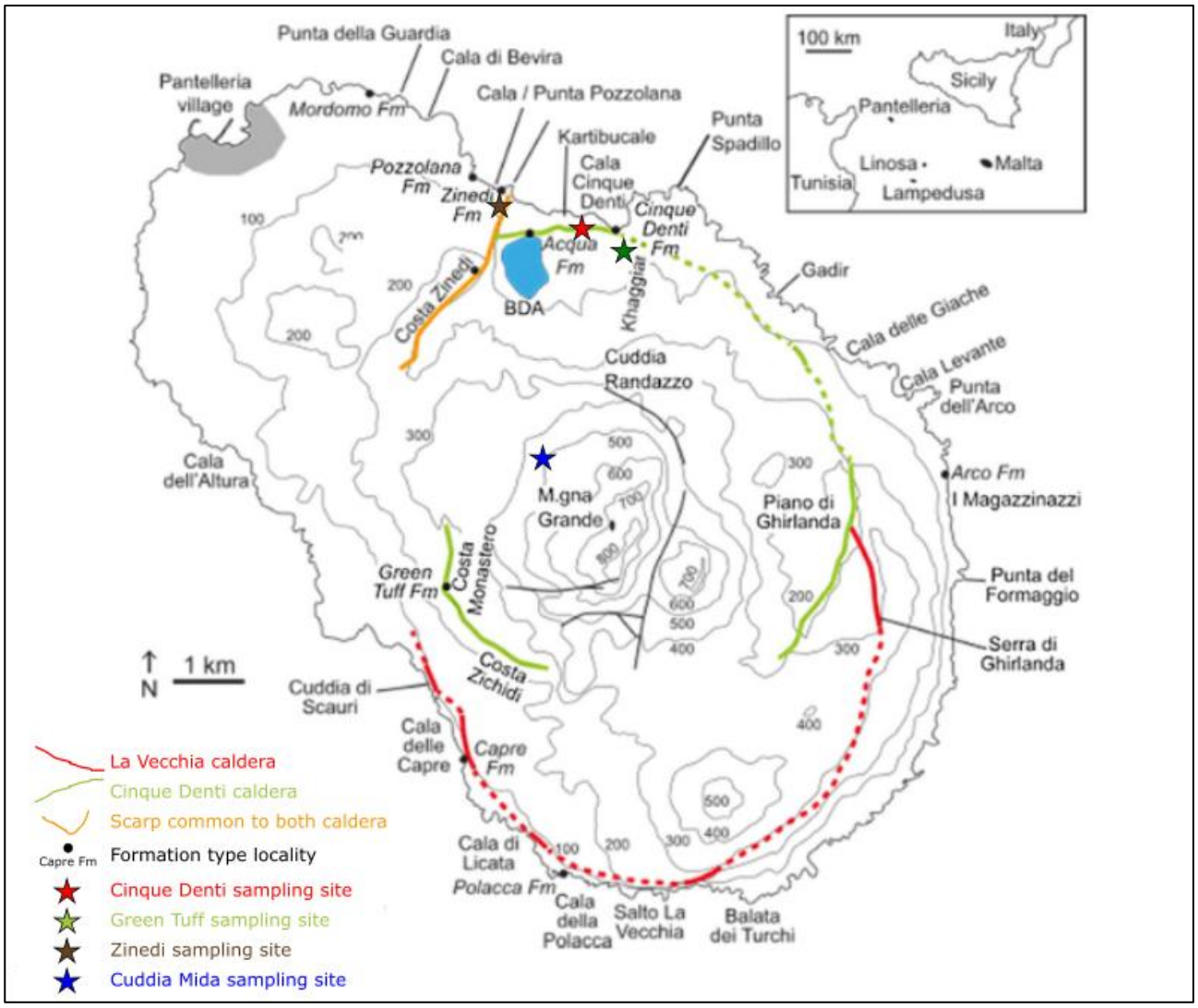


*Fig. 1.5 Map of Pantelleria showing topography (CI = 100 m), proposed calderas (after Mahood and Hildreth, 1986), post-caldera faults, with indicated the sampling sites for the analysed fallout pumices. (modified after Romano et al., 2017).*

## 1.4 Theoretical background

### 1.4.1 Vesicle nucleation and growth theory

Volatiles play the central role in governing the ascent and eruption of magma. Volatile solubility is primarily pressure dependent, with a positive correlation; a secondary dependence is present on temperature, melt composition (McMillan 1994, Blank and Brooker 1994, Zhang et al., 2007). Formulations for volatile solubility can be thermodynamic or empirical. Liu et al. (2005) provided an empirical formulation for combined solubility of $H_2O$ and $CO_2$ in rhyolitic melts. Allabar et al. (2022) provided an empirical formulation for $H_2O$ solubility in peralkaline melts. More accurate models for generic compositions are also available in literature (Dixon 1997, Newman and Lowenstern 2002, Papale et al.,

2006). The decrease in volatile solubility during magma ascent (i.e., decompression-induced) leads to nucleation of bubbles that will grow and coalesce over time, as a consequence of both volatile exsolution and expansion (Sparks, 1978) and even separate completely from the residual melt (e.g., Sparks et al. 1994). The presence of an isolated gas phase allows for significant magma compressibility and buoyancy, ultimately making eruption possible (Pyle and Pyle 1995, Woods and Cardoso 1997). The vesiculation of a magma, especially the size and number of bubbles, changes magma viscosity and density, thus, significantly affecting the eruptive style and triggering explosive behavior. The ability of magma to degas is controlled by several factors, primarily the volatile concentration in the melt and its gas solubility. Moreover, the formation of bubbles depends on the efficiency of volatile diffusion from melt to bubble (a complicated function of composition, viscosity, and time), as well as the time available for expansion, which is the time spent by magma in the conduit and/or at the surface (Toramaru 1995; Lyakhovsky et al. 1996; Proussevitch and Sahagian 1996; Gardner, 1999). In the last decades, several research groups worked on the experimental investigation of bubble forming processes in silicate melts. Because water solubility most strongly depends on pressure, the trigger to nucleate bubbles can be approximated by a drop in pressure (besides to second boiling due to microlites growth). The classical nucleation theory predicts that magma starts to nucleate when it becomes super-saturated in a volatile phase as soon as the pressure in the system decreases. On the basis of the supersaturation pressure, the nucleation can be homogeneous or heterogeneous. In the case of homogeneous nucleation of bubbles, an extremely high supersaturation pressure is required (Mangan and Sissan, 2000; Gardner et al., 1999). Thus, fragmentation of magma occurs largely above the volatile saturation pressure in the conduit. On the other hand, the existence of impurity in the melt, such as tiny microlites, provides preferential site for the formation of new bubbles, where activation energy (ie., the supersaturation pressure) required to nucleate is much lower (Hurwitz and Navon 1994; Sparks et al., 1994; Gardner and Denis 2004; Gardner, 2007; Iacono Marziano et al. 2007; Larsen 2008).

### 1.4.2 Degassing process and vesicularity of silicate melts

As magma rises through the conduit, the pressure decreases, along with the solubility of the volatiles dissolved in the melt. If the concentration of dissolved volatiles exceeds the equilibrium solubility at a given pressure, the melt is

supersaturated: volatiles will start to exsolve forming small clusters of gas molecules which grow through volatile diffusion in the melt, decompression and coalescence (Proussevitch et al. 1993; Proussevitch and Sahagian 1998). Supersaturation, ΔP, is defined as the difference between actual pressure of the melt and the pressure at which the concentration of dissolved volatiles would be in equilibrium with the co-existing vapor phase (Gonnerman and Mangan, 2012). The saturation required for nucleation ($\Delta P_N$) corresponds to the energy that must be supplied to increase the surface area between two fluids, bringing to a decrease of surface tension. The formation of a stable nucleus of bubbles is described through thermodynamic expression (Sparks, 1978), in terms of free energy of formation (ΔG*):

$$\Delta G* = \frac{16\sigma^3}{3\,(\Delta P_N)^2} \quad (1.1)$$

where $\sigma$ is the surface tension or melt-bubble interfacial energy. Exsolution of bubbles will take place if a supersaturation pressure is achieved to overcome the activation energy, or the surface tension: the ratio between these two factors determines the criterion for the critical size of nucleus $r_c$ ($r_c = 2\sigma/\Delta P_N$), after which a bubble will spontaneously grow, thus defining the possibility of homogeneous or heterogeneous nucleation to happen. Heterogeneous bubble nucleation is promoted by the presence of wetted crystal surfaces that can act as bubble nucleation sites, lowering considerably the energy barriers to overcome the critical bubble radius, $r_c$. Particularly it has been proven that Fe-Ti oxides are the preferred nucleation sites, owing to smaller contact angle with the bubble, minimizing the surface tension term (Hurwitz and Navon, 1994; Mangan and Sisson, 2005). Typically, the supersaturation pressure is lower when heterogeneous bubble nucleation happens (few MPa) than in the case of homogenous nucleation (~10 to 100 MPa) (Fig. 1.6) (e.g., Hurwitz and Navon 1994; Gardner and Denis 2004; Gardner, 2007; Iacono Marziano et al. 2007; Larsen 2008). Mangan et al. (2004a) showed, based on numerical modeling using available experimental data, that heterogeneous bubble nucleation is trigged in water-saturated rhyolite at supersaturation pressures $\Delta P_N$ < 5-20 MPa, while a supersaturation pressure above 120–150 MPa is required for homogeneous nucleation (Fig. 1.6).

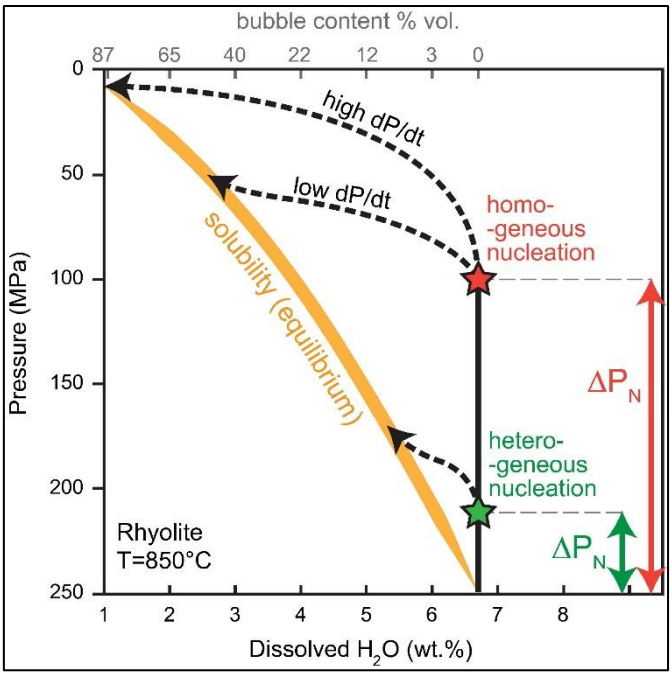


*Fig. 1.6 The influence of nucleation behavior on degassing efficiency of a rhyolite melt (modified after Mangan and Sisson, 2000), expressed in terms of Pressure (y-axis) vs. dissolved water content (lower x-axis) and the equivalent melt porosity (upper x-axis). A water-saturated melt ascends from a storage region at ~250 MPa and either (1) starts to exsolve early via heterogeneous nucleation and tracks a near-equilibrium path defined by the solubility curve, or (2) exsolves late through homogeneous nucleation after attaining large values of supersaturation ($\Delta P_N$), in which case non-equilibrium degassing ensues. The extent of this departure from equilibrium will depend on the decompression rates. (From Shea, 2017).*

The nucleation rate is expressed as a function of T and P as:

$$J = J_0 exp\left[\left(\frac{-16\pi\sigma^3}{3kT\Delta P^2}\right) * \varphi\right] \quad (1.2)$$

where $\sigma$ is surface tension, ΔP is the super-saturation pressure, T is temperature, and k is Boltzmann's constant (Hirth et al., 1970; Hurwitz and Navon, 1994). $\phi$ is a geometrical factor that depends on θ, the contact angle between bubble and crystal, and is given by:

$$\phi = \frac{(2 - cos\theta)\,(1 + cos\theta)^2}{4} \quad (1.3)$$

values of $\phi$ ranges between 0 and 1 and determine a boundary between heterogeneous and homogeneous nucleation mechanism (eg., Shea, 2017). Surface tension, which expresses the energy required to create and maintain an interface between the bubble and the melt, is one fundamental factor, as it is elevated to the cube in the exponential term of the equation (1.2) and appears also in the pre-exponential term $J_0$, which equation is modified by Navon and Lyakhovsky (1998) as:

$$J_0 = \frac{n_0^2 D}{8\pi(\frac{\sigma}{kT})^2} \quad (1.4)$$

where $n_0$ is the concentration of water molecules per volume melt, D is the diffusivity of $H_2O$ at the bubble-melt interface and $\sigma$/kT) can be assumed as a geometrical factor. Clearly, even a small variation in surface tension can held great impact on the kinetic of nucleation. Hence, various recent works focused on the study of this property of magma, giving particular attention to the strong influence of melt composition and water content on the variation in $\sigma$, with contrasting results (Bagdassarov et al. 2000; Mourtada-Bonnefoi and Laporte 1999, 2002, 2004; Mangan and Sisson 2000, 2005; Iacono Marziano et al. 2007; Gardner, 2012; Gardner et al., 2013). For instance, Mangan and Sisson (2005) showed a positive correlation between surface tension and increasing silica content, for evolved silicic melts, which will negatively affect the nucleation rate. On the other side, following a series of experimental studies on degassing behavior for different melt compositions, Gardner et al. (2013) concluded that chemical composition has a minimal impact on surface tension. They observed that despite wide variations in silica content (within 25 wt%) and other chemical components (e.g., total alkalis, Fe and Mg contents), surface tension doesn't seem to vary systematically, varying within a narrow range, in agreement with other previous published results (eg., Bagdassarov et al., 2000; Walker and Mullins, 1981). The growth of existing gas bubbles requires lower energies and can occur progressively through a combination of three processes:

1. volatile diffusion from the melt into adjacent existing bubbles;
2. volume expansion (Boyle gas law) due to decreasing ambient pressure;
3. bubble – bubble interaction (coalescence).

**Diffusion**

Growth by diffusion involves the migration into a bubble nucleus of molecules of oversaturated volatiles at constant pressure. The diffusion process is influenced by many factors, especially the magma composition, the magma temperature, and the mixture of other gas species present and the variation of solubility of the gas species in response to decompression (Proussevitch et al., 1993; Proussevitch and Sahagian, 1998). The diffusion of volatiles through the melt is

particularly important at the first stages of growth of a bubble, as even a relatively small amount of gas causes a relatively large increase in the size of the bubble. Besides, the movement of water molecules close to the bubble establishes a concentration gradient around the bubble that acts in driving more molecules towards the center, thus further growing can occur (Fig. 1.7). However, in the later stages of the process, growth by diffusion becomes progressively less significant, both because the relative increase in bubble volume decreases and, more importantly, because as the magma becomes progressively more anhydrous (and possibly cooler), its viscosity increases and the diffusivity of water decreases. Under these conditions, the dominant growth mechanisms become bubble expansion and coalescence.

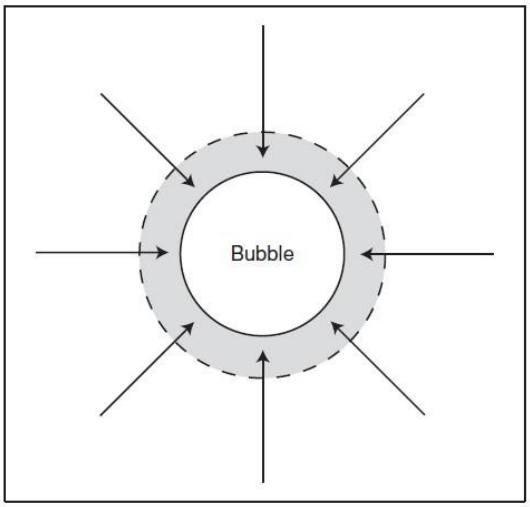


*Fig. 1.7 Water concentration gradient generated by diffusion of molecules into a bubble from the surrounding liquid. The migration of volatiles driving molecules into an area of low concentration, towards the bubble, increasing growth (from Parfit and Wilson, 2008).*

### Volume expansion

The gases contained in a bubble tend to expand as pressure decreases, according to the Boyle's gas law: PV = constant, or $P_1V_1=P_2V_2$. This means that, as magma rises close to the surface and lithostatic pressure decreases, the gas bubbles contained in the magma will subsequently grow in volume by gas volume expansion. This process is particularly significant when bubbles start nucleating at great depths, hence the pressure change experienced during rising is also high. Magma ascent rates play a key role in degassing and bubble growth, associated with the development of a certain water oversaturation at the surface. Bubble growth is kinetically preferred over bubble nucleation at lower degrees of supersaturation when the necessary nucleation pressure has not been reached

yet. The growth rate ($G_R$) is given by the increase of the bubble radius over a unit of time. Bubble growth can occur at equilibrium conditions or be viscous-limited or diffusion-limited. Equilibrium degassing is consequence only of the solubility variation due to decreasing ambient pressure and is only possible at slow decompression rates (<0.1 m/s) (Proussevitch and Sahagian, 1998).

**Viscous limited bubble growth**

In the viscous-limited case, bubble growth is controlled by viscosity of the melt: if the viscous timescale exceeds decompression timescale bubble growth is retarded, following an exponential growth law (Lensky et al., 2004). Viscous limit to bubble growth is the consequence of fast decompression rates relative to the viscous deformation of melt by the growing bubbles and is most significant at melt viscosities in excess of $10^9$ Pa s (Sparks et al., 1994). Because of retarded bubble growth, pressure of gas $P_g$ decreases at a slower rate than pressure of melt $P_m$, resulting in the buildup of overpressure: $P_g - P_m \gg \sigma/r$. At the same time, a high $P_m$ inhibits volatile exsolution, causing supersaturated conditions.

**Diffusive limit**

In the diffusive-limit, supersaturation of volatile, which increases with decreasing pressure, strongly affects growth by diffusion. During decompression, the volatile concentration at the melt–vapor interface, decreases, producing a concentration gradient which increases volatiles diffusion into the bubble and exsolve (Fig. 1.7; Sparks, 1978; Proussevitch and Sahagian, 1998). If decompression timescales are shorter than those for diffusivity (ie., $\tau_{dec} \ll \tau_{dif}$), volatile concentrations will remain close to equilibrium throughout the melt. On the other hand, at high decompression rates (ie., $\tau_{dec} \gg \tau_{dif}$ and higher than 0.1 MPa/s) the melt becomes fastly supersaturated, favouring nucleation of new bubbles instead of growth of pre-existing bubbles (Lensky et al., 2004). Furthermore, in the diffusive limit, volatiles with different diffusivities may fractionate (Gonnermann and Manga, 2005b; Gonnermann and Mukhopadhyay, 2007).

**Solubility limit**

Furthermore, solubility is also a limiting factor for growth, as at solubility condition bubbles are close to mechanical and chemical equilibrium, and that both overpressure and supersaturation required are small. Conditions favourable

to solubility-limited bubble growth are low melt viscosity and/or low magma ascent rates.

**Coalescence**

Last case for bubble growth is coalescence. Bubbles are always buoyant compared with the rising magma due to the low density of the gases they contain. For this reason, a buoyancy force causes the bubble to rise through the magma with a relatively different velocity, counteracted by the drag force of friction exerted at melt-gas. If the velocity of the bubble is low it maintains a spherical shape and the drag force is controlled just by the viscosity of the magma:

$$F_D = 6\pi r\eta u \quad (1.5)$$

where u is the rise speed of the bubble, r is the bubble radius and η is magma viscosity. Equilibrium between bubble velocity and magma rise speed is reached when the drag force equals the buoyancy force and, thus, the rise speed, u, of the bubble is:

$$u = \frac{\frac{2}{9}(\rho_g - \rho_m)gr^2}{\eta} \quad (1.6)$$

where $\rho_g$ is density of gas phase, $\rho_m$ is density of melt, g is gravitational constant and r is bubble radius. Larger bubbles rise disproportionately faster than smaller ones. This difference in the rise speeds of bubbles of different size is a major factor in bubble coalescence. Coalescence takes place when bubbles coming into increasingly proximity reduce the melt film in-between and eventually collapses (Klug and Cashman, 1996). Bubble growth from coalescence is an essential element in the last stages of degassing, beginning when a certain porosity is already developed (above 43%, as proved by Burgisser and Gardner, 2004). Particularly, coalescence controls the development of a permeability network, affecting the transition between explosive and effusive eruptive regimes (eg., Klug and Cashman, 1996; Yoshida and Koyaguchi, 1999; Burgisser and Gardner, 2004).

The importance of bubble formation is linked to the possibility that a permeability network develops, providing efficient gas escape routes for outgassing (eg., Sparks, 2004). The ability of gases to exsolve from a magma and eventually outgas is of primary importance in the development and/or inhibition of explosive

eruption. The final number density and size distribution of bubble populations in a volcanic rock depends not only on the available volatile concentrations, but also on the ability of the gas phase to diffuse through the melt, as well as the time available for expansion (time spent by magma in the conduit and/or at the surface; Toramaru 1995; Lyakhovsky et al. 1996; Proussevitch and Sahagian 1996). The final number density and size distribution of bubble population may represent a useful proxy to characterize storage, ascent dynamics and eruption conditions (Klug and Cashman, 1994). Differences in timing and rates of bubble nucleation, growth, and coalescence can be quantified by textural vesicularity analysis. The rock vesicularity are commonly investigated through the vesicle size distribution (VSD) and the vesicle number density (VND), giving valuable parameters in understanding and tracing volatile exsolution processes and kinematics of nucleation density and growth rate of bubbles as well as to characterize storage, ascent and eruption conditions (e.g. Marsh, 1988; Klug and Cashman, 1994). VSD refers to the number of bubbles per unit volume within a series of defined size intervals (typically shown in a histogram plot of population density vs. size; Marsh 1988), whereas VND stands for the total number of bubbles per unit volume and can be described as (cf. Toramaru 1995; Gardner et al. 1999):

$$VND = \phi_m \sum \left(\frac{n_i}{N_T * V_i}\right) \quad (1.7)$$

where $\phi_m$ is the vesicle volume fraction, $n_i$ is the bubble number, $N_T$ is the total number of bubbles and $V_i$ is the bubble volume at a diameter i. The tendency of VND to increase with eruption intensity has been experimentally and numerically linked to the dependence of VND on decompression rate, and on other properties such as diffusivity, viscosity, and surface tension (Mangan and Sisson 2000; Lensky et al. 2004; Mourtada-Bonnefoi and Laporte 2004; Namiki and Manga 2006; Toramaru 2006; Cluzel et al., 2008). In particular, it has been proven that decompression rate (r = dP/dt) exerts a strong influence on VND, particularly at fast ascent rates (eg., Toramaru, 2006). The correlation between VND and decompression rates has been modelled from Toramaru (2006) as a reliable decompression rate meter for explosive eruptions. According to this method, based on the vesiculation present in pumices, their Vesicle Number Densities can be used as a valuable tool to a direct estimation of decompression rates (≈ magma ascent rates). The nucleation rate J and subsequent $N_B$ (number of

bubbles) are proportionally linked to decompression (initial pressure ($P_i$) – final pressure ($P_f$)) (Gardner and Ketcham, 2011). Decompression experiments run by Gardner and Ketcham (2011) on rhyolitic and dacitic melts, showed a higher number of bubbles for lower $P_f$, thus increasing J. Nucleation rate J was calculated by dividing the VND by the time allowed for nucleation ($t_N$; eg., Gardner and Ketcham, 2011), in order to evaluate $\sigma$. Higher VND values are an indicator for a large number of bubbles thus, are a record of dominating bubble nucleation over bubble growth (e.g., Mourtada-Bonnefoi and Laporte, 2004; Nowak et al., 2011), as a result of fast decompression rate. Furthermore, the volatile exsolution and nucleation of gas bubbles is strongly dependent on the diffusivity of the volatile species in the melt. Hence, a possible delay in bubble nucleation can occur between a fast and a slow diffusing volatile component, affecting VND. On the other hand, a sudden change to faster decompression rate can also lead to a second nucleation event in magmas with preexisting bubbles as experimentally investigated and modelled by Toramaru (2014) and others (e.g., Masotta et al. 2014). Secondary nucleation events result in complex, multi-peak VSD patterns (Toramaru, 2014) as observed in many studies on natural samples (Sparks and Brazier, 1982; Klug and Cashman, 1994; Klug et al., 2002; Formenti and Druitt, 2003; Polacci et al., 2003, 2008; Lautze and Houghton, 2007; Giachetti et al., 2010; Shea et al., 2010).

### 1.4.3 Textural analysis

Textural characterization of volcanic rocks from explosive eruptions provides valuable insights complementary to field, theoretical and experimental studies in understanding the physical processes that control eruptive style, magma vesiculation, fragmentation and ascent dynamics (Houghton and Wilson, 1989; Klug and Cashman, 1994; Gardner et al., 1996; Blower et al., 2001; Polacci et al., 2001; Klug et al., 2002). Volcanic rocks thus record the sequence of processes occurring before, during and after the eruption (Sparks, 1978; Cashman and Mangan, 1994). A well-established framework now exists to investigate (1) the role of bubble deformation and coalescence in developing permeability for efficient gas escape in highly viscous magma (Klug and Cashman, 1994; Polacci et al., 2007; Colombier et al., 2017); (2) the influence of microlites and nanolites in increasing magma viscosity, constraining bubble growth, and recording syn- or inter-eruptive degassing (Gardner et al., 1998; Di Genova et al., 2017; Cáceres et al., 2020); and (3) how bubble and crystal textures reflect magma decompression

and ascent rates (Cashman and Blundy, 2000; D'Oriano et al., 2005). In general, vesicle number density (VND) increases with eruption intensity (Mangan and Sisson, 2000; Lensky et al., 2004; Namiki and Manga, 2006; Toramaru, 2006), reflecting greater disequilibrium during magma ascent. Among the most widely studied textural parameters are the size and shape distributions of vesicles, which record the magma's degassing history, from volatile exsolution to bubble growth, expansion and gas escape. The final vesicle number density and size distribution depend not only on the volatile content but also on volatile diffusivity in the melt and the time available for bubble expansion during magma ascent and eruption (Toramaru, 1995; Proussevitch and Sahagian, 1996). Hence, the analysis of vesicles and crystals textures (VSD and CSD) are pivotal to characterize magma storage conditions as well as to reconstruct decompression and ascent rates (Geschwind and Rutherford, 1995; Cashman and Blundy, 2000; Polacci et al., 2001; Toramaru, 2006; Shea et al., 2010) and the nature of magma fragmentation (Klug and Cashman, 1994). Vesicle number density per volume (VND) depends on diffusivity, viscosity, and surface tension of the melt (Mangan and Sisson, 2000; Lensky et al., 2004; Mourtada-Bonnefoi and Laporte, 2004; Namiki and Manga, 2006; Toramaru, 2006; Cluzel et al., 2008). It has been observed, indeed, that vesicle number densities are typically higher in explosive silicic eruptions ($10^6 – 10^9$ $mm^{-3}$), when homogeneous nucleation occurs (Mangan and Sisson, 2000; Mangan et al., 2004). This is mainly due to the high supersaturation conditions reached for these eruptions, driven by the high rising velocity and high viscosity of these magmas. Conversely, vesicle number densities of basaltic scoria are drastically lower ($10^4 – 10^6$ $mm^{-3}$), as a result of heterogeneous nucleation at lower supersaturation pressure (Gardner, 1999) typical of Strombolian type eruptions (Toramaru, 1989; Cashman and Mangan, 1994; Toramaru, 1995; Mangan and Cashman, 1996; Mangan and Sisson, 2000; Polacci et al., 2001; Lensky et al., 2004; Mourtada-Bonnefoi and Laporte, 2004; Namiki and Manga, 2006; Toramaru, 2006; Cluzel et al., 2008; Sable et al., 2009; Shea et al., 2010). Hence, VND is expected to scale with SiO2 content (e.g., Sable et al., 2006) and physical eruption parameters such as magma discharge rate or column height (e.g., Gurioli et al., 2008). Because vesicles vary significantly both in size and in number, textural data are always displayed as distributions. The most common ways to represent the textural characteristics of pyroclasts display in terms of either size (L) or number densities ($N_v$) and can be summoned as:

vesicle volume distributions, VVD; cumulative volume distributions, CVVD; vesicle size distribution, VSD; cumulative vesicle size distributions, CVSD.

**VVD**: Vesicle Volume distribution plots are used to infer the nature and the number of nucleation and/or coalescence events during the vesiculation history of pyroclasts (e.g., Klug and Cashman, 1994). In the histogram each mode is interpreted as a distinct pulse of nucleation and growth (Klug et al., 2002; Polacci et al., 2003; Lautze and Houghton, 2008). The presence of a positive skew or distinct larger mode is associated to the occurrence of coalescence (Gurioli et al., 2008; Adams et al., 2006) while, on the other hand, ripening produces a negative skewness (Mangan and Cashman, 1996). Bubble collapse significantly reduces either the total vesicle volume fraction or the modal size of the distribution (Burgisser and Gardner, 2004; Sable et al., 2006).

**CVVD** plots are complementary to VVDs. They provide essential information about the contribution of each size range to the total vesicularity. Unimodal distributions are represented by a sigmoid-shaped curve, while multiple modes add bulges to the curve. Coalescence produces a slope decrease in the upper portions of the sigmoid; ripening results in a right shift of the curve accentuating the lower portion of the sigmoid; collapse generates a curve shifted to the smaller bubble sizes (Klug et al., 2002; Adams et al., 2006; Mongrain et al., 2008). Modes, means and standard deviations can be extracted from VVD and CVVD plots.

**VSD** is a semilogarithmic plot showing population density ln(n) vs. size L (mm), with L equivalent diameter. Such diagram is used commonly used to infer kinematics of nucleation density and growth rate both for crystals and bubbles (e.g., Marsh, 1988, 1998, 2007). According to Mangan and Cashman (1996), linear distributions denote steady-state nucleation and growth. Upward inflexion towards smaller sizes reflects ripening processes while downward inflexion towards larger objects may be caused by coalescence (Fig. 1.8C). In turn, bubble collapse may produce a curve plunging rapidly to the larger size classes. From the segments of the VSD curve it is possible to determinate several physical parameters. In theory, assuming that nucleation and growth rates remain constant during the vesiculation and/or crystallization process, the growth rates (G; mm $s^{-1}$) can be easily calculated as the inverse of the slope. From the intercept at L=0 the initial number density ($n_0$; $mm^{-3}$) can be extracted. The theory is based on the steady-state conservative exponential equation:

$$n = n_0 exp \frac{L}{G_\tau} \ (1.8)$$

assuming that a constraint exists on the time scale for nucleation and growth, τ. Thus, the nucleation rate (J; $mm^{-3}$ $s^{-1}$) is given by

$$J = n_0 G \ (1.9)$$

If the data have a linear trend on the VSD plot, the total number density of vesicles per volume melt can be obtained from the zeroth moment of the previous equation (Cashman and Mangan, 1994):

$$N_{Vfit} = n_0 G_\tau \ (1.10)$$

The first moment gives the dominant diameter, so:

$$L_{fit} = G_\tau \ (1.11)$$

If no time constraint exists, it is possible to derive from the slope of the distribution only the total vesicle number density ($N_{tot}$ in Mangan and Cashman, 1996) and the dominant diameter $L_{Vfit}$. Moreover, the calculated $N_{Vfit}$ can be compared to the $N_{tot}$ directly measured to test if the trend adequately represents the data. If they are similar, the fit can be considered robust.

**CVSD** represents the cumulative distribution of population number density considering the number of objects per cubic mm with diameter greater than L (log($NV>L$) vs. log(L). It has been demonstrated that a power-law distribution could better accommodate the vesicle size distributions produced by continuous/accelerating nucleation (Gaonac'h et al., 1996; 2005; Blower et al., 2001a; 2001b; 2003). Blower et al. (2002) demonstrated, by numerical models, that an exponential log($NV>L$) vs. log(L) curve can be generated by one to three nucleation events:

$$Log\ NV > L \propto e^{-L} \ (1.12)$$

Conversely, numerous nucleation events or continuous nucleation and growth produce a power-law linear trend:

$$Log\ NV > L \propto e^{-D} \ (1.13)$$

where D is the power-law exponent. For this reason, CVSD plots are generally used to differentiate between exponential and power-law distributions, as well as between single, multiple or continuous nucleation (Gaonac'h et al., 1996, 2005;

Blower et al., 2001, 2002; Polacci et al., 2008). Gaonac'h et al. (1996, 2005) predicted that a D value equal to 2.5, close to the Apollonian packing value (Blower et al., 2001), could be apply to a large number of natural samples, from lava flows to pumice. Nevertheless, a broad variability of D is found in literature. In basaltic scoria from Izu Oshima sub-Plinian eruption, D values are similar to the predicted value (D ~2.5; Blower et al., 2002); for the basaltic scoria of Stromboli (Polacci et al., 2007; Bai et al., 2008) and Etna (Simakin et al., 1999) D is 2.8; D range from 2.7 to 2.9 in the 122 BC Etna Plinian basaltic scoria (Sable et al., 2006). It is observed an increase in the D values for explosive silicic eruption, varying from 3.3 in rhyo-dacitic pumice (Klug et al., 2002) and 3.9 in dacitic pumice (Adams et al., 2006). Numerical models by Blower et al. (2001) demonstrated that D exponent increases with the increasing of nucleation events, finally converging on the value predicted for the three-dimensionally Apollonian packing configuration (2.5; Anishchik and Medvedev, 1995). The model showed that 7-10 nucleation events are required to produce an exponent between 2 and 3, which is the typical values of most of natural samples (Blower et al., 2001). Therefore, the exponent D is a measure of the nucleation events, as well as of the growth timescale. The occurrence of coalescence phenomena during the growth tends to produce nearly exponential curves, with a more horizontal tail towards the larger sizes (Polacci et al., 2008; Bai et al., 2008). In turn, collapse textures may produce curves rapidly decreasing towards low log (NV) values, becoming near-horizontal as largest sizes are approached. Fig. 1.8 displays examples of the four categories, as well as examples of the processes that may contribute to generate or modify them (from Shea et al., 2010).

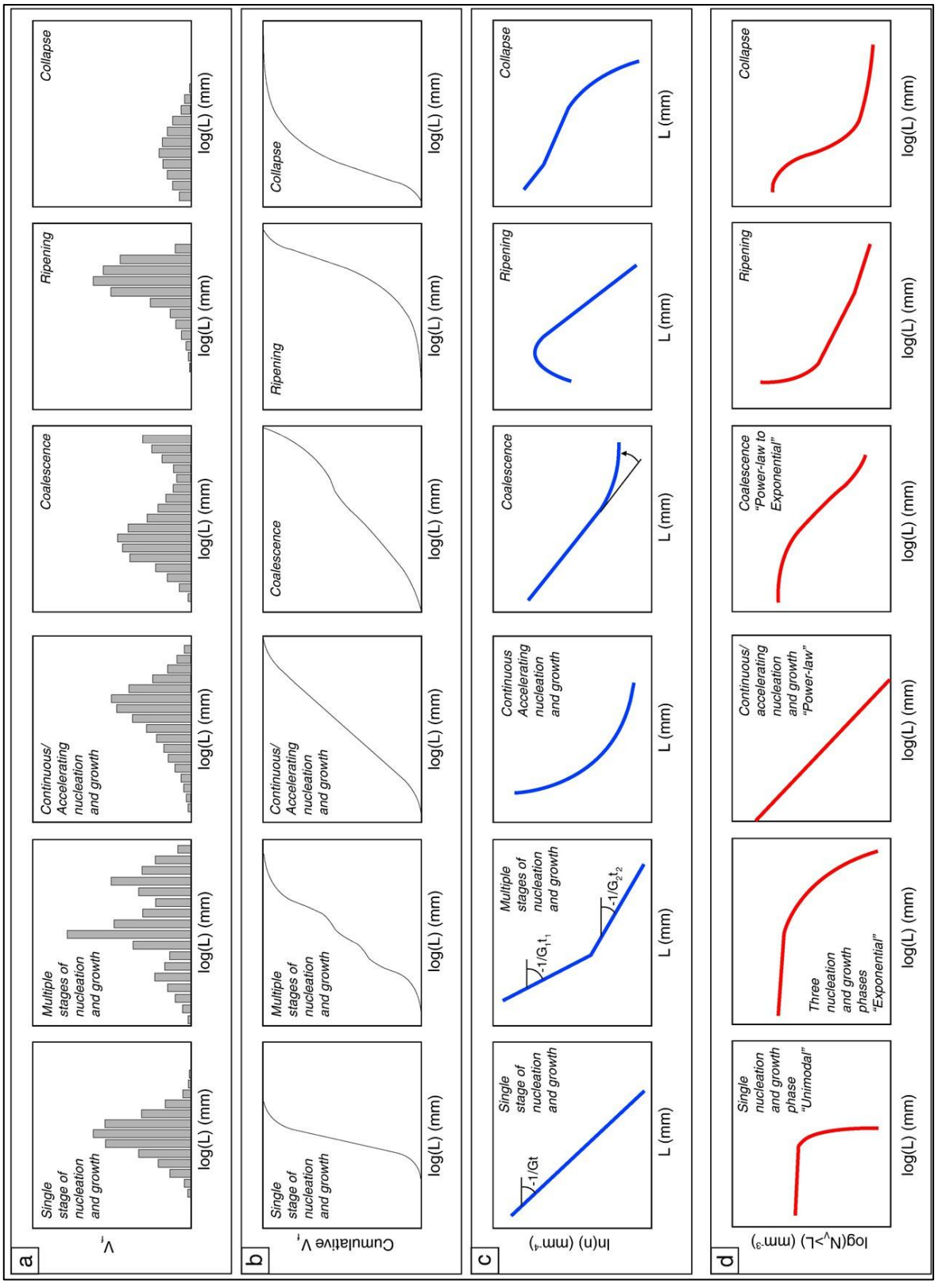


*Fig. 1.8 Various ways to display textural characteristics through size (L) and number density (n or $N_V$) plots, and processes that they may be associated with (single or few nucleation events, multiple nucleation and growth events, continuous nucleation and growth, coalescence, ripening, and collapse). (a) Simple volume fraction ($V_f$) size distribution (VVD), (b) Cumulative volume fraction size distribution (CVVD), (c) Vesicle size distributions (VSD) in terms of number density n, and (d) Cumulative number density plots log ($N_V$>L) vs. log(L) (CVSD). Because during magmatic ascent multiple vesiculation and degassing processes may occur simultaneously and overprint each other, such plots call for interpretative prudence. G is growth rate and t is time.*

### 1.4.4 Rheology

The viscosity of a fluid is the measure of its resistance to gradual deformation under an applied stress. The viscosity of magma is largely function of its liquid viscosity, temperature, crystal and bubble content, strain rate and pressure. The viscous response of magmatic systems controls the fluid dynamics of magma ascent and thus the eruption dynamics. Moreover, viscosity has a valuable effect on physico-chemical processes such as degassing and crystallization in magmas and ultimately controls magma transport on the surface. Viscosity in natural magmatic systems varies of more than 14 orders of magnitude (10 to $10^{14}$ Pa s) primarily in response to variations in melt composition (X), volatile content, temperature (T), pressure (P), as well as in the proportions and distributions of suspended solids and vesicles. Understanding how magma evolves with time, in an active volcanic system, and predicting possible future eruptive scenarios, is crucial for the hazard assessment and risk mitigation.

### Pure liquid viscosity

Viscosity is defined as the resistance to flow under specific applied stress (σ) conditions and may be expressed by a complex function of applied stress, resulting strain ($\gamma$) and strain-rates (e.g., Herschel and Bulkley 1926). For a Newtonian liquid the Newtonian viscosity $\eta$ is given as:

$$\sigma = \eta\gamma \quad (1.14)$$

The viscosity of a pure liquid is a function of composition, temperature and pressure, although the influence of pressure has a minor effect up to about 20 kbar (e.g., Scarfe et al., 1987; Dingwell et al., 1993) and can thus be neglected when discussing near surface volcanic processes. It is known that viscosity is sensitive to the structural configuration (distribution of atoms) of the melt. The most important structural element in silicate melt is constituted by the $SiO_4^{4-}$tetrahedra. These tetrahedral units are connected from oxygen atoms, that are called “bridging oxygen” (BO). The “degree of polymerization” is defined by the number of BO per cations in tetrahedral coordination T. Cations in tetrahedral coordination bonded to a BO are called “network former/stabilizer cations”. Generally, in silicate melts, the principal network former cations are $Si^{4+}$, $Al^{3+}$, $Fe^{3+}$, $Ti^{4+}$ and $P^{5+}$ (e.g., Mysen 1988). When $Al^{3+}$ substitutes for $Si^{4+}$ in the tetrahedral framework an excess negative charge is generated, which must be compensated

by nearby cations such as $Na^+$, $K^+$ or $Ca^{2+}$. These are referred to as charge-balancing cations, as they maintain electrical neutrality within the aluminosilicate network. Conversely, cations constituting non-tetrahedral polyhedron are defined "network modifying" cations. The main network modifying cations and molecules are $Na^+$, $K^+$, $Ca^{2+}$, $Mg^{2+}$, $Fe^{2+}$, $F^-$ and H2O (e.g., Mysen, 1988). Oxygen atoms that link from a tetrahedron to a non-tetrahedral polyhedron is called non-bridging oxygen (NBO). The relationship between "network modifying" cations and "network forming/stabilizing" cations with viscosity is critical to the understanding of the structure of a magmatic liquid and vice versa. This relationship is specified by the ratio NBO/T. In general, the viscosity decreases as the polymerization degree of the melt decreases (NBO/T increases), that is as the proportion of the network modifier cations increases in the melt. This is mainly due to the decrease of the average bond strength of the NBO over the BO bonds. Regardless of the exact nature of the microscopic mechanism of viscous flow, the activation energy of viscous flow depends primarily on the strengths of the bonds in the silicate structure. Highly depolymerized melts, having a higher proportion of weak NBO bonds, have lower viscosities. Viscosity also varies as a function of the nature of the network former or modifier present in the melt. The second most important network forming cation in the melt is Al. The observed systematic decrease in activation energy of viscous flow with the addition of Al (Riebling 1964; Rossin et al. 1964; Riebling 1966; Urbain et al. 1982) can be interpreted to reflect decreasing the "(Si, Al) – bridging oxygen" bond strength with increasing Al/(Al+Si). There are, also, significant differences between the viscous behaviours of aluminosilicate melts as a function of the type of charge-balancing cations for $Al^{3+}$. In general, the most effective network modifier in melts is $H_2O$. The viscosity of a rhyolitic melt at eruptive temperature, decreases from 1 to 6 orders of magnitude by adding an initial 0.1 and 1 $H_2O$ wt%, respectively (e.g., Hess and Dingwell, 1996). However, the effect strongly diminishes with further addition of water and tends to level off over 2 $H_2O$ wt%. Iron content, in both $Fe^{3+}$ and $Fe^{2+}$ oxidation states, also affects melt viscosity. Because NBO/T (and consequently the degree of polymerization) depends on $Fe^{3+}/\Sigma Fe$, also the viscosity is influenced by the presence of iron and by its redox state (Cukierman and Uhlmann, 1974; Dingwell and Virgo, 1987; Dingwell, 1991). Virgo and Mysen (1985) demonstrated that $Fe^{3+}/\Sigma Fe$ ratio decreases systematically as the temperature increases. Water also seems to provide a

restricted contribution to the oxidation of iron in relatively reduced magmatic liquids, whereas in oxidized calk-alkaline magma series, the presence of dissolved water does not largely influence melt ferric-ferrous ratios (Gaillard et al., 2001). Based on spectroscopic studies, ferrous iron behaves as a network modifier in most of silicate melts (Cooney et al., 1987; Waychunas et al., 1983). On the other hand, ferric iron occurs both as a network former (coordination IV) and as a modifier. In $Fe^{3+}$-rich melts, $Fe^{3+}$ is charge balanced with alkali metals and alkaline earths (Cukierman and Uhlmann, 1974; Dingwell and Virgo, 1987). Even if the situation is more complicated, in general, the viscosity increases as the $Fe^{3+}/\Sigma Fe$ increases in the melt, as the polymerization of the melt also increases as a function of the abundance of $Fe^{3+}$ (Virgo and Mysen, 1985; Dingwell and Virgo, 1987). However, the relationship between melt structure, bond strength and viscosity is not straightforward. These correlations generally hold at high temperatures, whereas at lower temperatures, multiple crossovers in viscosity-temperature curves occur that cannot be explained solely by variations in bond strength. According to the configurational entropy theory proposed by Adam and Gibbs (1965), viscosity is controlled by the number of configurational states accessible to the melt structure. Although this theory provides a valuable conceptual framework, it cannot be directly applied to natural magmatic systems. In the absence of comprehensive physical models, the temperature dependence of silicate melt viscosity is therefore commonly described using empirical parameterizations, such as the Vogel–Fulcher–Tammann (VFT) equation. More recently, the MYEGA (Mauro–Yue–Ellison–Gupta–Allan) model has provided a physically grounded alternative by relating viscosity to the concept of liquid fragility. For specific magma compositions, such as peralkaline systems, viscosity has been parameterized by Di Genova et al. (2013), whose formulation reproduces the behavior of highly depolymerized melts under volcanic conditions.

## Crystal-bearing magma rheology

Firstly, the presence of a solid phase or a gaseous phase to form a solid or bubble suspension can yield non-Newtonian behaviour, expressed in the more general equation:

$$\sigma = \sigma_0 + K\gamma n \quad (1.15)$$

where $\sigma_0$ is a stress threshold to be overcome in order to have flow, namely the yield stress; K is the flow consistency (which corresponds to shear viscosity at $\gamma$ =1 $s^{-1}$) and n is the flow index which describes the degree of non-Newtonian behaviour, being equal to 1 for Newtonian fluids, n>1 for shear-thickening and n <1 for shear-thinning fluids. Assuming zero yield stress, the relative viscosity (ratio between stress and strain rate divided by the viscosity of the suspending liquid, $\eta_l$) can be written as:

$$\eta_r = \frac{K}{n_l}\gamma n \quad (1.16)$$

In the case of a solid phase presence, such as crystals, the variation of viscosity as a function of crystal content follows a sigmoidal trend (Lejeune and Richet, 1995) (Fig. 1.9). For low values of the viscosity increase is linear and the fluid has a Newtonian type of behavior; beyond a critical value, ϕc, the influence of the solid phase becomes binding, with exponential trend and non-Newtonian effects, Binghamian type and/or shear thinning effects. As the concentration of solid particles increases, their effect tends to increase until a plateau is reached above a critical threshold, the maximum packing factor ϕm, beyond which the rheological behavior of the liquid-crystal system is given entirely by the solid fraction, effectively losing the capacity for viscous flow, and culminating in brittle fragmentation.

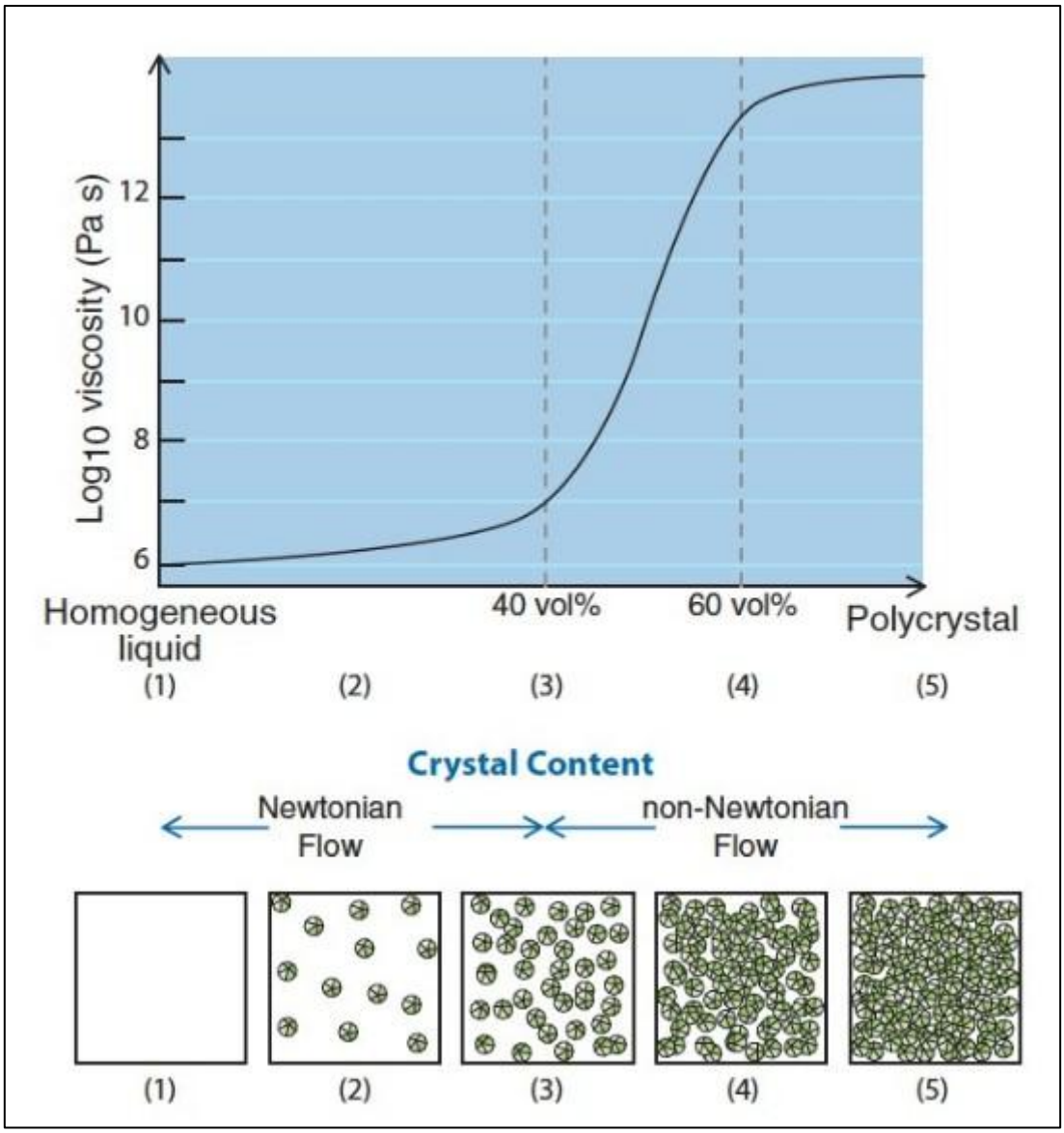


*Fig. 1.9 Effect of adding spherical particles; y-axis shows viscosity normalized to reference (melt) viscosity; dashed lines at 40% and 60% particles show locations of rapid viscosity increase and maximum packing, respectively. Diagrams show schematic representation of particle concentrations (modified from Lejeune and Richet, 1995).*

The influence of crystals on magma viscosity is a function of several parameters such as concentration, shape, size, and orientation of the crystals as well as the rate of deformation to which the moving fluid is subjected. (e.g. Ryerson et al., 1988; Pinkerton and Stevenson, 1992; Lejeune and Richet, 1995; Pinkerton and Norton, 1995; Sato, 2005; Caricchi et al., 2008; Ishibashi and Sat, 2007; Ishibashi, 2009; Petford, 2009; Vona et al., 2011; Campagnola et al., 2015). As far as the deformation rate is concerned, studies show that as the deformation rate increases, the fluid behavior can change from Newtonian to non-Newtonian due to shear thinning and/or yield stress overcoming effects (Binghamian fluid). It is generally recognized that, for higher fractions of suspended solid particles, the

increase of the strain rate favours the transition from a Newtonian to a non-Newtonian rheology (Krieger, 1972; van der Werff & de Kruif, 1989; Brueckner & Deubener, 1997; Caricchi et al., 2007). For high values of strain rate the relative viscosity of the liquid tends to decrease: this effect is known as shear thinning and is characteristic of pseudo-plastic materials (Webb & Dingwell, 1990). Caricchi et al., (2007) observed that the shear thinning effect is much more pronounced as crystal content increases, due to the geometric redistribution of crystals parallel to the direction of flow. crystals parallel to the direction of flow (Fig. 1.9). In addition, Mader et al. (2013) showed that the occurrence of the shear-thinning effect depends not only on the crystal content, but also on the aspect ratio. Thus, these works emphasize the particular importance of not only the number of suspended particles, but also their shape and deformation rate. Vona et al., (2011) proposed a parameterization of the effect of crystals in basaltic systems in which the proportionality between and is characterized by an exponential factor dependent on the deformation rate:

$$\eta_r = \left(1 - \frac{\phi}{\phi_m}\right)^{-2[1-\alpha log(\gamma)]} \quad (1.17)$$

$\phi_m$ represents the maximum packing fraction and is strongly dependent on crystal shape (i.e., on the aspect ratio, R): $\phi_m$ = 1 / (0.321R + 0.302) (from Mueller et al., 2010). A recent study by Frontoni et al. (2022) presented a comprehensive rheological database encompassing most of the available experimental data on crystal-bearing magmas. The authors compiled viscosity measurements from the scientific literature, covering a wide range of volcanic conditions in terms of crystal content (1-80%), crystal aspect ratio (R = 1-13), and strain rate ($10^{-7}$-$10^{2}$ $s^{-1}$). This dataset was used to develop a general, systematic model describing the relative viscosity of liquid–solid magmatic mixtures as a function of melt viscosity, crystal concentration, particle shape and applied strain rate. Their model successfully reproduces the non-Newtonian behavior of crystal-bearing magmas and provides a quantitative framework for understanding the rheology of partially crystallized systems under natural volcanic conditions. Equation proposed by Frontoni et al. (2022) is described as follow:

$$\eta_r\,(\dot{\varepsilon}, R) = \frac{1 + \varphi^{\delta(\dot{\varepsilon},R)}}{[1 - F(\dot{\varepsilon}, R)]^{B\phi*(\dot{\varepsilon},R)}} \quad (1.18)$$

Empirical parameters used in this equation can be found in Frontoni et al. (2022).

## Bubble-bearing magma rheology

The presence of bubbles in a bubble-melt mixtures influences the rheological response of a suspension. The relative viscosity of a bubble-melt mixture can be expressed as:

$$\eta_r = \frac{\eta_s}{\phi\,\eta_l} \quad (1.19)$$

where $\eta_s$ is the viscosity of the suspension, $\eta_l$ is the viscosity of the pure liquid phase as a function of the gas volume-fraction $\phi$. Liquid viscosity $\eta_l$ can increase or decrease depending on the conditions of shear and on the bubble-relaxation time λ (Manga et al., 1998; Spera and Stein 2000; Llewellin et al., 2002a, 2002b; Stein and Frank, 2002; Rust and Manga, 2002; Llewellin and Manga, 2005; Mader et al., 2013).. Considering a single bubble in an infinite medium:

$$\lambda = \frac{\eta_s}{R\Gamma} \quad (1.20)$$

where R is the undeformed bubble radius and Γ is the bubble-liquid interfacial tension. Several authors demonstrated that λ is an increasing function of $\phi$ (Oldroyd, 1953; Oosterbroek and Mellema, 1981; Loewenberg and Hinch, 1996; Llewellin et al. 2002a). However, Rust et al. (2003) showed that the dependence of λ on $\phi$ is rather weak, so the previous equation can be used for all $\phi$. The effect of bubbles on the magma rheology depends on the type of magma flow. According to Llewellin and Manga (2005) the magma flow can be simplified as “steady” or “unsteady”. The steady flow occurs when the condition of shear has remained constant for a time $t \gg \lambda$ (Llewellin et al., 2002; Rust and Manga, 2002). For a steady flow, the viscous regime is controlled by the capillary number Ca (Llewellin et al., 2002a; Rust and Manga, 2002; Stein and Spera, 2002). Ca is a parameter that describes the relative importance of viscous stresses, which tend to deform the bubbles, and interfacial stresses, which tend to restore them to sphericity and is defined as:

$$Ca = \lambda\gamma = \frac{\eta_s}{\Gamma} \quad (1.21)$$

where $\gamma$ is the shear strain-rate. Given a steady flow, Ca refers to the equilibrium between the viscous and interfacial stresses, thus, the bubble shape is also constant. The bubbles are described as relaxed and bubble deformation is

considered in equilibrium. If Ca ≪ 1, interfacial tension forces dominate and bubbles are approximately spherical (e.g., Taylor, 1934). If Ca≫1 viscous forces dominate, and bubbles will be elongated (e.g. Hinch and Acrivos, 1980). So, the shape of the bubbles will affect differently the viscosity of a suspension: bubbles can deform flow lines within the suspending medium, producing an increase in viscosity, or they can provide free-slip surfaces, decreasing the viscosity. For small Ca, bubbles are almost spherical, the flow-line are distorted, and the free-slip surface area is small ($\eta$r > 1). On the other hand, for large Ca, elongated bubbles produce small distortion on the flow-lines and free-slip surface area is great ($\eta$r < 1).

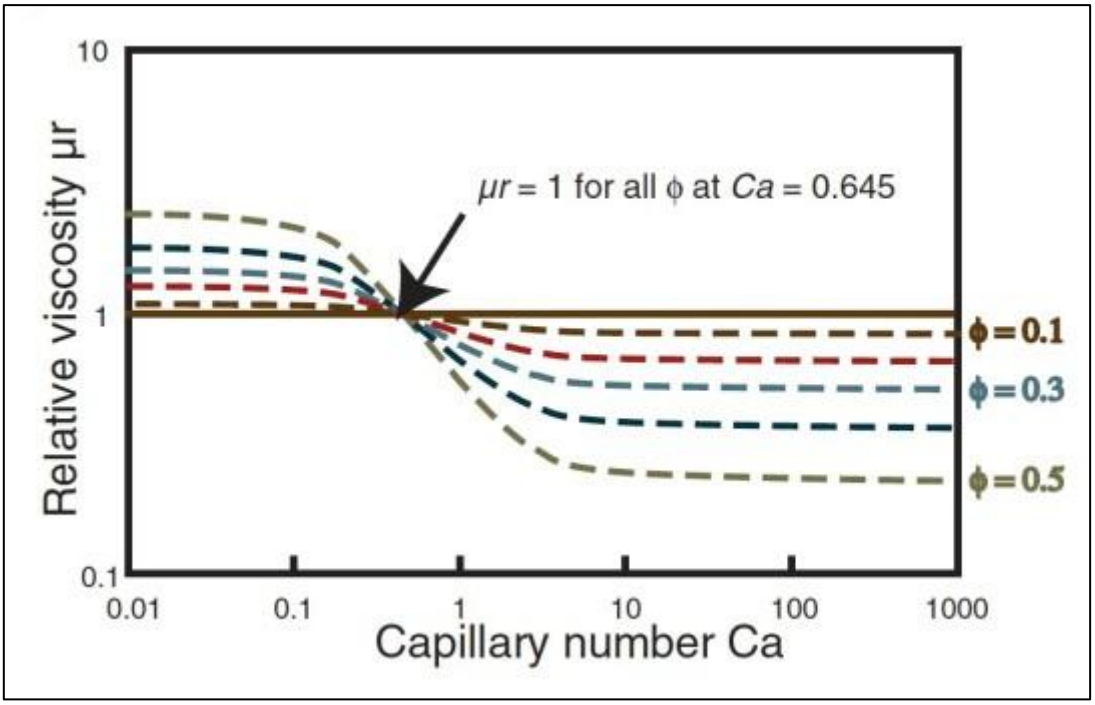


*Fig. 1.10 Effect of adding bubbles; viscosity is normalized to bubble-free values and shown as a function of Ca for different bubble concentrations (ϕ; modified from Pal, 2003).*

From these observations, the rheology of the suspension can be predicted simply determining the shape of bubbles as a function of Ca and $\phi$ (e.g., Batchelor, 1970). The problem, however, lies in determining bubble shape. Analytical results are available for small deformations (e.g., Taylor, 1934) and highly elongated bubbles (e.g., Hinch and Acrivos, 1980) in the case of dilute suspensions. Models are also derived for intermediate deformation (e.g., Wu et al., 2002). In general, theoretical results for bubble shape agree with experimental measurements (e.g., Rust and Manga, 2002; Hu and Lips, 2003; Yu and Bousmina, 2003). Conversely, if the suspension is no longer dilute, the interactions between bubbles affect their

shapes and consequently the rheology. Unfortunately, the rheology can be predicted accurately only if the bubble shape is accurately known (Cristini et al., 2002). When the shear strain rate has faster variation than the bubble-relaxation time λ, the bubble-liquid flow is unsteady. Llewellin et al. (2002a, b) showed that the different degrees of steadiness of a flow exist can be described using the dynamic capillary number Cd given by:

$$Cd = \lambda \frac{\ddot{\Upsilon}}{\dot{\gamma}} \quad (1.22)$$

where $\ddot{\Upsilon}$ is the rate of shear strain-rate variation. Cd therefore compares the timescale over which the bubbles can respond to changes in their shear environment (λ) with the timescale over which the shear environment changes ($\ddot{\Upsilon}$). If Cd≪1, the bubbles are able to respond continuously to the changes in shear environment. Consequently, the bubbles are always approximately in their equilibrium deformation conditions and the flow can be considered approximately as steady. Then, the dynamic regime is controlled by the capillary number Ca. On the contrary, if Cd≫1, the shear environment changes too rapidly for the bubbles to respond, therefore the bubbles are unrelaxed. Since the bubbles never reach their equilibrium deformation, Ca is undefined, and the flow is described as unsteady. In an unsteady flow, the bubbles do not have time to respond elastically to changes in shear. Hence, they behave as if they have no bubble-liquid interfacial tension. If no elastic force affects the shape of the bubbles, their response to the local shearing of the suspending liquid is purely viscous. Because bubbles have negligible viscosity, they deform passively with the suspending liquid. According to Llewellin et al. (2002a) such a behavior produces a decrease of the flow-lines distortion around the bubbles leading to a decrease in the viscosity of the suspension as $\phi$ increases. In summary: if Cd ≪ 1, flow is approximately steady, hence the regime is determined by Ca; if Cd ≫ 1, flow is unsteady, and viscosity decreases with gas volume-fraction increase. Therefore, the rheology of a suspension can be calculated for steady flows, as well as for unsteady flows if the evolution of bubble shape is known (e.g., Tucker and Moldenaers, 2002). Llewellin and Manga (2005) parameterized the effect of bubbles on the relative viscosity of a bubbly suspension, considering two single equations for the positive and negative dependence of $\eta_r$ on $\phi$ regardless of whether the decrease in viscosity in the negative case is related to steady (Ca>1) or unsteady (Cd>1) flow. The authors suggested two different parameterizations

for each viscous regime (increasing and decreasing $\eta_r$), considering two limiting cases corresponding to a minimum and a maximum effect of the bubbles on the viscosity of the suspensions.

For Ca<1, in which $\eta_r$ increase:

MIN = $\eta_r = (1 - \phi) - 1$ (1.23)

MAX = $\eta_r = (1 + 9\phi)$ (1.24)

simplifying Pal (2003; MIN) and Bagdassarov and Dingwell (1992; MAX) equations.

For Ca>1 or Cd>1, in which $\eta_r$ decreases:

MIN = $\eta_r = (1 - \frac{5}{3}\phi) - 1$ (1.25)

MAX = $\eta_r = (\frac{1}{1+22.4\phi})$ (1.26)

simplifying Pal (2003; MIN) and Bagdassarov and Dingwell (1992; MAX) equations.

Vona et al. (2016) investigated experimentally the effect of bubbles on magma bulk viscosity. They proposed a two-parameter empirical equation describing the decreasing in bulk viscosity at the increase of vesicle content:

$$log_{10}\eta_{Bulk} = log_{10}\eta_0 - 1.47\left[\frac{\phi}{1-\phi}\right]^{0.48} \quad (1.27)$$

The parameterization proposed, combined with Maxwell relaxation theory, is used to identify the onset of non-Newtonian behavior, such as shear localization, as a function of melt viscosity, vesicularity, and strain rate conditions. They found that vesicular magma behaves as a non-Newtonian fluid at lower strain rates, enhancing strain localization and magma fragmentation (explosive or non-explosive). The model can be used to reveal the conditions promoting the onset of shear localization.

## Three phase mixtures

Only very few studies have explored the rheology of crystal and bubble-bearing magmas. Lavallée et al. (2007), Avard and Whittington (2012) and Vona et al. (2013) have investigated natural samples by uniaxial deformation experiments. The authors have observed pseudo-plastic behavior with a strong shear thinning component for all the investigated magmas and provided equations describing

the apparent viscosity as a function of temperature and strain rate for the multiphase magmas. The individual effect of crystal and bubbles was theoretically parameterized by Phan-Thien and Pham (1997) and later applied by Harris and Allen (2008)) for the study of basaltic magmas from Mauna Loa and Mount Etna. Phan-Thien and Pham (1997; 2000; 2006) considered three cases as a function of relative size of crystals and bubbles and express the relative viscosity as a function of variable crystal and bubble fraction.
In case 1, crystals are smaller than bubbles:

$$\eta_r(\phi_{xls}, \phi_{bub}) = [1 - \phi_{xls} / (1 - \phi_{bub})]^{-\frac{5}{2}}(1 - \phi_{bub})^2 \quad (1.28)$$

In case 2, d bubbles are of the same size range:

$$\eta_r(\phi_{xls}, \phi_{bub}) = [1 - \phi_{xls} - \phi_{bub})]^{-(5\phi_{xls} + 2\phi_{bub})/2(\phi_{xls}+\phi_{bub})} \quad (1.29)$$

In case 3, crystals are larger than bubbles:

$$\eta_r(\phi_{xls}, \phi_{bub}) = [1 - \phi_{bub}/(1 - \phi_{xls}))]^{-1} (1 - \phi_{xls})^{-\frac{5}{2}} \quad (1.30)$$

This treatment does not take into account the effect of textural variability, being applicable to spherical particles only, and strain rate dependency on the rheology.

# 2. Methodology

## 2.1 Grain size distribution and density analysis

The grain size distribution (GSD) was determined by dry sieving of all selected samples. Before conducting GSD analysis, pumice clasts have been dried at 110 °C for 24 hours. The grain-size ranges from 32 mm to <0.063 mm were separated and weighted. The GSD are shown for each section in the data graphs recalculated at phi intervals. We selected 16-8 mm interval as modal size. This size class has been taken as the more representative for the successive analyses.

Density measurements have been conducted by using a hydrostatic balance. Pumice clasts selected from the 16-8 mm grain size class, were cleaned and dried at T> 100°C for 24h and then ranked and numbered from large to small in a set of 100 clasts (Shea et al., 2010). According to the method described by Houghton and Wilson (1989), each clast was first weighted in air ($m_{air}$) and then, once waterproofed, was weighed in water ($m_{H2O}$) to obtain the clast density (ρ) according to the following:

$$\text{Clast } \rho = m_{air} /(m_{air} – m_{H2O})*(\rho H2O- \rho Air)+\rho Air \quad (2.1)$$

The pumice clasts were waterproofed with a thin cellulose film in order to avoid water intrusion in pumices pores. It is important to note that the correction to the waterproofing film is not necessary as it can be assumed that its weight is irrelevant.

Finally, the Dense Rock Equivalent (DRE), obtained by measuring powdered samples in a He–Pycnometer, in HP-HT Lab at INGV-Istituto Nazionale di Geofisica e Vulcanologia (Rome, Italy), was used to calculate the sample vesicularity (Clast ϕ) as follows (Russell and Giordano, 2007):

$$\text{Clast } \phi = ((DRE – Clast\rho)/DRE)*100 \quad (2.2)$$

Both density and vesicularities of the pumice samples datasets were plotted on a histogram in order to choose only few selected clasts that represent the different endmembers from the entire distribution. In this manner, 6 pumice clasts were chosen to characterize low (1 clast), modal (4 clasts) and high (1 clast) density, for each bulk sample. All the selected clasts were prepared for textural analysis by embedding in epoxy then sectioning, polishing, and carbon coating.

## 2.2 Textural analysis

Textures of pyroclasts, specifically vesicle size distribution, vesicle shape, vesicle number density and abundance of microlites, can be quantified from image analysis and used to study conduit processes (Cashman and Mangan, 1994; Mangan and Cashman, 1996; Hammer and Rutherford, 2002). Vesicles in volcanic rocks are typically heterogeneous in distribution and size. Characterizing this range of vesicle sizes requires image acquisition over similar size ranges (Shea et al., 2010). As stated in the previous paragraph, 6 pumice clasts were selected for each analyzed eruption, as endmembers of three density classes. Thick sections of pumice rims (100 μm) were prepared by embedding the top of a pumice clast in epoxy on a microscope slide. The thick section, polished and carbon coated were imaged using the Scanning Electron Microscope at HP-HT Lab at INGV-Istituto Nazionale di Geofisica e Vulcanologia (Rome, Italy). Images were captured at two different magnifications (60x and 300x) to ensure a good representation of the heterogeneity in vesicle size and shape for each clast. Back Scattered Electron (BSE) images collected using the nested approach of Shea et al. (2010) were converted to binary form and processed using the ImageJ software package. For each clast, from 12 to 20 binary images, about 300 images analyzed, with increasing magnification from 60x to 300x were processed in FOAMS (Matlab based program, Shea et al., 2010) to obtain a complete quantitative vesicle textural analysis. To ensure that all vesicles were adequately represented, a plot of the number density of vesicles per areas, NA vs. equivalent diameter L, was constructed at different magnification. Overlapping size bins for adjacent magnifications enabled us to select the cut-off size for each magnification and allowed to verify that all classes were adequately represented. (Shea et al., 2010). Resulting VNDs require a correction for vesicularity, that was given for each clast by the density measurements described in the previous section.

## 2.3 Rheology

### 2.3.1 Sample preparation and synthesis

Rheological properties of the eruptive products have been examined through a series of experimental techniques: Concentric Cylinder (CC) apparatus for high T - low η field measurements and differential scanning calorimeter (DSC) and micropenetration technique (MP) for low T - high η field measurements and for

glass transition temperature determinations. Viscosity analyses were performed on natural melts, obtained by the synthesis of anhydrous glass using as a starting material fine ash (<0.63mm) crushed from the pumices. The syntheses were performed by melting the powdered pumices in a Nabertherm static furnace at superliquidus temperature. Considering the possible loss of highly volatile elements, Na and K, at high temperatures, abundant in the pantelleric melt, plus the high viscosity of the rhyolite, the syntheses of this product was a delicate process. After multiple attempts, a glass synthesis was achieved through melting at a constant temperature of 1400°C, in a Pt crucible that was slowly filled with the ash, with multistep process. The melt was quenched and crushed again to follow with a second and third step of melting at 1400°C, kept for several hours, to allow complete exsolution of water with longer diffusion timescale. Chemical analysis on natural products and natural glass confirms that there has not been an alkali loss during the process.

### 2.3.2 Pure liquid viscosity determination

Liquid viscosity measurements at low and high temperature have been performed at the Experimental Volcanology and Petrology Laboratory (EVPLab) of Roma Tre University (Rome, Italy).

### 2.3.3 Differential Scanning Calorimeter (DSC) measurements

A DSC 404F3 Pegasus was employed to measure the onset ($T_{onset}$) and peak temperature ($T_{peak}$) of heat flow curves over the glass transition temperature interval. Different heating and cooling cycles ($q_{c,h}$) were set at 5, 10 or 20°C $min^{-1}$ under a constant $N_2$ flux (5.0 atm at a flow rate of 30 ml $min^{-1}$) using $Pt_{80}Rh_{20}$ crucibles. The mass of the glass samples was approximately 25 ± 5 mg. The calibration of the DSC temperature was performed up to ~1050°C using the melting points of reference materials (In, Sn, Bi, Zn, Al, Ag, and Au) (Di Genova et al., 2020; Scarani et al., 2023; Stabile et al., 2021). Baseline measurements were conducted with two empty Pt crucibles. Following the protocol described by Di Genova et al. (2020), each sample was subjected to heating at 10°C $min^{-1}$ from room temperature to 50°C and maintained at this temperature for 20 min to achieve DSC signal equilibrium. Subsequently, to erase the thermal history of the glass, the temperature was increased with a heating rate of 10°C $min^{-1}$ to approximately the $T_{peak}$ and then decreased to 50°C at 5, 10 or 20°C $min^{-1}$. Finally,

a matching cycle of $qc_{,h}$ at 5, 10 or 20°C $min^{-1}$ was applied to derive the $T_{onset}$ and $T_{peak}$ for each $q_{c,h}$.

### 2.3.4 Micropenetration (MP) measurements

The micropenetration technique (Hess et al., 1995; 1996) consists in determining the rate at which a rod equipped with a hemispherical iridium termination (indenter), penetrates the polished surface of the sample. For each sample were used two to three doubly polished cylindrical 0.3 cm height and diameter glass cores. The sample was heated up in two steps: initially, a heating rate of 10 °C $min^{-1}$ was imposed up to a temperature 100 °C below the target temperature; for the last 100 °C until target temperature, a rate of 3 °C $min^{-1}$ was employed in order to minimize the sample overshoot (±3 °C). The sample was allowed to thermally equilibrate for 10 min at the final temperature before deformation. The viscosity measurement was performed at isothermal conditions applying a constant load of 150 g for approximately 10 min on the polished surface of the sample. The indentation rate is measured as a function of time transforming the displacement of the rod on the surface of the samples. The absolute viscosity is calculated with the following equation (Pocklington, 1940; Tobolsky and Taylor, 1963):

$$\eta = \frac{0.1875Lt}{r^{0.5}\alpha^{1.5}} \quad (2.3)$$

where L is the applied load (N), t is the penetration time (s), r is the radius of the hemisphere (m) and $\alpha$ is the indentation distance (m). The applied force for the measurements performed in the present study is about 1.0 N. This method provides an accurate viscosity determination if the indentation distance is lower than 150-200 μm with an instrumental error of ±0.06 Pa s logarithmic units.

### 2.3.5 Concentric Cylinder (CC) measurements

Viscosity measurements at high temperature were conducted using the concentric cylinder (CC) viscometer at the Experimental Volcanology and Petrology laboratory (EVPLab, University of Roma Tre, Italy) following the methodology outlined by Dingwell (1986). The viscometer head featured a torque full-scale of 75 mNm. Prior to high-temperature (HT) experiments, glass chips from distinct melting batches underwent remelting in a $Pt_{80}Rh_{20}$ crucible (6.2 cm in height, 3.56 cm inner diameter, 0.3 cm wall thickness). The molten samples

were stirred at 10 $s^{-1}$ using a $Pt_{80}Rh_{20}$ spindle under air redox conditions at 1400 °C for 3 h to ensure chemical and thermal homogeneity (Di Fiore et al., 2022, Di Fiore et al., 2024). The rheometer was calibrated against the NIST 717a standard reference material, ensuring an accuracy of 0.06 log units (Di Fiore et al., 2022). Temperature measurements employed a S-type thermocouple with an accuracy of ±2 °C. The initial temperature measurement was set at 1400 °C, aligning with a superliquidus state of the melt, while a shear rate (γ) of 10 $s^{-1}$ was consistently applied throughout the experiment. Subsequent temperature decrease was carried out incrementally in steps of 50 °C. At each temperature step, conditions were maintained until a steady torque and temperature were attained (approximately 30–45 min), ensuring precision in the measurement of liquid viscosity ($\eta_{liquid}$). Viscosity is defined as:

$$\eta = \tau/\gamma \quad (2.4)$$

where τ is the stress and γ is the strain rate. In the viscometer apparatus, the stress is a function of applied torque and spindle geometry, while the strain rate is a function of the angular velocity and cylinder geometry. These relationships can be expressed by the following equations:

$$\tau = M/2\pi Ri^2 h \quad (2.5)$$

$$\gamma = 2\omega/(1-(Ri/Ro)^2) \quad (2.6)$$

where M is the torque, Ri and Ro are the inner and outer radius of the cylinder, ω is the angular velocity and h is the length of the immersed spindle. The angular velocity can be described as: $\omega=2\pi 60N$. Where N is the number of revolutions per minute of the spindle. In the present study, $\gamma$ has been set at $10^{-1}s^{-1}$.

## 2.4 Microprobe Analysis

For chemical analysis, samples were washed in an ultrasonic bath with distilled water for ~15 minutes and then dried in an oven at 110 °C for 24 hours. Samples were crushed using mechanical agata mortar in order to create powder. Micropobe Analysis were carried out by Activation Laboratories Ltd. (Actalabs), Ontario (Canada), using 4B package – Lithium Metaborate/Tetraborate Fusion – ICP. Samples are prepared and analyzed in a batch system. Each batch contains a method reagent blank, certified reference material and 6% replicates. Samples are mixed with a flux of lithium metaborate and lithium tetraborate and fused in

an induction furnace. The molten melt is immediately poured into a solution of 5% nitric acid containing an internal standard, and mixed continuously until completely dissolved. The samples are run for major oxides and selected trace elements (4B) on an ICP. Calibration is performed using 14 prepared USGS and CANMET certified reference materials. One of the 14 standards is used during the analysis for every group of ten samples. The detection limit for major elements is below <0.01% (0.001 for $TiO_2$ and 0.005 for MnO).

## 2.5 Raman spectroscopy

Samples were structurally characterized both before and after the CC and DSC measurement to test for potential chemical and structural alterations due to temperature exposure above $T_g$. Analyses were conducted using a Jobin Yvon LABRAM HR800 Horiba equipped with a 532 nm green laser (60 mW nominal power), calibrated with a silicon standard at the EVPLab. For each sample, 10 spectra were acquired to investigate the experimental reproducibly of the results. Spectra were collected using a 100× objective, covering the range between 100 and 1500 $cm^{-1}$ and from 2700 to 4000 $cm^{-1}$ hereafter defined as the low wavenumber (LW) and high-wavenumber (HW) regions respectively, with a 30 s acquisition time and 6 accumulations. Raman spectroscopy has been also used for the estimation of dissolved water which represents in silicate melts a crucial issue for the understanding, and modeling, of various magmatic processes. Water is usually measured both in glass inclusions in minerals and in the groundmass. Inclusions represent melt pockets trapped during the crystallization of the host mineral (e.g., Wallace et al., 1999, 2003), thus they give information on the pre-eruptive water content. On the other hand, residual glasses in eruption products represent the late stage melt and can be used to characterize the residual volatile contents (Johnson et al., 1994). Recently, several authors have demonstrated the potential of confocal microRaman spectroscopy for measuring water contents of silicate glasses and melt inclusions (Thomas, 2000; Chabiron et al., 2004; Behrens et al., 2006; Thomas et al., 2008; Frezzotti et al., 2012; Le Losq et al., 2012, Di Genova et al., 2017). Raman spectroscopy presents important advantage over other methodologies, such as: high spatial resolution of 1-2 $\mu m^2$; non-destructive nature; minimum sample preparation. The most important shortcoming is related to the high fluorescence background that may

obscure the water signal and the necessity of an accurate calibration to quantify the volatile content.

## 2.6 Melt inclusions analysis

Melt inclusions are small droplets of silicate melt (typically <100 mm in the longest dimension) that are trapped in minerals during their growth and they are subsequently quenched to glass (Roedder, 1984). Melt inclusions provide critical evidence for the composition of silicate melts and associated exsolved fluids prior to geological processes such as eruption, devolatilization and crystallization (Lowenstern, 2003). Once incorporated within their host mineral, melt inclusions usually retain much of their initial compositional attributes (Audétat and Lowenstern, 2014). They offer several key advantages over whole-rock samples: (1) they can record pristine concentrations of volatiles and metals usually lost by degassing and fractionation during magma solidification, (2) they allow a more detailed, time-resolved view into magmatic processes than whole rocks because melt inclusions are snapshots in time, whereas whole rocks are the time-integrated products, and (3) they are unaffected by sub-solidus alteration as long as their host crystal remains stable (Audétat and Lowenstern, 2014). Due to these characteristics, melt inclusions are an ideal source of insight into the compositional evolution of melts during processes (Audétat and Lowenstern, 2014). Nevertheless, there exist challenges to working with melt inclusions: (1) they are absent in some samples, (2) they can be difficult to recognize (especially in slowly cooled rocks), (3) they may be compromised due to post entrapment deformation and/or compositional modifications, and (4) their small size and commonly heterogeneous nature can render them difficult to analyze (Audétat and Lowenstern, 2014).

## 2.7 Simultaneous thermal analysis (STA) and evolved gas analysis by mass spectrometry (EGA-MS)

Before starting simultaneous thermal analysis (STA) and evolved gas analysis by mass spectrometry (EGA-MS), pumice clasts were previously dried for 24 h at 110 °C and then manually crushed into fine chips (≤ 2 mm). A Mettler Toledo TGA/DSC 3+ apparatus was used for the STA. The sensor of this device is located in a high-temperature furnace and features a twin crucible holder. This consists of a twin platinum-rhodium disk that is fitted into an alumina frame. The right disk is the

sample position: for each analysis, each crushed sample (mass between 15 and 25 mg) was placed into an $Al_2O_3$ crucible covered by a perforated lid, to avoid any potential sample explosion, dispersion, and contamination into the furnace. $Al_2O_3$ crucibles are the most convenient ones for repeated STA and EGA-MS analysis because of their relatively affordable cost, as well as their stable chemical and thermal properties at high temperatures, allowing accurate measurements of both sample mass and temperature. The left disk is the reference position, which is occupied by an empty $Al_2O_3$ crucible covered by an $Al_2O_3$ perforated lid. An R-type thermocouple (± 2 °C) positioned under the reference side disk measured the reference temperature. An additional R-type thermocouple (± 2 °C) measured the temperature difference between the sample and the reference side, producing a differential thermal signal, which is directly proportional to the calorimetric raw data, measured as the heat flow in mW. The sensor is also connected to a highly sensitive microbalance (± 0.1 µg), providing sample mass change for each analysis. STA was systematically corrected by reproducible baseline measurements performed with empty crucibles at both sample and reference sides. A fused quartz capillary (internal diameter of 10 µm) enclosed in a heated transfer line connects the STA device to a ThermoStar Pfeiffer Vacuum GSD 320 EGA-MS, which simultaneously identifies the targeted volatile species released during each analysis. This EGA-MS is equipped with an inlet heater that heats up the transfer line to 150 °C to avoid gas condensation within the capillary. It is also equipped with an integrated vacuum pump that creates a $10^{-9}$ bar environment to collect the gases from the STA furnace through the capillary, allowing a relatively immediate response and synchronous analysis of the released volatile species (delay of about ca. 1 s between the STA and the EGA-MS signals). The EGA-MS consists of four cylindrical rods (quadrupole) set parallel to each other. The collected gases are ionized by a filament and separated in the rod system based on their mass-to-charge (m/z) ratio and on the stability of their trajectories in the oscillating electric fields that are applied to the rods. The ions are then electrically detected with a Continuous Secondary Electron Multiplier (C-SEM) detector (sensitivity of 1 ppm). Before each analysis, the STA furnace was systematically purged at room temperature (RT) and pressure, with a 25 min-long 120 mL/min Argon (Ar) flow, followed by a 20 min-long nominal 40 mL/min Ar flow in order to remove air and stabilize a baseline of gas concentration in the furnace. Next, each sample was heated from 40 °C (which was the

maximum RT) to 1300 °C with a heating rate of 25 °C/ min. Finally, each sample was cooled down to RT at a rate of 25 °C/min. Each analysis lasted ca. 160 min, resulting in a completely melted and re-solidified sample, adhering to the crucible which were thus not re-used. The Ar purging flow (Ar used is Ar 4.8 for spectrometry with a guaranteed purity of 99.998%), which enables the conduction of analyses under relatively dry and reduced conditions, allows to measure simultaneously the release of H2O (m/z =18), CO2 (m/z =44), Cl (m/z =35), F (m/z =19) and SO2 (m/z =64), all of which do not interfere with the signal of Ar (m/z = 40).

# 3. Results

## 3.1 Density and porosity measurements

The grain size distribution (GSD) has been determined by dry sieving of all selected pumices from the bulk samples. The grain-size ranges have been sieved from 16 mm (-4 ϕ) to <0.063 mm (>4 ϕ) and weighted. The cumulative grain size distribution curves for Cinque Denti, Green Tuff, Zinedi and Cuddia Mida are shown in Fig. 3.1.

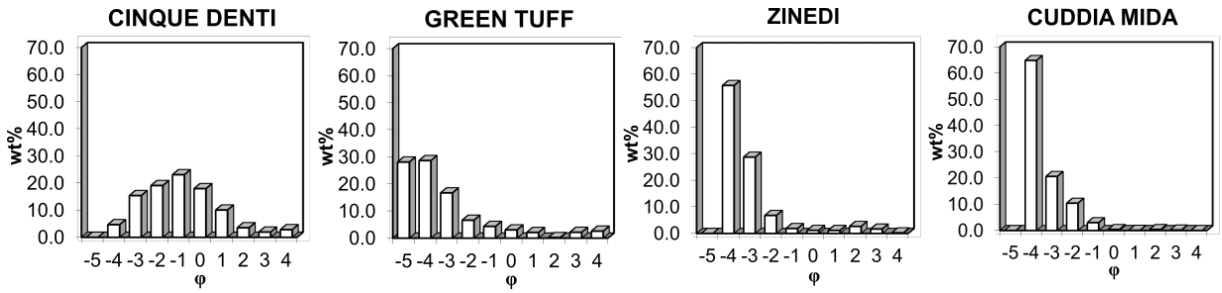


*Fig. 3.1 Grain size distribution for Cinque Denti, Green Tuff, Zinedi and Cuddia Mida.*

The GSD is different for each eruption. Cinque Denti eruption shows a good Gaussian distribution while Green Tuff, Zinedi and Cuddia Mida show a skewness towards larger pumices. It is worth noticing here that the samples were probably taken at different distances from the vent, depending on the accessibility of the sampling sites. Based on previous study, we selected pumices from -4ϕ/-3ϕ or 16-8 mm grain size class for density, porosity and textural analysis. Density measurements have been carried out with a hydrostatic balance after selecting, from the 16-8 mm grain size class, a set of 100 pumice clasts dried at T> 100°C. Fig. 3.2 shows density distribution for each eruption. We choose 0.2 bin to illustrate density measurements in order to have a clear view of density distribution. The four eruptions show a Gaussian distribution. Density distribution show outlier for Cuddia Mida at 1.32 g/cm$^3$ and Zinedi at 1.26 g/ cm$^3$. A tail of high-density pumices is present for Cinque Denti, Green Tuff and Cuddia Mida eruptions.

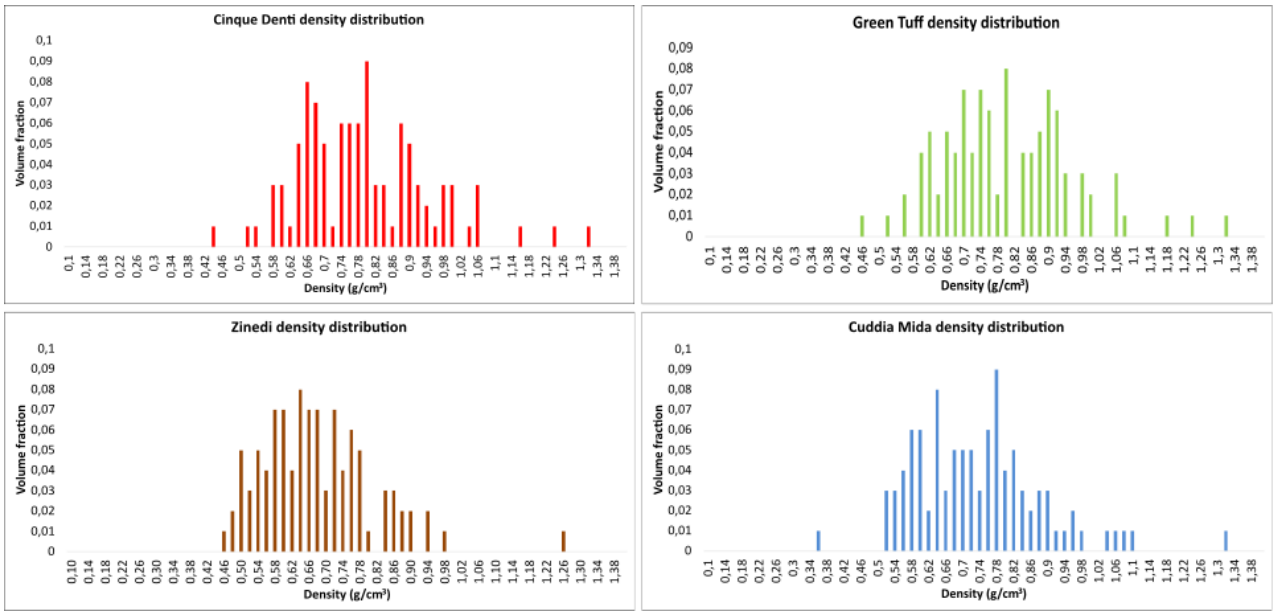


*Fig. 3.2 Density distribution for Cinque Denti, Green Tuff, Zinedi and Cuddia Mida batch samples (100 samples).*

For each eruption, 6 clasts have been chosen to characterize low (1 clast), medium (4 clast) and high (1 clast) density, for each bulk sample, in order to perform textural analyses. All the selected clasts have been prepared for SEM analysis by embedding in epoxy, sectioning, polishing, and carbon coating. Finally, the Dense Rock Equivalent (DRE) (Tab. 3.1), obtained by measuring powdered samples in a He–Pycnometer, was used to convert clast densities into porosities.

| **Eruption** | **DRE (g/cm$^3$)** |
|---|---|
| Cinque Denti | 2.497 |
| Green Tuff | 2.487 |
| Zinedi | 2.472 |
| Cuddia Mida | 2.454 |

*Tab. 3.1 Dense Rock Equivalent (DRE) values measured with He-Pycnometer.*

Each eruption presents a porosity mean at 70-80% (Fig. 3.3) and it reflect the average porosity range for acidic explosive eruptions from 70 to 90% (Klug and Cashman 1996; Polacci et al. 2003).

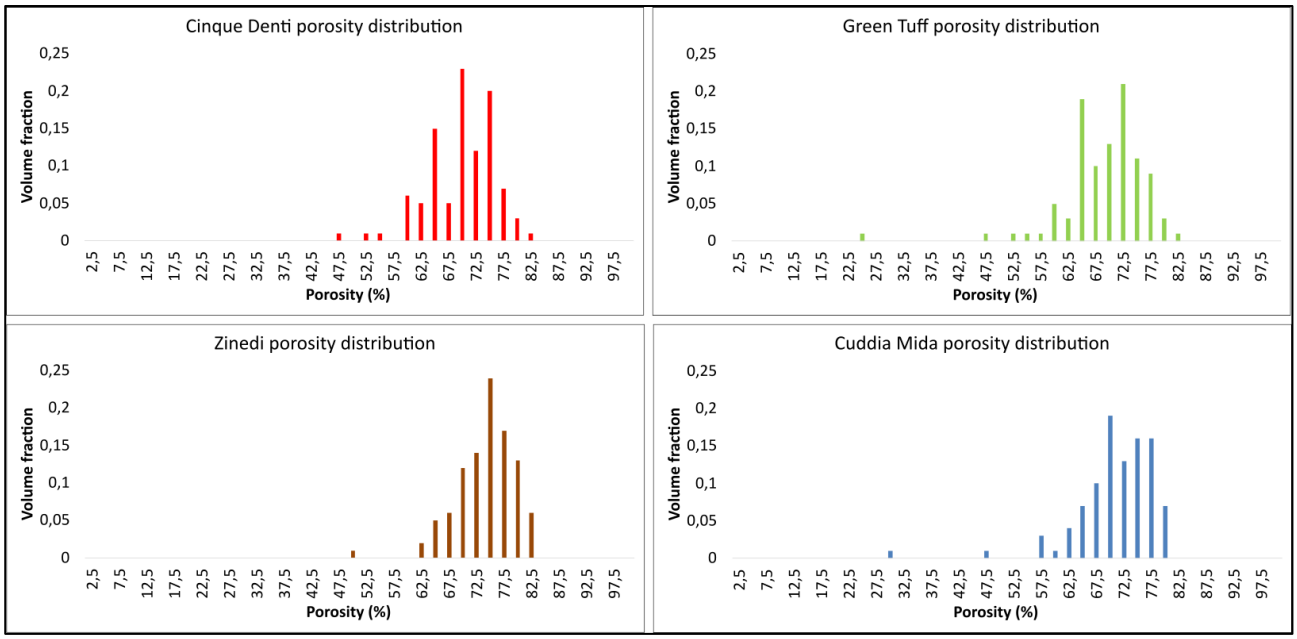


*Fig. 3.3 Porosity distribution for Cinque Denti, Green Tuff, Zinedi and Cuddia Mida pumices batch samples (100 samples).*

Tab. 3.2 resumes low, medium and high density values for selected clasts, and porosity related, for each eruption.

| | Density LD ($g/cm^3$) | Porosity LD (%) | Density MD ($g/cm^3$) | Porosity MD (%) | Density HD ($g/cm^3$) | Porosity HD (%) |
|---|---|---|---|---|---|---|
| Cinque Denti | 0.53 | 78.59 | 0.80 | 67.58 | 1.06 | 57.58 |
| Green Tuff | 0.51 | 79.49 | 0.81 | 67.36 | 1.31 | 47.23 |
| Zinedi | 0.45 | 81.64 | 0.70 | 71.55 | 0.98 | 60.52 |
| Cuddia Mida | 0.51 | 79.12 | 0.78 | 68.22 | 1.08 | 55.84 |

*Tab. 3.2 Low (LD), medium (MD) and high (HD) density and porosity values for selected clasts.*

## 3.2 Microprobe Analysis

Major element composition (in wt%) of the natural starting material, pumices, and natural glass synthesis are summarized in the following table (Tab. 3.3). As explained in Methodology section (Chapter 2), by comparing the chemical composition of the natural starting material and synthesized natural glass, we can infer that no alkali loss occurred during synthesis procedure.

| | Cinque Denti Natural | Cinque Denti Glass | Green Tuff Natural | Green Tuff Glass | Zinedi Natural | Zinedi Glass | Cuddia Mida Natural | Cuddia Mida Glass |
|---|---|---|---|---|---|---|---|---|
| $SiO_2$ | 66,52 | 66,25 | 69,49 | 70,16 | 66,90 | 67,22 | 69,89 | 70,67 |
| $Al_2O_3$ | 14,09 | 14,80 | 8,65 | 8,64 | 11,84 | 11,85 | 8,24 | 8,50 |
| $Fe_2O_3$(T) | 6,39 | 6,07 | 9,11 | 9,17 | 8,48 | 8,33 | 9,17 | 9,19 |
| MnO | 0,23 | 0,22 | 0,31 | 0,31 | 0,31 | 0,30 | 0,31 | 0,30 |
| MgO | 0,65 | 0,63 | 0,18 | 0,17 | 0,44 | 0,47 | 0,13 | 0,16 |
| CaO | 1,32 | 1,46 | 0,46 | 0,47 | 0,66 | 0,67 | 0,43 | 0,44 |
| $Na_2O$ | 5,66 | 5,73 | 6,74 | 6,45 | 6,03 | 5,98 | 6,98 | 6,39 |
| $K_2O$ | 4,25 | 4,00 | 4,51 | 4,08 | 4,67 | 4,49 | 4,49 | 4,00 |
| $TiO_2$ | 0,78 | 0,75 | 0,53 | 0,52 | 0,62 | 0,63 | 0,34 | 0,34 |
| $P_2O_5$ | 0,11 | 0,10 | 0,02 | 0,03 | 0,05 | 0,06 | 0,02 | 0,00 |
| TOT | 100 | 100 | 100 | 100 | 100 | 100 | 100 | 100 |
| P.I. | 0.96 | 0.92 | 1.78 | 1.74 | 1.23 | 1.24 | 1.91 | 1.74 |

*Tab. 3.3 Major element composition of the natural starting pumices and natural glass synthesis from this work.*

By converting major element composition from wt% to mol%, it's possible to define Peralkalinity Index (P.I.) [$(Na_2O+K_2O)/Al_2O_3$] (e.g. Dingwell et al., 1998; Di Genova et al., 2013). P.I. it's an important parameter for peralkaline magmas because of their alkali-rich nature and it describes the alkali excess over alumina. The Tab. 3.3 summarizes P.I. for the four targeted eruptions. Cinque Denti eruption, based on the P.I., classifies as metaluminous melt.

## 3.3 Textural analysis

### 3.3.1 Qualitative observation

All samples observed present a low or negligible amount of phenocrysts. In this section only few selected images representative of the samples will be shown. All analysed images can be found in Supplementary Material.

Generally, Cinque Denti clasts (Fig. 3.4), at 60x of magnification, show high porosity, well-rounded vesicles, well-preserved septa and in some cases elongated vesicles. There is no evidence of coalescence except in low-density clast.

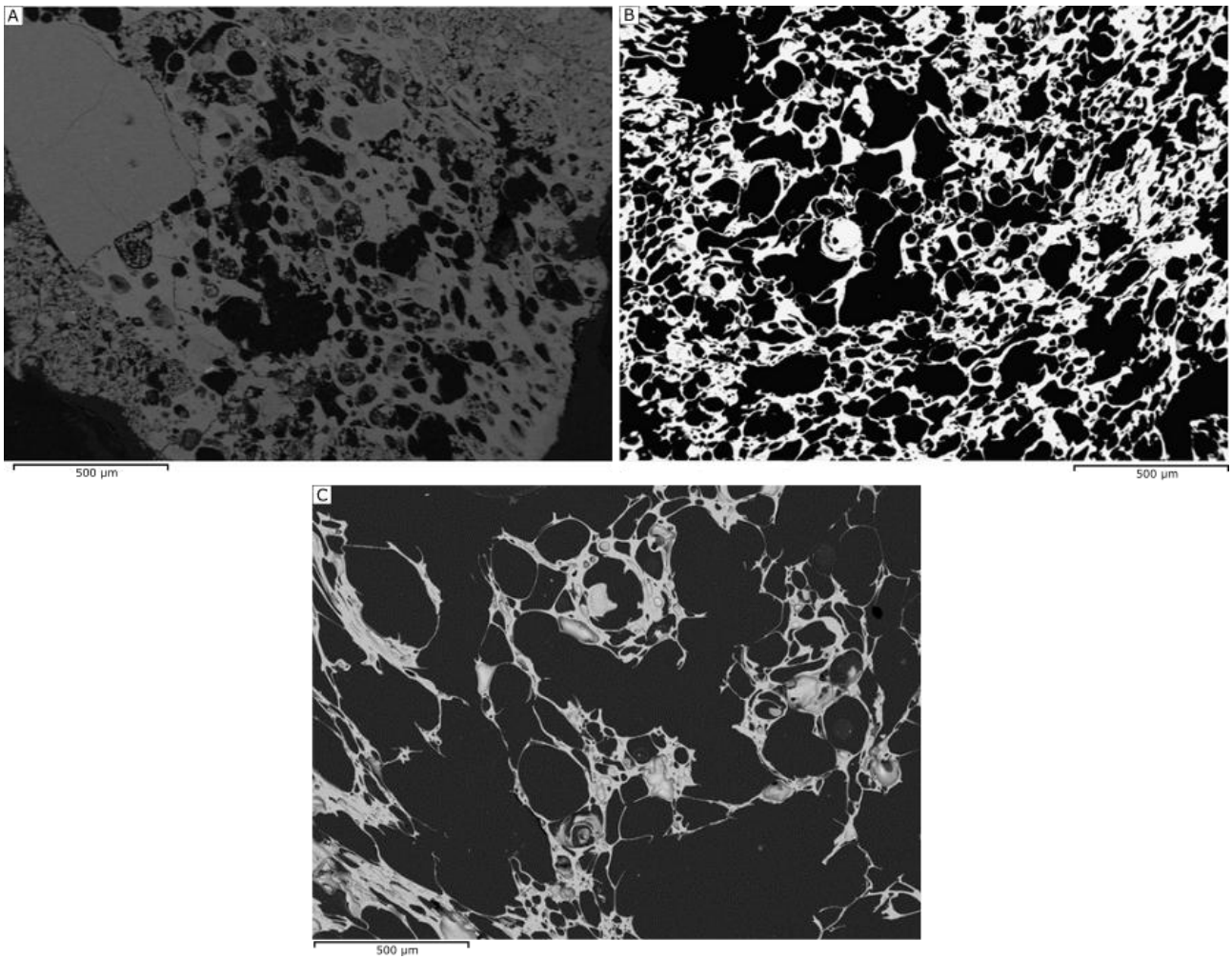


*Fig. 3.4 Cinque Denti 60x magnification SEM images. A: high density, B: medium density, C: low density. A ~500 µm, on major axes, feldspar crystal can be observed in image A.*

Green Tuff clasts (Fig. 3.5), at 60x of magnification, presents different texture compared to Cinque Denti clasts even if both are caldera-forming-eruption. Green Tuff clasts show high porosity, similar to Cinque Denti, septa are not well preserved and they are highly deformed. Vesicle are smaller, in diameter, than Cinque Denti. Coalescence (indicated with red arrow) is clear in both low, medium and high density clasts but exceptionally bigger vesicles can be observed in low density clast (Fig. 3.5C).

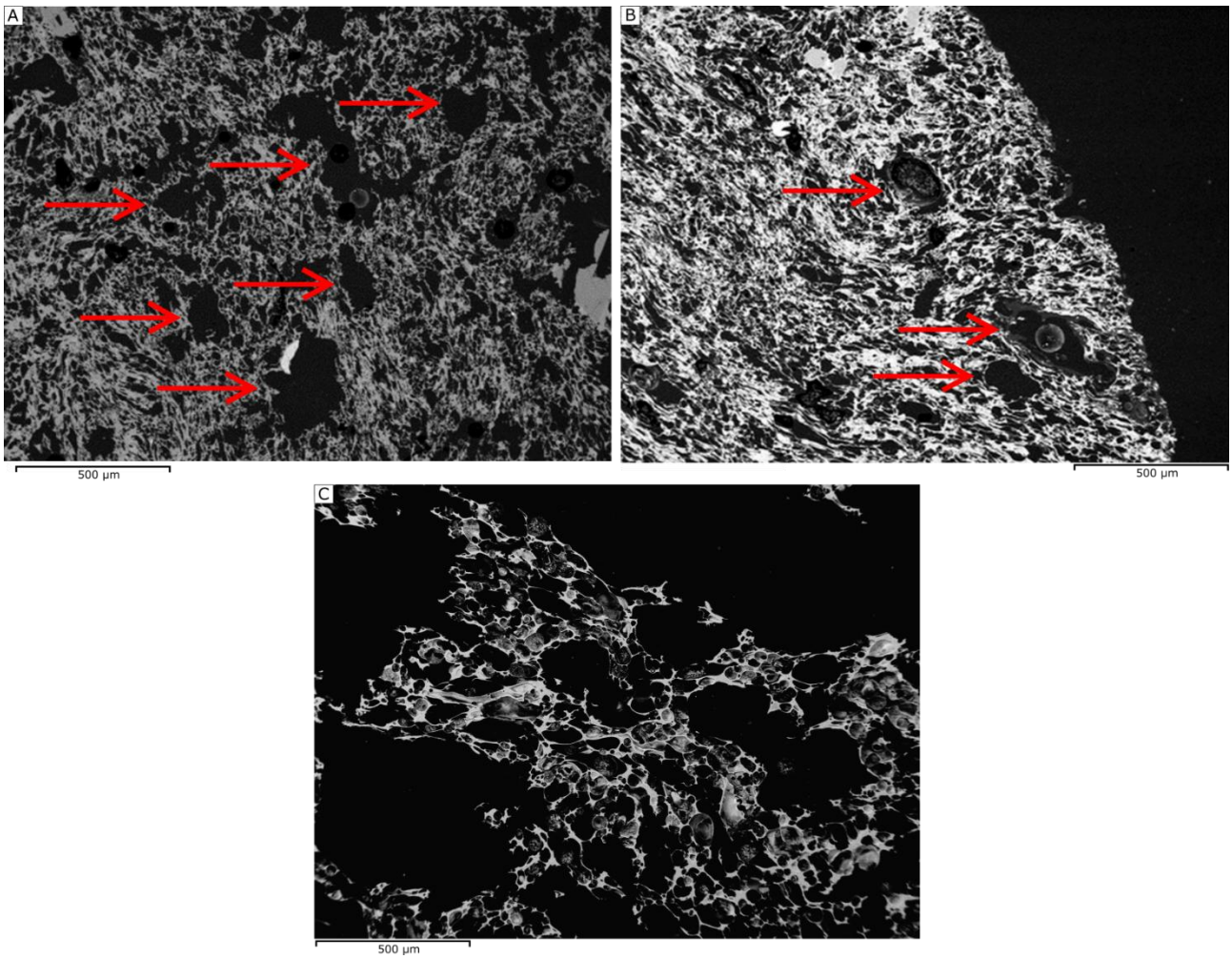


*Fig. 3.5 Green Tuff 60x magnification SEM images. A: high density, B: medium density, C: low density. Red arrows indicate coalescence. Exceptionally bigger vesicles can be observed in low density clast.*

Zinedi clasts (Fig. 3.6), at 60x of magnification, show high porosity, septa are not well-preserved, well-rounded vesicles are alternated with elongated vesicles. There is clear evidence of coalescence in low density clast and evidence of coalescence in some medium density clasts.

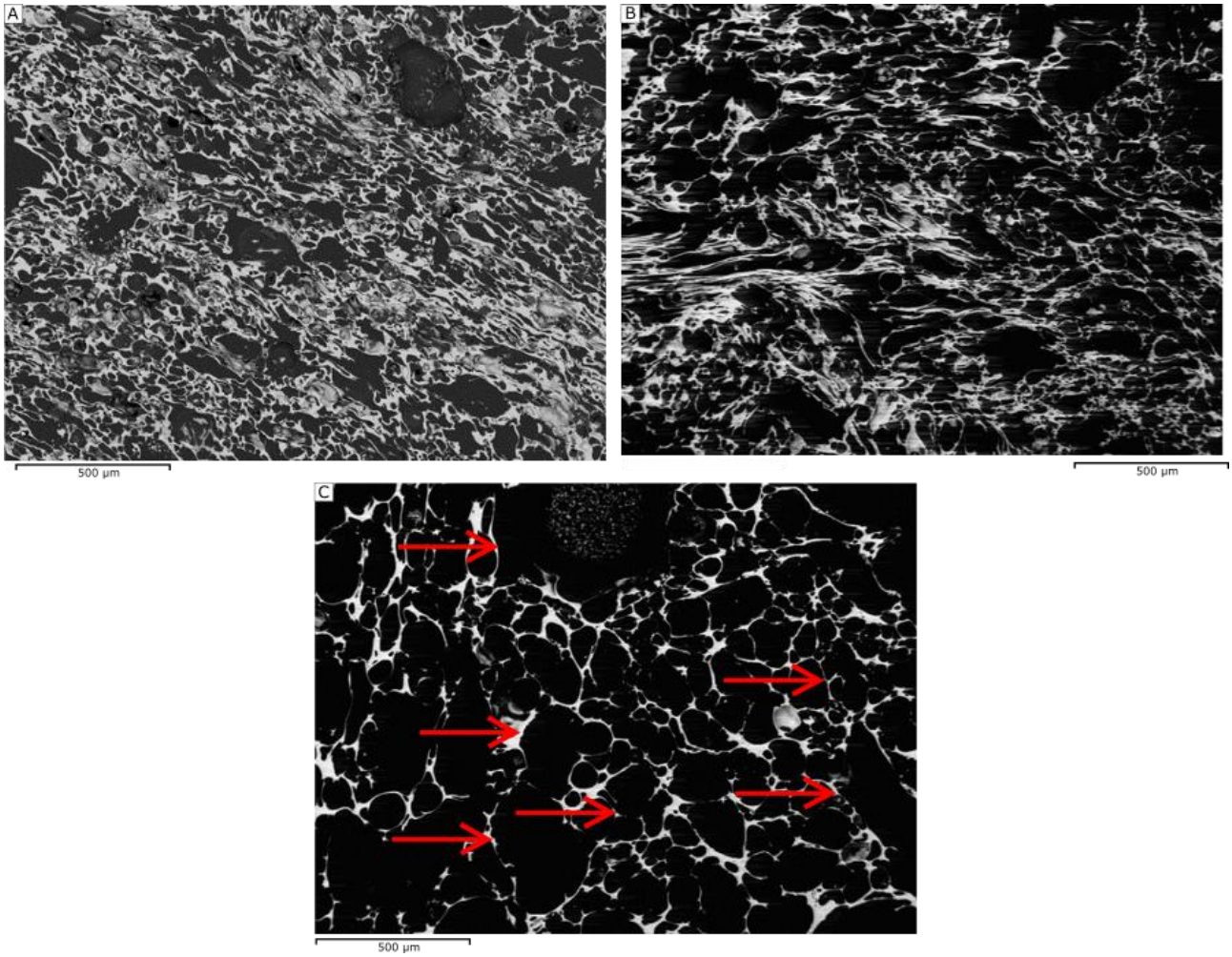


*Fig. 3.6 Zinedi 60x magnification SEM images. A: high density, B: medium density, C: low density. Red arrows indicate few examples of clear coalesced bubble.*

Cuddia Mida clasts (Fig. 3.7), at 60x of magnification, show high porosity, septa are well-preserved, well-rounded vesicles are alternated with elongated vesicles. There is clear evidence of coalescence in low and medium clasts except for high density clast.

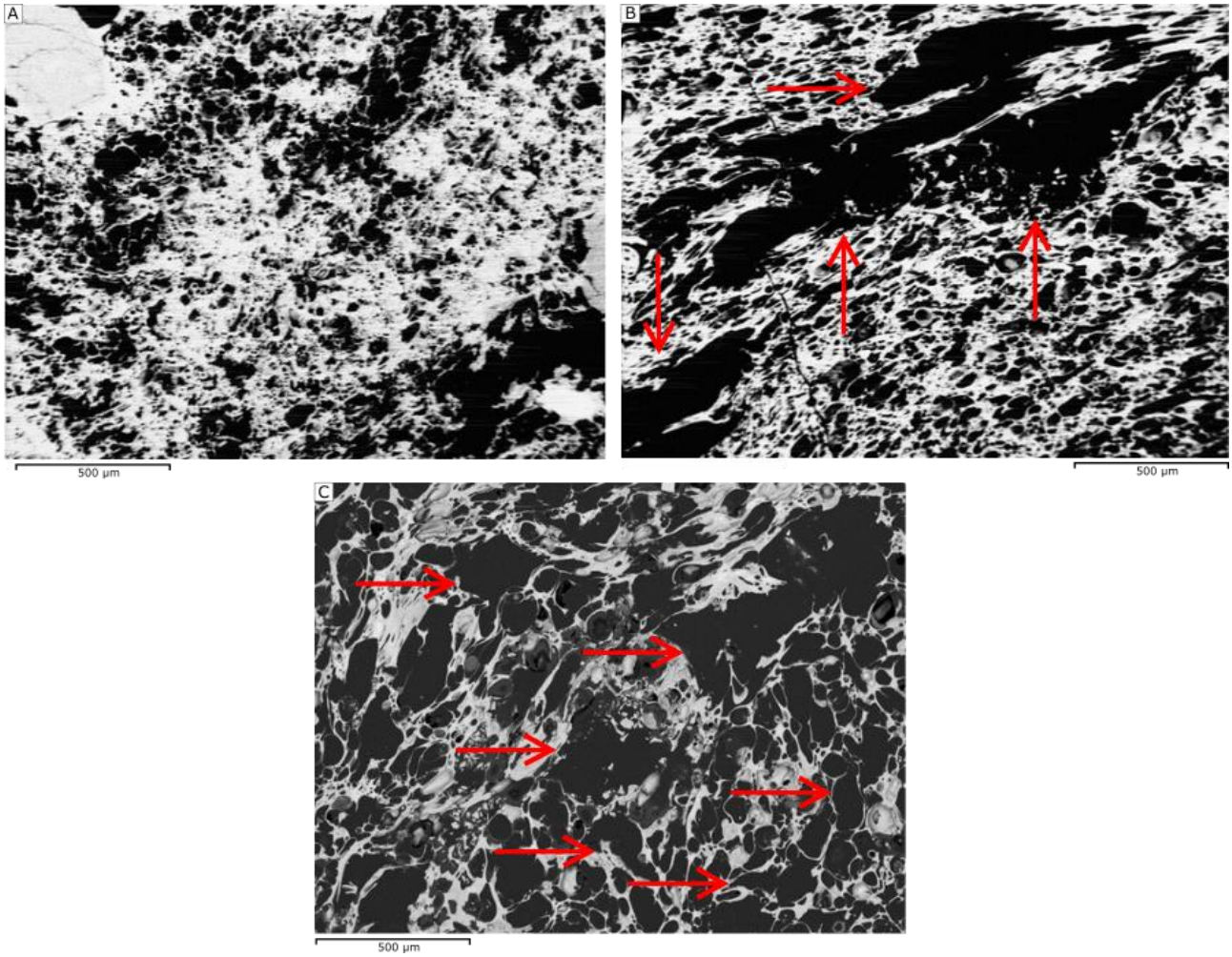


*Fig. 3.7 Cuddia Mida 60x magnification SEM images. A: high density, B: medium density, C: low density. Red arrows indicate few examples of clear coalesced bubble.*

At 300× magnification, clasts from medium density class of Cinque Denti, Green Tuff, Zinedi and Cuddia Mida (Fig. 3.8) display the same texture (round vesicle alternated with elongated vesicles, coalescence and absence of visible crystals) as observed at 60× magnification.

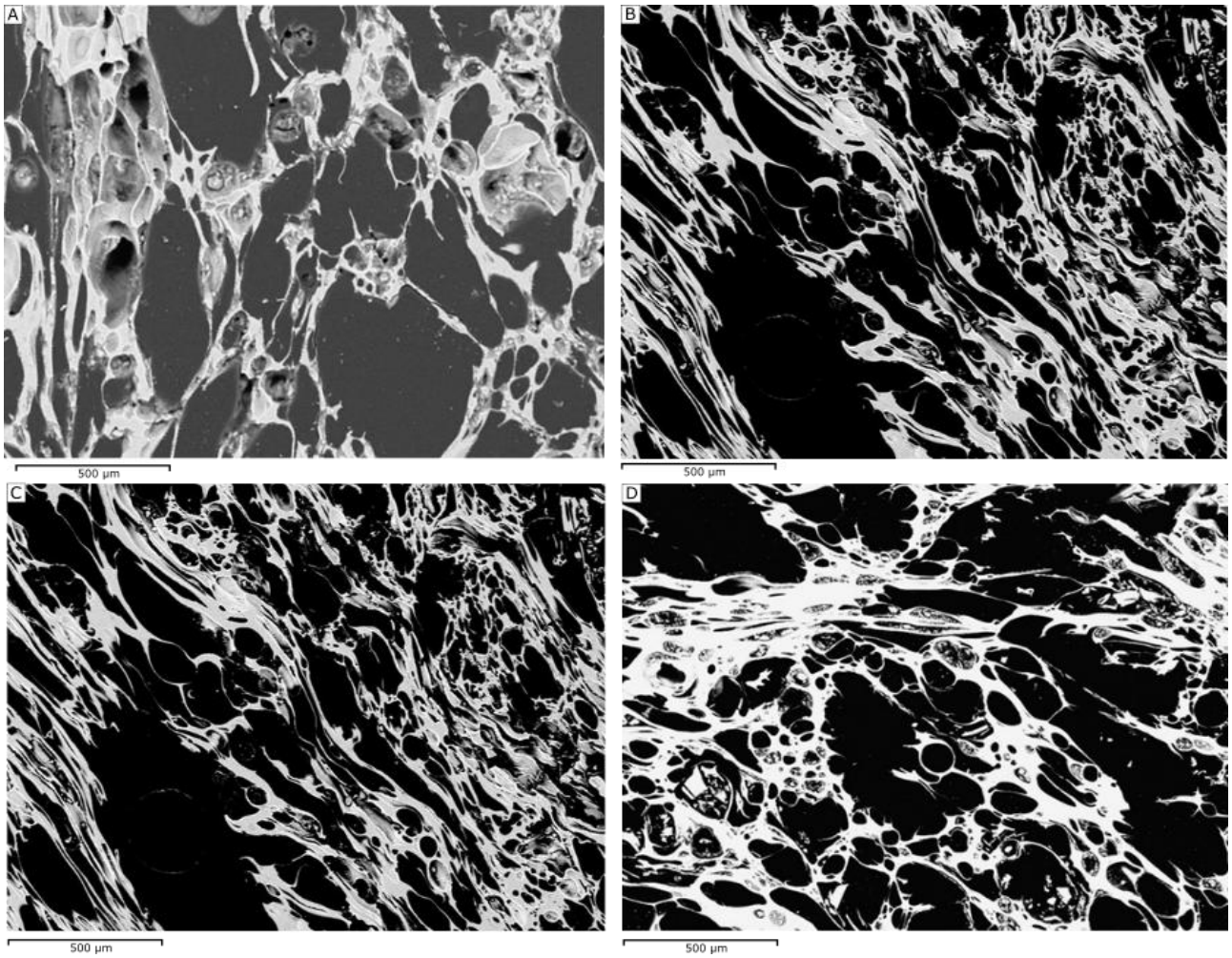


*Fig. 3.8 300x magnification SEM images from medium density class. A: Cinque Denti, B: Green Tuff, C: Zinedi, D: Cuddia Mida.*

### 3.3.2 Quantitative analysis

Textures of pyroclasts, specifically vesicle size distribution, vesicle shape, and shape distribution of microlites, which are typically heterogeneous in volcanic rocks, can be quantified from image analysis and used to study conduit processes (Cashman and Mangan, 1994). To detect heterogeneity in volcanic rocks, images at increasing magnifications (60x and 300x) have been captured as indicated in the methodology described by Shea et al. (2010). To ensure that all vesicle sizes have been adequately represented, a plot of the number density of

vesicles per areas NA vs. equivalent diameter L was constructed at different magnification (Fig. 3.9).

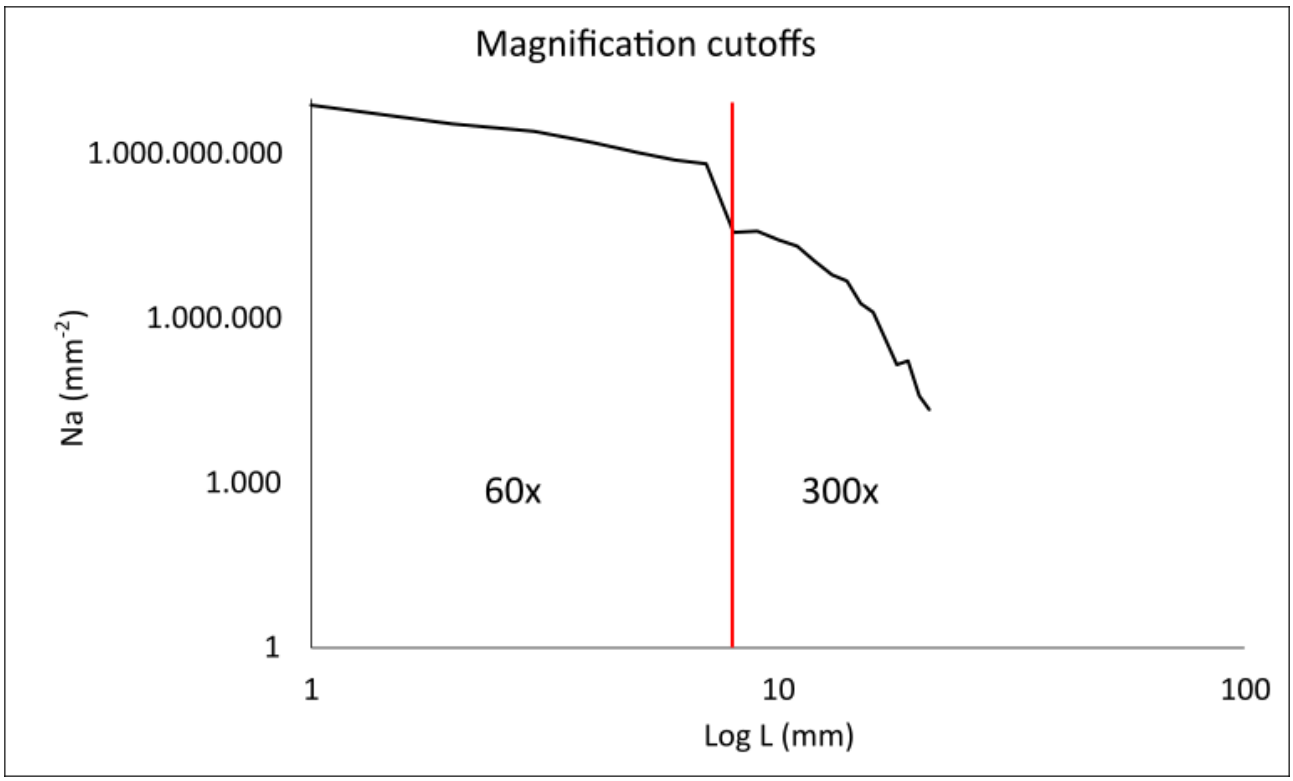


*Fig. 3.9 Illustration of the influence of how magnification cutoffs are chosen. A plot of Na vs. equivalent diameter L for each magnification results in decreasing NA with increasing L for each decreasing magnification.*

Because vesicles vary significantly both in size and in number, textural data are always displayed as distributions. One of the most common textural parameters measured is Vesicle Volume Distribution (VVD). VVDs are commonly used to infer the nature and numbers of nucleation and/or coalescence events during the vesiculation history of pyroclasts (Klug and Cashman, 1994; Shea et al., 2010). Shea et al. (2010) provide modelled distribution which can be related to different processes that can occur during magma ascent (Fig. 3.10). For this reason, by comparing our VVDs with those provided from Shea et al. (2010), we can postulate which is or which are the processes that have occurred during magma ascent.

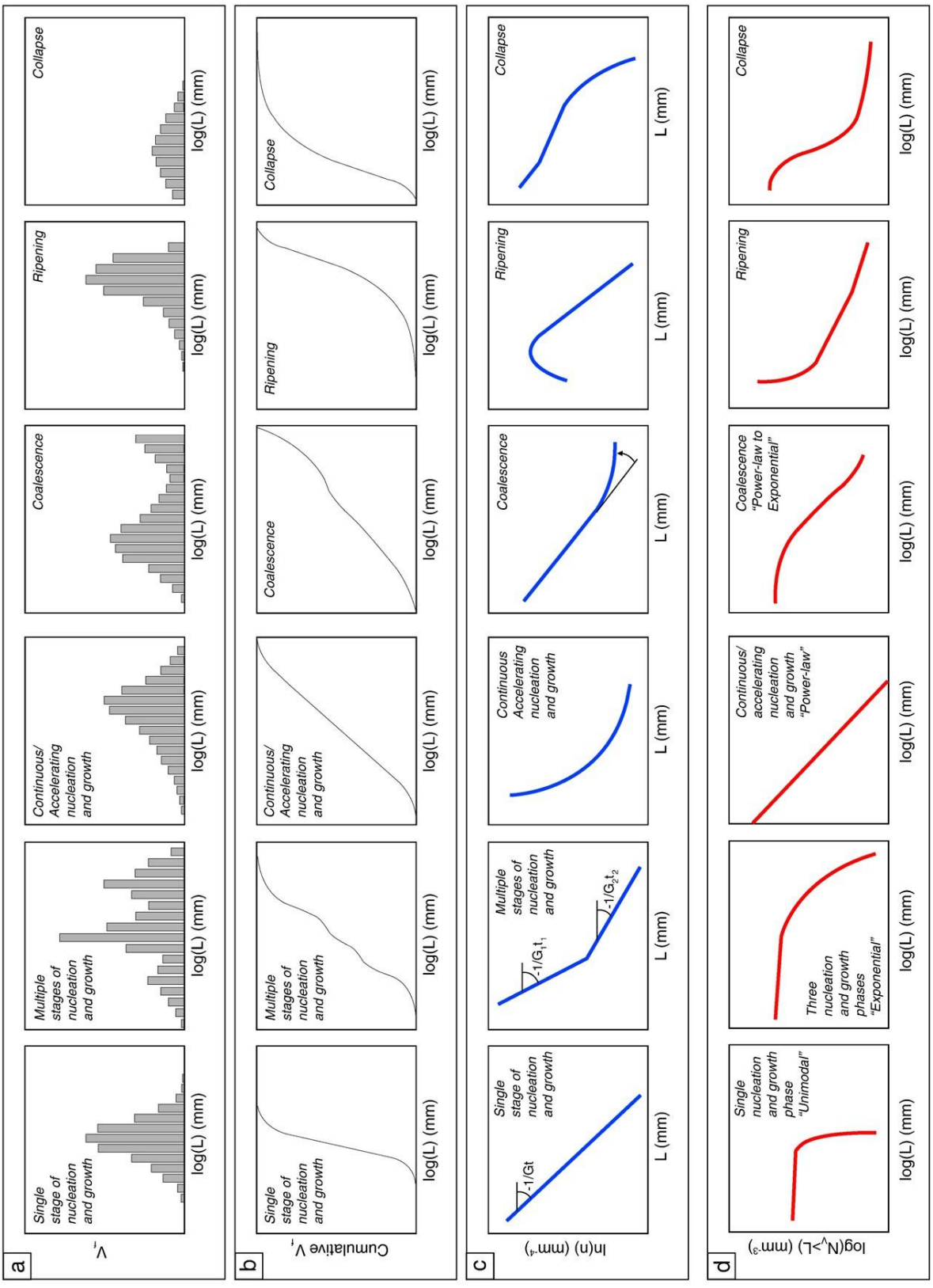


*Fig. 3.10 Various ways to display textural characteristics through size (L) and number density (n or $N_V$) plots, and processes that they may be associated with (single or few nucleation events, multiple nucleation and growth events, continuous nucleation and growth, coalescence, ripening, and collapse). (a) Simple volume fraction ($V_f$) size distribution (VVD), (b) Cumulative volume fraction size distribution (CVVD), (c) Vesicle size distributions (VSD) in terms of number density n, and (d) Cumulative number density plots log ($N_v$>L) vs. log(L) (CVSD). Because during magmatic ascent multiple vesiculation and degassing processes may occur simultaneously and overprint each other, such plots call for interpretative prudence. G is growth rate and t is time.*

Cinque Denti VVDs (Fig. 3.11) show unimodal distribution. Coalescence, noticeable from the peak at a vesicle size of 1 mm, can be observed only for low density clast 5D40. Comparing Cinque Denti VVDs with those provided by Shea et al. (2010), we can suggest a continuous nucleation and growth of vesicles during rapid magma ascent for Cinque Denti eruption.

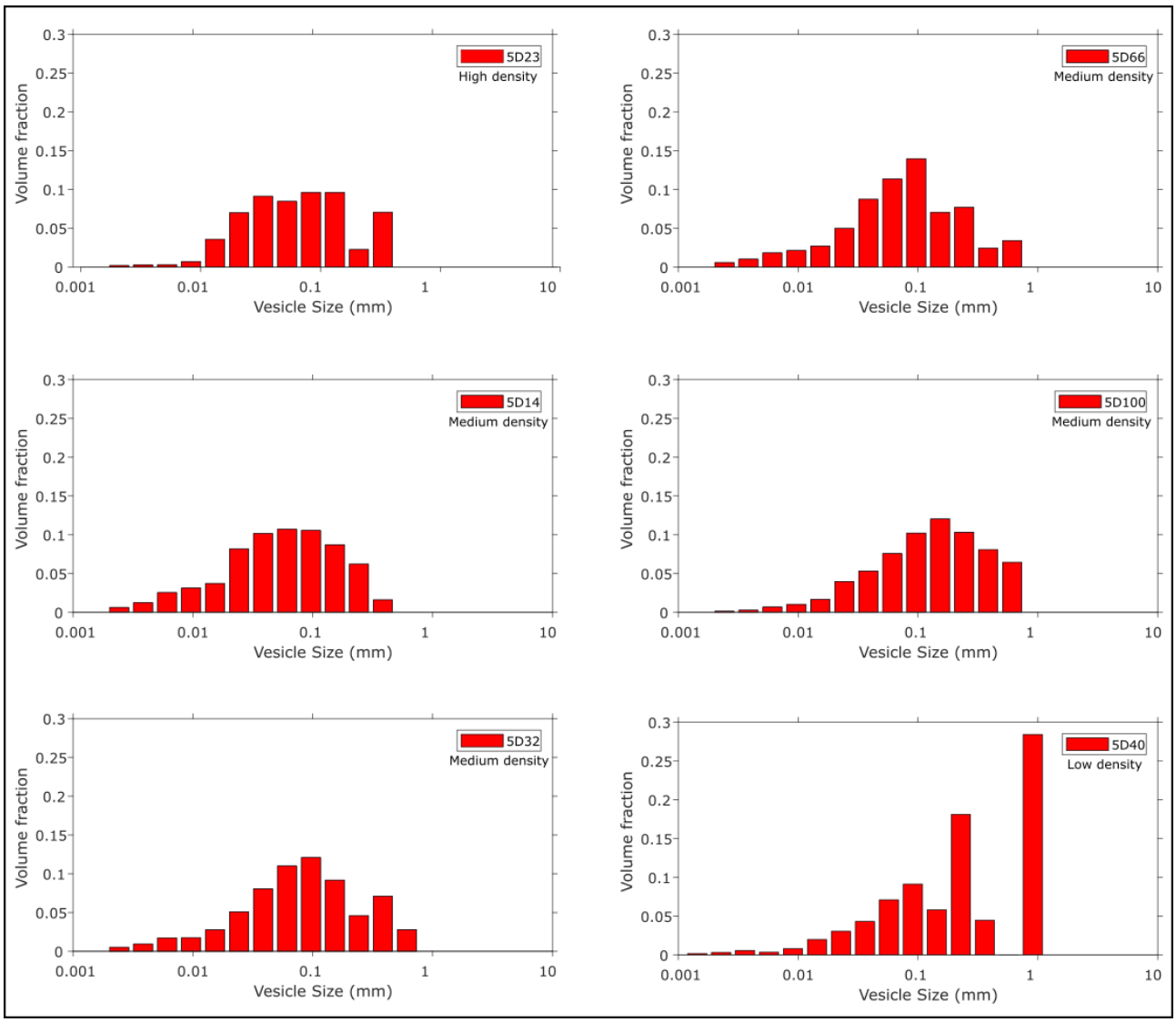


*Fig. 3.11 Vesicle Volume Distribution plot for Cinque Denti eruption. High density clast: 5D23; Medium density clasts: 5D66, 5D14, 5D100, 5D32; Low density clast: 5D40. Clear evidence of coalescence for 5D40.*

Green Tuff VVDs (Fig. 3.12) show plurimodal distribution. Tail at large vesicle size (1 mm) is present for all samples and can be interpreted as due to coalescence processes. Comparing Green Tuff VVDs with those provided by Shea et al. (2010), we can suggest a multiple stage of nucleation and growth of vesicles during magma ascent for Green Tuff eruption.

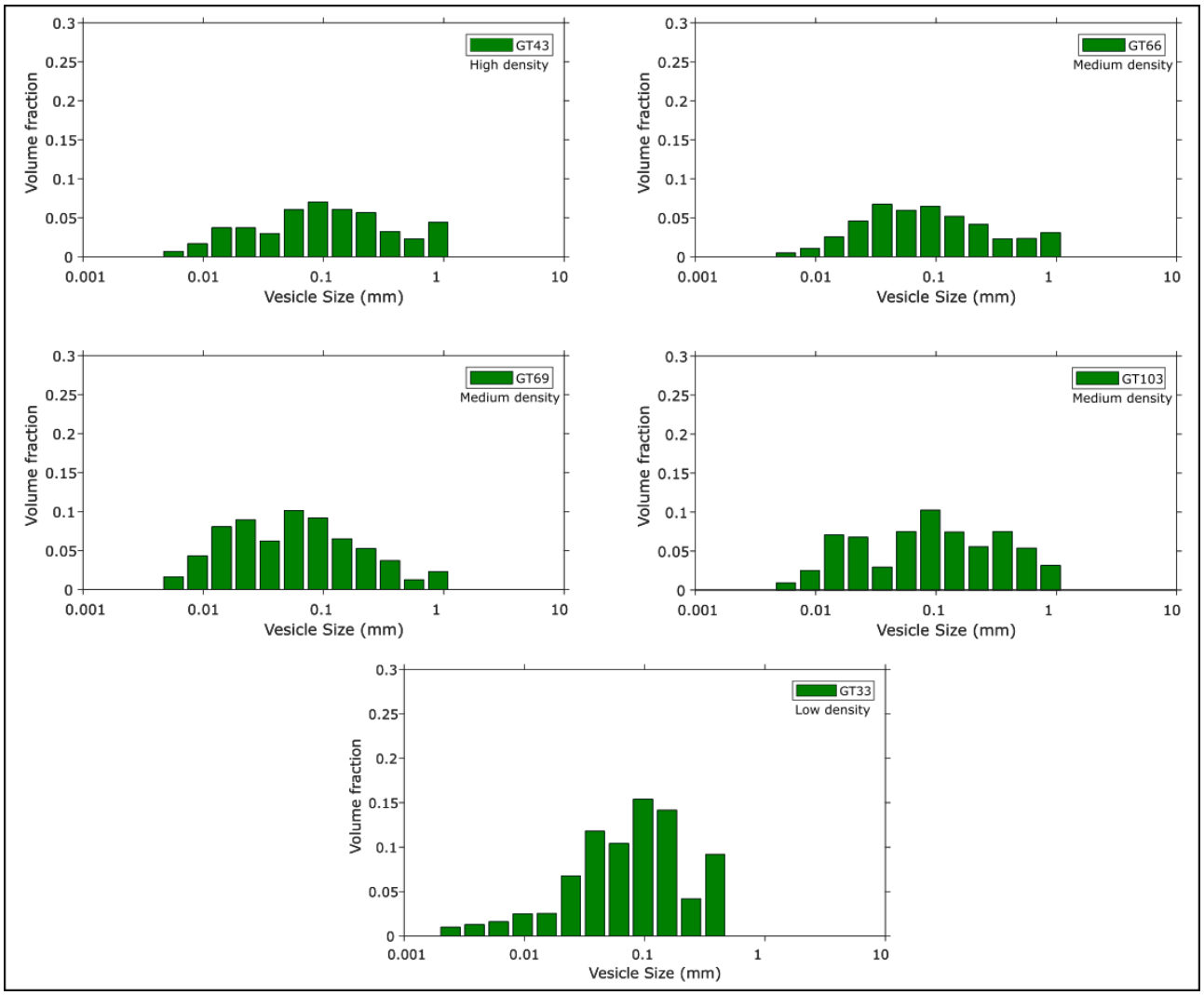


*Fig. 3.12 Vesicle Volume Distribution plot for Green Tuff eruption. High density clast: GT43; Medium density clasts: GT66, GT69, GT103; Low density clast: GT33. Coalescence can be observed for each clast and it's strongly present for low density clast.*

Zinedi VVDs (Fig. 3.13) show unimodal distribution. Coalescence can be observed for low density clast Z88 and for medium density clast Z13 and Z18. Comparing Zinedi VVDs with those provided by Shea et al. (2010), we can suggest a continuous nucleation and growth of vesicles during magma ascent for Zinedi eruption.

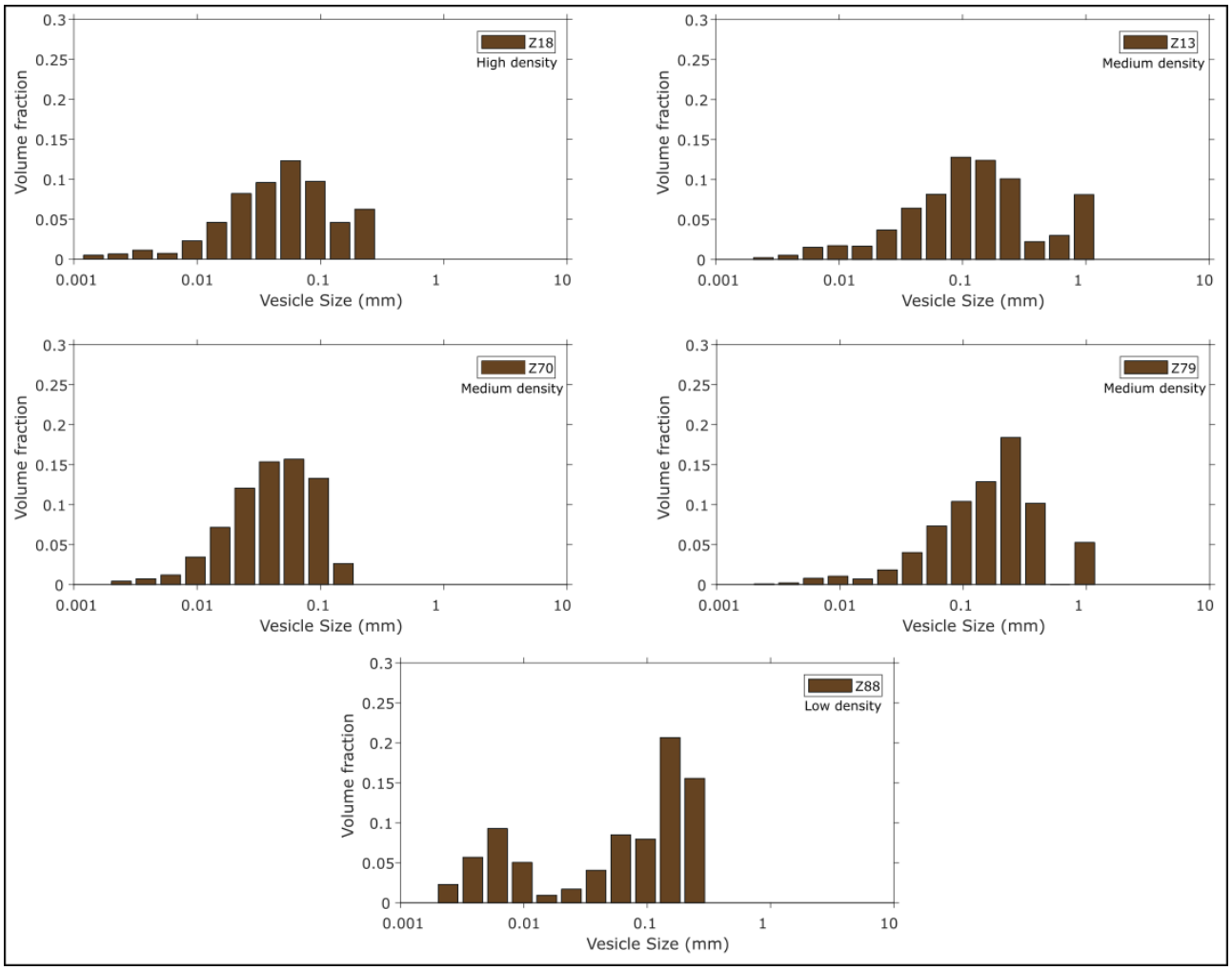


*Fig. 3.13 Vesicle Volume Distribution plot for Zinedi eruption. High density clast: Z18; Medium density clasts: Z13, Z70, Z79; Low density clast: Z88. Incipient coalescence can be observed for Z13 (medium density class) and Z88 (low density class).*

Cuddia Mida VVDs (Fig. 3.14) show plurimodal distribution. Coalescence can be clearly observed for medium density clasts and low density clast. Comparing Cuddia Mida VVDs with those provided by Shea et al. (2010), we can suggest a multiple stage of nucleation and growth of vesicles during magma ascent for Cuddia Mida eruption.

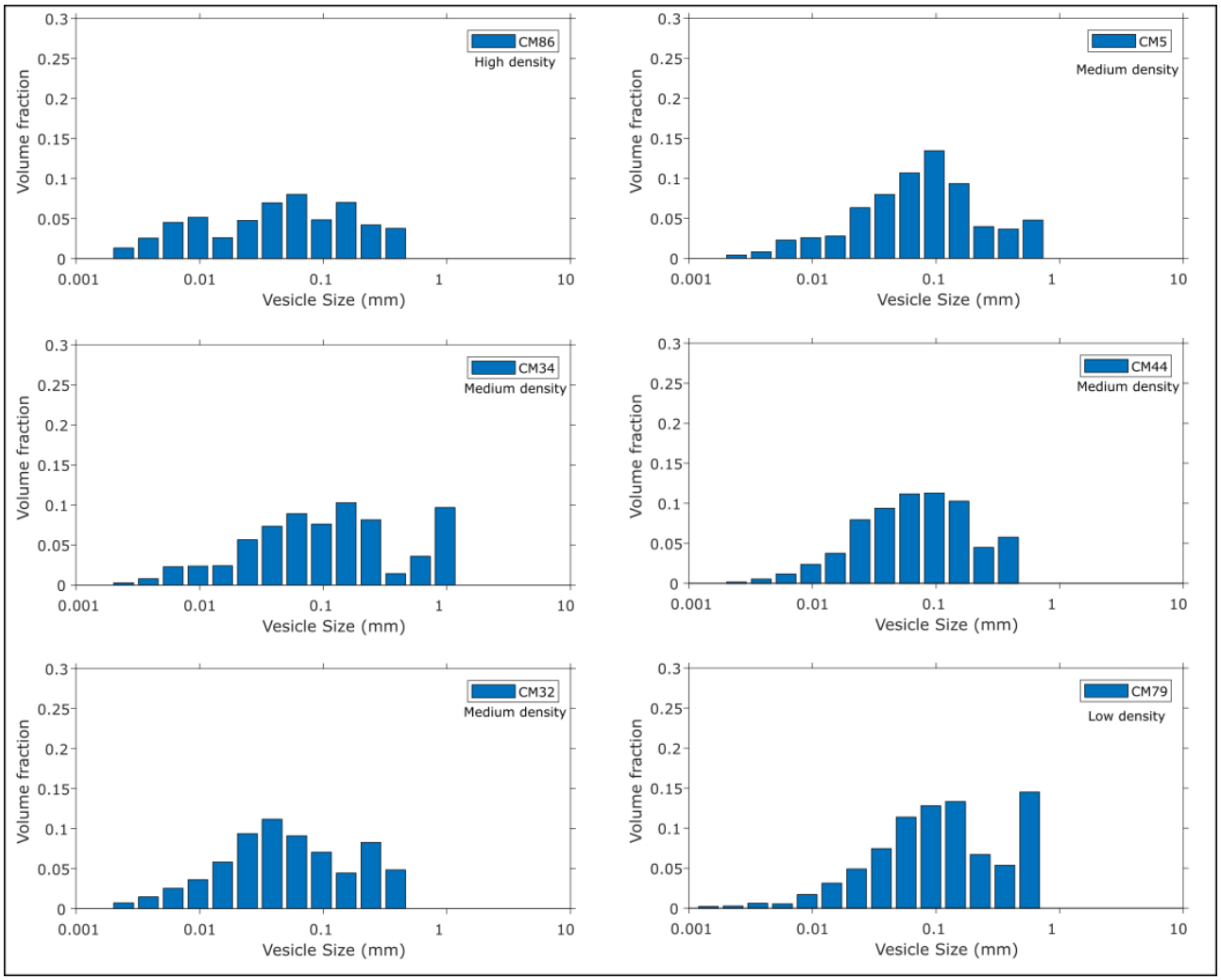


*Fig. 3.14 Vesicle Volume Distribution plot for Cuddia Mida eruption. High density clast: CM86; Medium density clasts: CM5, CM34, CM44, CM32; Low density clast: CM79. Coalescence can be observed for medium density clasts and low density clast.*

### 3.3.3 Vesicle Number Density (VND)

Vesicle number density (VND) is one of the most important parameters for comparing eruptions with different eruptive style. It represents the integrated result of bubble nucleation through time and provides information on bubble nucleation rate and decompression rate through the conduit (Toramaru, 1989; Cashman & Mangan, 1994; Toramaru, 1995; Klug, Cashman & Bacon, 2002; Toramaru, 2006, 2010). VNDs are referenced to the melt volume and depend on the time available for the bubbles to nucleate and grow, on the magma rise speed, on the initial concentration of exsolving gases and on the volatile diffusivity. Total vesicle number densities for the fall out pumice clasts range from $4.80x10^5$ $mm^{-3}$ to $6.06x10^6$ $mm^{-3}$ for Cinque Denti eruption, from $2.16x10^5$ $mm^{-3}$ to $6.05x10^6$ $mm^{-3}$ for Green Tuff eruption, from $3.21x10^5$ $mm^{-3}$ to $5.52x10^6$ $mm^{-3}$ for Zinedi eruption and from $1.04x10^6$ $mm^{-3}$ to $5.20x10^6$ $mm^{-3}$ for Cuddia Mida eruption. Tab. 3.4 shows VNDs and other textural parameters values for each clast analysed.

| Eruption | Clast ID | Porosity (%) | VND ($mm^{-3}$) | Max L (mm) | Mean L MD (mm) |
|---|---|---|---|---|---|
| Cinque Denti HD | 23 | 57,58 | $4.80x10^5$ | 0,385 | 0,440 |
| Cinque Denti MD | 66 | 68,12 | $1.75x10^6$ | 0,485 | |
| Cinque Denti MD | 14 | 67,5 | $1.73x10^6$ | 0,485 | |
| Cinque Denti MD | 100 | 67,8 | $6.06x10^6$ | 0,306 | |
| Cinque Denti MD | 32 | 67,57 | $1.71x10^6$ | 0,485 | |
| Cinque Denti LD | 40 | 78,59 | $2.67x10^6$ | 0,721 | |
| Cinque Denti mean MD | | | $2.81x10^6$ | | |
| | | | | | |
| Green Tuff HD | 43 | 47,23 | $2.60x10^5$ | 0,897 | 0,836 |
| Green Tuff MD | 66 | 67,85 | $2.17x10^5$ | 0,897 | |
| Green Tuff MD | 69 | 66,89 | $2.49x10^5$ | 0,897 | |
| Green Tuff MD | 103 | 66,86 | $2.16x10^5$ | 0,713 | |
| Green Tuff LD | 33 | 79.49 | $6.05x10^5$ | 0,306 | |
| Green Tuff mean MD | | | $2.27x10^5$ | | |
| | | | | | |
| Zinedi HD | 18 | 60,52 | $5.52x10^6$ | 0,228 | 0,564 |
| Zinedi MD | 13 | 71,2 | $3.21x10^5$ | 0,769 | |
| Zinedi MD | 70 | 71,6 | $4.72x10^5$ | 0,153 | |
| Zinedi MD | 79 | 72,1 | $5.30x10^5$ | 0,769 | |
| Zinedi LD | 88 | 81,64 | $9.60x10^5$ | 0,243 | |
| Zinedi mean MD | | | $4.41x10^5$ | | |
| | | | | | |
| Cuddia Mida HD | 86 | 55,84 | $1.78x10^6$ | 0,306 | 0,486 |
| Cuddia Mida MD | 5 | 68,3 | $1.17x10^6$ | 0,485 | |
| Cuddia Mida MD | 34 | 68,22 | $1.04x10^6$ | 0,769 | |
| Cuddia Mida MD | 44 | 68,36 | $5.20x10^6$ | 0,306 | |
| Cuddia Mida MD | 32 | 68,18 | $2.27x10^6$ | 0,385 | |
| Cuddia Mida LD | 79 | 79.12 | $1.65x10^6$ | 0,455 | |
| Cuddia Mida mean MD | | | $2.42x10^6$ | | |

*Tab. 3.4 VNDs and other textural parameters (Max L= vesicle maximum diameter; Mean L MD= vesicle mean diameter for medium density clasts) values for each clast analysed. Mean VNDs for MD class are expressed as we are going to use it for numerical simulation later in this work.*

## 3.4 Pure liquid viscosity determination

High temperature, low viscosity of the samples was determined by Concentric Cylinder (CC) measurements at T between 1200° and 1450° C, in the viscosity interval from $10^{2.66}$ to $10^{4.56}$ Pa·s (Fig. 3.15). Low-temperature, high viscosity was determined by Differential Scanning Calorimeter (DSC) and Micropenetration (MP) measurements (Fig. 3.16). Calorimetric measurement allowed to derive $T_g$, which is the glass transition temperature corresponding to the viscosity of $10^{12}$ Pa·s. Tab. 3.5 summarizes viscosity measurements in the low and high temperature interval. In the Tab. 3.5, order of DSC measurements is: $T_{peak}$ at $q_{c,h}$ 5, 10 and 20 °C $min^{-1}$ and $T_{onset}$ $q_{c,h}$ 5, 10 and 20 °C $min^{-1}$. $T_g$ for each eruption is highlighted in red. Since DSC and MP measurements cover the same low-temperature range, MP experiments were performed at the DSC target temperatures to better constrain viscosity.

| | CINQUE DENTI | | GREEN TUFF | | ZINEDI | | CUDDIA MIDA | |
|---|---|---|---|---|---|---|---|---|
| | T (°C) | Log η (Pa·s) | T (°C) | Log η (Pa·s) | T (°C) | Log η (Pa·s) | T (°C) | Log η (Pa·s) |
| **CC** | 1450 | 3,11 | 1450 | 2,66 | 1450 | 2,96 | 1450 | 2,88 |
| **CC** | 1400 | 3,34 | 1400 | 2,80 | 1400 | 3,16 | 1400 | 3,10 |
| **CC** | 1350 | 3,61 | 1350 | 3,03 | 1350 | 3,41 | 1350 | 3,33 |
| **CC** | 1300 | 3,88 | 1300 | 3,31 | 1300 | 3,69 | 1300 | 3,59 |
| **CC** | 1250 | 4,21 | 1250 | 3,59 | 1250 | 3,99 | 1250 | 3,88 |
| **CC** | 1200 | 4,56 | 1200 | 3,93 | 1200 | 4,34 | 1200 | 4,18 |
| **DSC $T_{peak}$ 5-5** | - | 10,92 | - | 10,92 | - | 10,92 | 619,8 | 10,92 |
| **DSC $T_{peak}$ 10-10** | 654,3 | 10,62 | - | 10,62 | 626,1 | 10,62 | 639,2 | 10,62 |
| **DSC $T_{peak}$ 20-20** | 672,3 | 10,32 | 666,6 | 10,32 | 652,3 | 10,32 | 648,2 | 10,32 |
| **DSC $T_{onset}$ 5-5** | - | 12,28 | - | 12,28 | - | 12,28 | 566,3 | 12,28 |
| **DSC $T_{onset}$ 10-10** | 626,3 | 11,98 | 591,5 | 11,98 | 573,4 | 11,98 | 570,0 | 11,98 |
| **DSC $T_{onset}$ 20-20** | 629,9 | 11,68 | 600,3 | 11,68 | 595,3 | 11,68 | 588,9 | 11,68 |
| **MP** | 619,9 | 13,05 | 583,4 | 11,28 | 590,3 | 12,55 | 648,2 | 10,87 |
| **MP** | 656,1 | 12,73 | 603,4 | 11,53 | 626,0 | 12,36 | 588,9 | 12,14 |
| **MP** | 675,2 | 12,63 | 623,4 | 11,11 | 652,3 | 12,19 | 619,8 | 12,19 |
| **MP** | 707,8 | 12,25 | 643,4 | 10,74 | 676,3 | 11,69 | 698,2 | 9,75 |
| **MP** | - | - | 666,8 | 10,17 | 684,8 | 11,33 | - | - |
| **MP** | - | - | - | - | 702,3 | 11,2 | - | - |

*Tab. 3.5 Summary of viscosity measurements for high (CC) and low (DSC-MP) temperature. $T_g$ for each eruption is highlighted in red. Errors related to CC measurements are ±2 °C and ±0.02 Pa·s. Errors related to DSC measurements are ±5 °C and ±0.15 Pa·s for $K_{onset}$ and ±0.2 Pa·s for $K_{peak}$. Error related to MP measurements are ±5 °C ±0.1 Pa·s.*

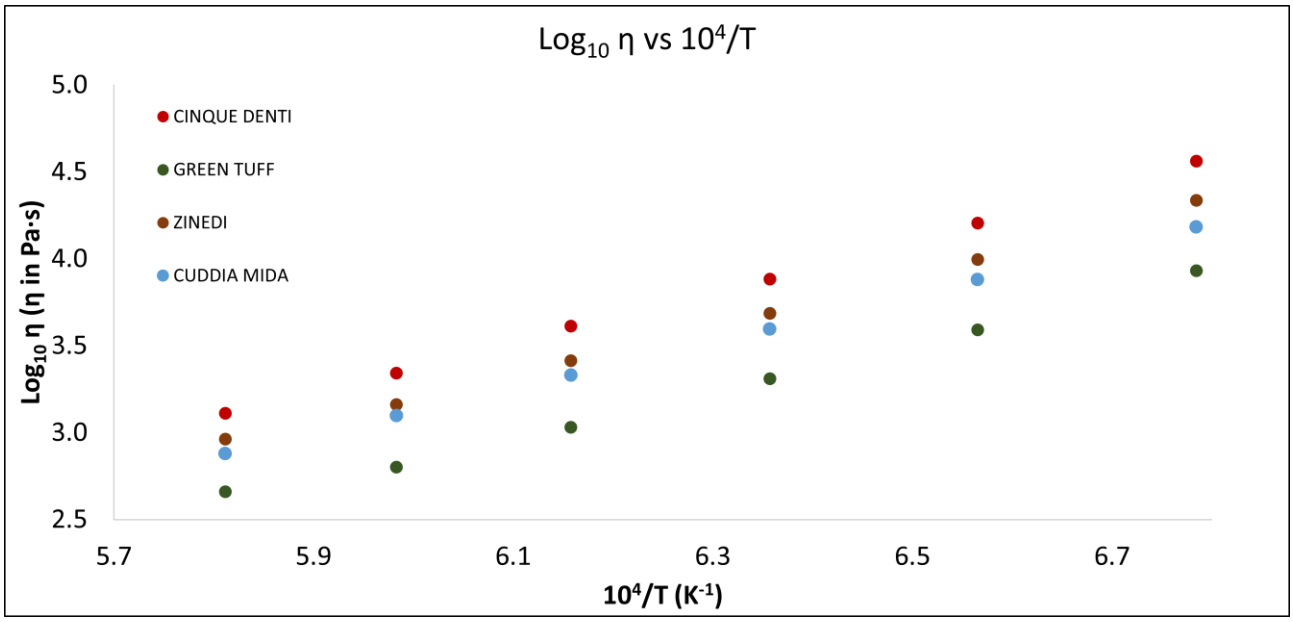


*Fig. 3.15 High-temperature viscosity measured with Concentric Cylinder (CC) apparatus. Errors (±2 °C and ±0.02 Pa·s) are smaller than symbols.*

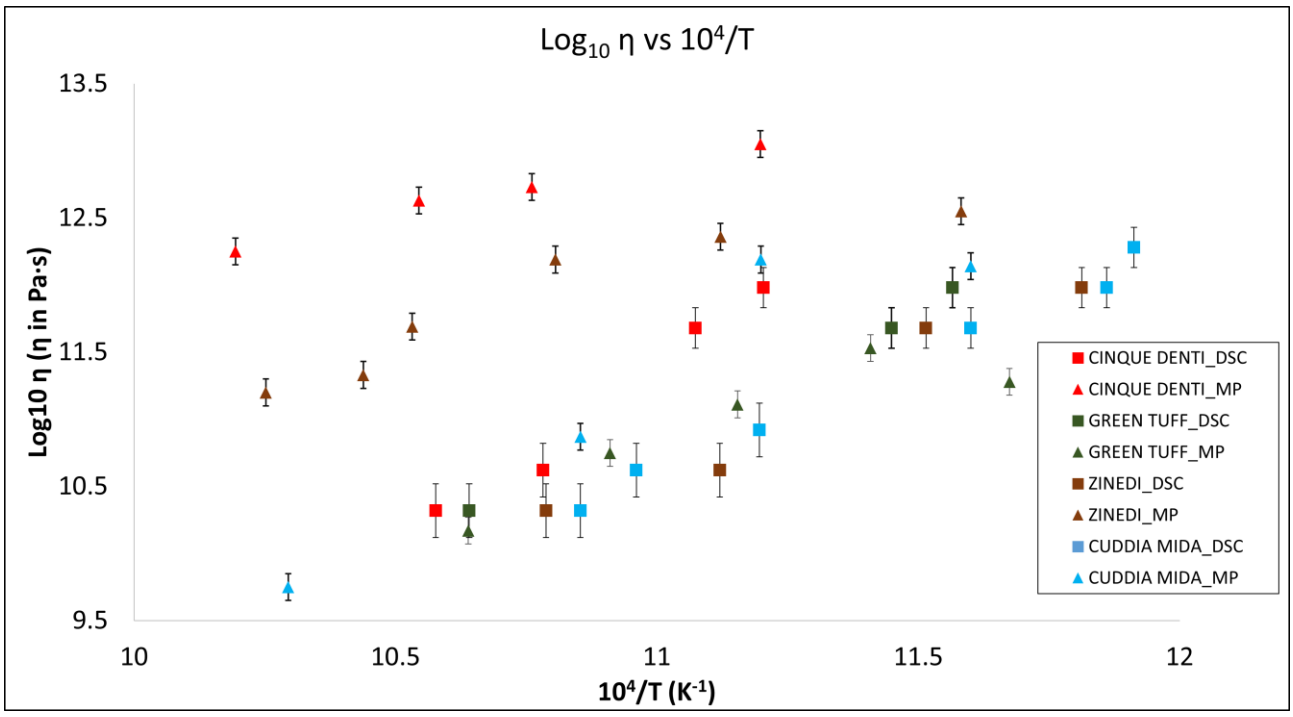


*Fig. 3.16 Low-temperature viscosity measured with Differential Scanning Calorimeter (square) and Micropenetration (triangle) technique. Errors are reported.*

In Fig. 3.15 viscosity measurements in high temperature regime are reported. Cinque Denti exhibits the highest anhydrous viscosity among the melts analysed while Green Tuff the lowest. In Fig. 3.16 viscosity measurements in low temperature regime are reported. We can notice how viscosity values are strongly different, for the same target temperature, between DSC and MP measurements. This discrepancy may reach up to two log units. As it will be discussed further in

this chapter, some structural changes occurred in the samples during MP measurements which may explain the different rheological behaviour. Low and high temperatures viscosity data have been fitted to a single and continuous temperature dependent viscosity relationship via the use of the Vogel-Fulcher-Tammann (VFT) equation (Vogel, 1921; Fulcher, 1925; Tammann and Hesse, 1926):

$$\log\ (\eta) = A + \frac{B}{T-C} \quad (3.1)$$

where $\eta$ is viscosity in Pa·s, T is the temperature in Kelvin and *A*, *B* and *C* are respectively the pre-exponential factor, the pseudo-activation energy and the Vogel temperature. The viscosity data have been fitted by assuming that the pre-exponential parameter *A* is a constant independent of composition (Richet and Bottinga 1986; Russell et al., 2003) with a value of A = -4.55 (Giordano et al., 2008). Despite the marked discrepancy between DSC and MP measurements, an initial fit was performed including data from both techniques. Values of *A*, *B* and *C* for each eruption are reported in Tab. 3.6. Fig. 3.17 shows viscosity values from each measurement and VFT fitting curve for each eruption.

| | **Cinque Denti** | **Green Tuff** | **Zinedi** | **Cuddia Mida** |
|---|---|---|---|---|
| A | -4.55 | -4.55 | -4.55 | -4.55 |
| B | 1.1E+04 | 1.09E+04 | 1.19E+04 | 1.16E+04 |
| C | 221.6163 | 196.99 | 164.16 | 157.4029 |

*Tab. 3.6 Summary of A, B and C values for viscosity measurements fitting.*

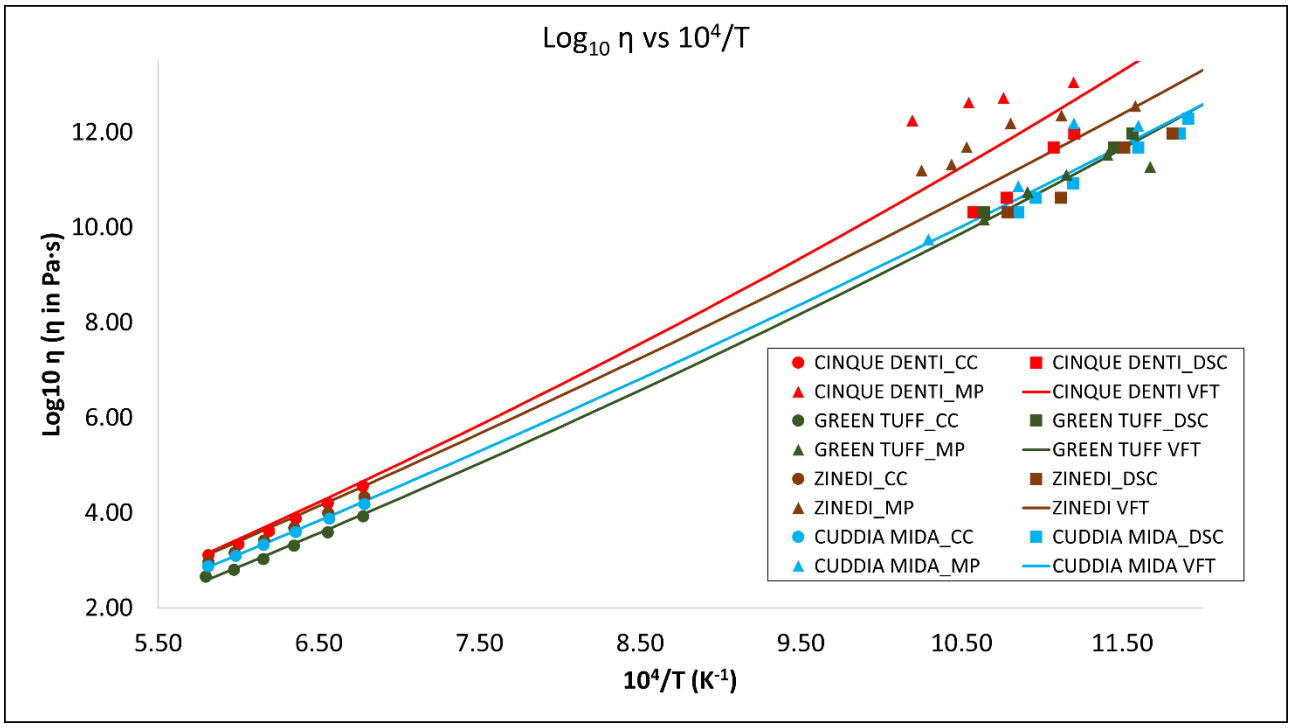


*Fig. 3.17 Measured viscosity data from high temperature (CC-circle) and low temperature (DSC-square; MP-triangle). Continuous curves correspond to VFT fitting curve derived from Vogel-Fulcher-Tammann (VFT) equation.*

## 3.5 Raman spectroscopy

Raman measurements have been carried out for all synthesis glasses both pre- and post- viscosity measurements. Raman analyses represent a helpful tool to estimate potential silicate melt structure changes occurring during experiments. Here we analyzed synthesis glass from Cinque Denti, Green Tuff, Zinedi and Cuddia Mida both in pre-experimental and post-experimental conditions. In the following figures the low wavelength spectra, representing the silicate structures for all samples, are shown. The spectral features can be categorized in three regions: 1) a low-frequency region (LF: ~250-600 $cm^{-1}$), 2) an intermediate-frequency region (IF: ~600-800 $cm^{-1}$), and 3) a high-frequency region (HF: ~800-1200 $cm^{-1}$). The broad band centered at ~500 $cm^{-1}$ represents vibrational motions involving bridging oxygens associated with a wide range of T-O-T environments (McMillan, 1984; Mysen et al., 1982; Di Genova et al., 2017). This region originates from rings of tetrahedra connected in three-, four-, five-, six or higher-members (Bell et al., 1968; Galeener, 1982; McMillan, 1984; Mysen et al., 1982; Poe et al., 2001; Seifert et al., 1982; Sharma et al.,1981). In the intermediate-frequency region, the peak at 670-690 $cm^{-1}$ reflects the presence of nanolites (Di Genova et al., 2017, Bondar et al., 2025). The presence of a peak at 310 $cm^{-1}$ can also be considered diagnostic of nanolites formation, as highlighted by the recent study

by Bondar et al. (2025). In that work, the authors propose that nanolites crystallization is characterized by distinct Raman peaks at both 310 and 670 $cm^{-1}$. Whereas the evolution of the 310 $cm^{-1}$ peak is controlled exclusively by the degree of nanolites crystallization, the appearance and evolution of the 670 $cm^{-1}$ peak are more complex, being temperature-dependent and difficult to detect above 500 °C. The region between 800 and 1200 $cm^{-1}$ results from T-O stretching vibrations and provides information on the distribution of bridging oxygens and therewith on the degree of polymerization of the structure (Bell and Dean, 1972; Furukawa et al., 1981; McMillan, 1984; Mysen, 2003). Moreover, recent studies (Di Muro et al., 2009; Di Genova et al., 2017) drew the attention to the effect of iron redox state on this region for anhydrous rhyolitic glasses. These studies reported direct correlations between the intensity of the band at 970 $cm^{-1}$ and the $Fe^{3+}/Fe_{tot}$ ratio of the glass. The high wavelength region of the spectra is not presented here as water was never detected in our samples, confirming their anhydrous nature. In the next pages, Raman spectra normalized to the highest Raman peak intensity for each measurement.

Fig. 3.18 shows Raman spectra for Cinque Denti eruption before (Pre-Run) and after CC (Post-CC). No variation in Raman features is detected.

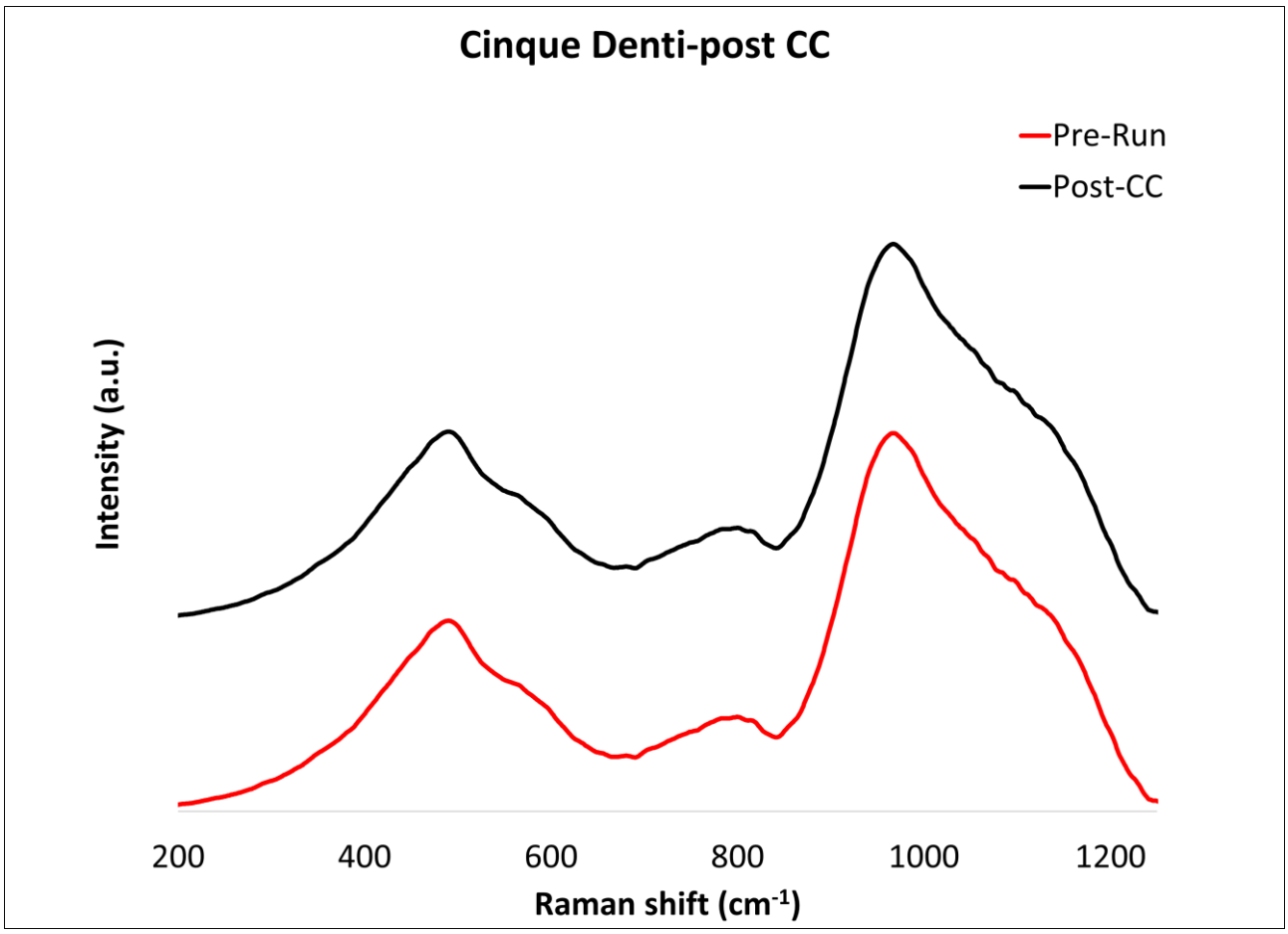


*Fig. 3.18 Baseline-corrected and normalized Raman spectra for pre-run and post-CC measurements for Cinque Denti anhydrous melt. No variation in Raman spectra is detected.*

Fig. 3.19 shows Raman spectra for Cinque Denti eruption before (Pre-Run) and after DSC (Post-DSC-) cycle 10-10 and cycle 20-20. Post-DSC Raman spectra show a peak at 670 $cm^{-1}$, attributed to nanolites formation (Di Genova et al., 2017; Bondar et al., 2025). An inverse relationship between the intensity of the 670 $cm^{-1}$ peak and the applied cooling rate could be detected. The post-DSC-10-10 cycle spectrum (lower cooling rate) displays in fact a more pronounced peak at 670 $cm^{-1}$ compared to the post-DSC-20-20 spectrum. Di Genova et al. (2018) associated this behaviour to a higher degree of nanolites crystallisation.

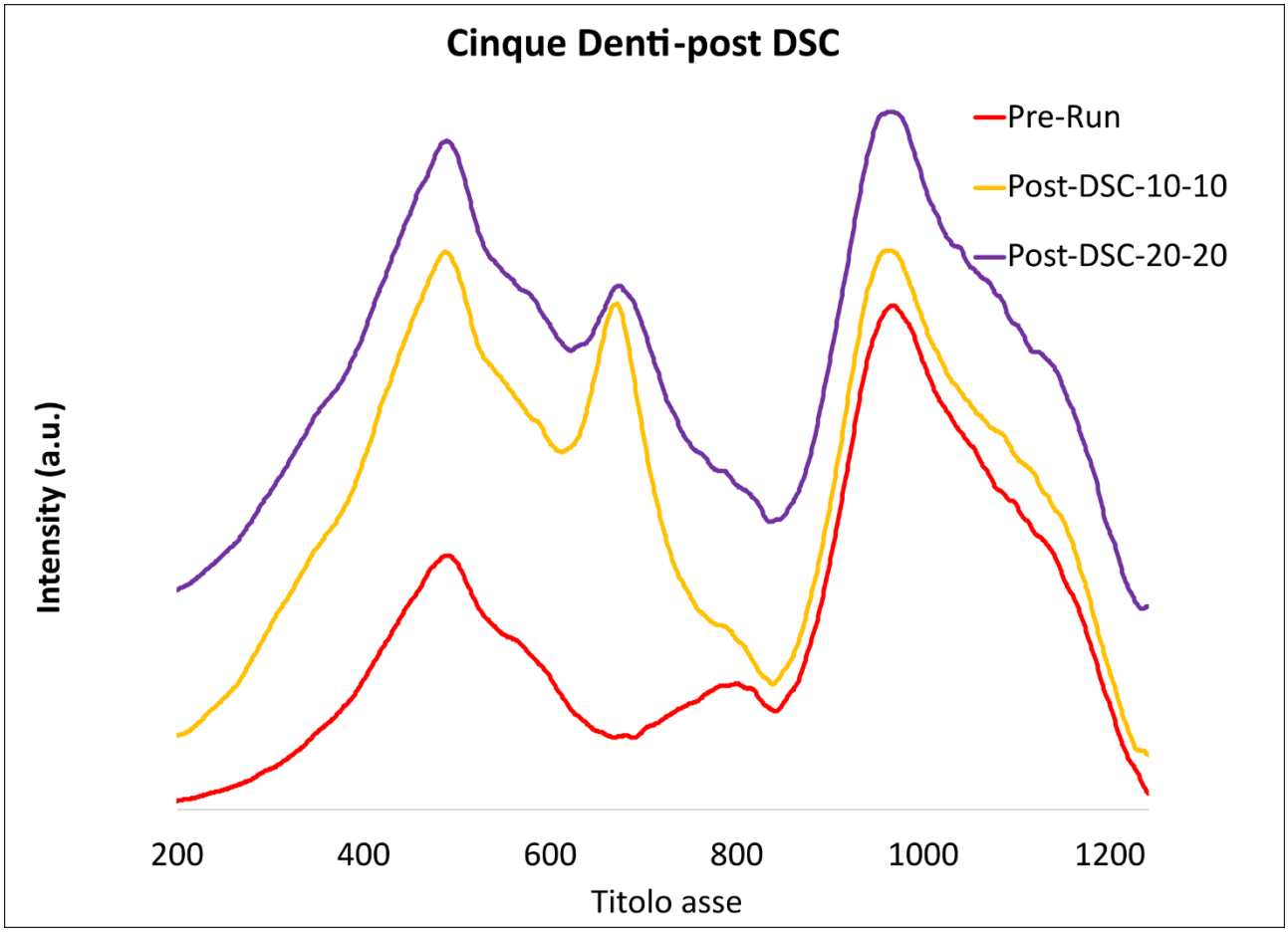


*Fig. 3.19 Baseline-corrected and normalized Raman spectra for pre-run and post-DSC measurements for Cinque Denti anhydrous melt. Peak at 670 $cm^{-1}$ is evident after DSC measurements.*

Fig. 3.20 shows Raman spectra for Cinque Denti eruption before (Pre-Run) and after MP (Post-MP-). As for the DSC measurements, post-MP Raman spectra also present a peak at 670 $cm^{-1}$, referred to nanolites formation (Di Genova et al., 2017; Bondar et al., 2025). Post-MP measurements Raman spectra show a direct relationship between 670 $cm^{-1}$ peak and temperature. It is evident as an increase in temperature results in an increase in 670 $cm^{-1}$ peak intensity. Moreover, the spectra appear to undergo more structural modifications compared to spectra from post DSC measurements. In particular, the low wavenumber region between 200 and 800 $cm^{-1}$ appear to strongly increase in intensity indicating different contributions to the internal structure. The increase in the intensity at ~485 $cm^{-1}$ in the LF region suggests the formation of oxygen atoms arranged in four-membered rings with breathing motion perpendicular to the Si-O-Si plane (Sharma et al., 1981; Galeener, 1982; Pasquarello and Car, 1998; Rahmani et al., 2003; Le Losq and Neuville, 2013). Thus, we infer that structural reorganization occurred during MP measurements, possibly resulting in the formation of new four-membered rings of tetrahedra.

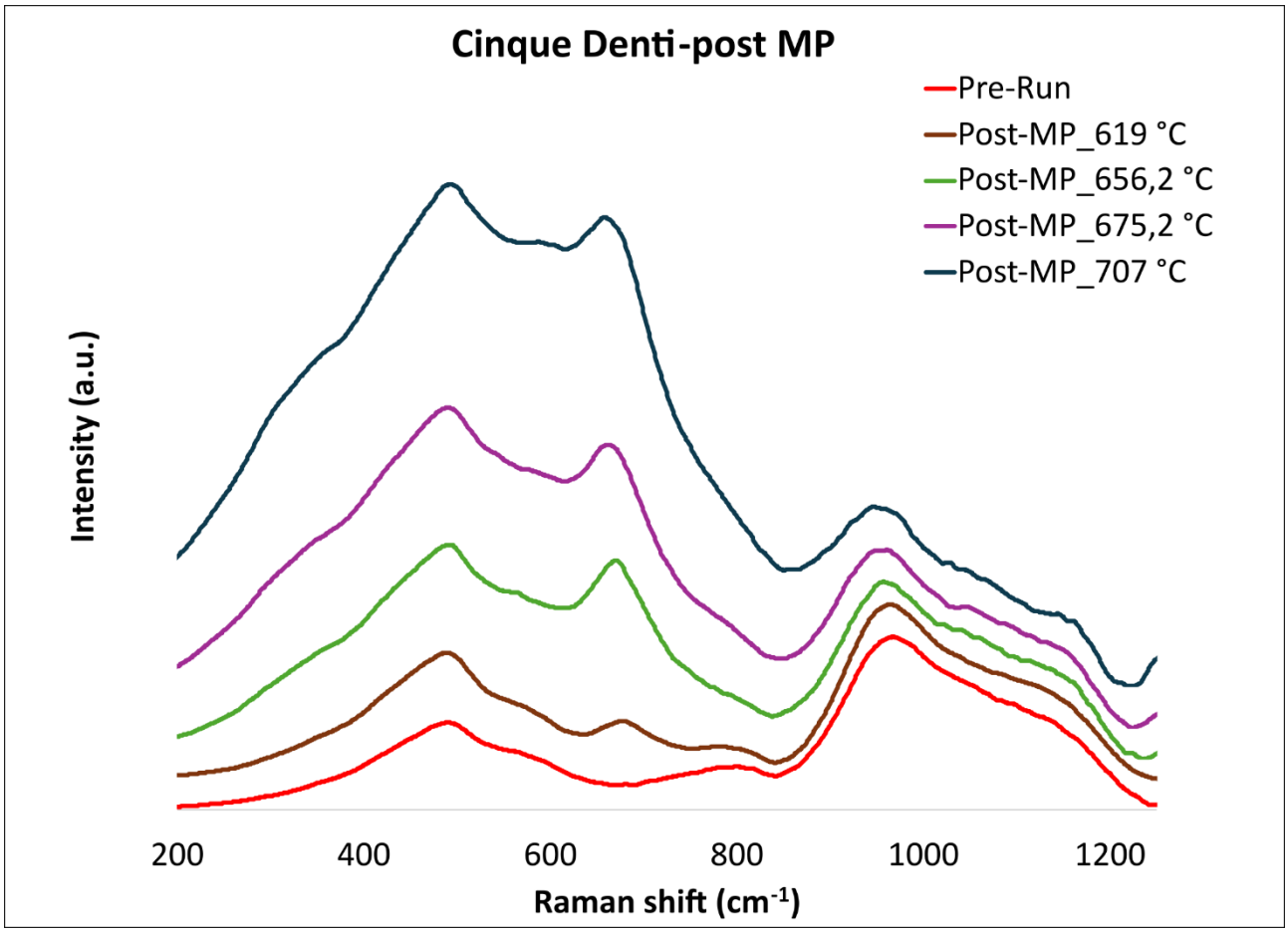


*Fig. 3.20 Baseline-corrected and normalized Raman spectra for pre-run and post-MP measurements for Cinque Denti anhydrous melt. Peak at 670 $cm^{-1}$ is evident after DSC measurements.*

Fig. 3.21 shows Raman spectra for Green Tuff eruption before (Pre-Run) and after CC (Post-CC). No variation in Raman spectra is detected.

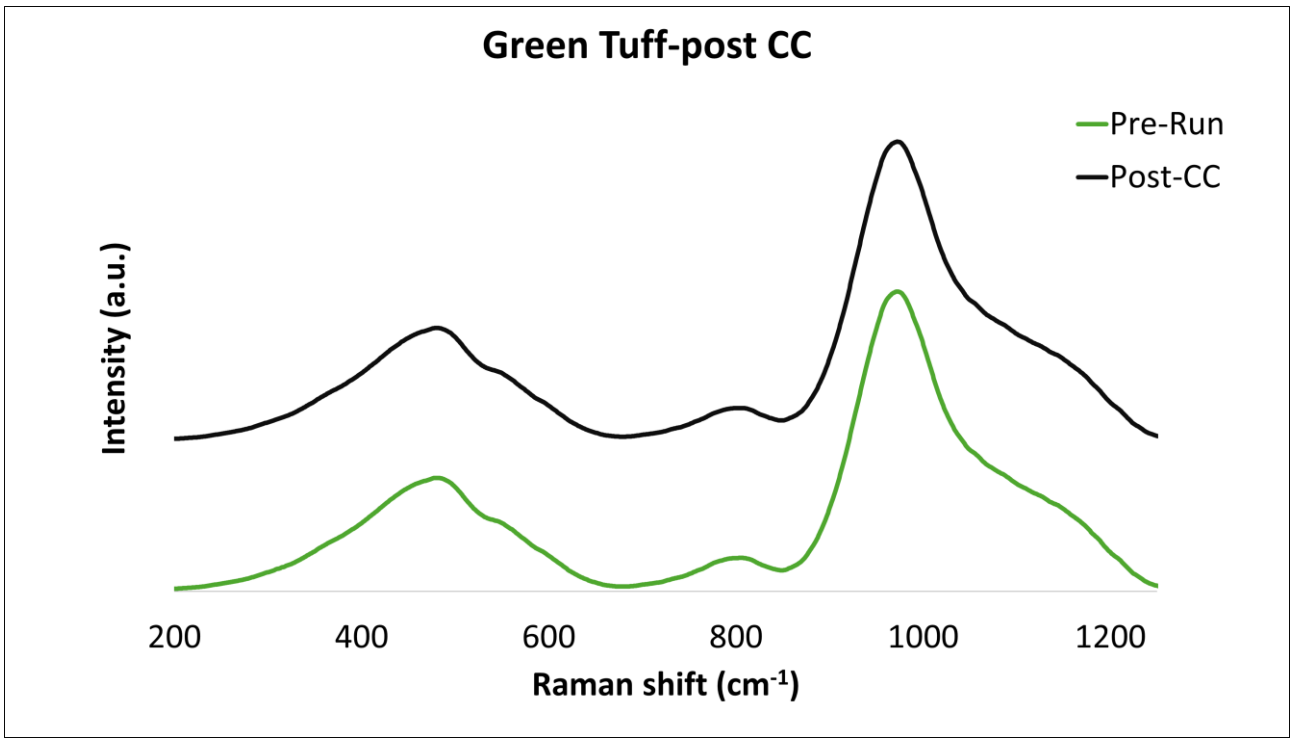


*Fig. 3.21 Baseline-corrected and normalized Raman spectra for pre-run and post-CC measurements for Green Tuff anhydrous melt. No variation in Raman spectra is detected.*

Fig. 3.22 shows Raman spectra for Green Tuff eruption before (Pre-Run) and after DSC (Post-DSC-) cycle 10-10 and cycle 20-20. No variation in Raman spectra is detected.

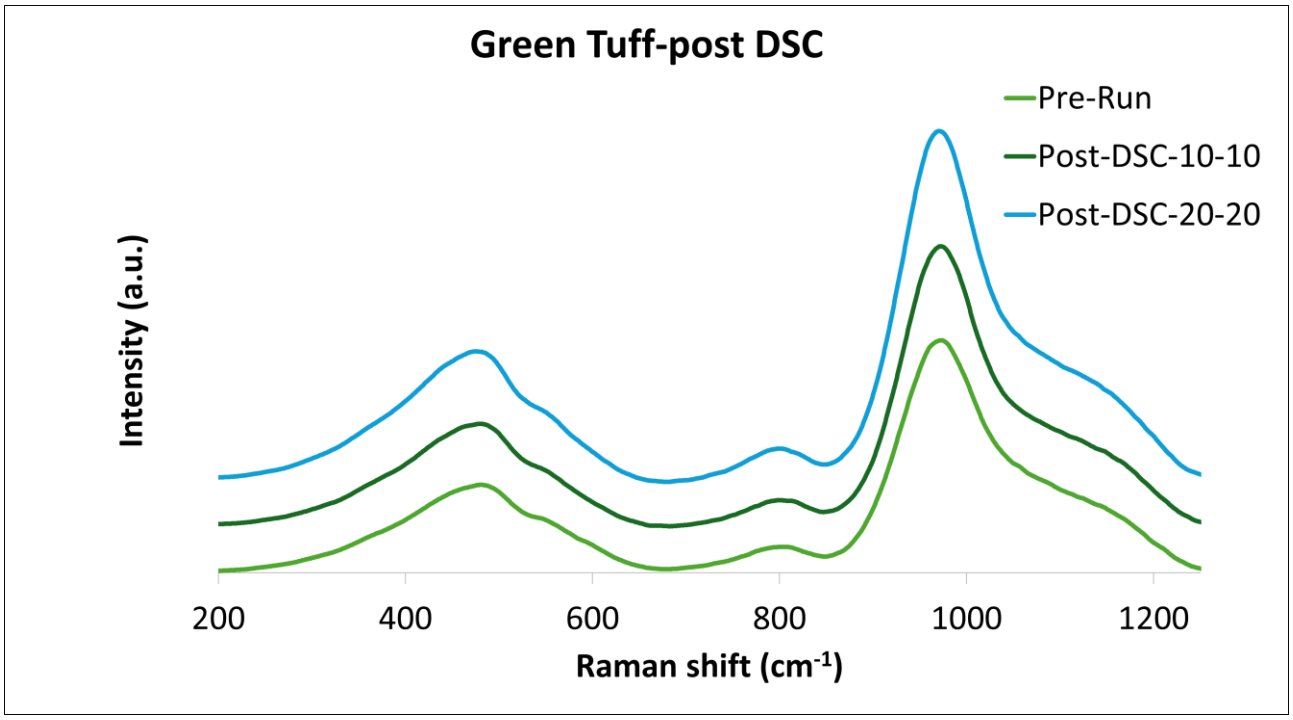


*Fig. 3.22 Baseline-corrected and normalized Raman spectra for pre-run and post-DSC measurements for Green Tuff anhydrous melt. No variation in Raman spectra is detected.*

Fig. 3.23 shows Raman spectra for Green Tuff eruption before (Pre-Run) and after MP (Post-MP-). No variation in Raman spectra is detected.

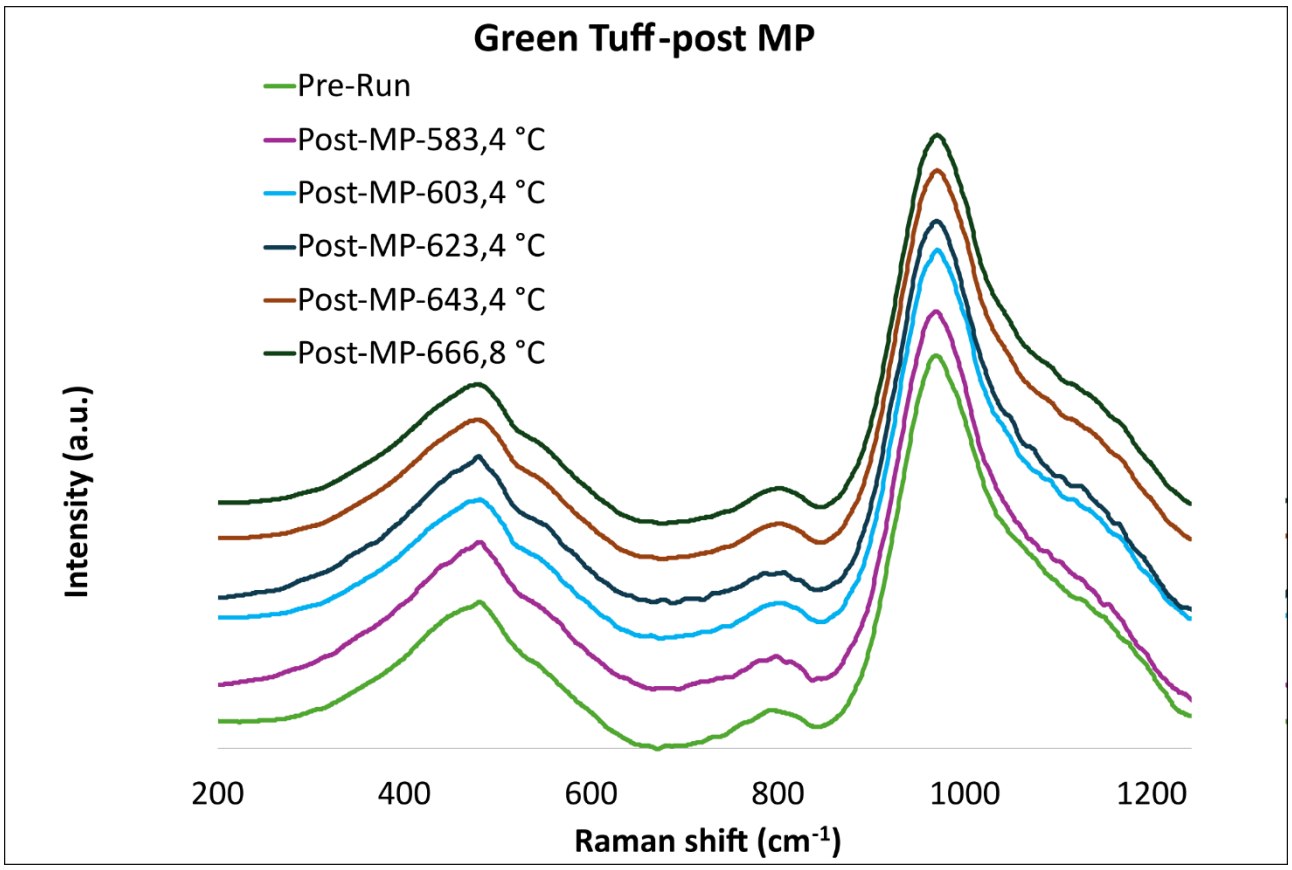


*Fig. 3.23 Baseline-corrected and normalized Raman spectra for pre-run and post-MP measurements for Green Tuff anhydrous melt. No variation in Raman spectra is detected.*

Fig. 3.24 shows Raman spectra for Zinedi eruption before (Pre-Run) and after CC (Post-CC). No variation in Raman spectra is detected.

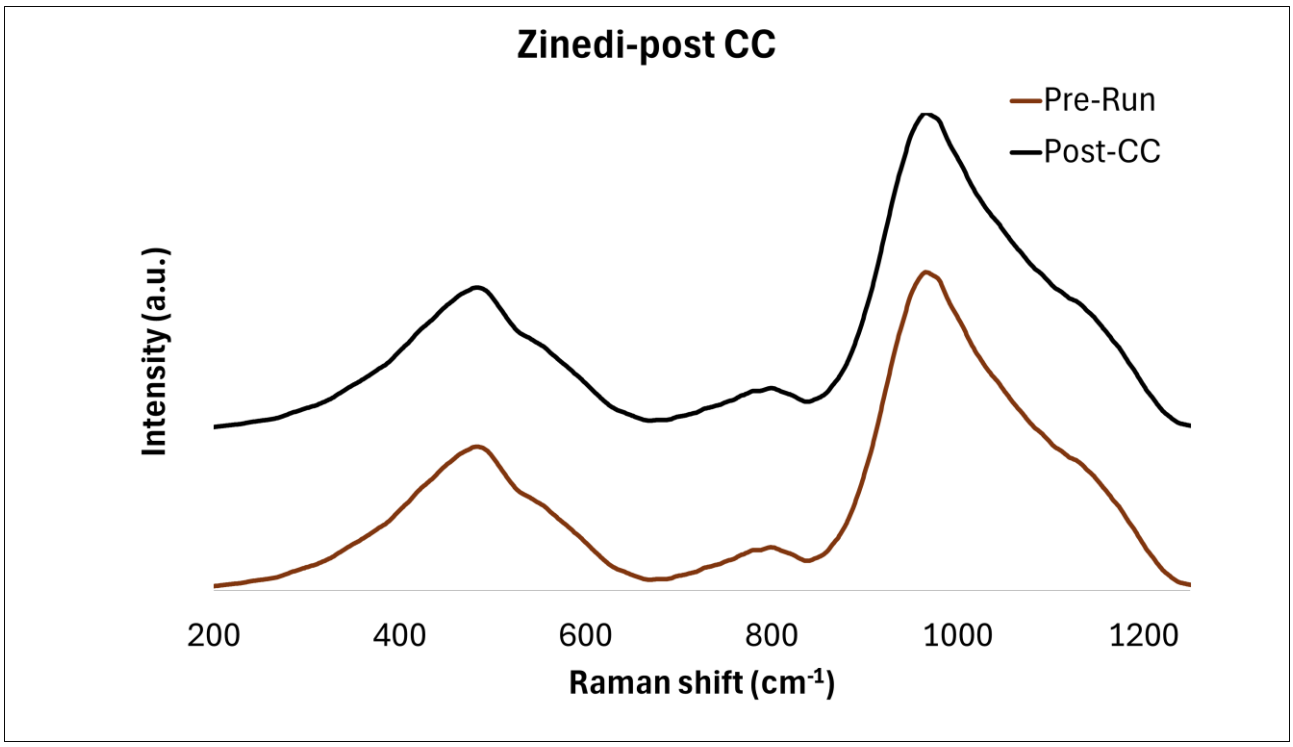


*Fig. 3.24 Baseline-corrected and normalized Raman spectra for pre-run and post-CC measurements for Zinedi anhydrous melt. No variation in Raman spectra is detected.*

Fig. 3.25 shows Raman spectra for Zinedi samples before (Pre-Run) and after DSC (Post-DSC-) cycle 10-10 and cycle 20-20. Post-DSC Raman spectra show a peak at 670 $cm^{-1}$, attributed to nanolites formation (Di Genova et al., 2017; Bondar et al., 2025). As for Cinque Denti eruption, a direct relationship between the intensity of the 670 $cm^{-1}$ peak and the applied cooling rate could be detected. The post-DSC-20-20 cycle spectrum (lower cooling rate) displays in fact a more pronounced peak at 670 $cm^{-1}$ compared to the post-DSC-10-10 spectrum. Di Genova et al. (2018) associated this behaviour to a higher degree of nanolites crystallisation.

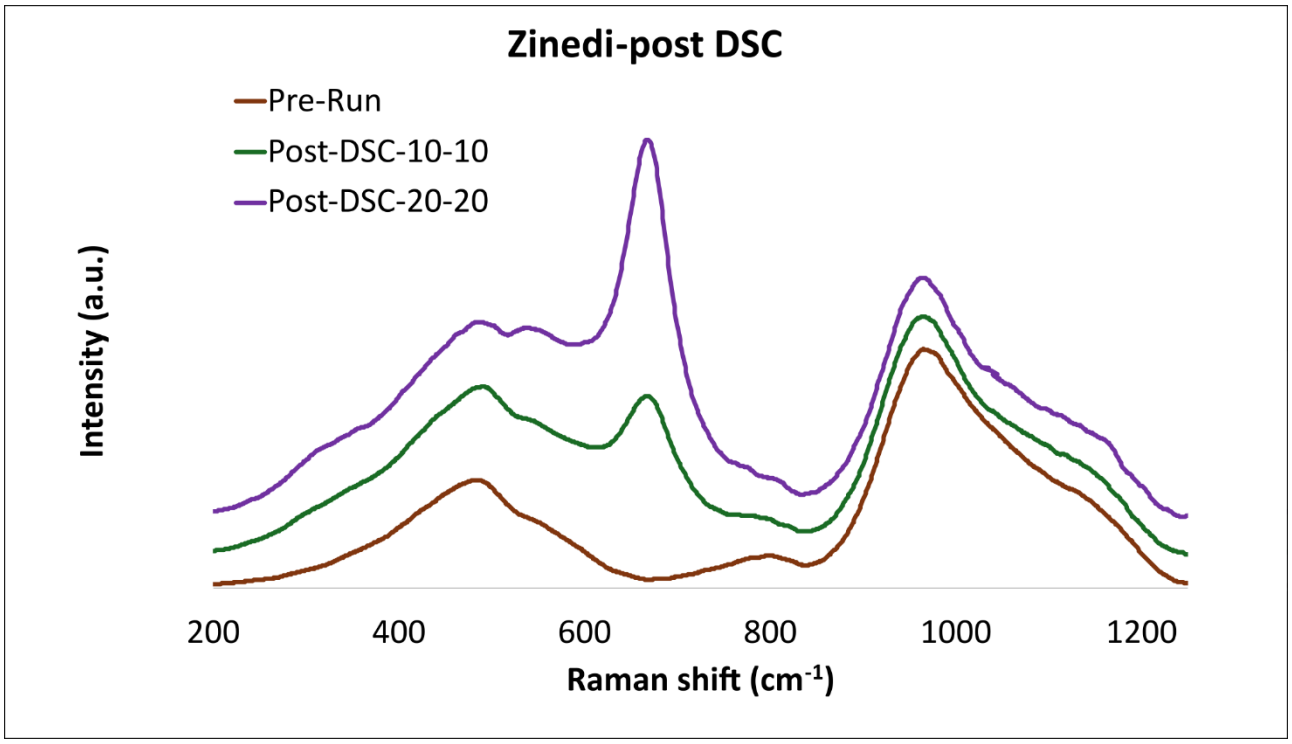


*Fig. 3.25 Baseline-corrected and normalized Raman spectra for pre-run and post-DSC measurements for Zinedi anhydrous melt. No variation in Raman spectra is detected. Peak at 670 $cm^{-1}$ is evident after DSC measurements.*

Fig. 3.26 shows Raman spectra for Zinedi eruption before (Pre-Run) and after MP (Post-MP-). As for the DSC measurements, post-MP Raman spectra also present a peak at 670 $cm^{-1}$, referred to nanolites formation (Di Genova et al., 2017; Bondar et al., 2025). Post-MP measurements Raman spectra show a direct relationship between 670 $cm^{-1}$ peak and the measurement temperature. It is evident as an increase in temperature results in an increase in 670 $cm^{-1}$ peak intensity. Moreover, the spectra appear to undergo more structural modifications compared to spectra from post DSC measurements. In particular, the low wavenumber region between 200 and 800 $cm^{-1}$ appear to strongly increase in intensity indicating different contributions to the internal structure. The increase in the intensity at ~485 $cm^{-1}$ in the LF region suggests the formation of oxygen atoms arranged in four-membered rings with breathing motion perpendicular to the Si-O-Si plane (Sharma et al., 1981; Galeener, 1982; Pasquarello and Car, 1998; Rahmani et al., 2003; Le Losq and Neuville, 2013). Thus, we infer that structural reorganization occurred during MP measurements, possibly resulting in the formation of new four-membered rings of tetrahedra.

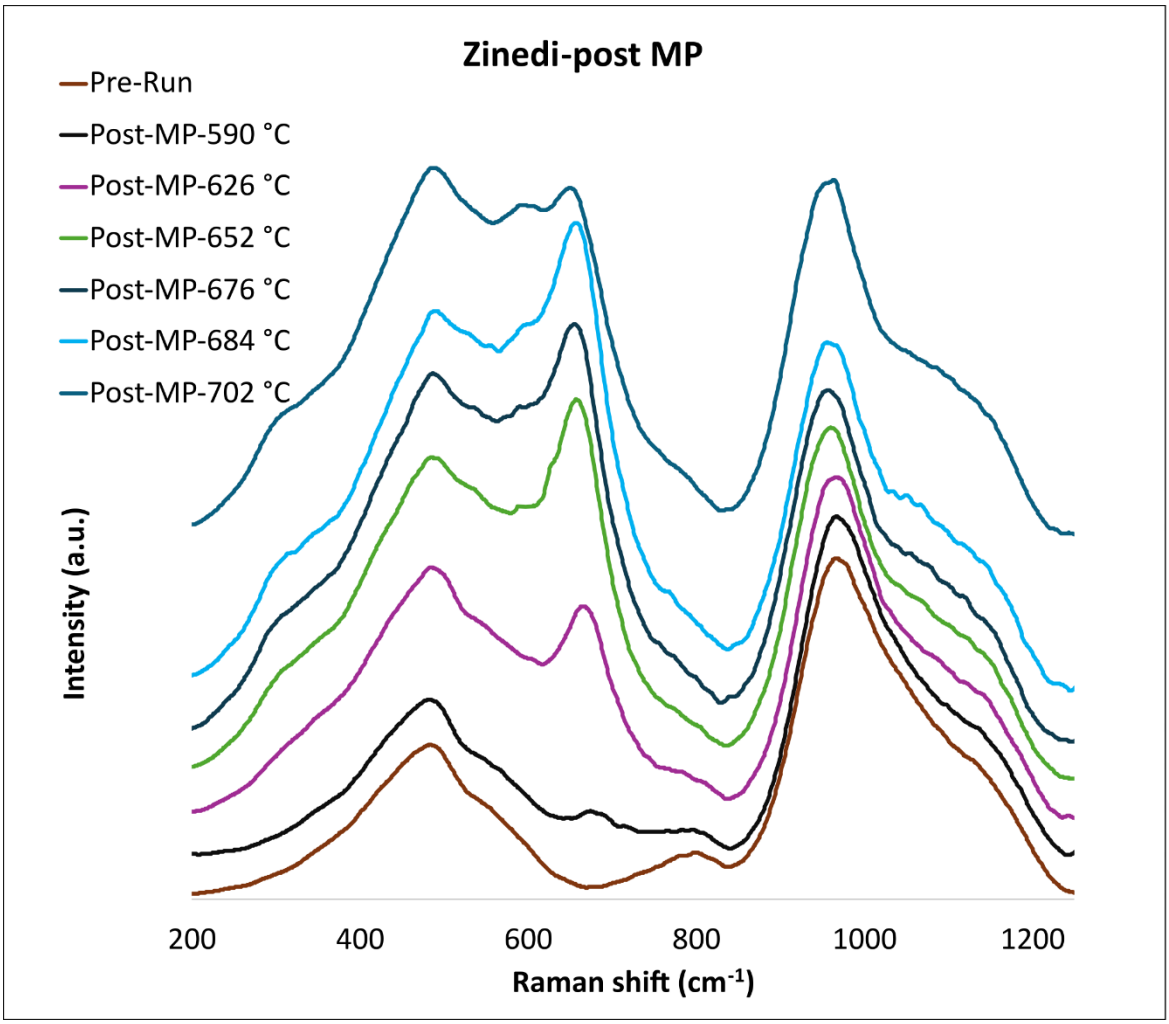


*Fig. 3.26 Baseline-corrected and normalized Raman spectra for pre-run and post-MP measurements for Zinedi anhydrous melt. Peak at 670 $cm^{-1}$ is evident after MP measurements as presence of nanolites.*

Fig. 3.27 shows Raman spectra for Cuddia Mida eruption before (Pre-Run) and after CC (Post-CC). No variation in Raman spectra is detected.

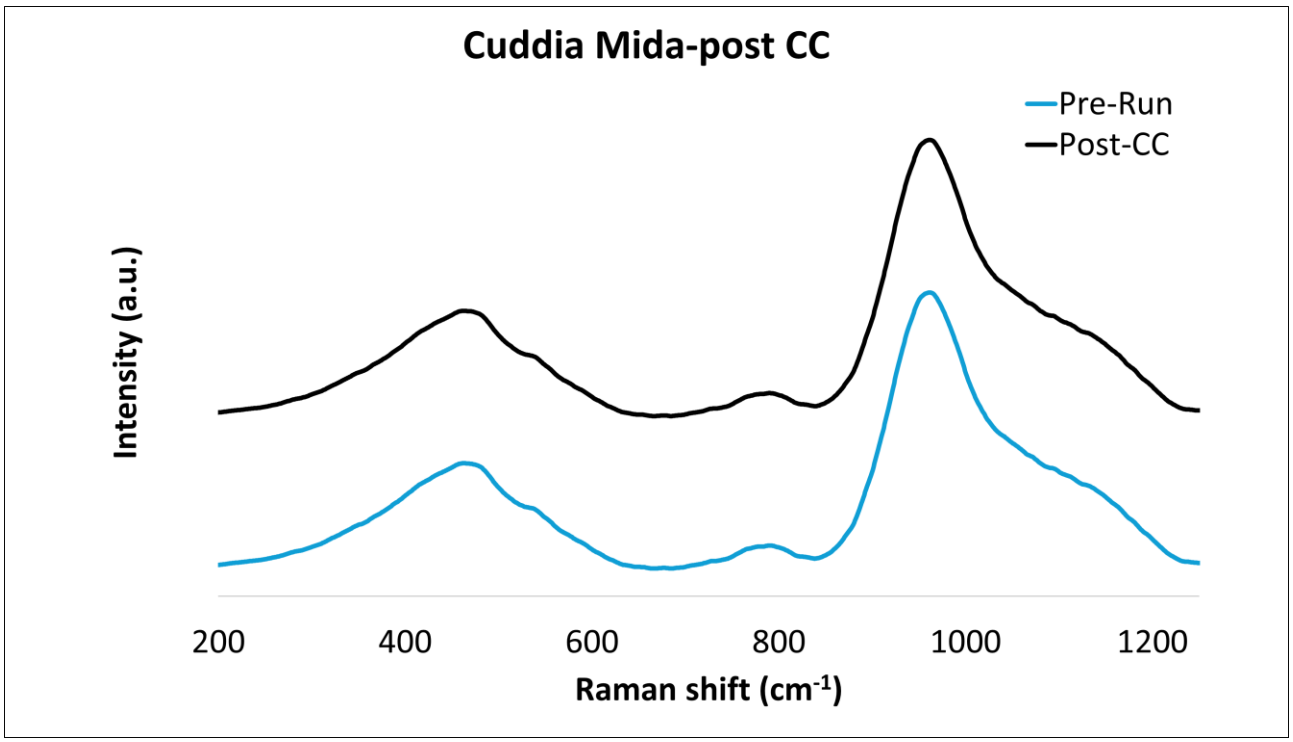


*Fig. 3.27 Baseline-corrected and normalized Raman spectra for pre-run and post-CC measurements for Cuddia Mida anhydrous melt. No variation in Raman spectra is detected.*

Fig. 3.28 shows Raman spectra for Cuddia Mida eruption before (Pre-Run) and after DSC (Post-DSC-). No variation in Raman spectra is detected.

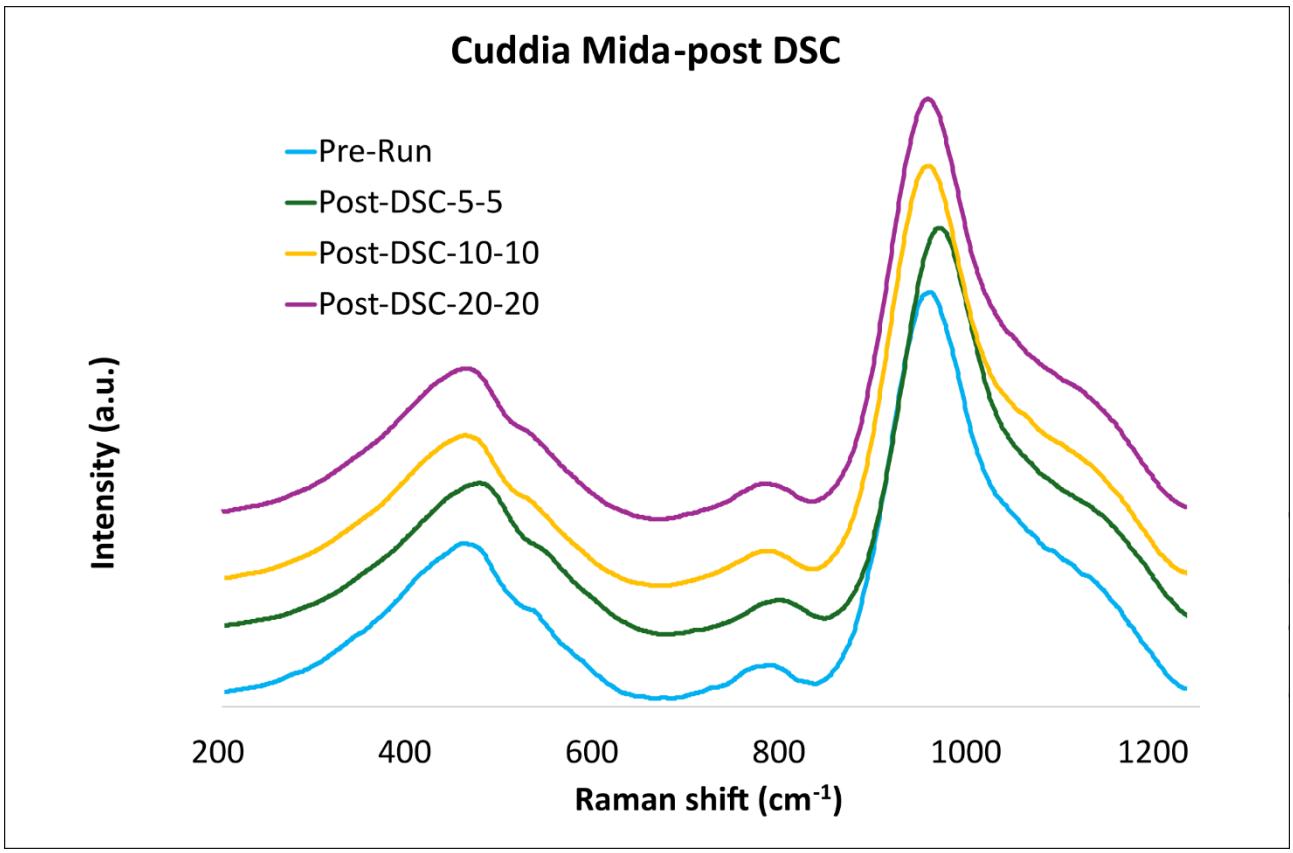


*Fig. 3.28 Baseline-corrected and normalized Raman spectra for pre-run and post-DSC measurements for Cuddia Mida anhydrous melt. No variation in Raman spectra is detected.*

Fig. 3.29 shows Raman spectra for Cuddia Mida eruption before (Pre-Run) and after MP (Post-MP-). No variation in Raman spectra is detected.

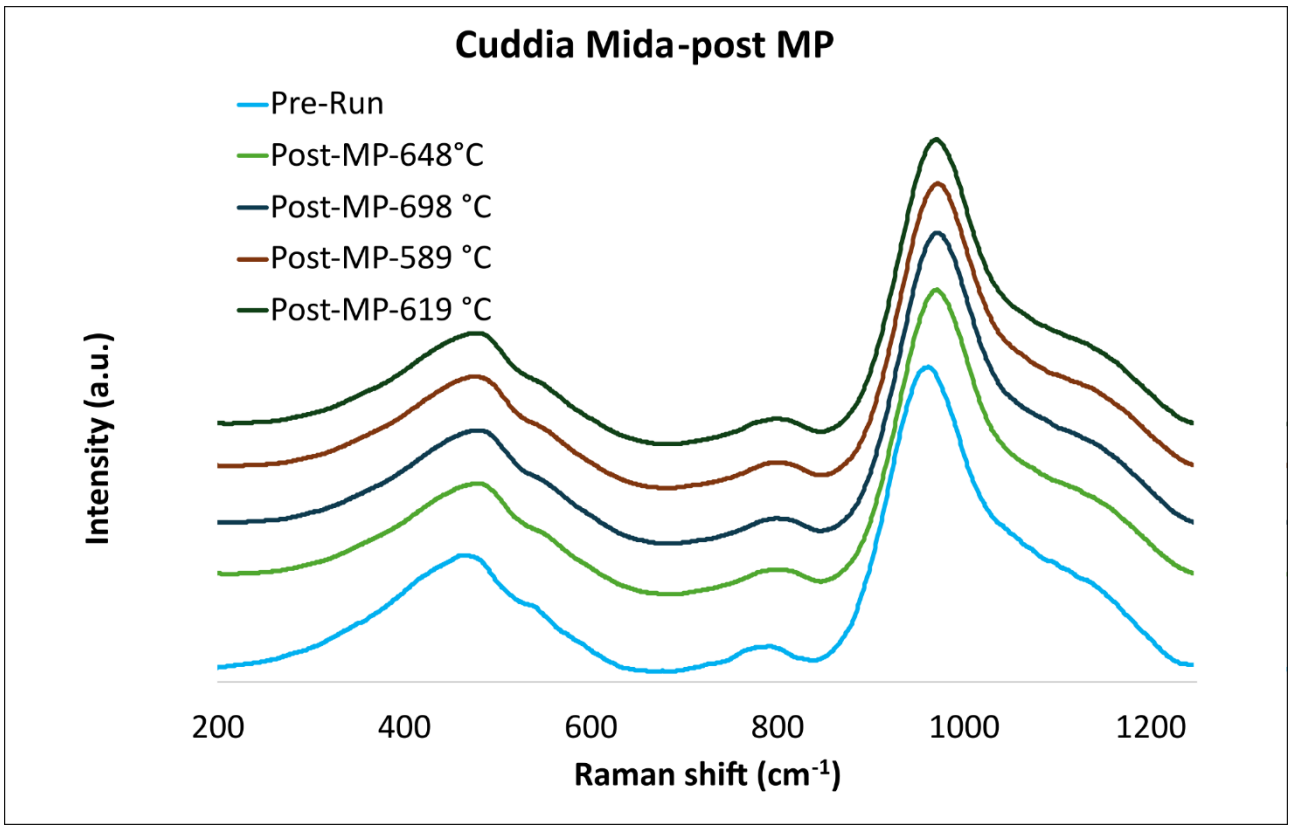


*Fig. 3.29 Baseline-corrected and normalized Raman spectra for pre-run and post-MP measurements for Cuddia Mida anhydrous melt. No variation in Raman spectra is detected.*

Generally, samples show no structural changes after high temperature viscosity measurements. The presence of nanolites has been detected for Cinque Denti and Zinedi after DSC measurements for $q_{c,h}$ 10 °C $min^{-1}$ and $q_{c,h}$ 20 °C $min^{-1}$ and after MP measurements. No nanolites contribution has been detected for Green Tuff and Cuddia Mida after low temperature measurements. The nanolite presence and the structural modifications of our samples is certainly related to the different chemistry of the magmas although a simple correlation is difficult to define. Cinque Denti and Zinedi nanolite-bearing samples have both lower silica content (Cinque Denti: 66.25 wt% $SiO_2$; Zinedi: 66.90 wt% $SiO_2$) and lower peralkaline index (Cinque Denti P.I. = 0.92; Zinedi = 1.24)compared to nanolite-free Green Tuff ($SiO_2$ = 70.16; P.I.= 1.74) and Cuddia Mida ($SiO_2$ = 70.67 wt%; P.I. = 1.74) samples, which pairs with their higher viscosities, both at low and at high temperatures. Higher viscosities should delay or prevent nanolite formation, unlike what observed. Possible correlations may be found between the overall silica and alumina content of the four magmas, where the nanolite bearing

samples have lower silica and higher alumina content (Cinque Denti $SiO_2$ = 66.25 wt%; $Al_2O_3$ = 14.80 wt%; Zinedi $SiO_2$ = 67.22 wt%; $Al_2O_3$ = 11.85 wt%) compared to the nanolite-free samples (Green Tuff $SiO_2$ = 70.16 wt%; $Al_2O_3$ = 8.64 wt%; Cuddia Mida: $SiO_2$ = 70.67 wt% ; $Al_2O_3$ = 8.50 wt%).

## 3.6 Melt inclusions analysis

In this study we have analyzed melt inclusions (MI) from Cinque Denti, Zinedi and Cuddia Mida in order to derive water content prior the eruption and to define the depth of the magmatic chamber. For this purpose, we selected only melt inclusions free of post-entrapment modifications such as fractures and channels. Green Tuff melt inclusions data have been taken from literature (Lanzo et al., 2013). In our study, we measured water from melt inclusions by Raman spectroscopy (see Method Chapter 2). Subsequently, water content values have been converted in depth by using Liu et al. (2005) model for Cinque Denti and Allabar et al. (2022) model for Green Tuff, Zinedi and Cuddia Mida. Cinque Denti melt is metaluminous, so Allabar et al. (2022) model could not be applied in our case. Therefore, we used the Liu et al. (2005) model, which is suitable for metaluminous rhyolitic melts. In this section, only selected images of MI and Raman spectra acquisition spots are presented. The entire MI dataset can be found in Supplementary-Material. Water contents retrieved by Raman measurements are presented in Tab. 3.7. For each melt inclusions, an average of X-Y measurements have been taken. In Tab 3.7 only average values are reported. The entire sets of measurements can be found in the Supplementary material.

Cinque Denti water content has been measured in 13 MI hosted in 4 alkali-feldspar crystals. MI show variable sizes, on their major axes, from 540 µm to 1400 µm. The selected MI are entirely glassy. They are both spherical and elongated. The dissolved $H_2O$ content in MI ranges from 0.62 wt% to 4.96 wt% (mean=2.60 wt%; mode=3.5 wt%). A total of 63 measurements have been performed (Supplementary Material). In Tab. 3.7, only average values are reported.

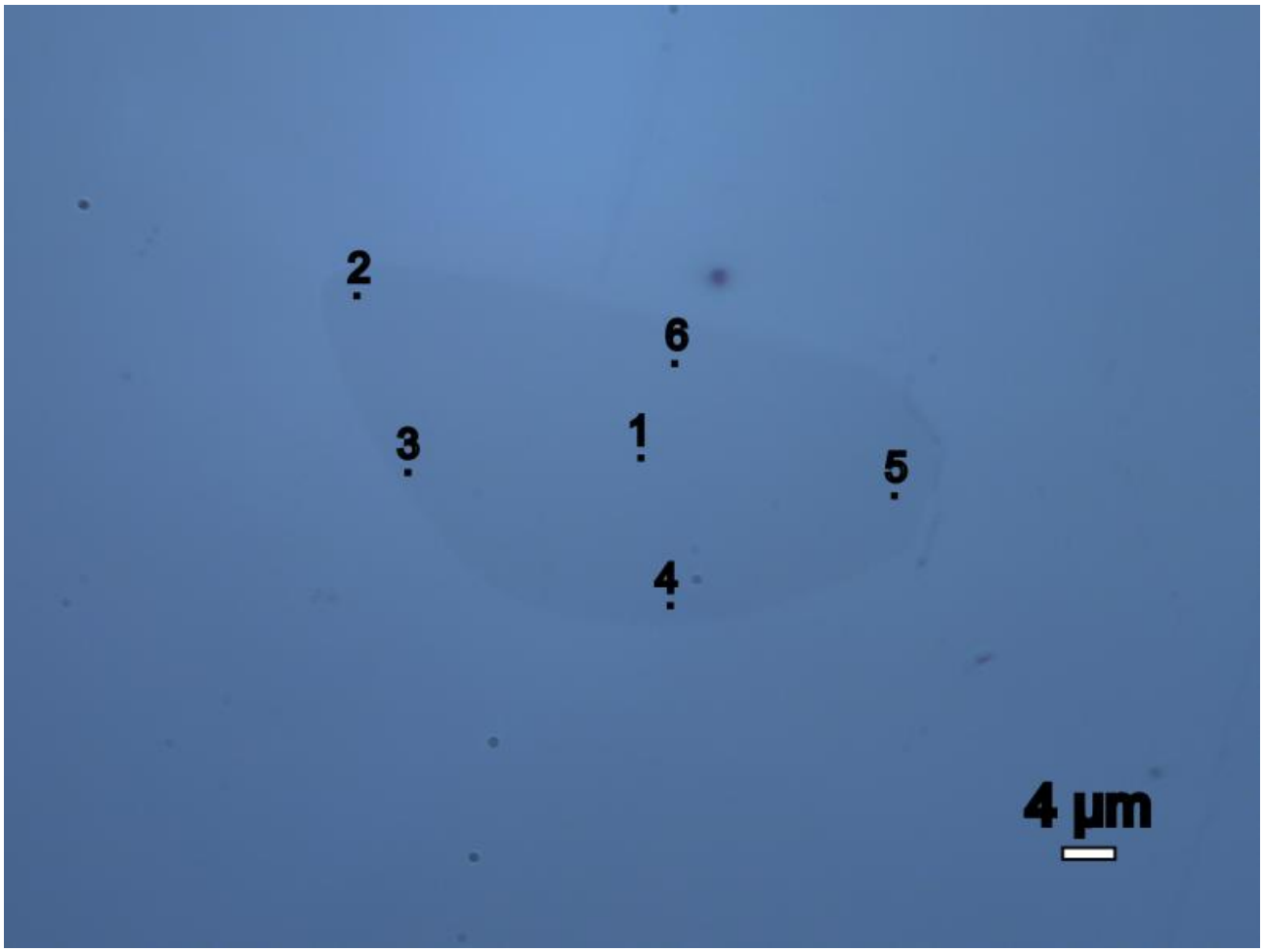


*Fig. 3.30 Example of elongated melt inclusion from Cinque Denti eruption at 50x of magnification (scale is reported). Spots for Raman spectra acquisition are indicated. Spots are chosen in order to cover all MI area.*

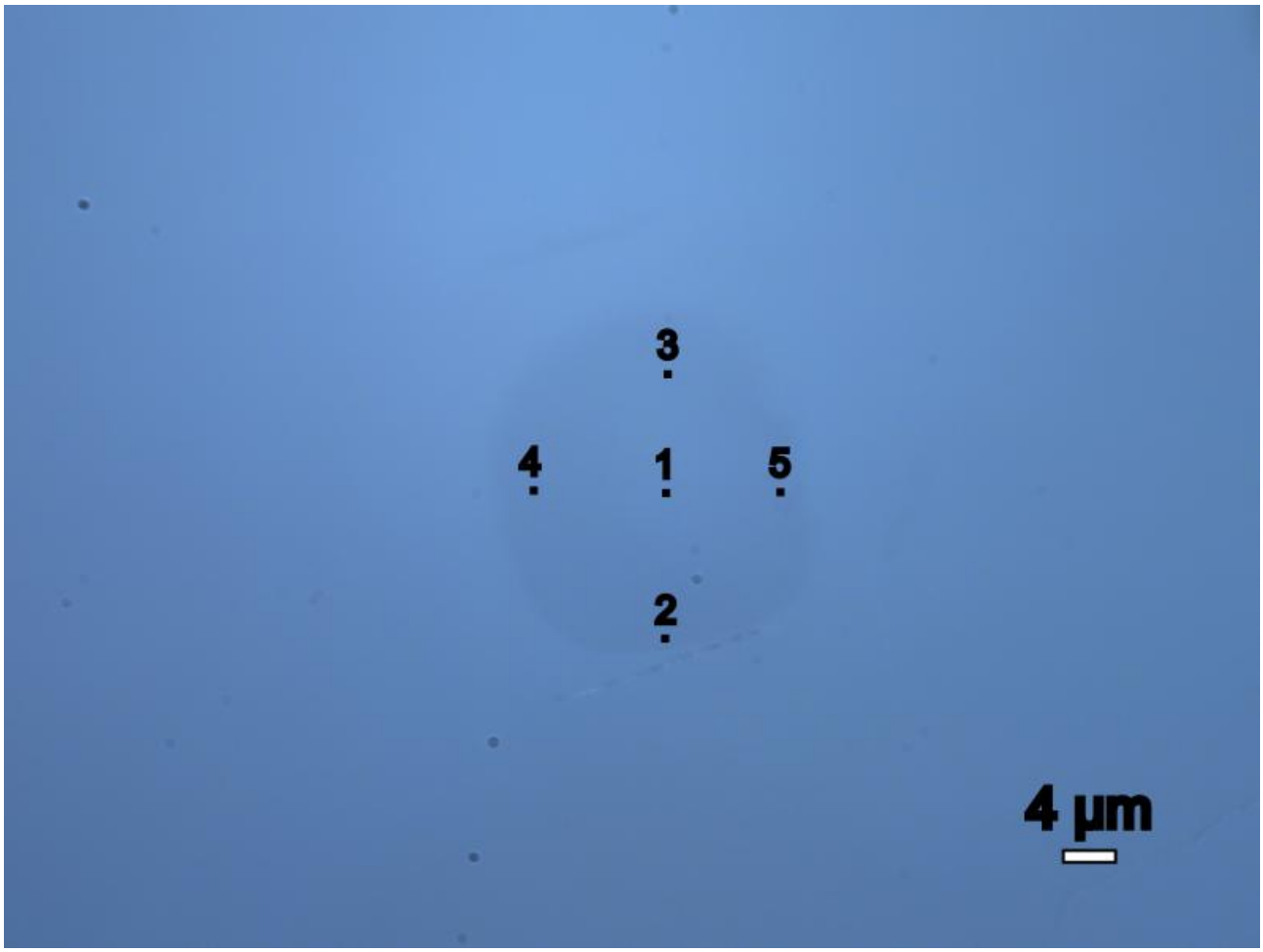


*Fig. 3.31 Example of circular melt inclusion from Cinque Denti eruption at 50x of magnification (scale is reported). Spots for Raman spectra acquisition are indicated. Spots are chosen in order to cover all MI area.*

| ID | $H_2O$ content (wt%) | Position in crystal | Dimension (μm) (major axis) | Shape |
|---|---|---|---|---|
| Crystal_1_MI1 | 0.75 | Rim | 1440 | Circular |
| Crystal_1_MI2 | 2.94 | Rim | 547 | Elongated |
| Crystal_1_MI3 | 2.54 | Rim | 543 | Elongated |
| Crystal_2_MI1 | 3.45 | Rim | 450 | Circular |
| Crystal_2_MI2 | 3.75 | Rim | 1404 | Circular |
| Crystal_2_MI3 | 4.34 | Rim | 795 | Elongated |
| Crystal_2_MI4 | 1.20 | Rim | 1026 | Elongated |
| Crystal_2_MI6 | 4.75 | Rim | 1400 | Elongated |
| Crystal_3_MI1 | 3.1 | Rim | 700 | Circular |
| Crystal_3_MI2 | 1.04 | Rim | 557 | Circular |
| Crystal_3_MI3 | 1.00 | Rim | 812 | Circular |
| Crystal_3_MI4 | 2.83 | Rim | 1480 | Circular |
| Crystal_5_MI2 | 3.71 | Rim | 557 | Elongated |

*Tab. 3.7 Melt inclusion dataset for Cinque Denti eruption. Only average values for each melt inclusions are reported.*

As shown in Fig. 3.32, Cinque Denti $H_2O$ content frequence has a bimodal distribution. The lower mode could be interpreted as due to water loss over time and for this reason we only consider the higher mode. No data about Cinque Denti $H_2O$ content from MI are available in literature and for this reason no comparison with previous data is possible.

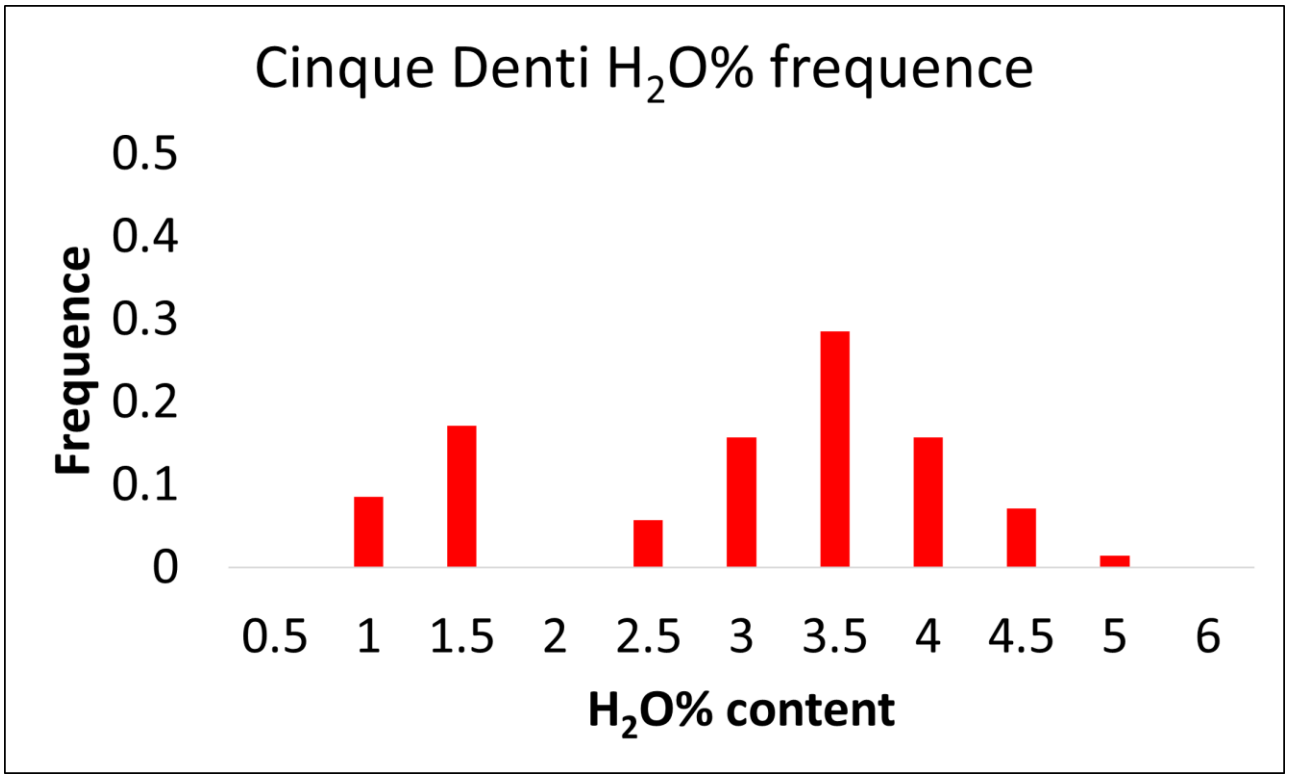


*Fig. 3.32 Water content distribution for Cinque Denti eruption.*

By converting water content mode, 3.5 wt%, in depth, by using solubility model from Liu et al. (2005), we obtain a value of 58 MPa or 1566 m.

Green Tuff water content is from Lanzo et al. (2013). In this study, authors analyzed 59 anorthoclase-hosted melt inclusions from the two basal pumice members of Green Tuff eruption using FT-IR spectroscopy. The authors estimated water content values for Green Tuff between 2.5-4 $H_2O$ wt%. These values constrained the magmatic chamber at a minimum depth of 2500 m (Lanzo et al., 2013). Depth results from Lanzo et al. (2013) can be re-calculated by using Allabar et al. (2022) model in order to obtain updated data. New results suggests that magmatic chamber for Green Tuff can be located between 850 and 2000 m of depth.

Zinedi water content has been measured in 2 MI hosted in 1 olivine crystal. MI display variable sizes, on their major axes, ranging from 417 μm to 1837 μm. The selected MI are entirely glassy and they are both elongated in shape. The dissolved $H_2O$ content in MI ranges from 2.5 wt% to 5.5 wt% (mean=3.88 wt%). A total of 20 measurements have been performed (Supplementary Material). In Tab. 3.8, only average values are reported.

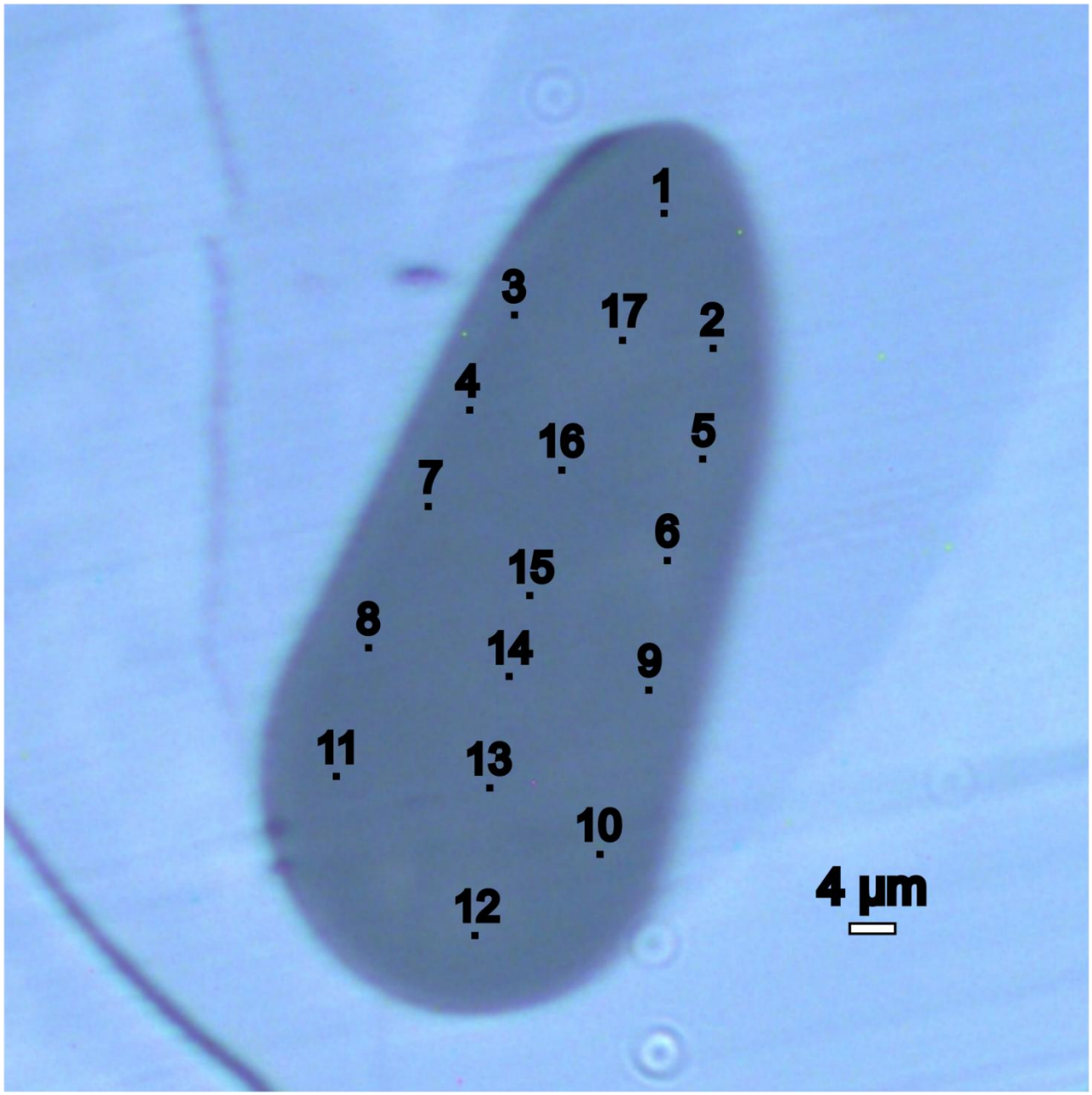


*Fig. 3.33 Melt inclusion from Zinedi eruption at 50x of magnification (scale is reported). Spots for Raman spectra acquisition are indicated. Spots are chosen in order to cover all MI area.*

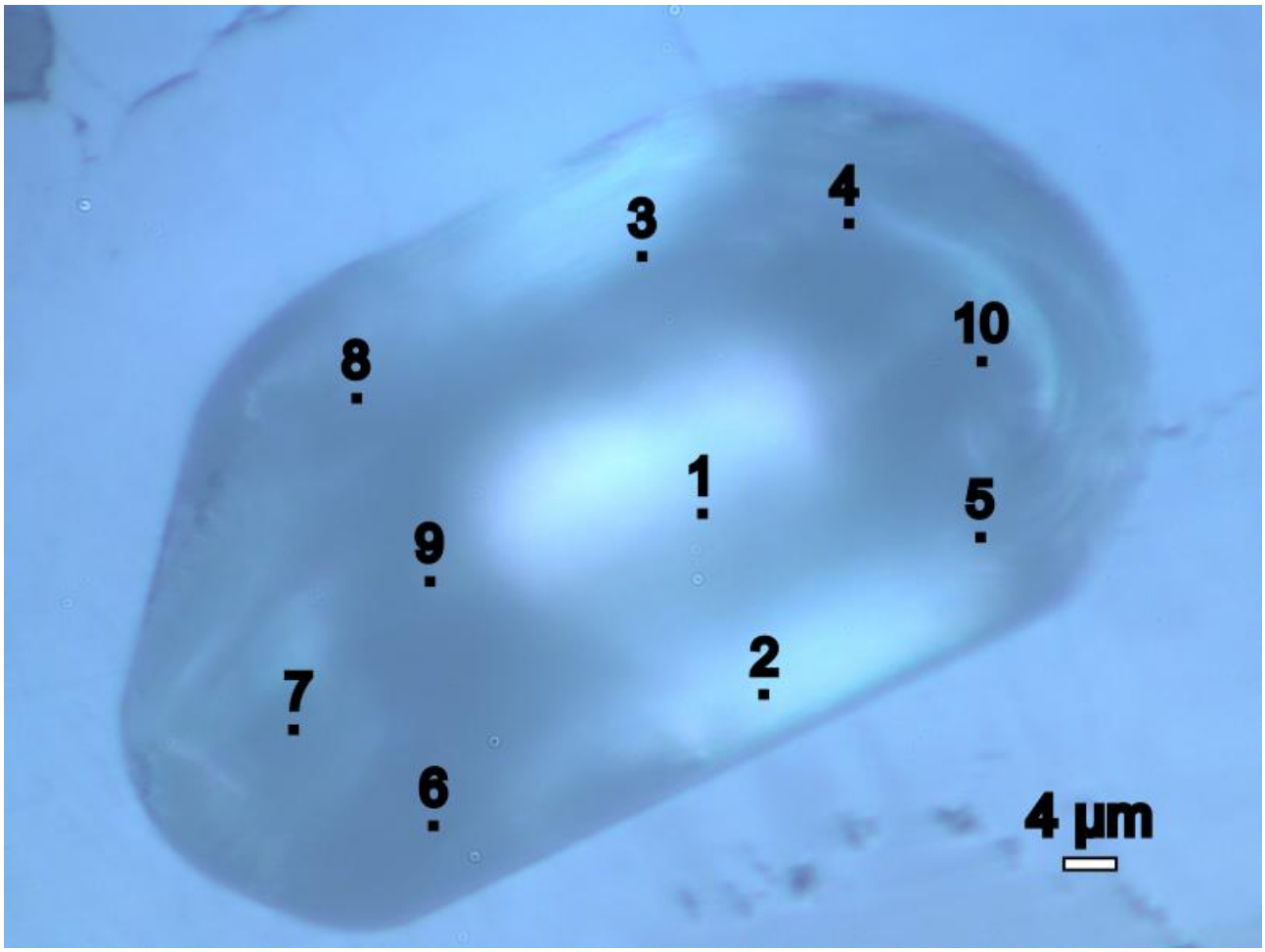


*Fig. 3.34 Melt inclusion from Zinedi eruption at 50x of magnification (scale is reported). Spots for Raman spectra acquisition are indicated. Spots are chosen in order to cover all MI area.*

| ID | $H_2O$ content (wt%) | Position in crystal | Dimension (µm) (major axis) | Shape |
|---|---|---|---|---|
| Crystal_1_MI1 | 2.4 | Rim | 517 | Elongated |
| Crystal_1_MI2 | 5.5 | Rim | 1837 | Elongated |

*Tab. 3.8 Melt inclusion dataset for Zinedi eruption. Only average values for each melt inclusions are reported.*

As shown in Fig. 3.35, Zinedi $H_2O$ content frequence has a bimodal distribution even within the same crystal. Different modes in the same crystal could be explained with a magma convection in magma chamber. No data about Zinedi $H_2O$ content from MI are available in literature and for this reason no comparison with previous data is possible.

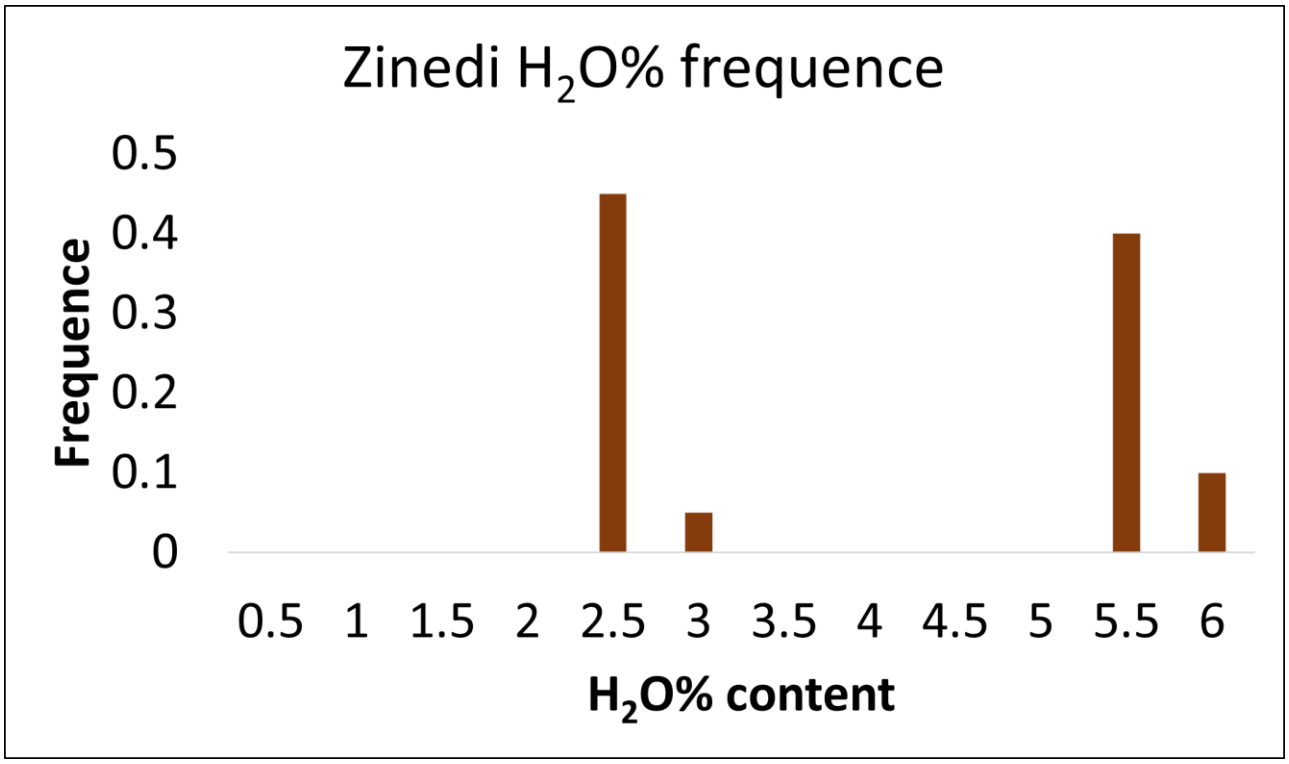


*Fig. 3.35 Water content distribution for Zinedi.*

By converting the two modes, 2.5 wt% and 5.5wt%, in depth, by using solubility model from Allabar al. (2022) we obtain respectively 31 MPa or 837 m and 150 MPa or 4050 m.

Cuddia Mida water content has been measured in 11 MI hosted in 5 pyroxene crystal. MI have variable sizes, on their major axes, ranging from 500 µm to 1837 µm. The selected MI are entirely glassy. They are mainly elongated and with irregular form. The dissolved $H_2O$ content in MI ranges from 1.16 wt% to 2.86 wt% (mean=2.13 wt%; mode=2.5 wt%). A total of 44 measurements have been performed (Supplementary Material). In Tab. 3.9, only average values are reported.

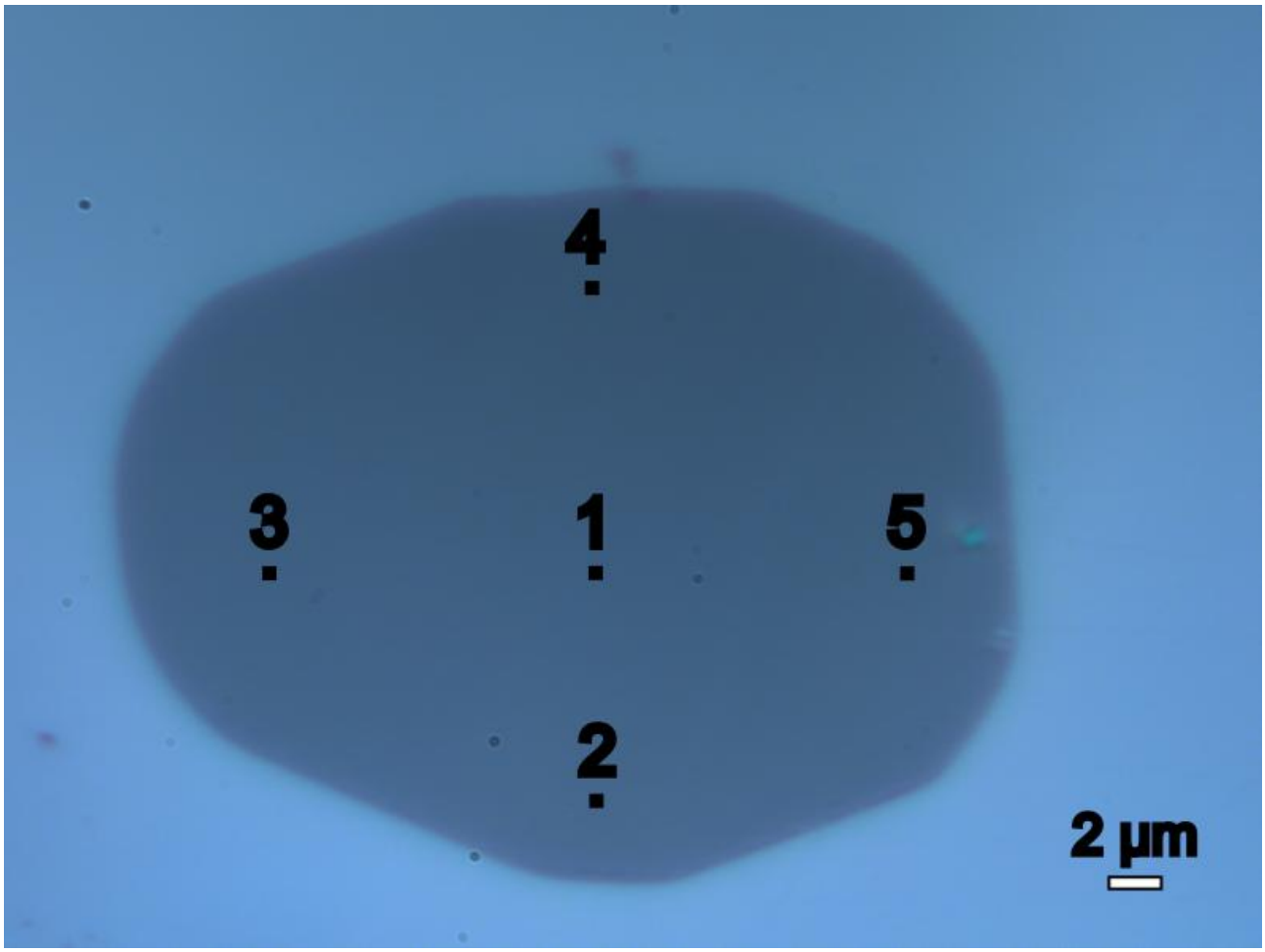


*Fig. 3.36 Melt inclusion from Cuddia Mida eruption at 100x of magnification (scale is reported). Spots for Raman spectra acquisition are indicated. Spots are chosen in order to cover all MI area.*


*Fig. 3.37 Melt inclusion from Cuddia Mida eruption at 50x of magnification (scale is reported). Spots for Raman spectra acquisition are indicated. Spots are chosen in order to cover all MI area.*

| ID | $H_2O$ content (wt%) | Position in crystal | Dimension (µm) (major axis) | Shape |
|---|---|---|---|---|
| 5_Crystal_1_MI1 | 2.29 | Rim | 500 | Elongated |
| 5_Crystal_1_MI2 | 1.27 | Central | 1837 | Elongated |
| 5_Crystal_1_MI5 | 2.48 | Rim | 1445 | Elongated |
| 5_Crystal_2_MI1 | 1.76 | Rim | 1077 | Elongated |
| 32_Crystal_1_MI1 | 2.63 | Rim | 1480 | Circular |
| 32_Crystal_1_MI2 | 2.51 | Center | 1519 | Elongated |
| 34_Crystal_1_MI1 | 2.16 | Rim | 510 | Circular |
| 34_Crystal_1_MI2 | 2.16 | Center | 803 | Circular |
| 34_Crystal_1_MI3 | 2.06 | Center | 1424 | Elongated |
| 34_Crystal_1_MI4 | 2.05 | Center | 933 | Elongated |
| 79_Crystal_1_MI1 | 2.53 | Center | 1134 | Elongated |

*Tab. 3.9 Melt inclusion dataset for Cuddia Mida eruption. Only average values for each melt inclusions are reported.*

As shown in Fig. 3.38, Cuddia Mida $H_2O$ content frequence presents a good gaussian distribution. No data about Cuddia Mida $H_2O$ content from MI are available in literature and for this reason no comparison with previous data is possible.

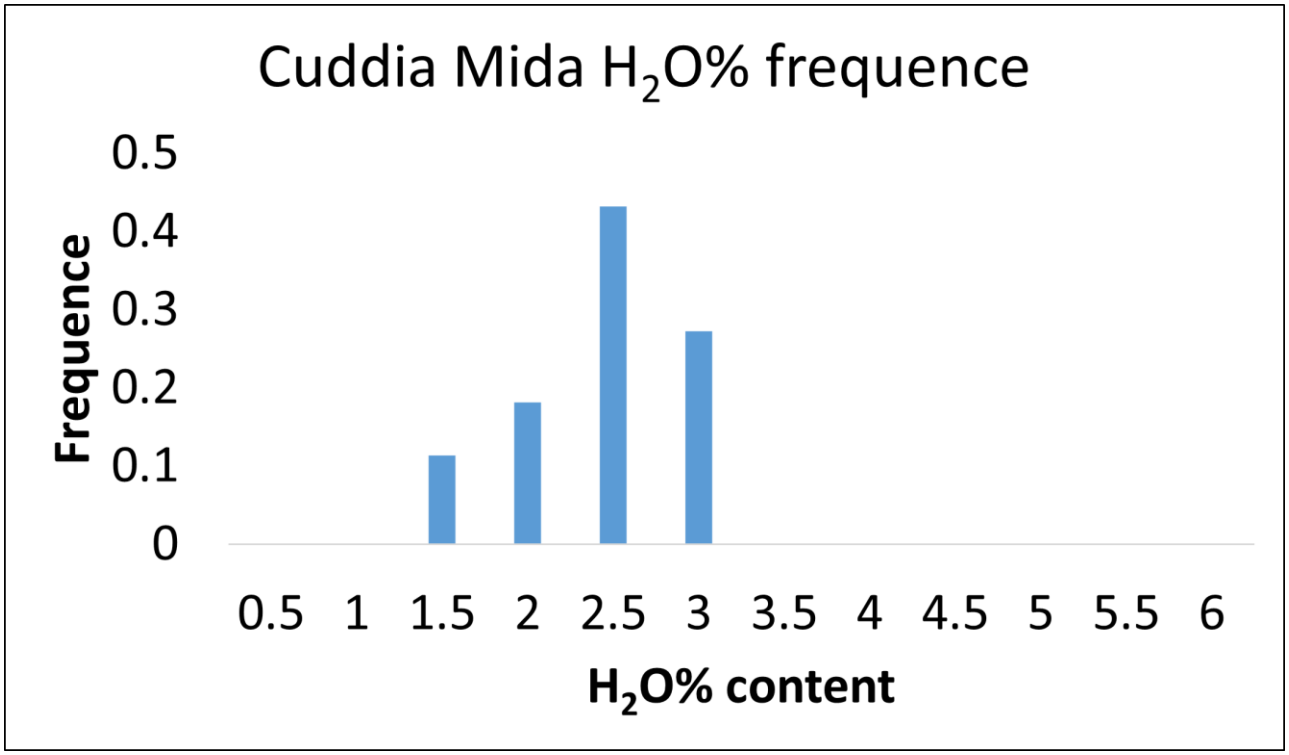


*Fig. 3.38 Water content distribution for Zinedi.*

By converting water content mode, 2.5 wt%, in depth, we obtain a value of 28 MPa or 756 m. Tab 3.10 summarizes water content mode for each eruption and the calculated magmatic chamber depth.

| | $H_2O$ mode1 (wt%) | $H_2O$ mode2 (wt%) | Depth1 (m) | Depth2 (m) |
|---|---|---|---|---|
| Cinque Denti | 3.5 | | 1566 | |
| Green Tuff (Lanzo et al., 2013) | 2.5 | 4 | 858 | 2050 |
| Zinedi | 2.5 | 5.5 | 837 | 4050 |
| Cuddia Mida | 2.5 | | 756 | |

*Tab. 3.10 Water content and depth conversion for each eruption. Cinque Denti, Zinedi and Cuddia Mida data are from this work. Green Tuff data are from literature (Lanzo et al., 2013). Depths are calculated using Liu et al. (2005) for Cinque Denti eruption, while depths for Green Tuff, Zinedi and Cuddia Mida are calculated using Allabar et al. (2022).*

Generally, for Cinque Denti and Zinedi eruption, no relationship has been found between host crystals and water content or between the MI location within the crystal and its water content.

## 3.7 Simultaneous thermal analysis (STA) and evolved gas analysis by mass spectrometry (EGA-MS) results

STA and EGA-MS analysis allowed us to measure weight loss due to the progressive and/or simultaneous release of $H_2O$ (m/z =18), $CO_2$ (m/z =44), Cl (m/z =35), F (m/z =19) and $SO_2$ (m/z =64) expressed as ion current (nA) with temperature. The fluorine signal appeared highly scattered and indistinct from the background noise; therefore, fluorine was not detected, as its concentration is considered to be below the limit of detection (LOD). Consequently, only the release of other volatile species is reported in the following figures. Pumice samples from the four eruptions studied were dried for 48 h at 60 °C prior to measurements. Then, all visible crystals were physically removed in order not to include crystal contribution in gas release during analysis. Subsequently, pumices were manually broken into small chips (≤ 2 mm). Care was taken to ensure that this fraction was homogeneous and representative of bulk sample. As we can notice in all figures, samples start to release $H_2O$ at very low temperature (ca. 200 °C). Water released at very low temperature can be related to the degassing of adsorbed external water (Denton et al., 2012; Giachetti et al., 2015; Biren et al., 2020). For this reason, it is important to properly define the glass transition temperature ($T_g$) value, above which only dissolved-magmatic volatiles from liquid melt are released. In the STA and EGA-MS measurements, the DSC signal (pink curve) is poorly defined, making it difficult to clearly recognize and accurately locate glass transition temperature ($T_g$). Previous DSC measurements on anhydrous melt samples provided $T_g$ values; however, the natural samples analysed here may contain volatiles, which can dramatically lower $T_g$ values. Although a negative peak can be observed in the DSC signal during STA and EGA-MS, its precise identification is challenging. Therefore, the $T_g$ values reported here are qualitative and should be considered as approximate estimates. Because volatile species release is expressed in ion current, by overlapping STA and EGA-MS graph, we can calculate volatile species release as weight loss. In the following pages, we present volatile species data for each eruption.

**Cinque Denti**

STA and EGA-MS analysis for Cinque Denti (Fig. 3.39) shows two volatile species released during heating, $H_2O$ and $CO_2$. Ion current is higher for $H_2O$ (ca. $10^{-10}$) than for $CO_2$ (ca. $10^{-11}$). At temperature between 25 °C to 500 °C, $H_2O$ and $CO_2$ are released. We can estimate approximately 3 wt% mass loss in this temperature interval. As indicated by previous studies (Roulia et al., 2006; Denton et al., 2012) gas contribution released below glass transition temperature can be considered external in origin, and therefore not taken into consideration for further discussion. In this case, $T_g$ is expected to be lower than 626 °C (the $T_g$ measured for the anhydrous glass), since the presence of volatiles typically decreases $T_g$. We can assume, nevertheless, that the observed 3 wt% mass loss below 500 °C is not related to magmatic dissolved volatiles, but rather to the release of adsorbed water. Because ion current is much higher for $H_2O$ than for $CO_2$, $10^{-10}$ vs $10^{-12}$ nA respectively, we ascribe this mass loss completely to adsorbed external water. This value, 3 wt% of total mass loss is large but is consistent with the old age of the eruption (125 ka). Crossing 600 °C, $H_2O$ ion current decrease while $CO_2$ ion current increase until it stabilises at 1100 °C. Because $CO_2$ release occurs after crossing this temperature, which is higher than 626°C and could represent $T_g$ of hydrous sample, we can ascribe this amount, ca. 0.5 wt%, to dissolved-magmatic $CO_2$. This release of $CO_2$ can be interpreted as the opening and outgassing of pre-existing, isolated, $CO_2$-rich vesicles. For this eruption and the other, we use the term vesicle as we do not know what kind of vesicle (melt inclusion or fluid inclusion) are present in the samples.

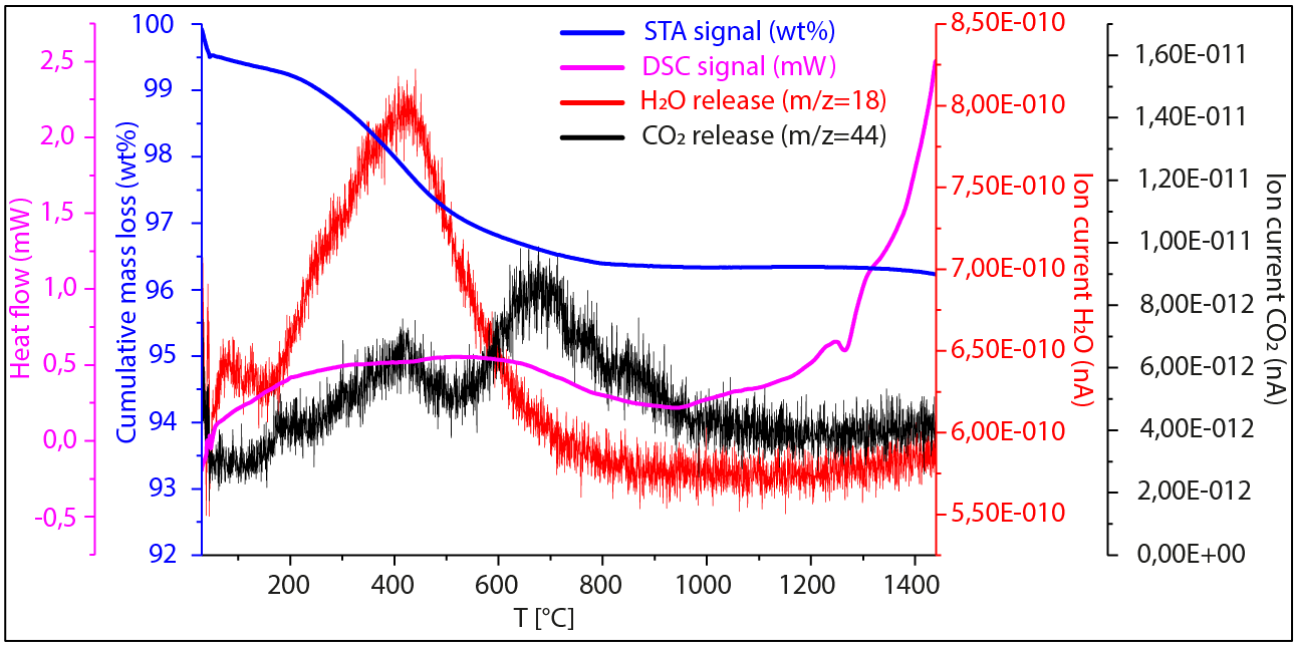


*Fig. 3.39 STA and EGA-MS analysis for Cinque Denti. Blue curve: STA signal, pink curve: DSC signal, red curve: $H_20$ ion current signal, Black curve: $CO_2$ ion current signal.*

### Green Tuff

STA and EGA-MS analysis for Green Tuff (Fig. 3.40) shows two volatile species released during heating, $H_2O$ and Cl. Ion current is higher for $H_2O$ (ca. $10^{-9}$) than for Cl (ca. $10^{-12}$). At temperature between 25 °C to ca. 600 °C only $H_2O$ is released. 600 °C is the temperature at which STA curve tend to stabilize. We can estimate 2.5 wt% mass loss in this temperature interval. As the anhydrous $T_g$ is 591,5 °C, we decided not to attribute any signal below this value to magmatic dissolved volatile, but rather to the release of absorbed water. This value, 2.5 wt% of total mass loss is high but is again consistent with the old age of the eruption (50 ka). Crossing 750 °C, which is the temperature where a negative peak in DSC curve can be observed as well, $H_2O$ ion current stabilizes while Cl ion current increase rapidly until it stabilises at ca. 1100 °C. Because Cl release occurs after crossing this temperature, which is higher than 591,5°C we can ascribe this amount, ca. 0.7 wt%, to dissolved-magmatic Cl. At higher temperature, between 1200 °C to 1450 °C (end of measurement) another weight loss, ca. 0.7 wt%, is observed. Because no ion current is registered for the four major elements analysed, we cannot ascribe this weight loss to a specific volatile species release. We suggest that this weight loss can be ascribed to the degassing of the remaining volatiles stored in the immiscible liquid droplets.

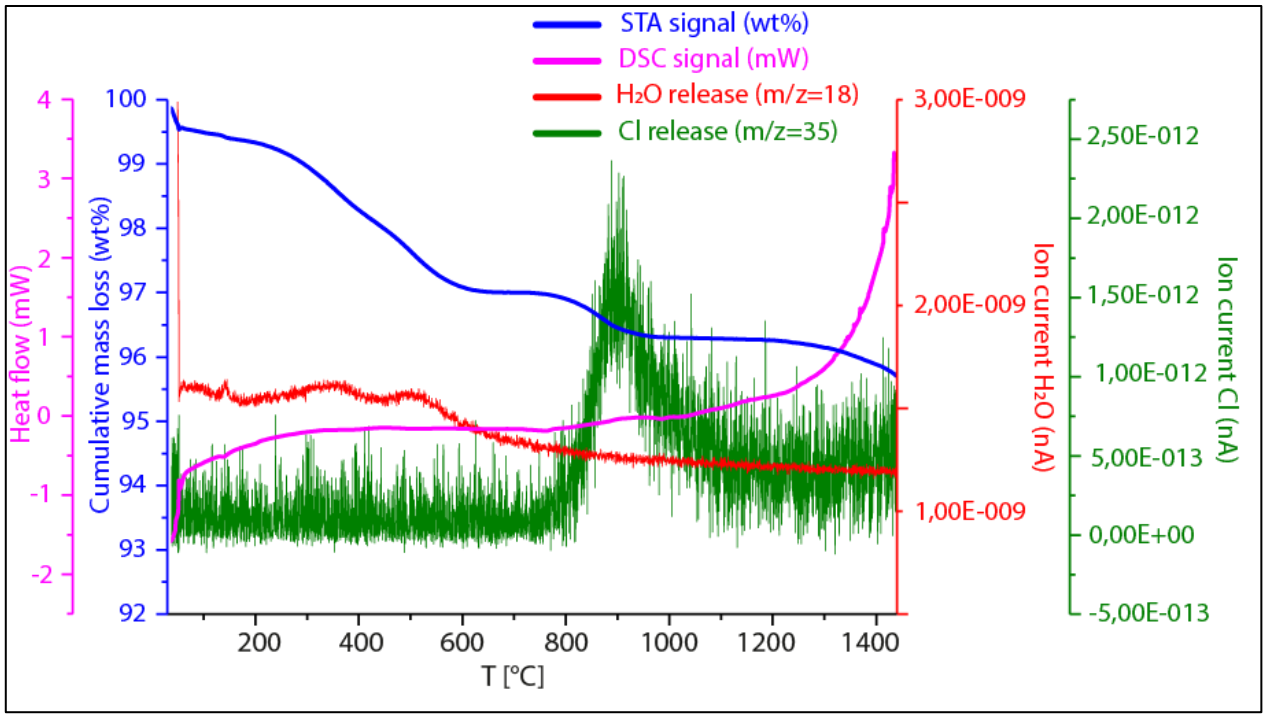


*Fig. 3.40 STA and EGA-MS analysis for Green Tuff. Blue curve: STA signal, pink curve: DSC signal, red curve: $H_20$ ion current signal, green curve: Cl ion current signal.*

### Zinedi

STA and EGA-MS analysis for Zinedi (Fig. 3.41) shows two volatile species released during heating, $H_2O$ and Cl. Ion current is higher for $H_2O$ (ca. $10^{-10}$) than for Cl (ca. $10^{-12}$). At temperature between 25 °C to 600 °C only $H_2O$ is released. 600 °C is the temperature at which STA curve tends to stabilize. We can estimate 2.5 wt% mass loss in this temperature interval. In this case, anhydrous $T_g$ is 573,4 °C so, as for the previous cases, we decided not to consider any mass loss below this value as due to magmatic volatile, but rather to the release of adsorbed water. This value, 2.5 wt% of total mass loss is high but is consistent with the old age of the eruption (189 ka). Crossing 650 °C, $H_2O$ ion current stabilizes while Cl ion current increase rapidly until it stabilizes at ca 1200 °C. Because Cl release occurs after crossing this temperature, we can ascribe this amount, ca. 0.9 wt%, to dissolved-magmatic Cl. At higher temperature, between 1200 °C to 1450 °C (end of measurement) another weight loss, ca. 0.5 wt%, is observed. Because no ion current is registered for the four major elements analysed, we cannot ascribe this weight loss to a specific volatile species release. We interpreted this behaviour as the same for Green Tuff.

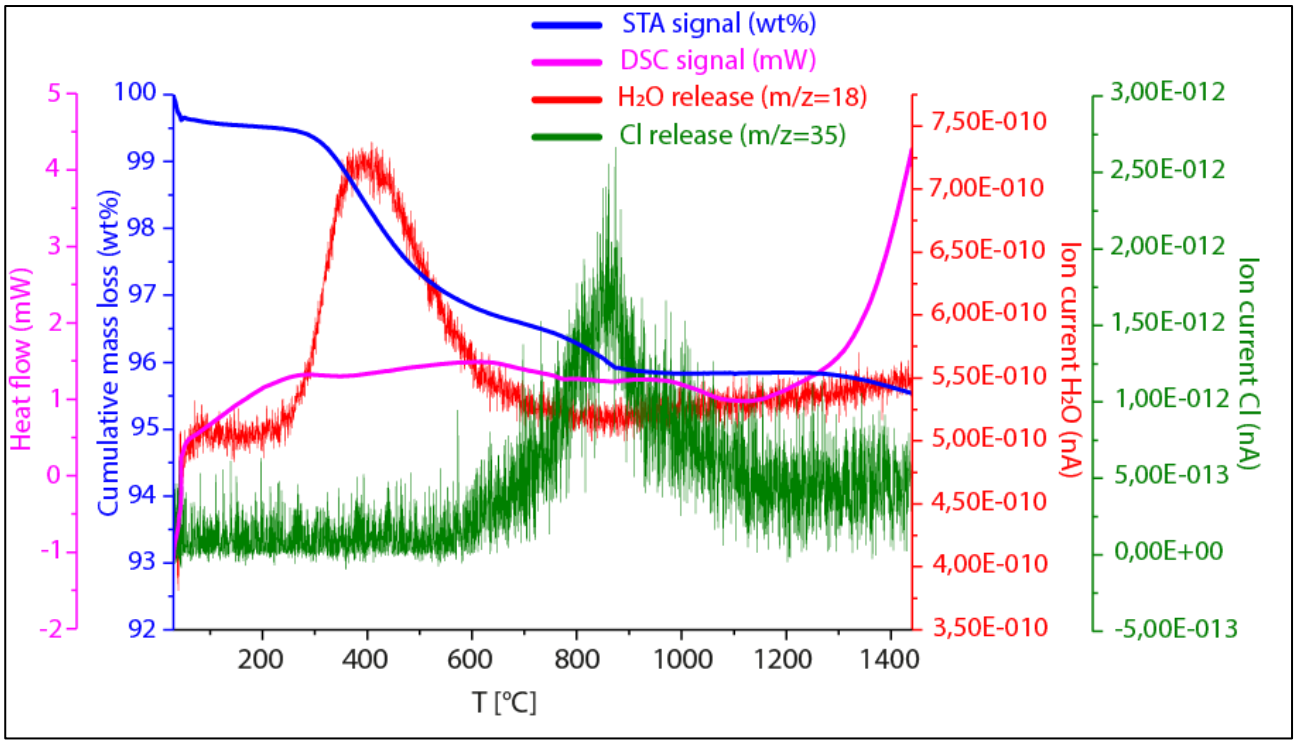


*Fig. 3.41 STA and EGA-MS analysis for Zinedi. Blue curve: STA signal, pink curve: DSC signal, red curve: $H_20$ ion current signal, green curve: Cl ion current signal.*

### Cuddia Mida

STA and EGA-MS analysis for Cuddia Mida (Fig. 3.42) shows all the four volatile species released during heating, $H_2O$, $CO_2$, Cl and $SO_2$. Ion current is higher for $H_2O$ (ca. $10^{-10}$), followed by $CO_2$ (ca. $10^{-11}$), Cl (ca. $10^{-12}$) and $SO_2$ (ca. $10^{-13}$). At temperature between 25 °C to 600 °C $H_2O$ and $CO_2$ is released. We can estimate 3 wt% mass loss in this temperature interval. In this case, anhydrous $T_g$ is 570 °C, so, as for the previous cases, we decided not to consider any mass loss below this value as due to magmatic volatile, but rather to the release of adsorbed water. This value, 3 wt% of total mass loss is high and it is not as consistent as the other eruptions with the age of the eruption (9.7 ka). Poor scattered release of $CO_2$ can be interpreted as the opening and outgassing of pre-existing, isolated, $CO_2$-rich vesicles. Crossing 750° C, which is the temperature where a negative peak in DSC curve can be observed as well, $H_2O$ ion current decrease while Cl and $SO_2$ ion current increase until they stabilize at 1200 °C. A small $CO_2$ ion current can be observed crossing this temperature. Because Cl, $SO_2$ and $CO_2$ release occurs after crossing this temperature, we can ascribe this amount, ca. 1.5 wt%, to dissolved-magmatic Cl, $SO_2$ and $CO_2$. At higher temperature, between 1200 °C to 1450 °C (end of measurement) another weight loss, ca. 0.7 wt%, is observed. Because no ion current is registered for the four major elements analysed, we

cannot ascribe this weight loss to a specific volatile species release. We interpreted this behaviour as the same for Green Tuff and Zinedi.

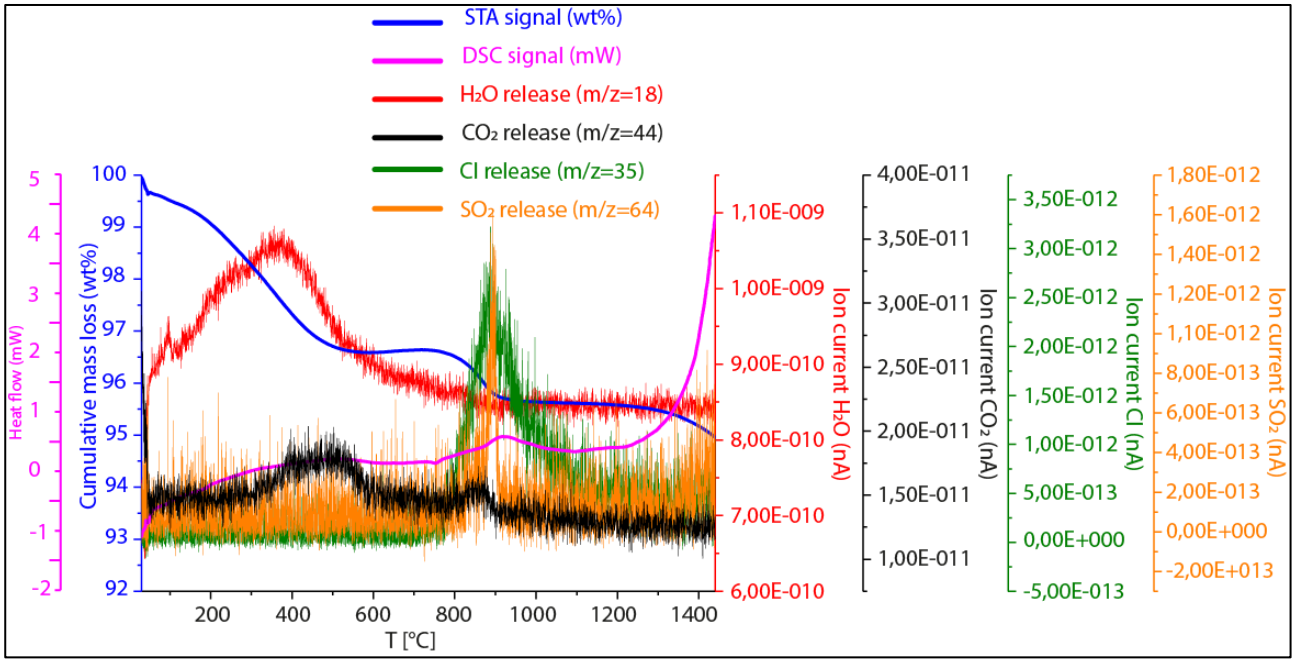


*Fig 3.42 STA and EGA-MS analysis for Cuddia Mida. Blue curve: STA signal, pink curve: DSC signal, red curve: H20 ion current signal, black curve: $CO_2$ ion current signal, green curve: Cl ion current signal, orange curve: $SO_2$ ion current signal.*

To summarise the findings of the STA and EGA-MS analyses, it can be concluded that (1) $H_2O$ release is mostly referred to the degassing of adsorbed external water, (2) $CO_2$ release can be ascribed to the outgassing of pre-existing, isolated, $CO_2$-rich vesicles. Only for Cinque Denti and Cuddia Mida we detected a certain amount of $CO_2$ of magmatic origin as ion current increase after crossing $T_g$, (3) Cl and $SO_2$ release always occur after crossing $T_g$. For this reason, Cl and $SO_2$ can be ascribed to dissolved-magmatic origin. Tab. 3.11 summarizes total weight loss and $H_2O$, $CO_2$, Cl and $SO_2$ loss. $H_2O$ is referred to adsorbed external water, $CO_2$ loss has been divided into two different contributions, Cl and $SO_2$ loss are always referred to dissolved-magmatic origin. The $CO_2$ release can be interpreted as the opening and outgassing of pre-existing, isolated, $CO_2$-rich vesicles, rather than residual $CO_2$ in glass. We did not observe $CO_2$ in melt inclusions nor in the residual glass.

| | Total loss (wt%) | $H_2O$ loss (wt%) | $CO_2$ loss (wt%) | $CO_2$-magmatic loss (wt%) | Cl loss (wt%) | $SO_2$ loss (wt%) |
|---|---|---|---|---|---|---|
| Cinque Denti | 3.76 | 3 | | 0.5 | | |
| Green Tuff | 4.26 | 2.5 | | | 0.7 | |
| Zinedi | 4.46 | 2.5 | | | 0.9 | |
| Cuddia Mida | 5.02 | 3 | | 1.5 | | |

*Tab. 3.11 STA and EGA-MS results. H2O is always referred to adsorbed external water, $CO_2$ loss is referred to non-magmatic $CO_2$, Cl and $SO_2$ are always referred to dissolved-magmatic origin.*

Furthermore, we performed Raman Spectroscopy measurements on residual glass (pumices) from the targeted eruption in order to retrieve residual volatile content after the eruption. We only detected $H_2O$ in residual glass and a summary of these values is reported in Tab 3.12.

| | Residual $H_2O$ (wt%) |
|---|---|
| Cinque Denti | 3.7 |
| Green Tuff | 1.25 |
| Zinedi | 1.98 |
| Cuddia Mida | 0.49 |

Tab. 3.12 $H_2O$ in residual glass from targeted eruptions.

# 4. Discussion

## 4.1 Textural analysis

Qualitative image analysis of the four analyzed eruptions suggests a net predominance of highly vesicular pumices for all four fall out deposits. This is also noticeable from total porosity distribution (Results, Fig. 3.3) and low, medium and high density clasts selected for this study (Results, Tab 3.2). These results also reflect the average porosity range for acidic explosive eruptions (70 to 90%; Klug and Cashman 1996; Polacci et al., 2003). While Cinque Denti (caldera-forming eruption), Zinedi (sub-Plinian eruption) and Cuddia Mida (Strombolian eruption) SEM images show features compatible with their eruptive style (Orsi et al., 1991; Hughes et al., 2017; Jordan et al., 2018), Green Tuff show peculiar features which are not typical of a caldera-forming eruption style. In particular, the Green Tuff pumices do not show well-preserved septa; instead, vesicle walls are highly deformed, a larger population of smaller vesicles than in the texturally similar Cinque Denti eruption is present, and, most importantly, coalescence is pervasive. Considering the low viscosity of the melt and the rheomorphic behavior of peralkaline magmas, we attribute these features to relaxation after fragmentation and/or to lithostatic pressure. Vesicle size distributions (VVDs) have been used as a proxy for nucleation and/or coalescence processes during conduit ascent, following the approach of Shea et al. (2010).

The Green Tuff VVDs (Results, Fig. 3.12) display a polymodal distribution, abundant coalescence in all clasts, and, most notably, a reduction in total vesicle fraction, which we interpret as bubble collapse. At the same time, they exhibit larger vesicles compared to all the other eruptions (see Results, Tab. 3.4), compatible with pervasive coalescence. Polymodal VVDs indicate multiple stages of nucleation and growth, suggesting a complex ascent history. They point to variable ascent rates, including episodes of deceleration or temporary stagnation in the conduit, which allow new vesicle populations to nucleate. Polymodal VVDs in low viscosity peralkaline systems can also be related to post-fragmentation processes such as relaxation, bubble coalescence, collapse, and secondary degassing favoured by prolonged high temperatures and low melt viscosities. After deposition in fact, the fallout deposit of the Green Tuff was overlain by a high-volume ignimbrite, which may have prolonged high-

temperature conditions (Scarani et al., 2023). We suggest that this delayed cooling allowed pumices to continue degassing and vesicles to deform and collapse under lithostatic pressure, i.e., post-fragmentation, leading to the observed peculiar features of Green Tuff textures. Peralkaline magmas, such as those of the Green Tuff, are characterized by significantly lower viscosities, especially at low temperatures, compared to their metaluminous counterparts (e.g., Dingwell and Tuffen, 2003). This supports the idea that such melts can cross the glass transition multiple times after fragmentation. Consequently, pumices reheated on the ground by the overlying pyroclastic density current deposit could have continued to degas, leading to further bubble growth, collapse, and coalescence.

The Cinque Denti VVDs (Results, Fig. 3.11) reflect a simple unimodal distribution with little to no coalescence, except in low-density clasts, supporting an interpretation of continuous nucleation and growth during ascent under rapid and near-constant acceleration (Klug and Cashman, 1989), typical of Plinian-style eruption.

Zinedi VVDs (Results, Fig. 3.13) show unimodal distribution of vesicles and coalescence can be observed for low density clast and for medium density clasts Z13 and Z79. We interpret this as a continuous nucleation and growth of vesicles during magma ascent. This can be reconducted to a rapid rise of magma in the conduit under rapid and near-constant acceleration (Klug and Cashman, 1989), typical of Plinian eruption and very similar to Cinque Denti textural features. The Zinedi deposit represents the only non-welded Plinian eruption on Pantelleria Island, likely reflecting a lower eruptive temperature, or slightly higher viscosities, which would explain the absence of welding features.

Cuddia Mida VVDs (Results, Fig. 3.14) show plurimodal distribution of vesicles and coalescence can be observed for medium and low density clasts. Polymodal VVDs indicate multiple stages of nucleation and growth, suggesting variable ascent rates, including episodes of deceleration or temporary stagnation in the conduit, which allow new vesicle populations to nucleate. This is compatible with the strombolian eruptive style of Cuddia Mida eruption. In this framework the coalescence may have simply occurred during magma ascent, although post-fragmentation coalescence cannot be excluded.

VND for the four eruptions here investigated (from $4.80x10^5$ $mm^{-3}$ to $6.06x10^6$ $mm^{-3}$ for Cinque Denti eruption, from $2.16x10^5$ $mm^{-3}$ to $6.05x10^6$ $mm^{-3}$ for Green Tuff eruption, from $3.21x10^5$ $mm^{-3}$ to $5.52x10^6$ $mm^{-3}$ for Zinedi eruption and from $1.04x10^6$ $mm^{-3}$ to $5.20x10^6$ $mm^{-3}$ for Cuddia Mida eruption) are in agreement with those measured in silicic Plinian eruptions (from $1x10^4$ $mm^{-3}$ to $1x10^7$ $mm^{-3}$; Klug and Cashman, 1994; Klug, Cashman and Bacon, 2002; Gurioli et al., 2005). Tab 4.1 resumes the mean VNDs value from medium-density clast for the four eruptions studied. VND values are very similar among the four eruptions investigated in this study, and, unexpectedly, no major differences are observed with respect to the different eruptive styles. In particular, the Strombolian eruption of Cuddia Mida exhibits a VND value that is actually very high and fully comparable to the VNDs of the others, more violent eruptions, especially considering that the coalescence process would have acted to decrease the VNDs.

| | **Cinque Denti** | **Green Tuff** | **Zinedi** | **Cuddia Mida** |
|---|---|---|---|---|
| **VND ($mm^{-3}$)** | $2.81x10^6$ | $2.27x10^5$ | $4.41x10^5$ | $2.42x10^6$ |

*Tab. 4.1 VNDs of the four eruptions studied. VNDs are expressed in $mm^{-3}$.*

For a better understanding of peralkaline magma behavior and in order to explore a wider range of eruptive styles, we included in our analysis other two eruptions from Pantelleria Island. For this purpose, we chose the sub-Plinian eruption Fastuca and the low-energy Strombolian eruption Altura. Data are taken from Anush Kazarian, PhD Thesis. The Fastuca eruption represents one of the most energetic pantelleritic eruptions relative to the post-Green Tuff cycle of activity at Pantelleria. It is classified as sub-Plinian eruption, and the eruptive center is located on the northern slope of Montagna Grande (Orsi et al., 1989). A recent re-estimation of its age by high resolution $^{40}Ar/^{39}Ar$ dating was given at 9.7±0.6 ka by Scaillet et al. (2011). The complete eruptive sequence is mostly exposed near Case Siracusa and is well described by Orsi et al. (1989) and Rotolo et al. (2007) as a succession of fall out layers of grey pumices and glassy pantelleritic obsidians with alternate trachytic lava fragments (Orsi et al., 1991). The deposit, with a maximum thickness of 10 m, can be subdivided into 3 members: (i) a lower 3 m thick pumice and lithics fall deposit, (ii) a median layer of well sorted pumices and (iii) an upper ungraded layer with coarse pumices (up to 80 cm). The samples were taken from a distant site fall out relative to the basal layer. The Altura

eruption (159±8 ka; K/Ar age; Mahood & Hildreth, 1986) consists of an eruptive sequence, exposed near Cala dell'Altura, in the south-western sector of the island, predating the formation of caldera La Vecchia collapse (146-140 ka; Speranza et al., 2012). It was described as a sequence of fall out units (Strombolian activity) and lava flows with local significance, i.e., emitted from an eruptive center located in the Altura area, directly in contact on the top with a pyroclastic flow deposit related to the Ignimbrite unit P (which is considered related to La Vecchia Caldera collapse, eg., Rotolo et al., 2013; Mahood and Hildreth, 1986). The samples consist of pumices pertaining to the basal fallout of the sequence. Tab 4.2 resumes the mean VNDs value of the medium density (MD) clast for all the six eruptions considered for this work.

| | **Cinque Denti** | **Green Tuff** | **Zinedi** | **Fastuca** | **Cuddia Mida** | **Altura** |
|---|---|---|---|---|---|---|
| **VND ($mm^{-3}$)** | $2.81x10^6$ | $2.27x10^5$ | $4.41x10^5$ | $2.63x10^5$ | $2.42x10^6$ | $2.20x10^5$ |

*Tab. 4.2 VNDs of the six eruptions considered in this work. VNDs are expressed in $mm^{-3}$and are related to medium density (MD) clasts. Eruptions are ordered from the more energic eruptive style to the less energic eruptive style. Cinque Denti and Green Tuff-Plinian eruptions; Zinedi and Fastuca-sub-Plinian eruptions; Cuddia Mida and Altura-Strombolian eruptions.*

In Fig. 4.1, the comparison of VNDs for explosive eruptions from literature data (see Supplementary Material), with a range of magma compositions indicated by bulk $SiO_2$ content, is shown (both for metaluminous, peraluminous and peralkaline compositions). The variation in eruptive style (from Strombolian to ultra-Plinian) is indicated with different colour scale. Our data are indicated with squares of different colour scale. This diagram shows that for most energetic explosive eruptions, ie., Plinian or phreatoplinian, VNDs span over at about two orders of magnitude ($10^5$ to $10^7$ $mm^{-3}$) regardless of $SiO_2$ content. A single high VND value of $10^9$ $mm^{-3}$ has been recorded from Mt Mazama eruption in 2002 (Klug et al., 2002) and a low value of $10^3$ $mm^{-3}$ from Tarawera eruption in 1886 (Sable et al., 2009). Sub-Plinian eruptions seem to present more uniform VND values on the lower end of Plinian eruptions, spanning one order of magnitude (between $10^5$ to $10^6$ $mm^{-3}$), again independent on $SiO_2$ content. A single eruption showing VND $10^4$ $mm^{-3}$ from "El Retiro" eruption (2 ka) from Turrialba volcano (Di Piazza et al., 2019), is reported in the diagram. Only two Vulcanian eruptions are considered here and both present VND as high as those reported for Plinian eruptions. Therefore, high-energy eruptions (Vulcanian, sub-Plinian, and Plinian) are characterized by VND values spanning one to two orders of magnitude, regardless

of chemical composition Within basaltic eruptions VND values seem to vary according to eruptive style, with Strombolian events having generally lower values than sub-Plinian and Plinian eruptions. In the peralkaline realm, the six eruptions analysed here, they all present similar VNDs despite very different eruptive styles going from Strombolian (Cuddia Mida and Altura) to sub-Plinian events (Zinedi and Fastuca) and two caldera-forming events (Cinque Denti and Green Tuff). Moreover, Green Tuff exhibits the lowest overall VND value similar to Altura's VND. On the other hand, Cuddia Mida, a low/average explosive Strombolian eruption, present a very high VND and high silica content. This apparent inconsistency between the $SiO_2$–VND–explosivity relationship and the present dataset highlights the peculiar rheological behavior of peralkaline magmasOur results show that Cuddia Mida VND is one order of magnitude higher that Green Tuff VND. The other Strombolian type eruption (Altura) exhibits VND comparable to the other sub-Plinian and Plinian samples here investigated. Cuddia Mida's VND calculated in this work ($2.42x10^6 mm^{-3}$) is in agreement with VND calculated from Hughes et al. (2017) ($3.25x10^6$ $mm^{-3}$), confirming the validity of our methodological approach and the robustness of our data. The relative low VNDs of Green Tuff with respect to the other eruptions here investigated can be explained, as hypothesized earlier, by a combination of low viscosity and slow cooling under the effect of lithostatic pressure. Slightly lower temperatures, higher viscosities, or a delay between the deposition of the fall units and the subsequent flow in the other Plinian and sub-Plinian eruptions may account for the absence of these textural features. The high VND of the two strombolian units does not have an immediate explanation. For these melts, the correlation between vesicle number density and ascent velocities seems not to be respected.

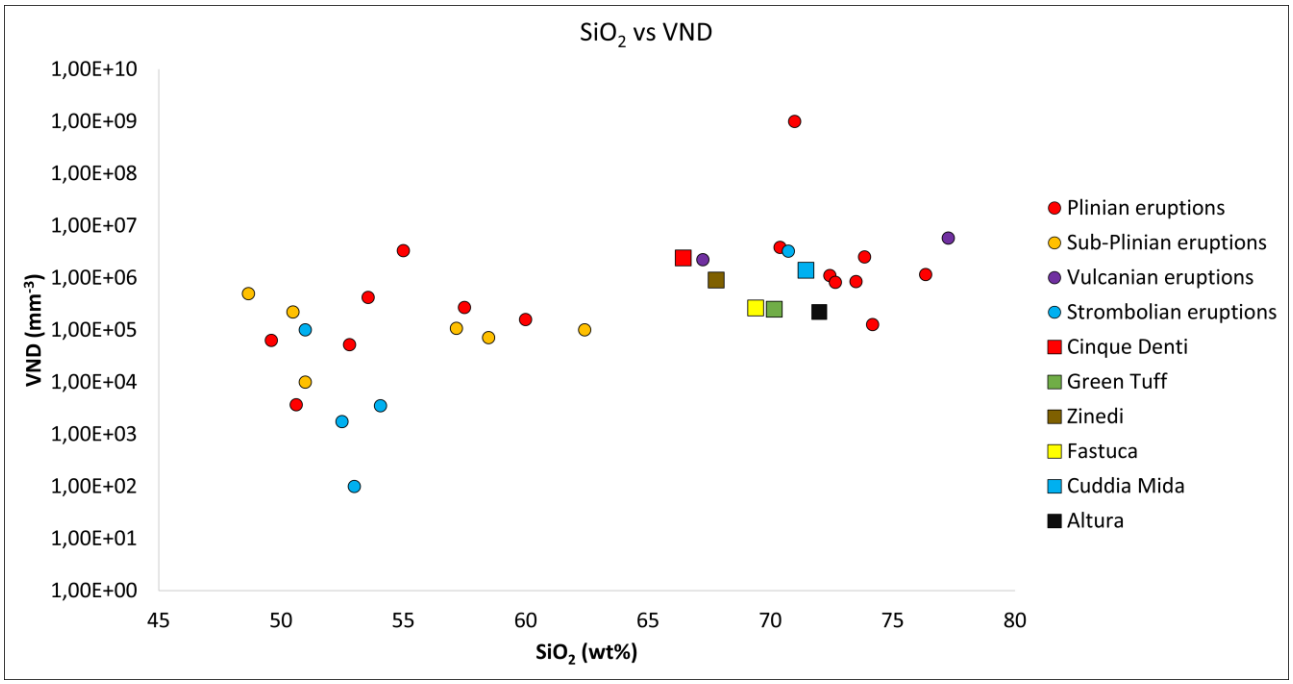


*Fig. 4.1 Comparison of vesicle number densities (VND) for explosive eruptions with a range of magma compositions indicated by bulk SiO2 content with our data (Tab. 4.2). Circles are data from literature. Squares are date from this work. Data are from: Klug et al. (1994, 2002); Rosi et al. (2004); Adams et al. (2006); Shimano et al. (2006); Giurioli et al. (2008); Carey et al. (2009); Polacci et al. (2009a, 2009b); Sable et al. (2006, 2009); Costantino et al. (2010); Giacchetti et al. (2010); Houghton et al. (2010); Shea et al. (2010); Cioni et al. (2011); Alfano et al. (2012); Stoval et al. (2012); Colombier et al. (2017); Pistolesi et al. (2017, 2021); Di Piazza et al. (2019); Romano et al. (2020); Toramaru (2021).*

Similarly, not an immediate correlation can be found among eruptive style and intensity and other main textural parameters, as porosity, maximum vesicle diameter for MD clasts and mean vesicles diameter for MD clasts. Fig. 4.2 shows textural parameters of the investigated samples in correlation with eruptive style. Vesicle diameter is in mm, porosity in % and VND in $mm^{-3}$. Whereas the highest maximum vesicle and mean vesicle diameter reported for Green Tuff can be ascribed to post-fragmentation coalescence processes, clearly evident for these samples, the other eruptions show similar values of all parameters, with differences in porosity and mean vesicle diameters not easily ascribable to any specific process. In conclusion, textural analysis indicates a great similarity among all the eruptions investigated in this study, despite the change in intensity and eruptive style, providing little insight into the conditions of brittle fragmentation in these relatively low-viscosity magmas and questioning the validity of the correlation between the VND parameters and the ascent velocity as postulated by Toramaru (1995, 2006) for peralkaline magmas.

The analyses presented in Figures 4.1 and 4.2 suggest that the peralkaline magmas examined in this study display comparable textural features that are not directly attributable to any specific eruptive style. This observation may be extended to silica-rich eruptions as a whole. Indeed, their VND values span more than one order of magnitude regardless of eruptive style. In basaltic realms, by contrast, a correlation between eruptive style and VND appears more plausible, although in both cases additional data are required to validate or challenge this interpretation.

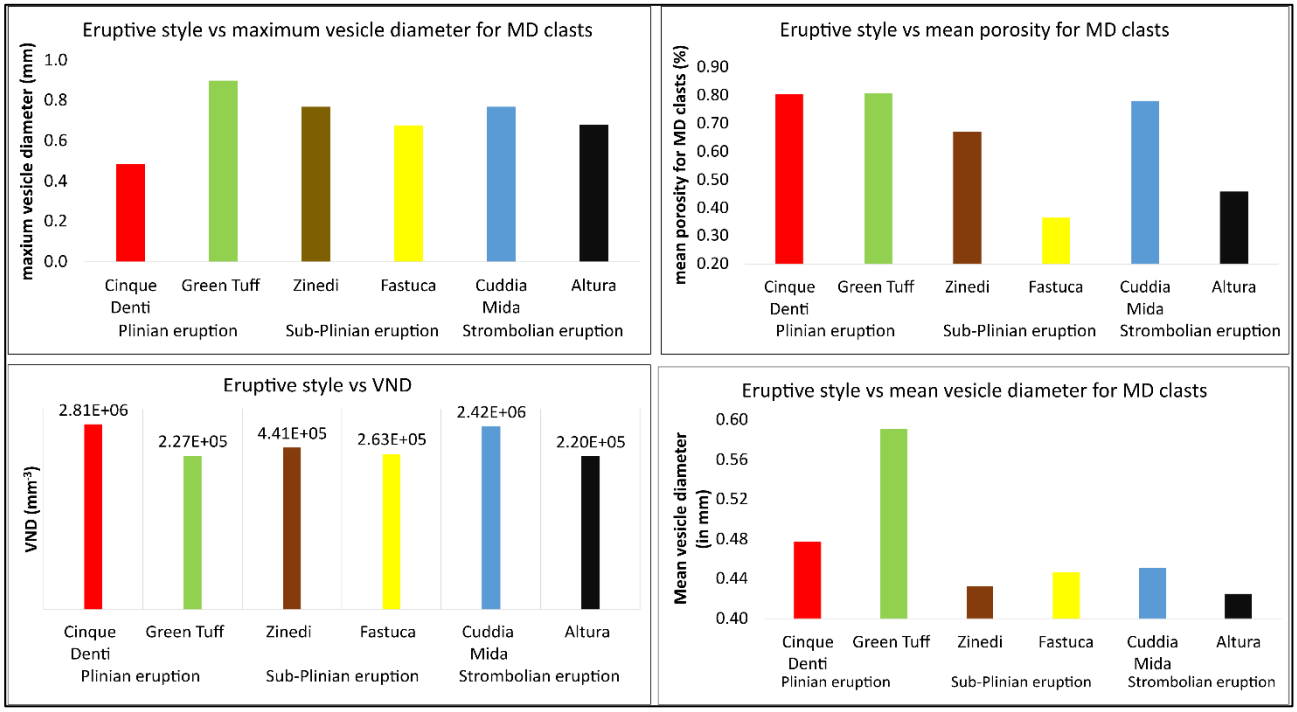


*Fig. 4.2 Comparison of textural parameters and eruptive style. Vesicle diameter is in mm, porosity in % and VND in $mm^{-3}$. Plinian eruption: Cinque Denti and Green Tuff; sub-Plinian eruptions: Zinedi and Fastuca; Strombolian eruptions: Cuddia Mida and Altura. No relationship between textural parameters and eruptive style is found.*

## 4.2 Viscosity

Viscosity measurements on anhydrous glasses were performed using a Concentric Cylinder (CC) apparatus for the high temperature-low viscosity regime, and Differential Scanning Calorimetry (DSC) and Micropenetration (MP) techniques for the low temperature-high viscosity regime. This paragraph explores the rheological behavior of anhydrous peralkaline melts. Since these measurements were carried out on anhydrous compositions, they are intended to assess the effect of anhydrous composition on melt viscosity, and therefore cannot be directly related to the eruptive style or explosivity of the studied eruptions. As shown in Fig. 3.16 of the Results chapter, we can notice that the

viscosity measurements performed by DSC and MP are not always in agreement. We interpreted this disagreement as due to the nanolitization process occurring in some samples in this temperature interval, as confirmed by the Raman spectra acquired on the same samples before and after the DSC and MP measurements. For Green Tuff, the DSC and MP measurements are in perfect agreement and no nanolites presence was observed by Raman spectroscopy before or after both sets of measurements. However, for the Cinque Denti and Zinedi samples, Raman spectroscopy revealed nanolites formation in the post-DSC and post-MP measurement samples, which was accompanied by a marked discrepancy between the DSC and MP data. Cuddia Mida DSC and MP measurements show a discrepancy not easily attributable to nanolites formation. We will discuss this particular outcome later in the paragraph. In some cases, the difference between DSC and MP viscosity can reach 2 log units (Fig. 3.16). In general, viscosity values derived from the MP method are systematically higher than those obtained by DSC, even though Raman spectroscopy revealed the presence of nanolites crystals after both sets of measurements. The viscosity increase in MP measurements related to nanolites presence may arise from different mechanisms. Although nanolites typically represent less than 10 vol%, melt entrapment within aggregates can effectively increase the solid fraction, thereby enhancing the overall magma viscosity (Di Genova et al., 2020a). Change in chemical composition due to diffusion of iron and titanium in (nano) crystalline oxides and iron oxidation in the residual melts may represent another viable mechanism leading to viscosity increase. In natural hydrous conditions, moreover, the nanolites presence can also promote heterogeneous bubble nucleation (Caceres et al., 2020; Di Genova et al., 2020a) and the consequent magma dehydration and/or inhibition of bubble coalescence (Knafelc et al., 2022; Yoshida et al., 2023). All these alterations can contribute to increase the relaxation timescale of the melt when subjected to shear deformation during MP measurements. Conversely, DSC measurements rely on a bulk property and do not appear to be significantly affected by the structural changes promoted by nanolites formation (Giuliani et al., 2024). Consequently, nanocrystalization leads to higher viscosity values in MP measurements compared to those obtained by DSC. As observed before, Cuddia Mida Raman spectra post-DSC and post-MP (3.28-29) show no sign of nanolites formation, despite a large discrepancy between DSC and MP measurements. This behaviour could possibly be related

to the presence of nanolites-rich subdomains that are below the detection limit of Raman spectroscopy, yet can still significantly contribute to the discrepancy between the DSC and MP measurements. These sub-microscopic heterogeneities may locally increase the melt viscosity due to the process just discussed, thus amplifying the apparent differences observed between the two methods. Since the MP viscosity measurements are strongly affected by the contribution of nanolites we decided to exclude them from this study and to rely only on the DSC measurements. This required a new fitting using the VFT equation, considering only the CC and DSC viscosity data for the Cinque Denti, Zinedi, and Cuddia Mida samples, and the CC, DSC, and MP viscosity data for the Green Tuff. Fig. 4.3 illustrates the new fitting. Values of A, B, and C for each eruption are reported in Tab. 4.3.

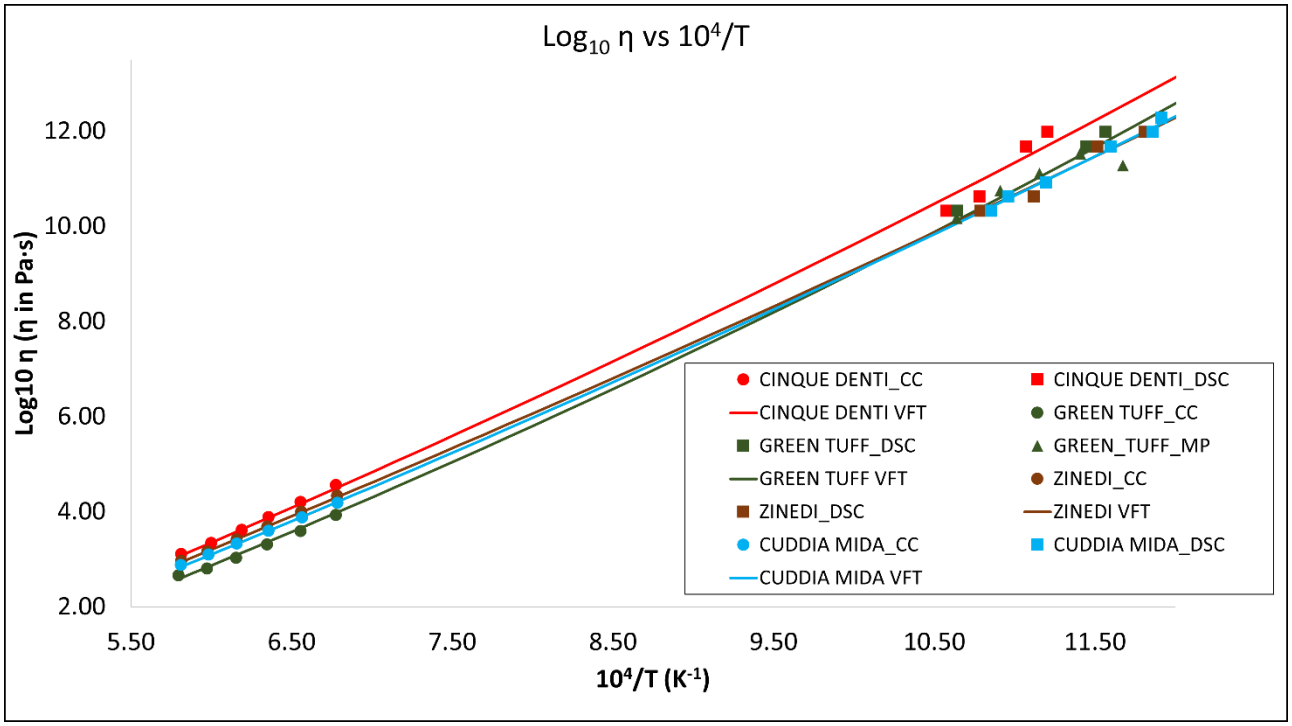


*Fig. 4.3 Measured viscosity data from low and high temperature (CC-circle) and low temperature (DSC-square; MP-triangle). Continuous curves correspond to VFT fitting curve derived from Vogel-Fulcher-Tammann (VFT) equation.*

| | **Cinque Denti** | **Green Tuff** | **Zinedi** | **Cuddia Mida** |
|---|---|---|---|---|
| A | -4.55 | -4.55 | -4.55 | -4.55 |
| B | 1.19E+04 | 1.09E+04 | 1.20E+04 | 1.17E+04 |
| C | 160.0692 | 196.99 | 122.009 | 141.114 |

*Tab. 4.3 Summary of A, B and C values for viscosity measurements fitting using CC and DSC measurements for Cinque Denti, Zinedi and Cuddia Mida. For Green Tuff CC, DSC and MP measurements have been considered.*

Viscosity measurements can be correlated with selected chemical parameters of the melts, such as NBO/T and P.I.. Fig. 4.4 illustrates the relationship between the viscosity from VFT fit, at both high (1450 °C–1675 K) and low (750 °C–1025 K) temperatures, and NBO/T, which quantifies the degree of polymerization of the silicate network, expressed as the ratio between non-bridging oxygens and tetrahedral cations. A clear relationship between viscosity and NBO/T is observed: higher NBO/T values correspond to lower viscosities, reflecting a more depolymerized silicate structure, and vice versa. Although the four studied eruptions display relatively small differences in viscosity and NBO/T, a consistent trend between these parameters is evident (Fig. 4.4).At temperatures lower than approximately 650°C, cross overs between the temperature curves yield more complicated non-linear relationships between viscosity and chemical-structural parameters.

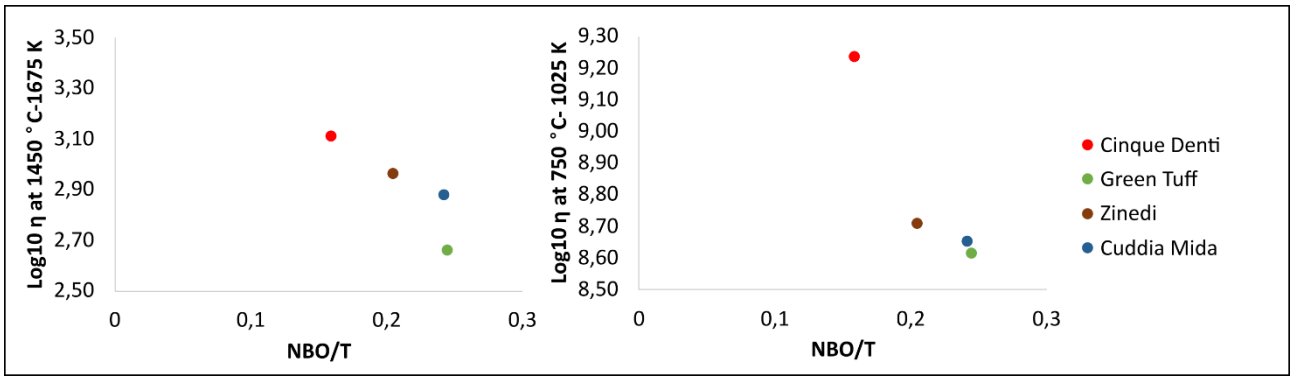


*Fig. 4.4 Viscosity-NBO/T relationship at high temperature-low viscosity (1450 °C - 1675 K) regime and at low-temperature-high viscosity (750°C - 1025 K).*

P.I. [$(Na_2O+K_2O)/Al_2O_3$] is a key chemical parameter for characterizing peralkaline magmas. Higher P.I. values indicate an excess of alkali relative to alumina, leading alkali to act as structural modifiers within the silicate network. Fig. 4.5 illustrates the relationship between viscosity from VFT fit, at both high (1450 °C–1675 K) and low (750 °C–1025 K) temperature and the P.I.. A clear correlation emerges: melts with higher P.I. values exhibit lower viscosities, consistent with a more depolymerized silicate structure, whereas lower P.I. values correspond to more polymerized and thus more viscous melts. Again, although the four eruptions studied show only minor differences in viscosity and P.I. values, a consistent trend between these parameters is evident (Fig. 4.5). As in the previous diagrams, at temperatures lower than approximately 650°C, cross overs between the temperature curves yield more complicated non-linear relationships between viscosity and chemical-structural parameters.

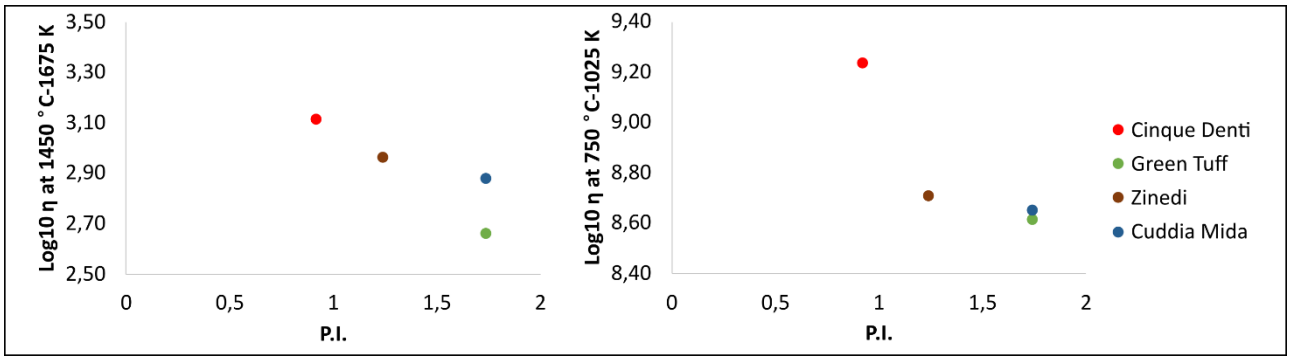


*Fig. 4.5 Viscosity-P.I. relationship at high temperature-low viscosity (1450 °C - 1675 K) regime and at low-temperature-high viscosity (750 °C - 1025 K).*

A summary of NBO/T and P.I. values are reported in Tab. 4.4.

| | **Cinque Denti** | **Green Tuff** | **Zinedi** | **Cuddia Mida** |
|---|---|---|---|---|
| **NBO/T** | 0.159 | 0.245 | 0.205 | 0.242 |
| **P.I.** | 0.92 | 1.74 | 1.24 | 1.74 |

*Tab. 4.4 NBO/T and P.I. of the four eruptions studied.*

As shown in the Results chapter, high temperature-low viscosity and low temperature-high viscosity regime data were fitted by using VFT equation. Furthermore, our viscosity data can be fitted by other equations as Mauro-Yue-Ellison-Gupta-Allan (MYEGA) equation (Mauro et al., 2009) that uses viscosity at infinite temperature ($log10\eta\infty$), glass transition temperature ($T_g$) and melt fragility (m) as parameters:

$$log_{10}\eta_s(T) = log_{10}\eta_\infty + (12 - log_{10}\eta_\infty)\frac{T_g}{T}\exp\left\{\left(\frac{m}{12 - log_{10}\eta_\infty} - 1\right)\left(\frac{T_g}{T} - 1\right)\right\} \quad (4.1)$$

For this fitting, the viscosity at infinite temperature was set to -2.93 (Cassetta et al., 2021; Langhammer et al., 2021, 2022; Zheng et al., 2011), while $T_g$ and m were set as fit parameters. Results from calculations are reported in Tab. 4.5, while the temperature-dependence of the viscosity is illustrated in Fig. 4.6.

| | **Cinque Denti** | **Green Tuff** | **Zinedi** | **Cuddia Mida** |
|---|---|---|---|---|
| $\boldsymbol{log_{10}\eta_\infty}$ | -2.93 | -2.93 | -2.93 | -2.93 |
| **$T_g$(°C)** | 627.3 | 591.50 | 573.4 | 570.00 |
| **m** | 24.15 ± 0.11 | 23.86 ± 0.14 | 21.15 ± 0.2 | 21.5 ± 0.22 |
| **$R^2$** | 0.99979 | 0.99972 | 0.99931 | 0.99923 |

*Tab. 4.5 MYEGA fit parameters.*

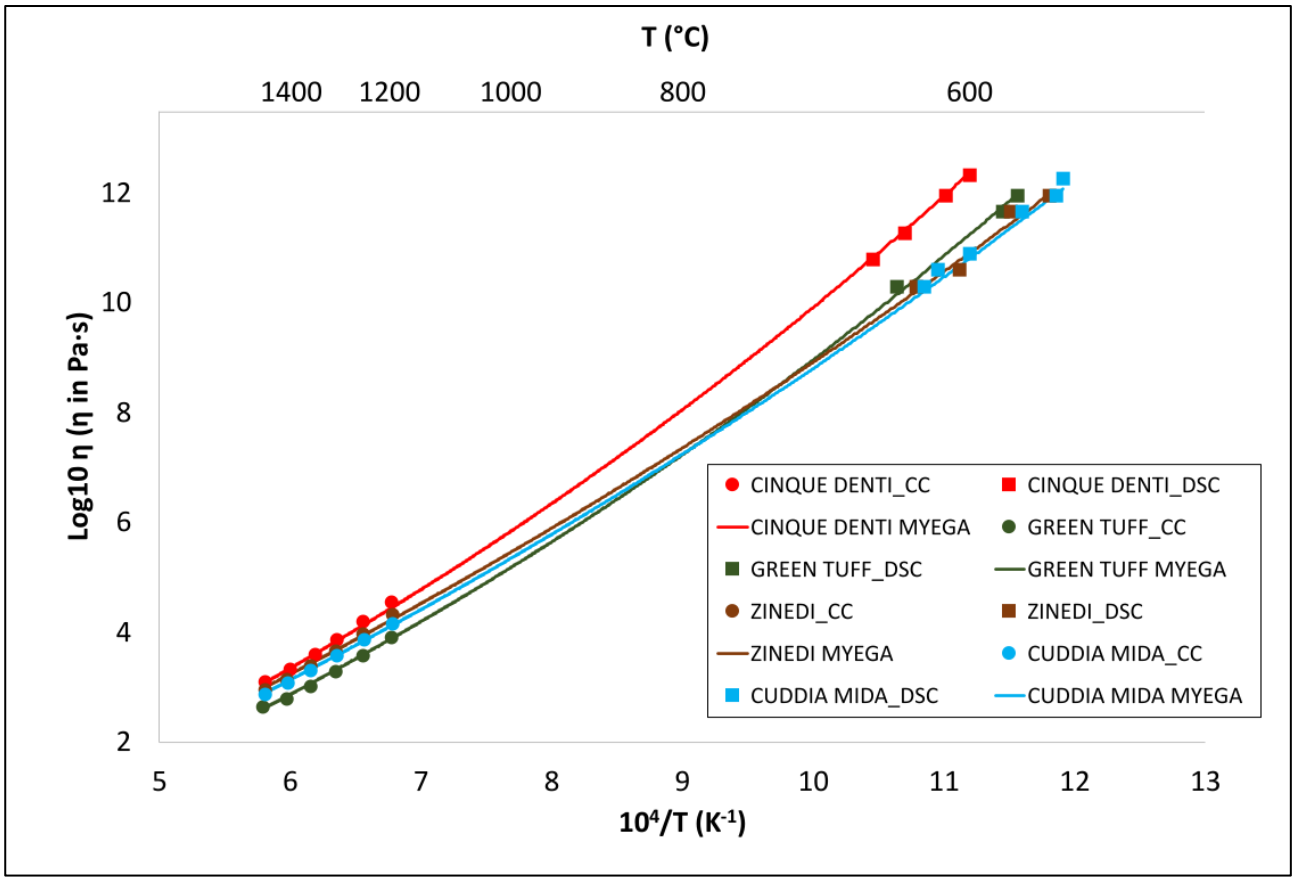


*Fig. 4.6 Viscosity data from CC and DSC measurements and MYEGA fits.*

Furthermore, MYEGA equation can also be used without considering $T_g$ as fixed parameter. Results from calculations are reported in Tab. 4.6, while the temperature-dependence of the viscosity is illustrated in Fig. 4.7.

| | **Cinque Denti** | **Green Tuff** | **Zinedi** | **Cuddia Mida** |
|---|---|---|---|---|
| $log_{10}\eta_\infty$ | -2.93 | -2.93 | -2.93 | -2.93 |
| **$T_g$(°C)** | 627.51 ± 0.7 | 591.72 ± 1.69 | 574.97 ± 2.48 | 574.83 ± 1.40 |
| **m** | 24.11 ± 0.10 | 23.87 ± 0.18 | 21.24 ± 0.25 | 21.83 ± 0.17 |
| **$R^2$** | 0.99982 | 0.99968 | 0.99926 | 0.99963 |

*Tab. 4.6 MYEGA fit parameters for $T_g$ not fixed as parameter.*

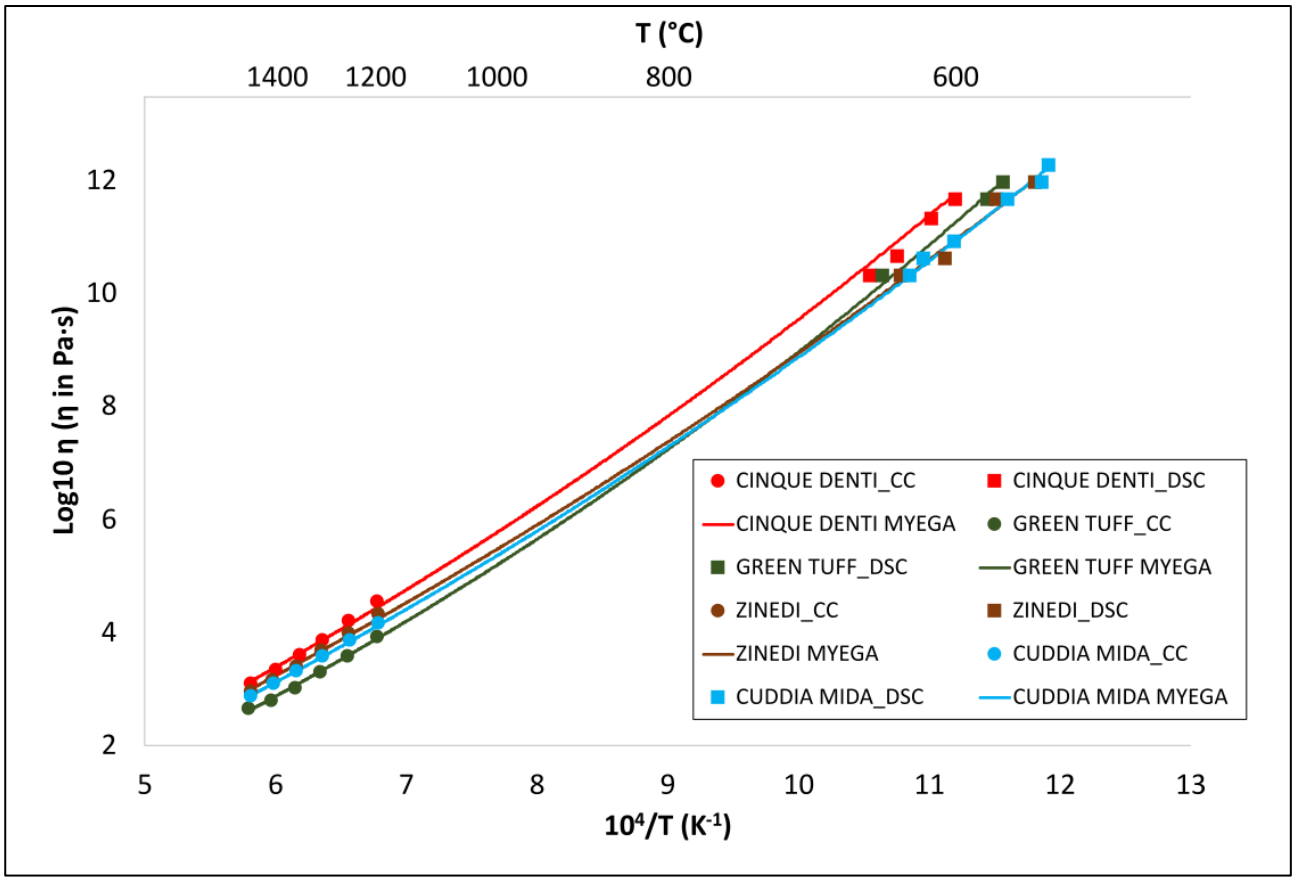


*Fig. 4.7 Viscosity data from CC and DSC measurements and MYEGA fits without fixing $T_g$ as parameter.*

The difference between the two MYEGA fits ($T_g$ fixed – $T_g$ free) are illustrated in Tab 4.7.

| | **Cinque Denti** | **Green Tuff** | **Zinedi** | **Cuddia Mida** |
|---|---|---|---|---|
| **$\Delta\ log_{10}\eta_\infty$** | 0 | 0 | 0 | 0 |
| **$\Delta$ $T_g$ (°C)** | -0.21 | -0.22 | -1.57 | -5.18 |
| **$\Delta$ m** | -0.04 | -0.012 | -0.091 | -0.32 |
| **$\Delta$ $R^2$** | -0.00003 | 0.00004 | 0.00005 | -0.0004 |

*Tab. 4.7 Difference between the two MYEGA fits ($T_g$ fixed – $T_g$ free).*

The four studied eruptions display only minor variations in the fitted parameters when comparing the $T_g$ fixed and $T_g$ free models. These results clearly indicate that the MYEGA equation provides an excellent fit to the viscosity data, regardless of whether Tg is constrained or allowed to vary, an interpretation further supported by the consistently high $R^2$ values obtained for both fitting approaches.

### 4.2.1 Comparison with models from literature

The viscosity data set obtained from this study has been compared with predictions of empirical models from literature: 1) the chemically-based GRD model from Giordano et al. (2008), and 2) the empirical model for peralkaline melts from Di Genova et al. (2013). 1) GRD model predicts the non-Arrhenian Newtonian viscosity of silicate melts as a function of T and melt composition and it is based on more than 1770 measurements of viscosity on multicomponent anhydrous and volatile-rich silicate melts. The non-Arrhenian T-dependence of viscosity is accounted for by the VFT equation [log η=A+B/(T(K)−C)]. The optimization assumes a common, high-T limit (A) for silicate melt viscosity and returns a value for this limit of −4.55. All compositional dependences are ascribed to the parameters B and C and are accounted for by additional 17 model coefficients. This model is continuous in composition- and temperature-space and predicts the viscosity of natural volatile-bearing silicate melts ($SiO_2$, $Al_2O_3$, $TiO_2$, $FeO_{tot}$, CaO, MgO, MnO, $Na_2O$, $K_2O$, $P_2O_5$, $H_2O$, $F_2O_{-1}$) over fifteen log units of viscosity ($10^{-1}$ – $10^{14}$ Pa·s). 2) Di Genova et al. (2013) model predicts peralkaline magmas viscosity over a wide range of temperature (from 613 K to 1673 K) and viscosity (from $10^{2.44}$ to $10^{11.37}$) as a function of chemical composition, in particular alkali excess expressed as AEX (mol%) = ($Na_2O$ + $K_2O$ - $Al_2O_3$), and temperature. Fig. 4.8 compares viscosity values obtained from the VFT fit with those predicted by the GRD model. The black dashed line represents the 1:1 correlation, while the red dashed lines indicate deviations of ±1 log unit from this reference. These bounds provide a quantitative measure of the agreement between the two approaches: data points lying on the 1:1 line indicate perfect concordance between the GRD predictions and the VFT fit values, whereas deviations from this line reflect the magnitude of the prediction error. As illustrated in Fig. 4.8, the GRD model reproduces the viscosity data with good accuracy, with no discrepancies exceeding 1 log unit for any of the four studied eruptions. Fig. 4.9 compares viscosity values obtained from the VFT fit with those predicted by the model of Di Genova et al. (2013). The black and dashed lines are represented in the same manner as in Fig. 4.8. Di Genova et al. (2013) model fails to reproduce the viscosity of Cinque Denti, as this melt is metaluminous. Moreover, the model does not predict the viscosities of Green Tuff, Cuddia Mida, and Zinedi with the same accuracy as the GRD model. The observed discrepancy most likely arises from the limited experimental dataset available for the

peralkaline compositional field on which the parameterization was based (58 measurements). In the present work, we propose a new parametrization for peralkaline magmas, building upon the Di Genova et al. (2013) model and incorporating both the viscosity dataset from this study and relevant data from the literature.

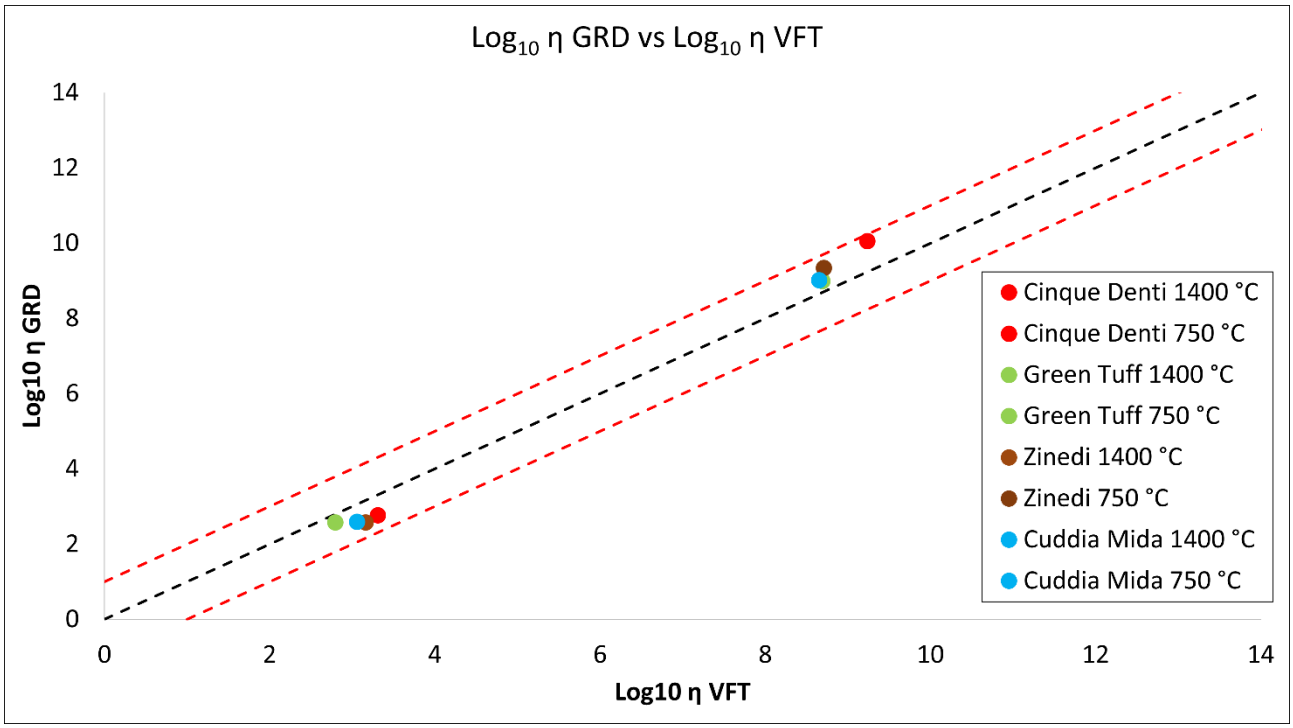


*Fig. 4.8 Melts viscosities defined at two different target temperatures of 1400 °C and 750 °C. Viscosities are from VFT fit and GRD model. GRD model predicts viscosity values with high accuracy at high temperature as well as at low temperature.*

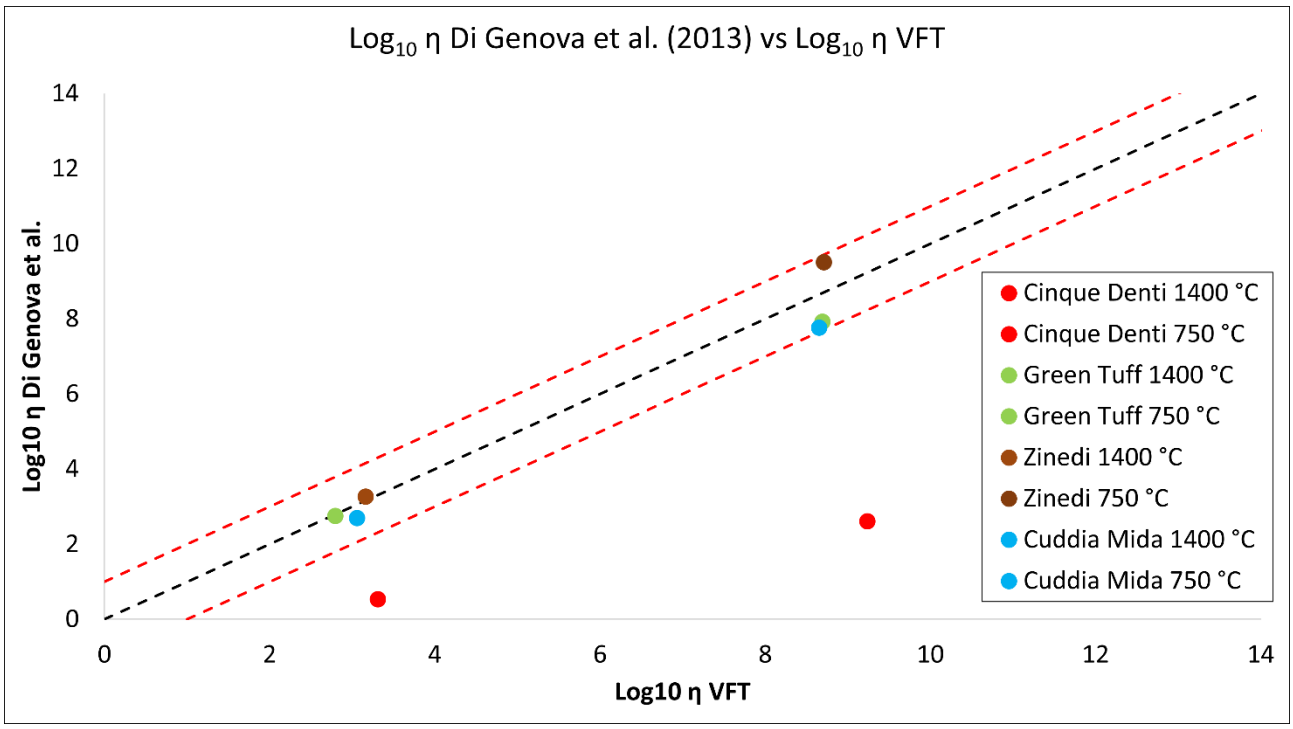

*Fig. 4.9 Melts viscosities defined at two different target temperatures of 1400 °C and 750 °C. Viscosities are from VFT fit and Di Genova et al. (2013) model. Di Genova et al. (2013) model failed to predict Cinque Denti viscosity as Cinque Denti is not peralkaline. Accuracy from GRD model in predicting viscosity of the four eruptions studied is higher than the accuracy from Di Genova et al. (2013) model.*

### 4.2.2 A new model for predicting peralkaline magmas viscosity

As discussed in the previous paragraph, the viscosity model of Di Genova et al. (2013) does not predict our measurements with the same accuracy as the GRD model. Therefore, by combining viscosity data from both the literature and this study, we developed a new viscosity model for predicting peralkaline magmas viscosity, building upon the framework of Di Genova et al. (2013). Cinque Denti was not included in this parametrization, for its metaluminous character. Tab. 4.8 summarizes the glass compositions used for the new model. The analysed glasses include: Green Tuff (this work); Zinedi (this work); Cuddia Mida (this work); the low-energy Strombolian eruption Altura from Pantelleria (Anush Kazarian, PhD thesis); the sub-Plinian eruption Fastuca from Pantelleria (Anush Kazarian, PhD thesis); 8 ka, a spatter-fed pantelleritic lava flow from Mayor Island, New Zealand (Stevenson et al., 1998); Td, a crystal-free phonolitic glass from Teide, Tenerife Island, with varying water content (Giordano et al., 2000); Punta Spadillo Total Rock (PS_TR; with different water content) and Punta Spadillo GroundMass (PS_GM; with different water content), both from Di Genova et al. (2013) and FAN, a glass of pantelleritic composition from Fantale (Scarfe, 1977). These liquids all exhibit a P.I. higher than 1.

| | Green Tuff | Zinedi | Cuddia Mida | Altura | Fastuca | 8 ka | Td | PS_GM | PS_TR | FAN |
|---|---|---|---|---|---|---|---|---|---|---|
| $SiO_2$ | 70.16 | 67.22 | 70.67 | 72.27 | 69.23 | 73.94 | 60.46 | 69.21 | 69.42 | 72.76 |
| $TiO_2$ | 0.52 | 0.63 | 0.34 | 0.38 | 0.46 | 0.22 | 0.56 | 0.50 | 0.46 | 0.39 |
| $Al_2O_3$ | 8.64 | 11.85 | 5.37 | 8.90 | 9.56 | 9.68 | 18.81 | 9.18 | 10.17 | 9.30 |
| $Fe_2O_3$ | 5.09 | 4.63 | 5.11 | 4.06 | 5.17 | | | 5.46 | 4.69 | 3.87 |
| FeO | 4.58 | 4.16 | 4.60 | 3.65 | 4.65 | 5.79 | 3.31 | 3.71 | 3.72 | 3.48 |
| MnO | 0.31 | 0.30 | 0.30 | 0.27 | 0.31 | 0.13 | 0.2 | 0.32 | 0.29 | 0.26 |
| MgO | 0.17 | 0.47 | 0.16 | 0.47 | 0.27 | 0.02 | 0.36 | 0.08 | 0.07 | 0.08 |
| CaO | 0.47 | 0.67 | 0.44 | 0.38 | 0.57 | 0.25 | 0.67 | 0.60 | 0.55 | 0.37 |
| $Na_2O$ | 6.45 | 5.98 | 6.39 | 5.63 | 6.07 | 5.99 | 9.76 | 6.52 | 6.03 | 5.41 |
| $K_2O$ | 4.08 | 4.49 | 4.00 | 4.38 | 4.19 | 3.99 | 5.45 | 4.35 | 4.55 | 4.45 |
| $P_2O_5$ | 0.03 | 0.06 | 0.00 | 0.02 | 0.03 | | 0.06 | 0.04 | 0.03 | 0.02 |
| P.I. | 1.74 | 1.24 | 1.74 | 1.57 | 1.52 | 1.5 | 1.2 | 1.7 | 1.5 | 1.06 |
| AEX | 3.58 | 1.82 | 3.99 | 3.22 | 3.15 | 2.82 | 2.08 | 3.98 | 2.99 | 0.56 |

*Tab. 4.8 Dry composition, in wt%, of selected glass.*

Mol% composition, alkali excess (AEX), Peralkalinity Index (P.I.) and viscosity data for the analysed glass are reported in Supplementary Material.

Viscosity data of all samples are shown in Fig. 4.10a-b as function of temperature ranging from 613 K to 1773 K and from $10^{2.20}$ to $10^{12.28}$ Pa·s.

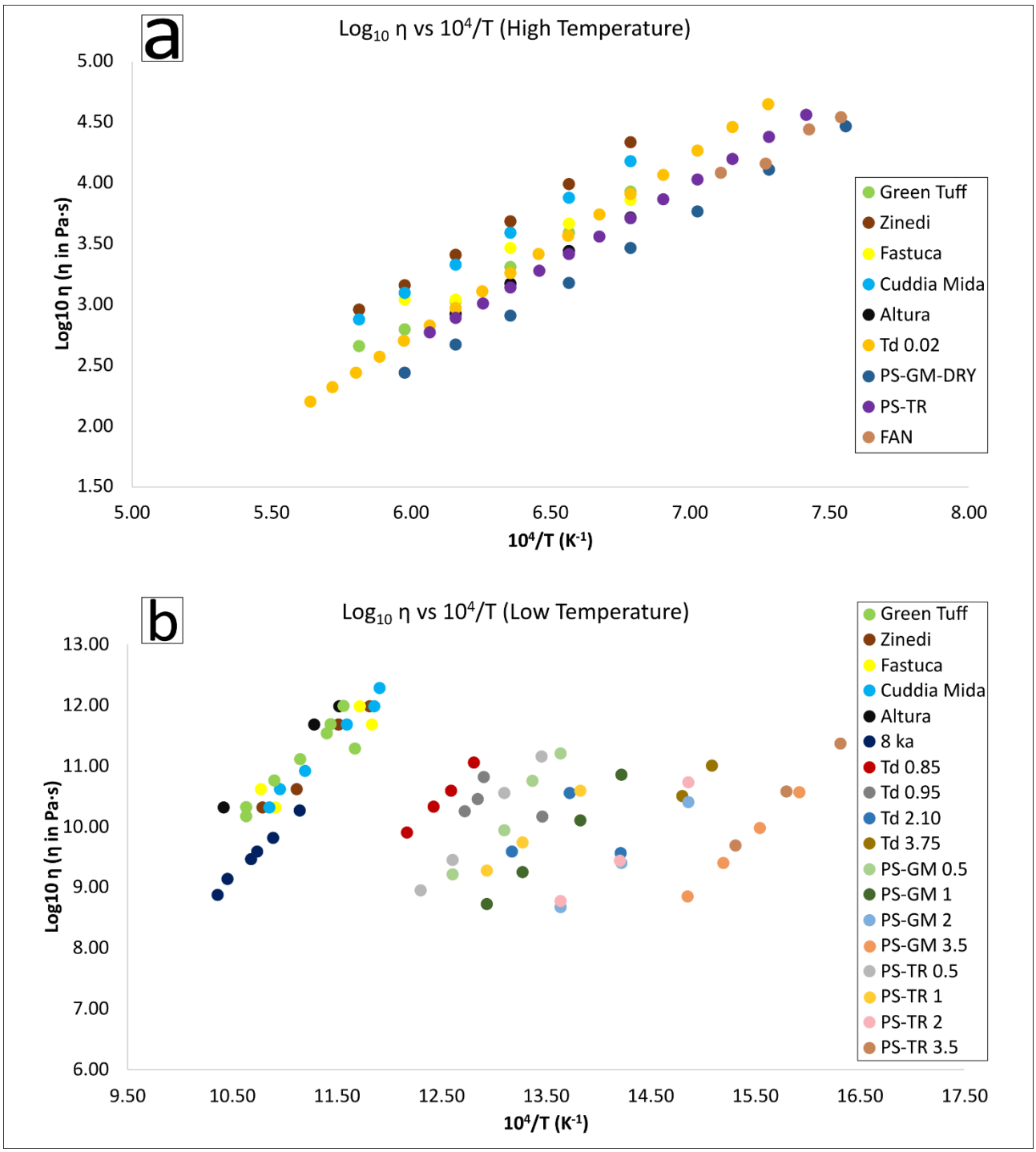


*Fig. 4.10 Melts viscosities from enlarged data set from Tab. 4.8. A. High temperature regime; B. Low temperature regime.*

The viscosity data obtained for the pantelleritic liquids here investigated were used to develop an empirical model capable of predicting melt viscosity as a function of temperature, water content and P.I.. Initially, we compared the newly

expanded dataset with viscosity values derived from the empirical models of Giordano et al. (2008) (GRD) and Di Genova et al. (2013).

In Fig. 4.11, the measured viscosities of the enlarged dataset are compared with those predicted by the GRD model. Substantial discrepancies are observed between the measured values and those calculated by this model, highlighting the need for an updated parametrization for peralkaline melts.

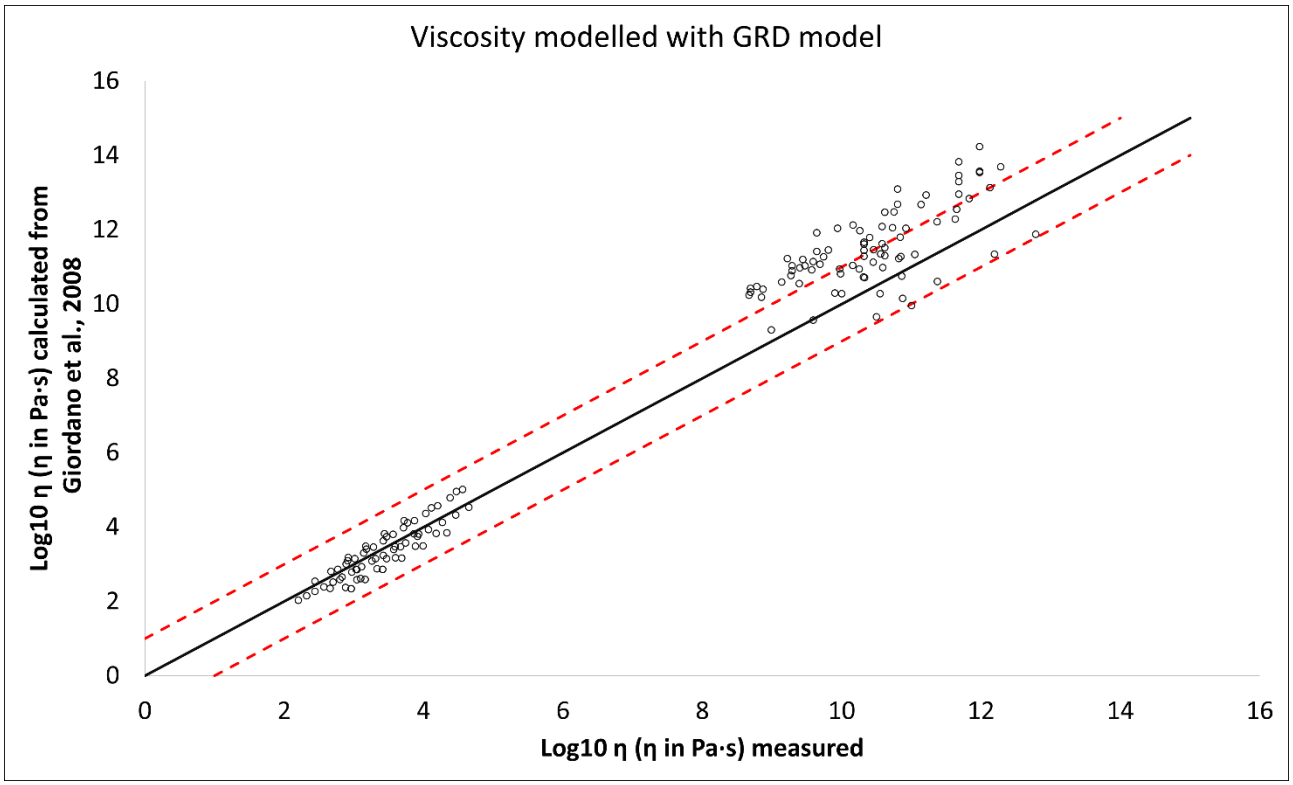


*Fig. 4.11 Comparison between measured and calculated viscosities from Giordano et al. (2008). Black and red dashed line have the same function as explained above.*

In the high-temperature, low-viscosity regime, the GRD model slightly underestimates enlarged dataset, with a root-mean-square error (RMSE) of 0.20 log units. At low temperatures, however, the GRD model substantially overestimates the measured viscosities, resulting in an RMSE of 1.04 log units. The overall RMSE for the entire dataset modelled with the GRD approach is 1.06 log units. Fig. 4.12 presents a comparison between the measured viscosities of the expanded dataset and those predicted by the Di Genova et al. (2013) model. Significant discrepancies are observed between the measured and calculated viscosities, again attributable to the limited peralkaline dataset available in the original Di Genova et al. (2013) parametrization study.

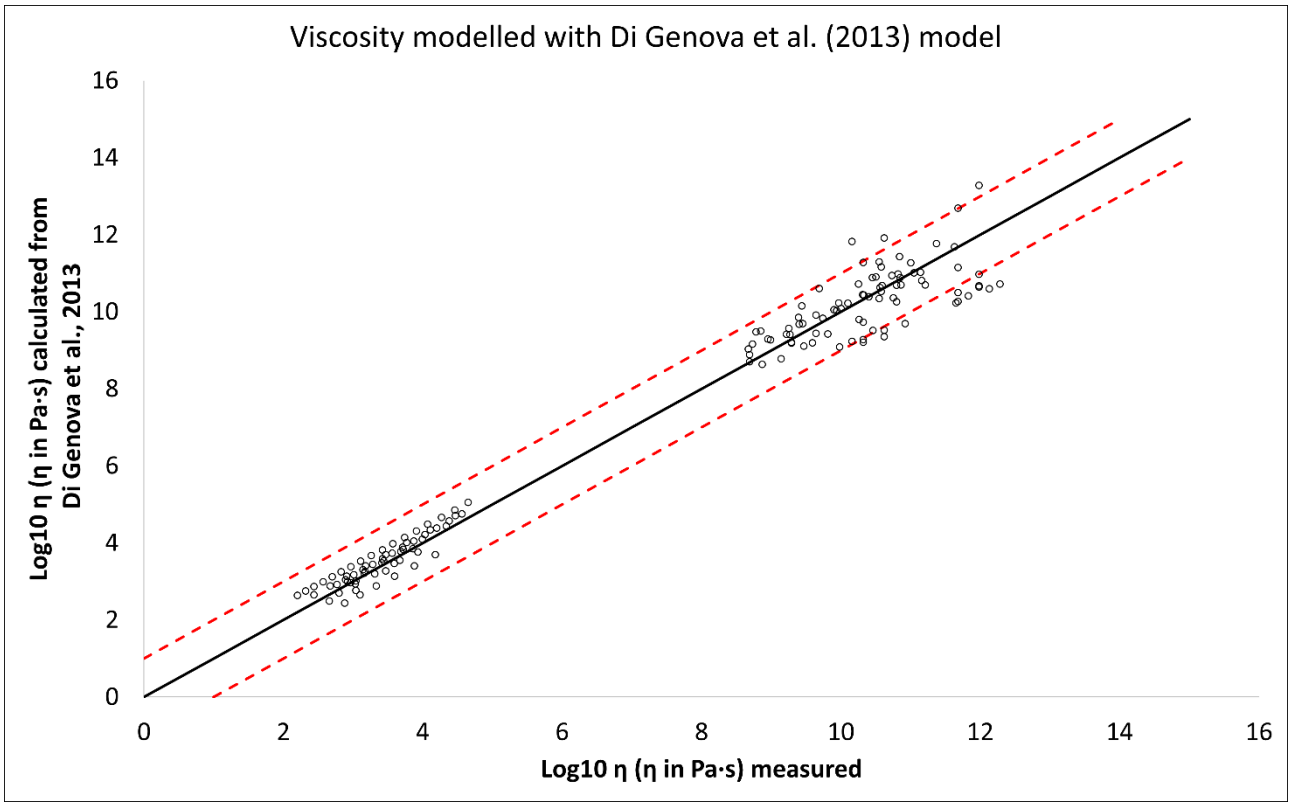


*Fig. 4.12 Comparison between measured and calculated viscosities from Di Genova et al. (2013). Black and red dashed line have the same function as explained above.*

In the high-temperature, low-viscosity regime, Di Genova et al. (2013) model slightly overestimates our data, with a root-mean-square error (RMSE) of 0.20 log units. At low temperatures, the model exhibits a larger misfit, with an RMSE of 0.54 log units. The overall RMSE for the entire dataset using the Di Genova et al. (2013) parametrization is 0.57 log units. The limited accuracy of viscosity predictions provided by both the GRD and Di Genova et al. (2013) models suggests that certain chemical parameters were not fully constrained, emphasizing the need for an updated empirical model for peralkaline melts. Much effort has been devoted to the study of the temperature-pressure-composition dependence of the structure of silicate melts and to its effects on melt viscosity through structure property models (Bottinga and Weill, 1972; Richet, 1984; Mysen, 1988; Giordano and Dingwell, 2003; Giordano et al., 2008). One chemical parameter that strongly affects the chemical and physical properties of silicate melts is the abundance and distribution of the alkaline and alkaline earth cations. All mono and divalent cations perform distinguishable roles as either network modifiers or charge balancers depending on the relative abundance and the overall chemical composition of the melt. GRD model is constructed on an empirical basis, simplifying the parameterization of the melt

composition for the purpose of predicting viscosity, without clearly considering the different distributions and roles of the cations in the melt. For chemical compositions with a particular abundance of such cations, like pantelleritic melts, or peralkaline melts in general, this model is more prone to failure. In addition to that, the overestimation produced by the GRD model may stem from the dataset used for the original parameterization. Although Giordano et al. (2008) employed a large and robust dataset, many of the low-temperature, high-viscosity experimental data were likely affected by nanocrystalization processes, as discussed above, processes particularly effective in peralkaline, low-viscosity magmas. This may have led to predicted viscosities significantly higher than those actually expected in this viscosity regime. Di Genova et al. (2013) model, on the other hand, underscored the importance of alkali in influencing melts viscosity, even though suffering from a limited viscosity dataset. For this reason, Di Genova et al. (2013) proposed the following equation in which viscosity is expressed as a function of temperature, water content and alkali-excess (AEX) in mol%. Eq. 4.2 is Di Genova et al. (2013) proposed equation for modelling peralkaline magmas viscosity.

$$log\eta = A_{VFT} + \frac{b_5 + b_6 \times \log(1 + H_2O)}{T - \left[\frac{c_5 + c_6 \times \log(1 + H_2O)}{AEX}\right]} \quad (4.2)$$

where the parameter $A_{VFT}$ is a constant independent of composition (Richet and Bottinga, 1985; Whittington et al., 2012) and has a value of −4.55 (Giordano et al., 2008a), $b_5$, $b_6$, $c_5$ and $c_6$ are fitting parameters, T is the temperature in K and $H_2O$ is the water concentration in mol% and AEX is the alkali excess in mol%. Best-fit values and standard deviations of the fitting parameters in Eq. (4.2) are reported in Tab. 4.9.

| | |
|---|---|
| $A_{VFT}$ | -4.55 |
| $b_5$ | 11442.32 (±121.09) |
| $b_6$ | -2708 (±250.42) |
| $c_5$ | 384.91 (±27.28) |
| $c_6$ | -128.38 (±58.00) |

*Tab. 4.9 Fit parameters for Eq. 4.2. Numbers in parentheses are standard deviations.*

Here, we introduce a new equation for modelling the viscosity of peralkaline magmas, derived from a modified form of Di Genova et al. (2013). In Fig. 4.13, the

measured viscosities of the enlarged data set presented in this work are compared with those predicted by our new model.

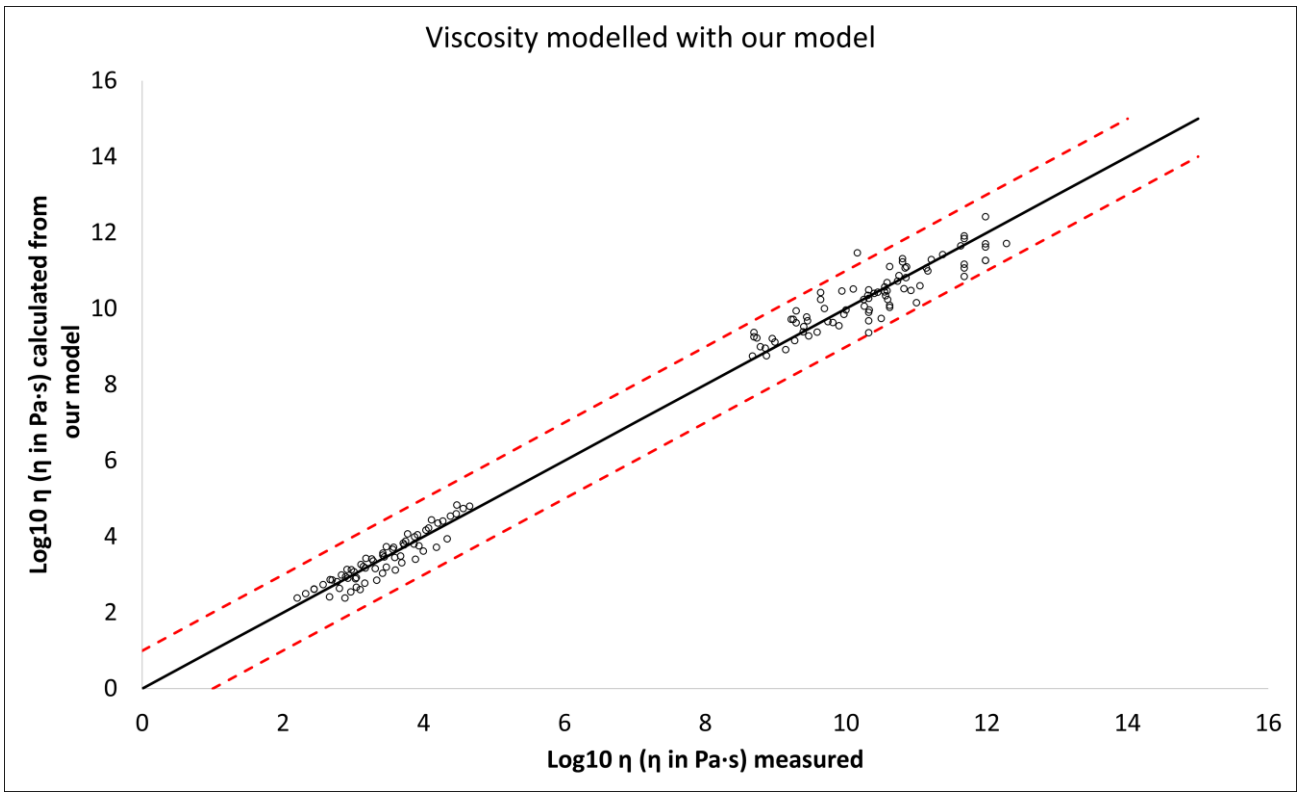


*Fig. 4.13 Comparison between measured and calculated viscosities from our model. Black and red dashed line have the same function as explained above.*

In the high-temperature low-viscosity regime, our model predicts data set with a RMSE of 0.19 log unit. At low temperatures, our model predicts data set with a RMSE of 0.33 log unit. The total RMSE for modelling our data set with our model is 0.36 log unit. In the new parameterization viscosity is expressed as a function of temperature, $H_2O$ and P.I.. Eq. 4.3 is the proposed equation for modelling peralkaline magmas viscosity.

$$log\eta = A_{VFT} + \frac{b_5 + b_6 \times log(1 + H_2O)}{T - \left[\frac{c_5 + c_6 \times log(1 + H_2O)}{\sqrt{P.I.}}\right]} \quad (4.3)$$

where the parameter $A_{VFT}$ is a constant independent of composition (Richet and Bottinga, 1985; Whittington et al., 2012) and has a value of −4.55 Pa·s (Giordano et al., 2008a), $b_5$, $b_6$, $c_5$ and $c_6$ are fitting parameters, T is the temperature in K, $H_2O$ is the water concentration in mol% and P.I. is the Peralkalinity Index. Best-fit values of the fitting parameters in Eq. (4.2) are reported in Tab. 4.10.

| | |
|---|---|
| $A_{VFT}$ | -4.55 |
| $b_5$ | 10763,0916639853 |
| $b_6$ | -3856,00433351342 |
| $c_5$ | 243,914003764948 |
| $c_6$ | -0,000506116899205378 |

*Tab. 4.10 Fit parameters for Eq. 4.3.*

We identified the Peralkalinity Index P.I. as the primary parameter controlling viscosity variations with temperature among anhydrous and hydrous pantelleritic liquids. Both in the high-temperature and low-viscosity regime and , in the low temperature-high viscosity regime, our model outperforms Di Genova et al. (2013) model, reducing the discrepancies observed in the original parametrization. Di Genova et al. (2013) emphasized the importance of both topological and chemical contributions to magma viscosity at low temperatures, which are challenging to quantify (Richet and Neuville, 1992; Toplis et al., 1997; Romano et al., 2001; Giordano et al., 2009). By better approximating these effects, our model achieves improved predictions, with a root-mean-square error of 0.36 log units compared to root-mean-square error of 0.57 log units for the Di Genova et al. (2013) model, demonstrating enhanced accuracy in modelling the viscosity of peralkaline magmas. Comparison of RMSE between our model and Di Genova et al. (2013) model is illustrated in Tab. 4.11.

| | Di Genova et al. (2013) model | Our model |
|---|---|---|
| RMSE High-T | 0.20 | 0.19 |
| RMSE Low-T | 0.54 | 0.33 |
| RMSE | 0.57 | 0.36 |

*Tab. 4.11 Comparison of RMSE between our model and Di Genova et al. (2013) model*

In Fig. 4.13-14-15-16-17 the viscosity modelling of the eruptions studied in this work are illustrated.

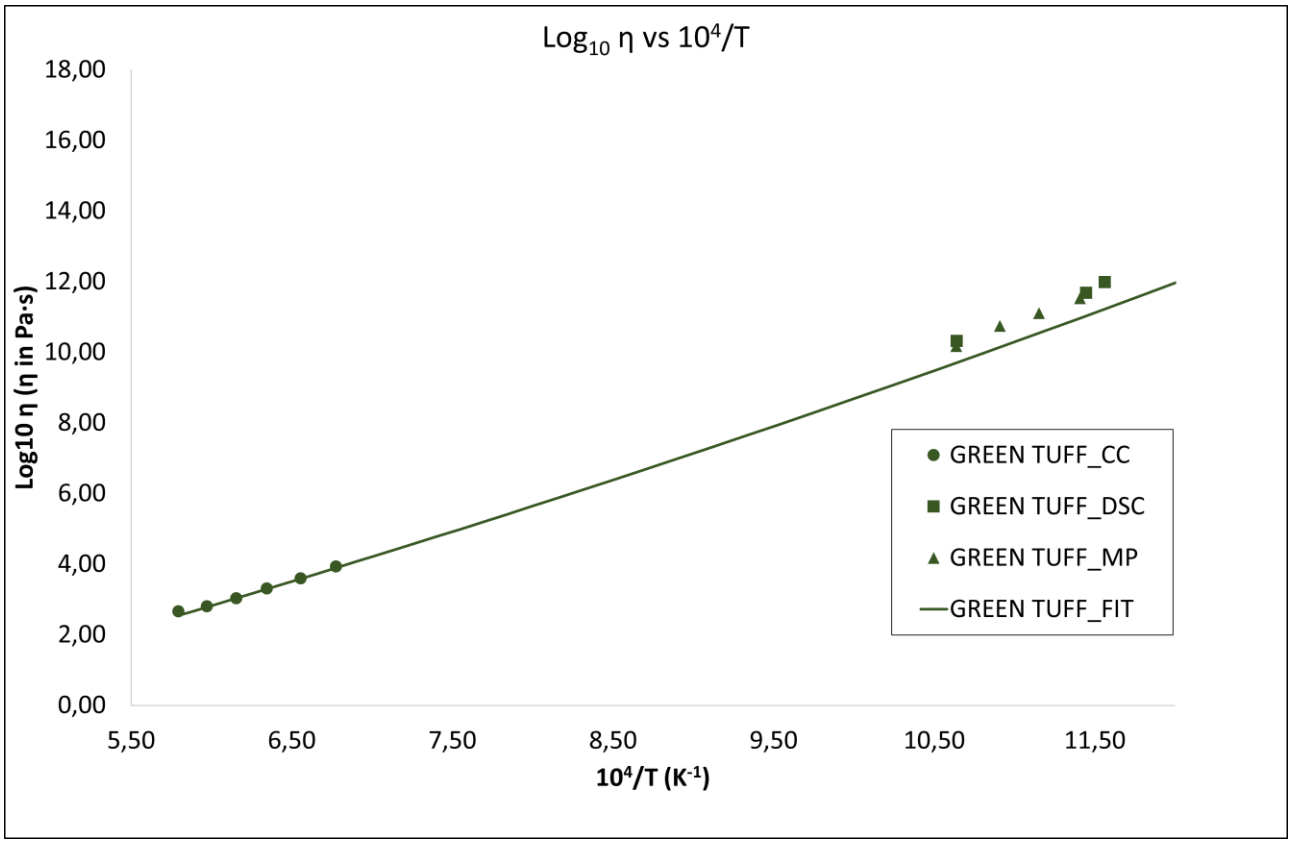


*Fig. 4.13 Measured viscosity data from low and high temperature (CC-circle) and low temperature (DSC-square; MP-triangle) and fitting curve with new parametrization for predicting peralkaline magma viscosity for Green Tuff eruption.*

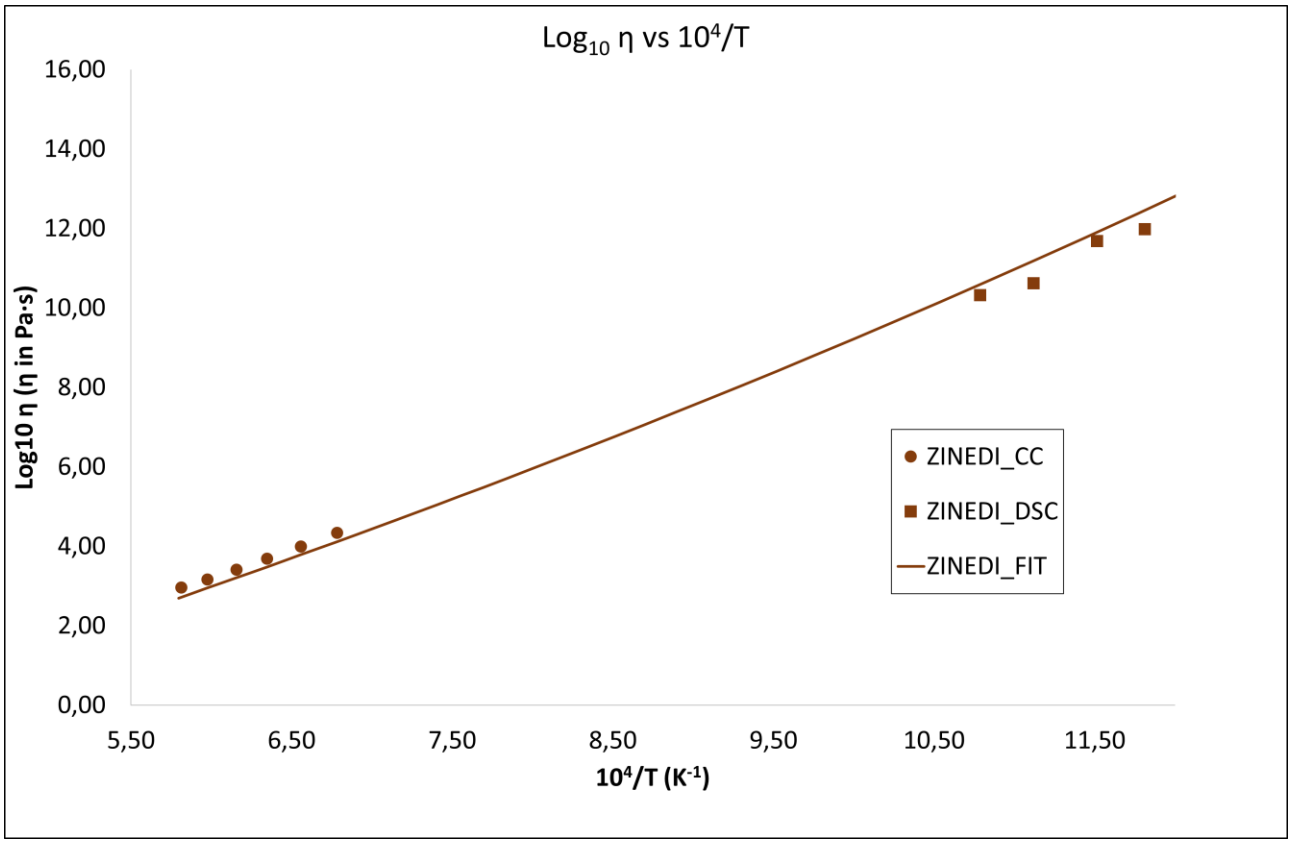


*Fig. 4.14 Measured viscosity data from low and high temperature (CC-circle) and low temperature (DSC-square) and fitting curve with new parametrization for predicting peralkaline magma viscosity for Zinedi eruption.*

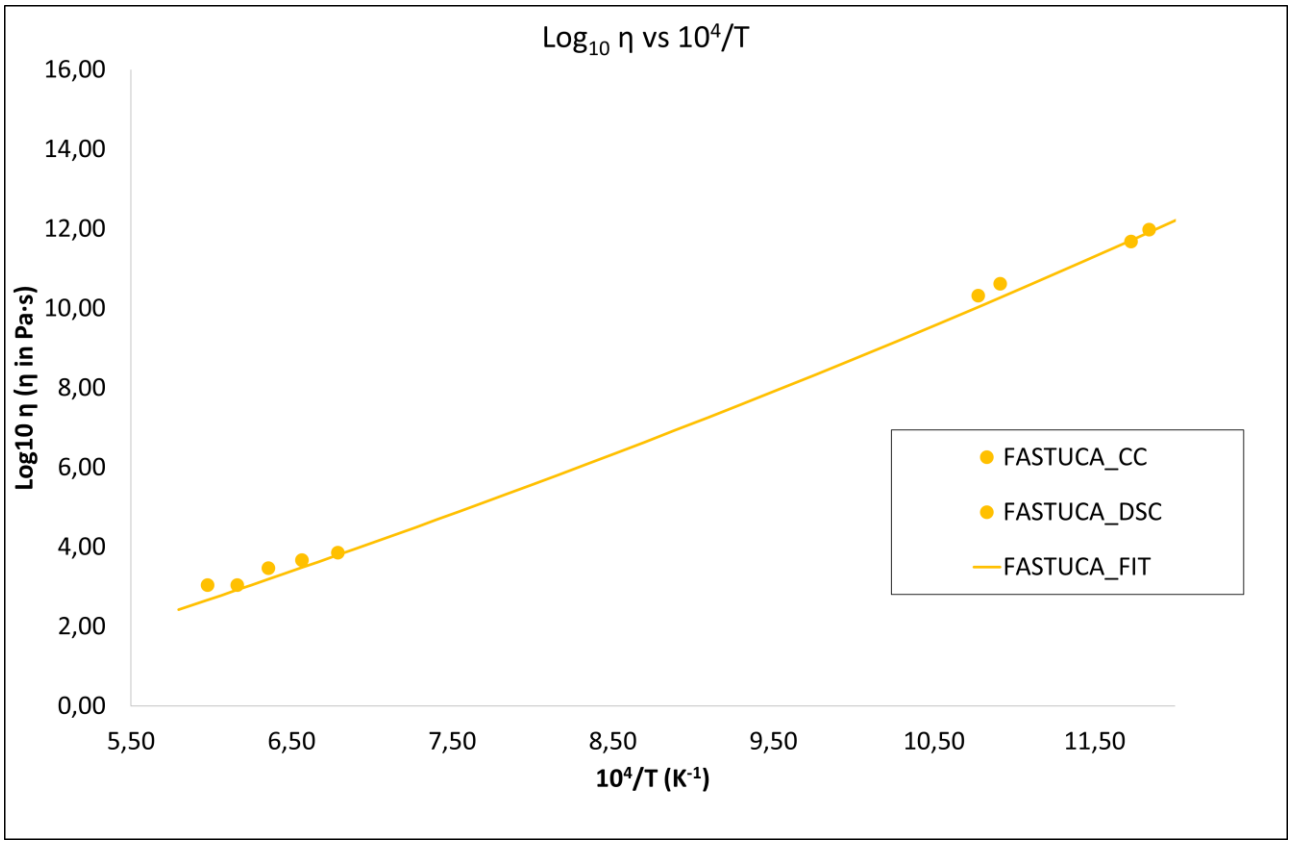


*Fig. 4.15 Measured viscosity data from low and high temperature (CC-circle) and low temperature (DSC-square) and fitting curve with new parametrization for predicting peralkaline magma viscosity for Fastuca eruption.*

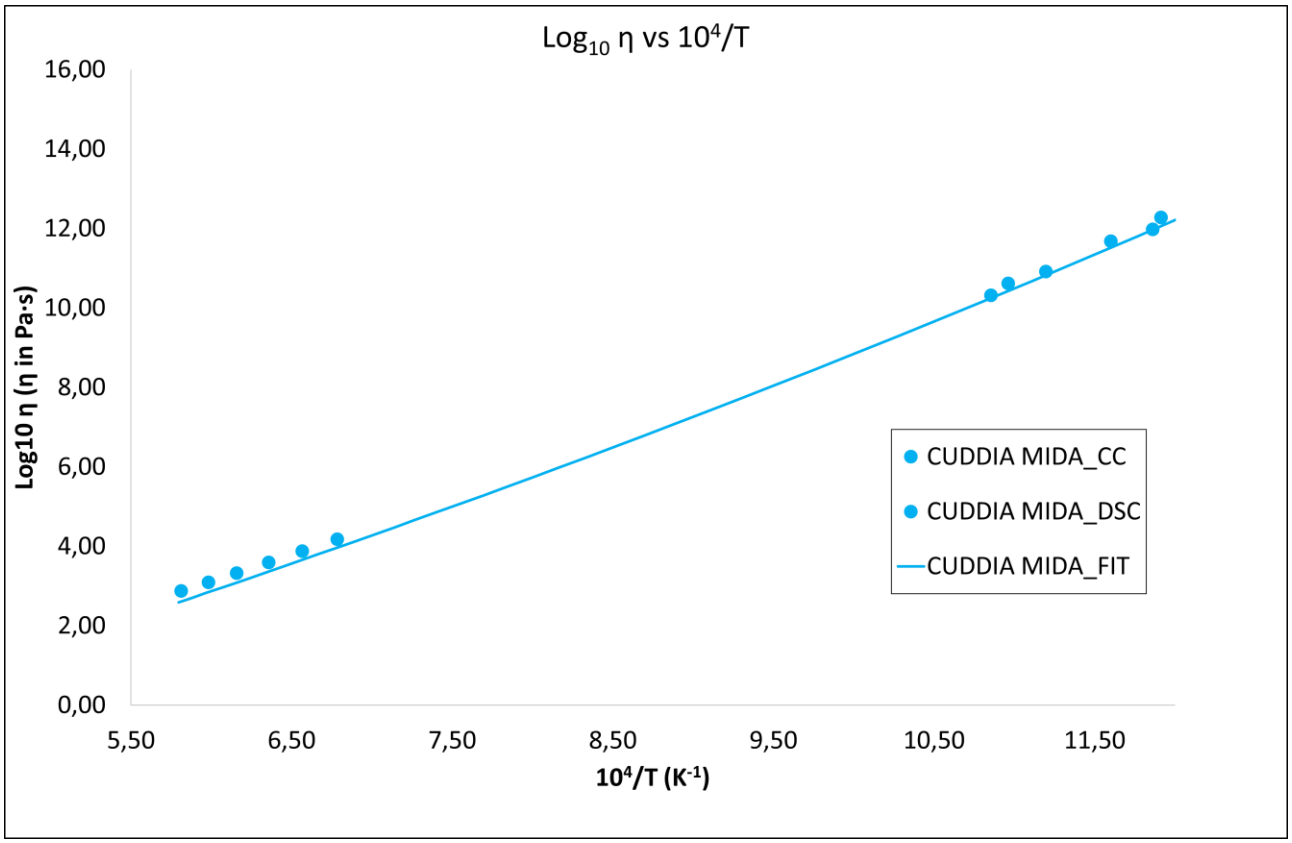


*Fig. 4.16 Measured viscosity data from low and high temperature (CC-circle) and low temperature (DSC-square) and fitting curve with new parametrization for predicting peralkaline magma viscosity for Cuddia Mida eruption.*

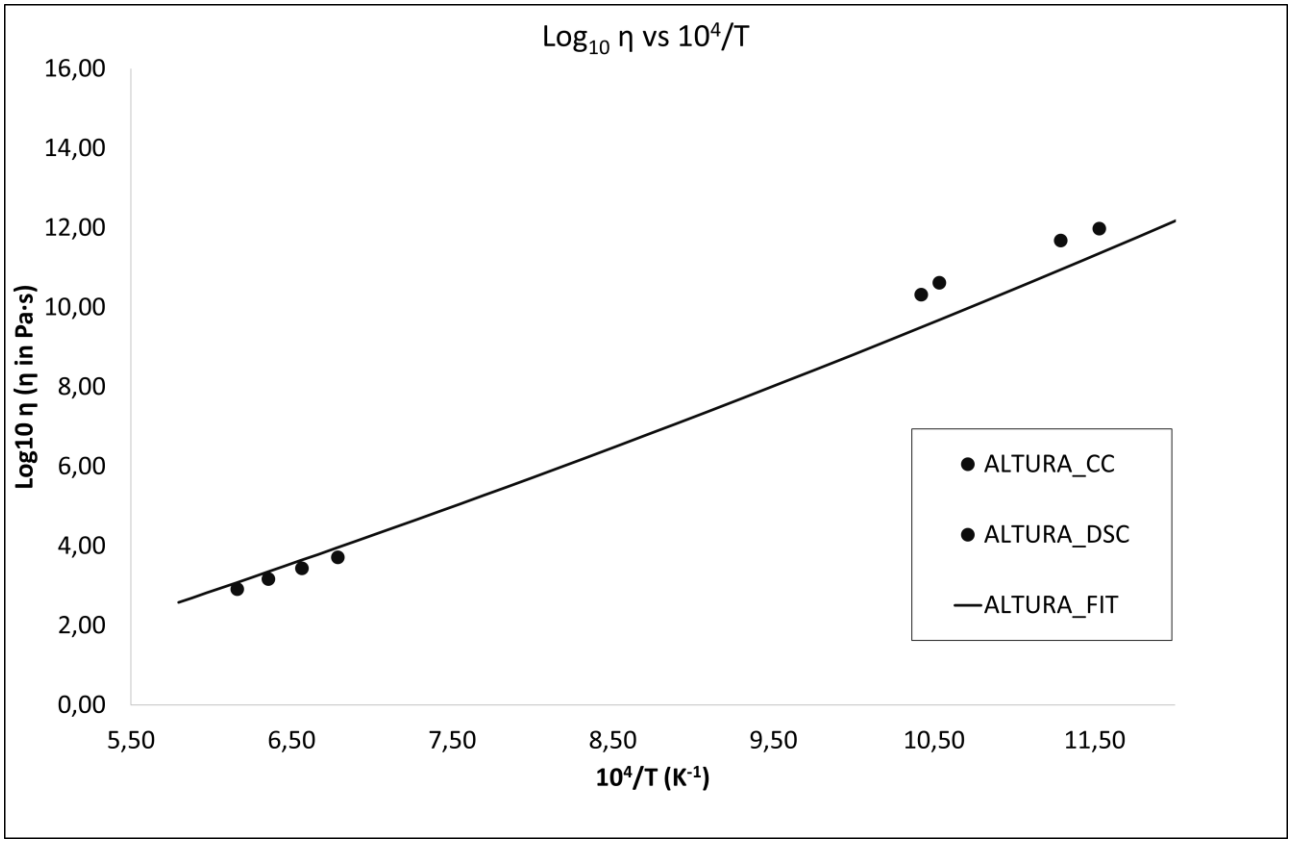


*Fig. 4.17 Measured viscosity data from low and high temperature (CC-circle) and low temperature (DSC-square) and fitting curve with new parametrization for predicting peralkaline magma viscosity for Altura eruption.*

The new model developed in this study reproduces our experimental data with generally good accuracy. However, for the Green Tuff and Altura eruptions a maximum deviation of approximately 0.5 log units is observed in the low temperature high-viscosity regime. In particular, the model systematically underestimates the measured viscosities for these samples. As illustrated in Fig. 4.10, the new parameterization incorporates a substantial number of hydrous compositions. This inevitably shifts the calibration toward lower viscosity values. As a result, the proposed parameterization tends to slightly underestimate our experimental dataset. Viscosity measurements can be correlated with selected chemical parameters of the melts, such as NBO/T and P.I.. Fig. 4.18 illustrates the relationship between the viscosity from new equation fit, at both high (1450 °C–1675 K) and low (625 °C–900 K) temperatures, and NBO/T, which quantifies the degree of polymerization or depolymerization of the silicate network, expressed as the ratio between non-bridging oxygens and tetrahedral cations. No clear relationship between viscosity and NBO/T is observed.

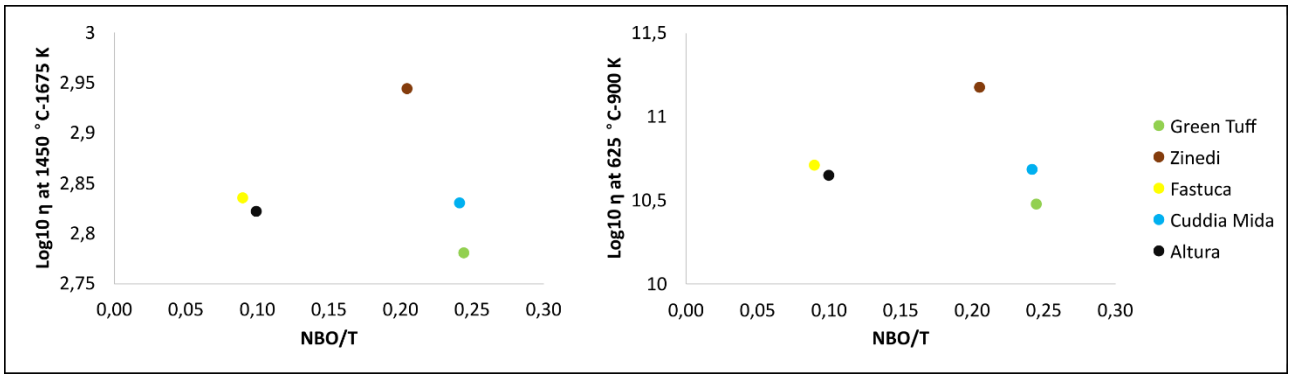


*Fig. 4.18 Viscosity-NBO/T relationship at high temperature-low viscosity (1450 °C - 1675 K) regime and at low-temperature-high viscosity (625 °C - 900 K).*

P.I. [$(Na_2O+K_2O)/Al_2O_3$] is a key chemical parameter for characterizing peralkaline magmas. Higher P.I. values indicate an excess of alkali relative to alumina, leading alkali to act as structural modifiers within the silicate network. Fig. 4.19 illustrates the relationship between viscosity from new equation fit, at both high (1450 °C–1675 K) and low (625 °C–900 K) temperature and the P.I.. A clear correlation emerges: melts with higher P.I. values exhibit lower viscosities, consistent with a more depolymerized silicate structure, whereas lower P.I. values correspond to more polymerized and thus more viscous melts. Again, although the five eruptions studied show only minor differences in viscosity and P.I. values, a consistent trend between these parameters is evident (Fig. 4.19).

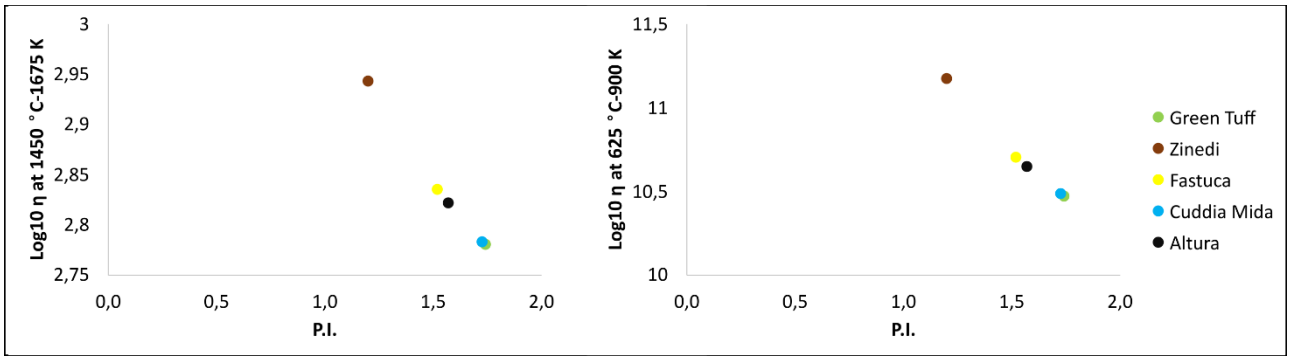


*Fig. 4.19 Viscosity-P.I. relationship at high temperature-low viscosity (1450 °C - 1675 K) regime and at low-temperature-high viscosity (625 °C - 900 K).*

# 5. Conduit dynamic model

## 5.1 MAMMA model

In order to reconstruct the ascent dynamics of magma through the conduit and discriminate the difference in eruptive conditions for Cinque Denti, Green Tuff, Zinedi, Fastuca, Cuddia Mida and Altura eruptions, we performed numerical simulations using MAMMA model, a Fortran written model from La Spina et al. (2021, 2022).

### 5.1.1 Governing equation of the 1D steady-state magma ascent model

MAMMA is a 1D steady-state FORTRAN written model for magma ascent in a cylindrical conduit described by La Spina et al., 2021. During magma ascent several processes are taking place at the same time, such as temperature changes, viscosity evolution, non-ideal gas behaviour, outgassing and both disequilibrium crystallisation and exsolution. This model can solve for all these processes for each depth of the conduit at once. The magmatic mixture is considered as a two-phase multicomponent compressible fluid. From the inlet of the conduit up to the fragmentation level, magma is assumed as a mixture of a liquid phase and a gas phase. The liquid phase (indicated by the subscript l) is made of a mixture of melt (subscript m), crystals (subscript c) and different dissolved gas components (subscript d). The gas phase (subscript g) represents bubbles of various exsolved gas components. If fragmentation occurs within the conduit, a transition from a bubbly-flow/permeable-flow regime towards a gas-ash flow regime is considered. Above that point up to the vent of the conduit magma is assumed to be a mixture of a dispersed particle phase (still indicated by subscript l) and a continuous gas phase. To characterise and describe each of the two phases and each component within each phase we use several parameters, i.e. the volume fraction ($\alpha_k$), mass density ($\rho_k$), mass fraction ($x_k$), velocity ($u_k$), specific internal energy ($e_k$), specific entropy ($s_k$), pressure ($P_k$) and temperature ($T_k$). We assume that all components within each phase have the same pressure, temperature and velocity (i.e. $P_m = P_{cj} = P_{di} = P_l$ and $P_{gi} = P_g$, and analogously for the temperature and velocity). Furthermore, the saturation constraints of $\alpha_l + \alpha_g = 1$ and $x_l + x_g = 1$ hold all along the conduit. Using the notations described previously, the mixture parameters can be defined as follows:

$$P = \alpha_1 P_1 + \alpha_g P_g \ (5.1);$$

$$\rho = \alpha_1 \rho_1 + \alpha_g \rho_g \ (5.2);$$

$$T = \alpha_1 T_1 + \alpha_g T_g \ (5.3);$$

$$x_1 = \frac{\alpha_1 \rho_1}{\rho} \ (5.4);$$

$$x_g = \frac{\alpha_g \rho_g}{\rho} \ (5.5);$$

$$u = x_1 u_1 + x_g u_g \ (5.6);$$

$$e = x_1 e_1 + x_g u_g \ (5.7);$$

$$s = x_1 s_1 + x_g s_g \ (5.8).$$

The magma ascent model allows for relative motion and overpressure between the two phases of the magmatic mixture, which are governed by corresponding relaxation parameters (described afterwards). The temperature of the two phases, instead, is assumed to be in equilibrium (but not constant within the conduit) between the two phases. The conservation equations for the mixture mass and momentum read as:

$$\frac{\partial}{\partial z}[\rho u] = 0, \ (5.9)$$

$$\frac{\partial}{\partial z}\left[\sum_{k=l,g} \alpha_k \rho_k u_k^2 + \alpha_k P_k\right] = -\rho g - f_{D_l} \frac{\rho_l u_l^2}{4r}(1 - \phi_f) - f_{D_g} \frac{\rho_g u_g^2}{4r} \phi_f \ (5.10).$$

where g is the gravitational acceleration, r is the conduit radius (assumed to be fixed from depth up to the surface), $\phi_f$ is a binary variable indicating whether fragmentation is met within the conduit or not, and $f_{Dl}$ and $f_{Dg}$ are the Darcy–Weisbach friction factors, which are dependent on the conduit wall roughness and the Reynolds number (following the empirically-derived Moody diagram). The mixture energy equation is formulated following Zein et al. (2010):

$$\frac{\partial}{\partial z}\left[\sum_{k=l,g} \alpha_k \rho_k u_k \left(e_k + \frac{P_k}{\rho_k} + \frac{u_k^2}{2}\right)\right] = -\rho g u \ (5.11)$$

The liquid volume fraction along the conduit is governed by the following transport equation:

$$\frac{\partial}{\partial z}[\rho \alpha_l u] = -\frac{1}{\tau^{(p)}}(P_g - P_l) \quad (5.12)$$

The relaxation parameter $\tau^{(p)}$ ($m^2\ s^{-1}$) defines the overpressure between gas and liquid phase. Following La Spina et al. (2021) is reasonable to assume pressure equilibrium between the two phases, obtained by setting $\tau^{(p)} = 10^{-5}\ m^2\ s^{-1}$. The following partial differential equations are adopted to describe each exsolved gas component and the corresponding dissolved contents:

$$\frac{\partial}{\partial t}\left[\alpha_{g_i}\rho_{g_i}\right] + \frac{\partial}{\partial z}\left[\alpha_{g_i}\rho_{g_i}u_g\right] = \frac{1}{\tau^{(e)}}\left(x_{d_i,m} - x_{d_i,m}^{eq}\right)\alpha_m\rho_m \quad (5.13);$$

$$\frac{\partial}{\partial t}\left[\alpha_m\rho_m x_{d_i,m}\right] + \frac{\partial}{\partial z}\left(\alpha_m\rho_m x_{d_i,m}u_l\right) = -\frac{1}{\tau^{(e)}}\left(x_{d_i,m} - x_{d_i,m}^{eq}\right)\alpha_m\rho_m \quad (5.14)$$

where $x_{d_i,m}$ is the mass fraction of the dissolved gas phase i with respect to the melt crystal–free component m, while $x_{d_i,m}^{eq}$ is the value at equilibrium. Since the mass fraction of the dissolved gas is always referred to the melt component, for simplicity authors omit the subscript m from its notation ($x_{d_i}$ and $x_{d_i}^{eq}$). The characteristic time $\tau^{(e)}$ (s) controls the exsolution rate and thus controls how close the dissolved gas mass fraction is to the equilibrium value. The variations of the volume fractions of each crystal component are governed by:

$$\frac{\partial}{\partial z}\left(\alpha_l\rho_{c_j}\beta_{c_j}u_l\right) = -\frac{1}{\tau^{(c)}}\alpha_l\rho_{c_j}\left(\beta_{c_j} - \beta_{c_j}^{eq}\right) \quad (5.15).$$

Here $\beta_j$ is the volume fraction of the crystal component j while $\beta_{c_j}^{eq}$j is the same physical quantity at equilibrium. As for exsolution of gas, the crystallisation rate is governed by the characteristic time $\tau^{(c)}$ (s). Following Arzilli et al. (2019) disequilibrium crystallisation is taken into account assuming a constant characteristic time $\tau^{(c)} = 10$ s. Finally, the relative motion between the two phases is controlled by the following partial differential equation:

$$\frac{\partial}{\partial z}[\Delta u] + \frac{\partial}{\partial z}\left[\frac{u_l^2}{2} - \frac{u_g^2}{2} + e_l + \frac{P_l}{\rho_l} - e_g - \frac{P_g}{\rho_g} - (s_l - s_g)T\right] =$$
$$-\frac{1}{\tau^{(f)}}\frac{\rho}{\rho_l\rho_g}(u_l - u_g) - f_{D_l}\frac{u_l^2}{4\alpha_l r}(1 - \phi_f) + f_{D_g}\frac{u_g^2}{4\alpha_g r}\phi_f \quad (5.16).$$

The degree of decoupling between the gas and the liquid phase is governed by a relaxation parameter $\tau^{(t)}$ ($kg^{-1}\ m^3\ s$). A detailed description of how $\tau^{(t)}$ is calculated within the conduit can be found afterwards.

### 5.1.2 Constitutive equations and equations of state

To simulate the magma ascent dynamics of the six eruptions studied, we adopted specific constitutive equations, such as rheological, crystallisation, wall friction, outgassing, fragmentation, and solubility models. The viscosity of the liquid phase (i.e. magma viscosity) is calculated as following:

$$\mu_l = \mu_{melt} \cdot \theta_c \cdot \theta_b \ (5.17)$$

where $\mu_{melt}$ is the viscosity of the bubble-free, crystal-free liquid phase, $\theta_c$ is a factor which increases viscosity due to the presence of crystals and $\theta_b$ is a factor taking into account the effect of bubbles on the magmatic mixture. To estimate the viscosity of the pure melt $\mu_{melt}$ , the authors propose different viscosity model taken from literature. We performed a first set of simulations using viscosity models from Giordano et al. (2008) and Di Genova et al. (2013). As a result, our melts did not reach fragmentation as the viscosity models do not replicate pure melt viscosity as shown in Discussion. For this reason, we improved MAMMA model potential by using our viscosity model in order to better replicate pure melt viscosity. The presence of crystals in the magmatic mixture produces a localization of the stress in the surrounding liquid. An approximation of the localization of the stress due to the presence of crystals, $\theta_{c,}$ in the magmatic mixture is given by the following relation (Cordonnier et al., 2012; Wadsworth et al., 2017):

$$\dot{\gamma} = \frac{\dot{\gamma}_m}{\left(1 - \beta/\beta_{pack}\right)} \ (5.18)$$

where $\dot{\gamma}_m$ is the strain-rate of the melt phase and $\beta_{pack}$ is the maximum packing fraction of the system. Regarding $\theta_{c,}$ we decided to set is as constant and equal to 1 because we did not observe micro- or nano- crystals in pumices thin sections. For this reason, we assumed that there is no crystallization during magma ascent as all crystals observed were listed as phenocrysts and already presents at the moment of the eruption. In a liquid mixture, the variation in viscosity due to the presence of bubbles depends on bubble response to shear stresses. Bubbles that remain spherical and undeformed serve to increase effective viscosity of the magma whereas those that deform easily serve to decrease effective viscosity (Llewellin et al. 2002; Llewellin and Manga 2005; Mader et al. 2013). This bubble response can be described by the capillary

number $Ca$, a dimensionless number representing the ratio between the viscous stress acting on the bubble and the restoring stress supplied by the surface tension. We adopted the general formulation for relative viscosity due to the presence of bubbles in a magmatic mixture presented by Llewellin et al. (2002) in a high capillary number regime because vesicles are strongly deformed as shown in Results. We used the theoretical model proposed by Pal (2003) for bubble-bearing melts to obtain the simplified following equation from Llewellin and Manga (2005):

$$\eta_r = (1-\varphi)^{\frac{5}{3}} \quad (5.19)$$

Where $\varphi$ is the gas volume fraction. An important role in affecting eruptive dynamics simulation in MAMMA model is attribute to Vesicle Number Density (VND) value. VND, in MAMMA model, is used to calculate magma-gas friction following equations from Degruyter et al. (2012). Moreover, VND is also used to simulate the effect of bubbles in magma-gas mixture viscosity (Eq. from Mader et al., 2013). As a consequence, VND affects the fragmentation threshold according to the fragmentation criterion (strain-rate criterion, Papale, 1999) used in this work (see next paragraph).

### 5.1.3 Fragmentation model

Here we consider fragmentation caused by rapid acceleration of magma in response to a downward-propagating decompression event. Fragmentation by rapid acceleration is initiated at depth, for example by intrusion of new hotter magma. This rapid acceleration results in a large elongational strain-rate of magma, that may cause fragmentation. Webb and Dingwell (1990) showed that magma fragmentation occurs when the Deborah number, which is ratio between the Maxwell relaxation time and the timescale of deformation, exceeds 0.01:

$$De = \frac{\tau_{rel}}{\tau_{def}} = \frac{\left(\frac{\mu_{melt}}{G_\infty}\right)}{\left(\frac{1}{\dot{\gamma}}\right)} \geq 0.01 \quad (5.20)$$

In this equation, μ is the viscosity of the melt, $G_\infty$ is the elastic modulus ($10^{10}$) in the pure elastic regime, and γ is the strain-rate. In MAMMA model, fragmentation equation, also considering the effect on viscosity of crystals is:

$$De_c = \left(\frac{\mu_{melt}}{G_\infty}\right)\frac{\dot{\gamma}_m}{\left(1-\beta/\beta_{pack}\right)} \geq 0.01 \ (5.21)$$

As explained above, the term $\frac{\dot{\gamma}_m}{(1-\beta/\beta_{pack})}$ is set as constant and equal to 1. For this reason, fragmentation occurs when the product of strain rate times viscosity reach a value of $10^8$ Pa. However, the presence of bubble weakens the mechanical strength of magmas and favours its fragmentation at a lower Deborah number. To take into account this effect, we implemented MAMMA numerical code by introducing the effect of bubble as following:

$$De_c = \left(\frac{\mu_{melt}}{G_\infty}\right)\frac{\dot{\gamma}_m}{\left(1-\beta/\beta_{pack}\right)}(1-\varphi)^{\frac{5}{3}} \geq 0.01 \ (5.22)$$

### 5.1.4 Boundary conditions and calculation of the solution

To calculate the numerical solution of the 1D steady-state model for magma ascent, boundary conditions have to be defined. At the inlet of the conduit, parameters are set as the initial pressure, temperature, total content of volatiles (water and/or carbon dioxide) and the initial crystal content (phenocryst content). At the vent of the conduit, instead, two boundary conditions are allowed: atmospheric pressure (0.1 MPa) and/or choked flow condition. The choked flow condition is met when the mixture velocity is equal to the speed of sound of the mixture (i.e. when the Mach number is equal to 1). For our purpose, we selected a chocked flow condition, which occurs when the geometry of the conduit is approximated as cylindrical, as in this case. In this case, the pressure at the vent of the conduit may be greater than the atmospheric pressure. The speed of sound of the mixture is calculated using the following equation:

$$C = \frac{1}{\sqrt{K\rho}} \ (5.23)$$

where $K=\alpha_l K_l + \alpha_g K_g$ is the compressibility of the mixture. The numerical solutions are calculated integrating all the system of partial differential equations coupled with appropriate constitutive equations, equations of state and boundary conditions, from the inlet of the conduit up to the vent. Specifically, the numerical solution is computed using a shooting technique, which consists of searching for the initial magma ascent velocity that satisfy the boundary conditions at the vent of the conduit (i.e. atmospheric pressure or choked flow condition). Furthermore,

when the solution begins to be highly non-linear the numerical solver refines automatically the step-size of integration. With a decrease in step-size, however, the approximation of the derivatives may introduce truncation errors due subtractive cancellations in the approximations, causing instabilities and difficulties in converging to the correct solution. To overcome this problem, we used a reliable method for calculating the derivatives, which is based on complex functions. This has been described in La Spina et al. (2017). By adopting the complex step derivative approximation, the step-size of integration can be as small as required, with no further numerical errors introduced in the solutions.

## 5.2 Numerical simulation

Understanding the mechanisms that cause the shift between large-scale explosive and mild effusive eruptions, as evidenced by the wide spectrum of eruptive styles and intensities, as well as the extended welding and large-scale rheomorphic structures commonly associated with silica-rich peralkaline magmas, represents a fascinating and intriguing question in volcanology. On the basis of the chemical composition, textural analysis, viscosity, estimated eruptive temperature and water content of the natural products, we parameterized the eruptive dynamics during the rise of the magma for three different eruption style and intensities (Strombolian, sub-Plinian and Plinian eruption) and determine, quantitatively, if and in which manner, the magma, under certain conditions, can fragment and erupt explosively. Input parameters for numerical simulation are the following: conduit depth (m), conduit diameter (m), sin-eruptive temperature (K), magmatic chamber pressure (Pa), volatile total content (%), density (g/cm$^3$), melt composition (wt%), initial crystal content (%), viscosity model, bubble relative viscosity model, crystal aspect ratio, Log VND. Tab. 5.1 resumes all input parameters for numerical simulation. A first set of numerical simulations was performed, systematically varying the input parameters to address the influence of each of them on the dynamics of ascent and eruption (initial water content, conduit geometry, VND, temperature, chemical composition). Afterwards, a second set of simulations was performed constraining the input parameters by means of literature data and data derived from this work to reproduce at best Cinque Denti, Green Tuff, Zinedi, Fastuca, Cuddia Mida and Altura eruptions.

| | Cinque Denti | Green Tuff | Zinedi | Fastuca | Cuddia Mida | Altura |
|---|---|---|---|---|---|---|
| Depth (m) | 4000 | 4000 | 4000 | 4000 | 4000 | 4000 |
| Diameter (m) | 10/20/30 | 10/20/30 | 10/20/30 | 10/20/30 | 10/20/30 | 10/20/30 |
| T (K) | 1100 | 1070 | 1090 | 1080 | 1090 | 1050 |
| T (°C) | 827 | 797 | 787 | 807 | 817 | 777 |
| Pressure (MPa) | 121 | 121 | 121 | 121 | 121 | 121 |
| $H_2O$ (wt%) | 3.5 | 3/4/5 | 2.5/5.5 | 2/3.5 | 2.5 | 1.5/2 |
| Crystal content (%) | 0.1 | 0.13 | 0.1 | 0.2 | 0.2 | 0.28 |
| Density (g/cm$^3$) | 2500 | 2510 | 2548 | 2500 | 2496 | 2493 |
| Log VND | 15.38 | 14.4 | 14.96 | 14.42 | 15.15 | 14.34 |
| Viscosity model | GRD | Our model | Our model | Our model | Our model | Our model |

*Tab. 5.1 Input data for the performed parametric simulations of Pantelleria eruptions.*

The depth of the magmatic chamber has been fixed at 4 km for each eruption as in literature there is a broad consensus for the presence of an active geothermal system and shallow magma reservoir (at ~ 4 km depth) which is currently deflating and cooling (Civetta et al., 1984, 1988, 1998; Gianelli and Grassi, 2001; Avanzinelli et al., 2004; White et al., 2005, 2009, 2020; Mattia et al., 2007; Civile et al., 2008; Di Carlo et al., 2010; Neave et al., 2012; Baginski et al., 2018; Liszewska et al., 2018; Romano et al., 2018, 2019, 2020; Giuffrida et al., 2020; Neave, 2020). Green Tuff eruptive temperature (720 °C; Di Carlo et al., 2010) is the only one currently constrained. However, different petrological studies (Scaillet and Macdonald, 2003; White et al., 2005, 2009; Di Carlo et al., 2010; Romano et al., 2018, 2019, 2020) suggest 750 °C as a temperature at which mineral phases are stable in pantelleritic melts. For this reason, we adjusted input temperature in order to obtain 750 °C as temperature output. Considering an average pressure gradient of 330 bar/km, we obtain 121 MPa of pressure as input. Initial water content has been derived for Cinque Denti, Cuddia Mida and Zinedi from melt inclusions in this work. Green Tuff initial water contents, 3-4 wt%, are from Lanzo et al. (2013) and Stabile et al. (2021). Fastuca initial water contents are from Stabile et al. (2021). Altura water contents are from Mimma Emanuela Gennaro, Master thesis. Density of melts have been derived using DensityX, a standalone program from Iacovino and Till (2019) to calculate the densities of dry and hydrous silicate melts at given pressures, temperatures and major oxide compositions in

wt% in the 10-component system $SiO_2$, $TiO_2$, $Al_2O_3$, $Fe_2O_3$, FeO, MgO, CaO, $Na_2O$, $K_2O$, $H_2O$. VND values used as input parameters are from this work and used for this set of simulation. The viscosity model adopted for Cinque Denti is the GRD model. It differs from those applied for the other eruptions because, unlike the other melts here analyzed, the magma has a metaluminous composition. A first set of simulations have been performed by changing conduit diameter and water content. Results of the simulations, for the six eruptions, are reported in Tabs. 5.2-6 for the output data and described in detail in the following section.

Cinque Denti numerical simulation output are reported in Tab. 5.2.

| Diameter (m) | Water content (wt%) | T exit (°C) | Exit velocity (m/s) | Mass flow rate(kg/s) | Fragmentation depth (m) | dP/dt (MPa/s) |
|---|---|---|---|---|---|---|
| 10 | 3.5 | 757 | 0.0352 | 5.17E+03 | -13 | 0.0007 |
| 20 | 3.5 | 754 | 121 | 2.00E+06 | -1937 | 0.12 |
| 30 | 3.5 | 755 | 121 | 6.12E+06 | -1598 | 0.14 |

*Tab. 5.2 Numerical simulation output for the performed parametric simulations of Cinque Denti eruption.*

Green Tuff numerical simulation output are reported in Tab. 5.3.

| Diameter (m) | Water content (wt%) | T exit (°C) | Exit velocity (m/s) | Mass flow rate(kg/s) | Fragmentation depth (m) | dP/dt (MPa/s) |
|---|---|---|---|---|---|---|
| 10 | 3 | 724 | 101 | 1.84E+05 | -407 | 0.027 |
| 10 | 4 | 709 | 114 | 1.88E+05 | -80 | 0.028 |
| 10 | 5 | 699 | 9 | 4.92E+06 | 1 | 0.079 |
| 20 | 3 | 724 | 101 | 9.52E+05 | -120 | 0.033 |
| 20 | 4 | 713 | 127 | 8.09E+06 | -425 | 0.319 |
| 20 | 5 | 706 | 145 | 1.11E+07 | -233 | 0.465 |
| 30 | 3 | 727 | 109 | 1.47E+07 | -419 | 0.239 |
| 30 | 4 | 714 | 129 | 2.26E+07 | -262 | 0.388 |
| 30 | 5 | 708 | 146 | 3.20E+07 | -92 | 0.587 |

*Tab. 5.3 Numerical simulation output for the performed parametric simulations of Green Tuff eruption.*

Zinedi numerical simulation output are reported in Tab. 5.4.

| Diameter (m) | Water content (wt%) | T exit (°C) | Exit velocity (m/s) | Mass flow rate(kg/s) | Fragmentation depth (m) | dP/dt (MPa/s) |
|---|---|---|---|---|---|---|
| 10 | 2.5 | 752 | 7.66E-03 | 8.86E+02 | -1 | 0.000122 |
| 10 | 5.5 | 724 | 6.96E-01 | 9.14E+05 | -1 | 0.015 |
| 20 | 2.5 | 752 | 2.19E-02 | 1.72E+04 | -12 | 0.000589 |
| 20 | 5.5 | 725 | 158 | 1.44E+07 | -955 | 0.704 |
| 30 | 2.5 | 752 | 9.49E-02 | 9.21E+04 | -16 | 0.001407 |
| 30 | 5.5 | 726 | 159 | 3.64E+07 | -714 | 0.758 |

*Tab. 5.4 Numerical simulation output for the performed parametric simulations of Zinedi eruption.*

Fastuca numerical simulation output are reported in Tab. 5.5.

| Diameter (m) | Water content (wt%) | T exit (°C) | Exit velocity (m/s) | Mass flow rate(kg/s) | Fragmentation depth (m) | dP/dt (MPa/s) |
|---|---|---|---|---|---|---|
| 10 | 2 | 752 | 2.17E-02 | 4.61E+03 | -2 | 0.000610 |
| 10 | 3.5 | 730 | 106 | 2.06E+05 | -336 | 0.031 |
| 20 | 2 | 753 | 8.30E-01 | 9.33E+04 | -26 | 0.003 |
| 20 | 3.5 | 732 | 114 | 5.86E+06 | -520 | 0.225 |
| 30 | 2 | 752 | 81 | 5.99E+06 | -543 | 0.094 |
| 30 | 3.5 | 733 | 114 | 1.64E+07 | -356 | 0.273 |

*Tab. 5.5 Numerical simulation output for the performed parametric simulations of Fastuca eruption.*

Cuddia Mida numerical simulation output are reported in Tab. 5.6.

| Diameter (m) | Water content (wt%) | T exit (°C) | Exit velocity (m/s) | Mass flow rate(kg/s) | Fragmentation depth (m) | dP/dt (MPa/s) |
|---|---|---|---|---|---|---|
| 10 | 2.5 | 754 | 88 | 2.27E+05 | -603 | 0.033 |
| 20 | 2.5 | 755 | 94 | 3.94E+06 | -625 | 0.145 |
| 30 | 2.5 | 755 | 94 | 1.07E+07 | -480 | 0.171 |

*Tab. 5.6 Numerical simulation output for the performed parametric simulations of Cuddia Mida eruption.*

Altura numerical simulations are not reported, as no stable solution was found. This indicates that no conditions for magma fragmentation were identified. This result is consistent with the eruptive style of Altura, which corresponds to a low-energy Strombolian eruption. The numerical model used here simulates

persistent eruptions, in which magma and volatiles are dynamically coupled. In contrast, Strombolian eruptions are intermittent, characterized by a decoupling between the magma ascent velocity and the gas bubble rise velocity. This decoupling promotes bubble coalescence and leads to a different eruptive style, not represented by the present model. In Strombolian eruptions, fragmentation is ductile rather than brittle, since the magma ascends slowly and has a low viscosity. Therefore, the absence of fragmentation in the simulations suggests that the magma is too fluid to fragment, in agreement with natural observations, even though the simulated eruptive regime differs from the actual Strombolian behavior.

### 5.2.1 Influence of water content

In this section we show the MAMMA numerical simulation results comparing the dynamics for different water contents. In this way, we are able to evaluate the effects of water content and porosity on the eruptive dynamics keeping depth (4 km), conduit diameter (20 m), pressure (121 MPa) constant and using VND values from textural analysis for each eruption. Input temperature has been systematically adjusted in order to obtain an exit temperature of 720 °C for Green Tuff and 750° for all the other eruptions. Tab. 5.7 show the numerical simulation output at different water contents for all compositions . Fig. 5.1-3 shows MAMMA numerical simulation results comparing the dynamics for different water contents. Altura numerical simulations results are not present as Altura does not reach conditions for brittle fragmentation. The water content for each composition is derived from melt inclusion analyses.

| Eruption | Water content (wt%) | Diameter (m) | Porosity (%) | T exit (°C) | Exit velocity (m/s) | Mass flow rate (kg/s) | Frag. depth (m) |
|---|---|---|---|---|---|---|---|
| Cinque Denti | 3.5 | 20 | 98 | 754 | 121 | 2.00E+06 | -1937 |
| Green Tuff | 3 | 20 | 99 | 724 | 101 | 9.52E+05 | -120 |
| Green Tuff | 4 | 20 | 94 | 713 | 127 | 8.09E+06 | -425 |
| Green Tuff | 5 | 20 | 93 | 706 | 145 | 1.11E+07 | -233 |
| Zinedi | 2.5 | 20 | NoFrag. | | | | |
| Zinedi | 5.5 | 20 | 91 | 725 | 158 | 1.44E+07 | -955 |
| Fastuca | 2 | 20 | NoFrag. | | | | |
| Fastuca | 3.5 | 20 | 95 | 732 | 114 | 5.86E+06 | -520 |
| Cuddia Mida | 2.5 | 20 | 98 | 755 | 94 | 3.94E+06 | -625 |
| Altura | 1.5 | 20 | NoFrag. | | | | |
| Altura | 2 | 20 | NoFrag. | | | | |

*Tab. 5.7 Numerical simulation output keeping depth, conduit diameter and pressure constant.*

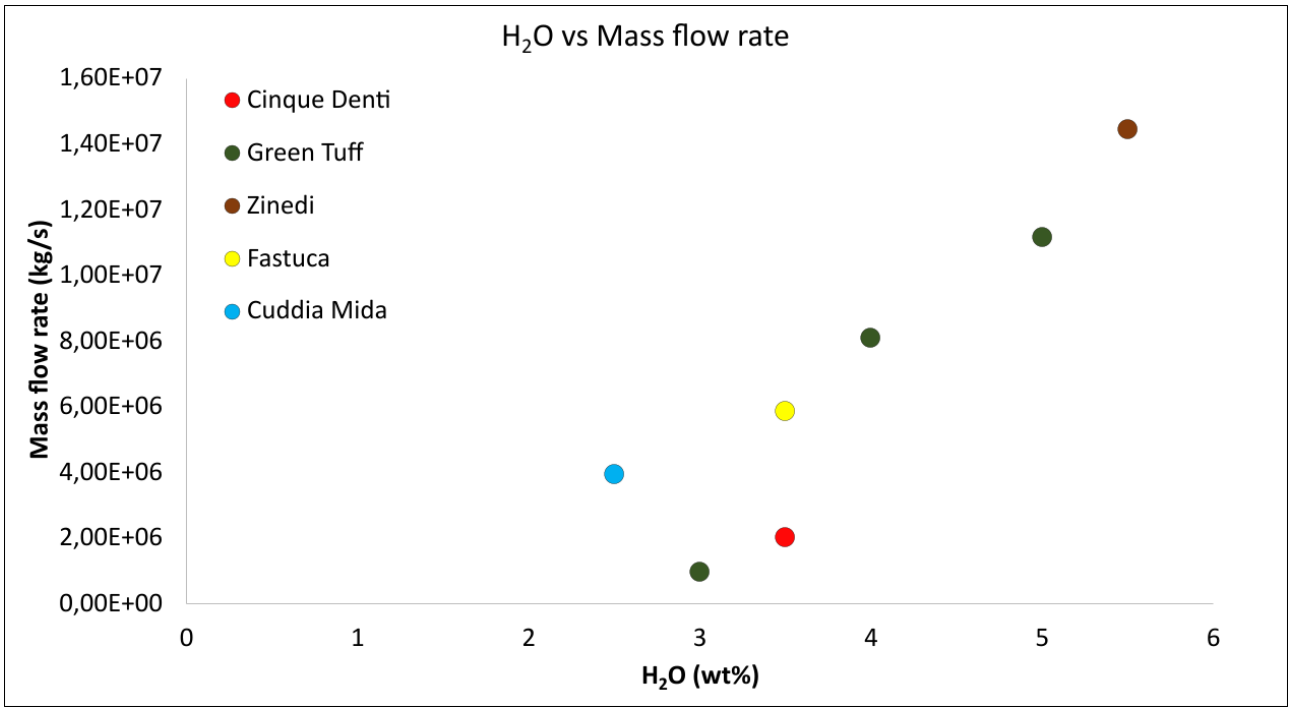


*Fig. 5.1 $H_2O$ vs Mass flow rate relationship for Cinque Denti, Green Tuff, Zinedi, Fastuca and Cuddia Mida numerical simulations results. Altura numerical simulations results are not present as Altura does not reach conditions for brittle fragmentation.*

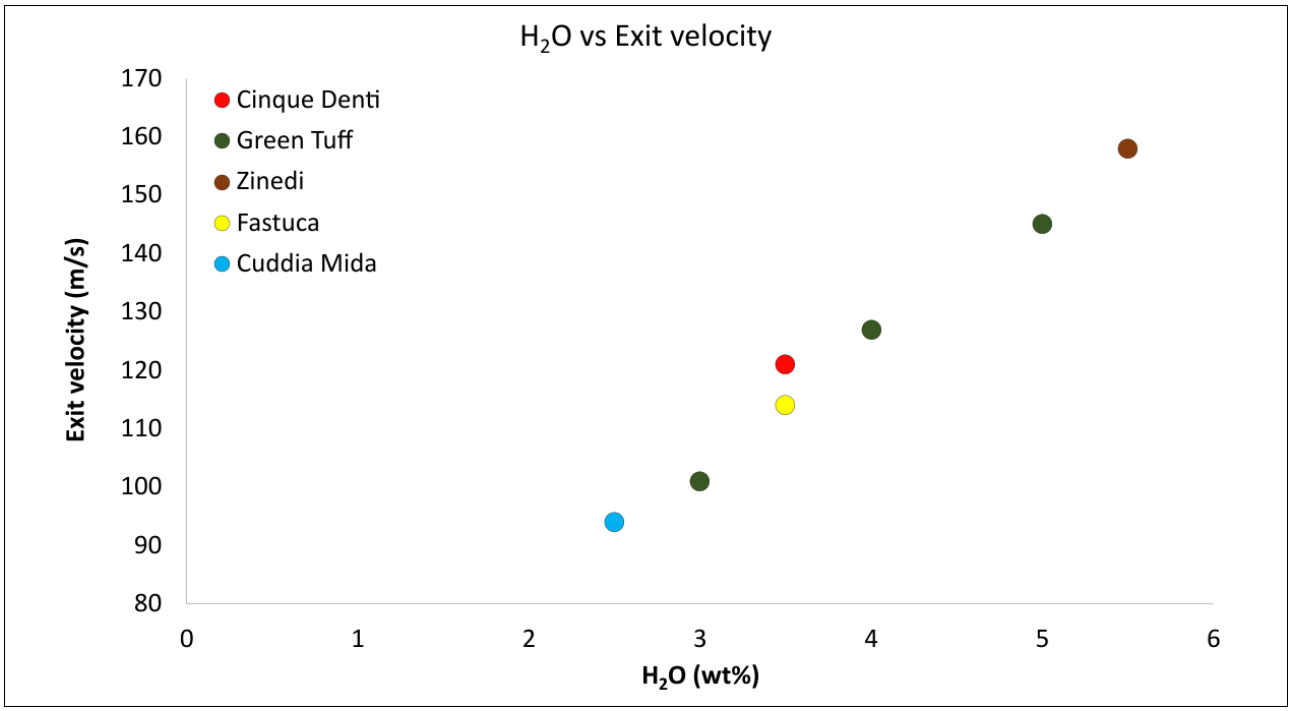


*Fig. 5.2 $H_2O$ vs Exit velocity relationship for Cinque Denti, Green Tuff, Zinedi, Fastuca and Cuddia Mida numerical simulations results. Altura numerical simulations results are not present as Altura does not reach conditions for brittle fragmentation.*

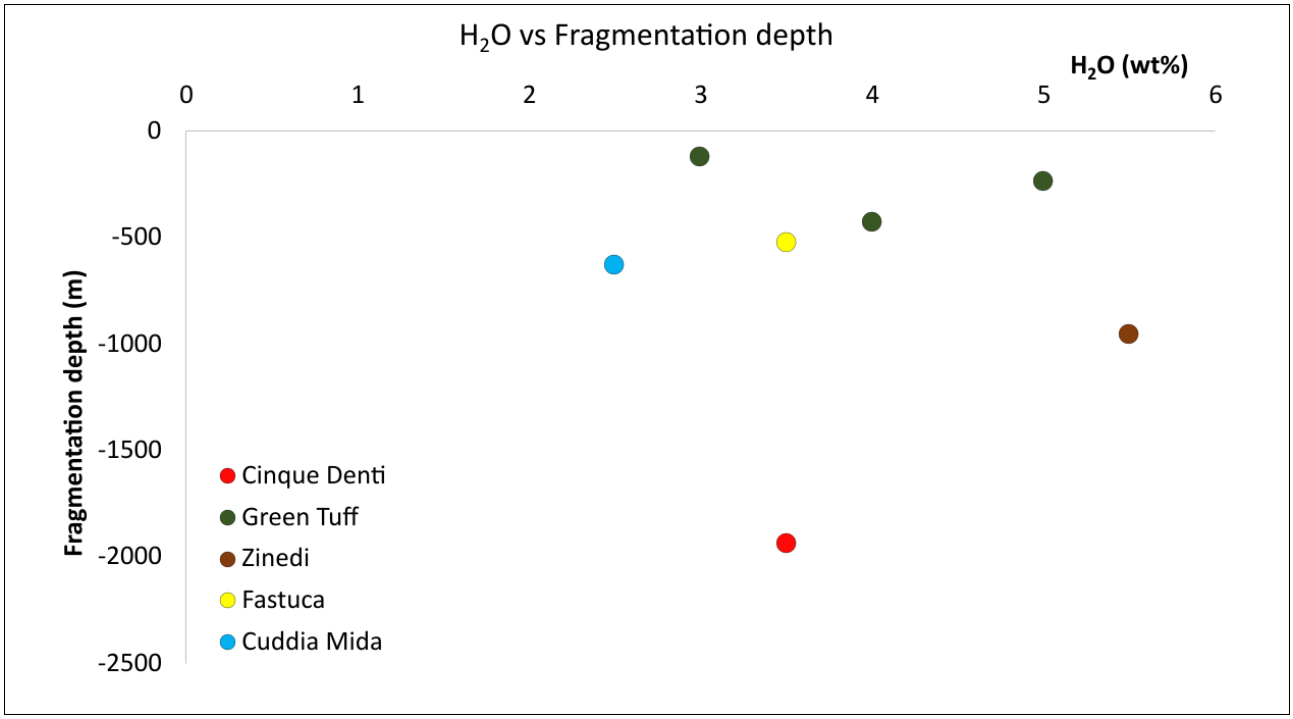


*Fig. 5.3 $H_2O$ vs Fragmentation depth relationship for Cinque Denti, Green Tuff, Zinedi, Fastuca and Cuddia Mida numerical simulations results. Altura numerical simulations results are not present as Altura does not reach conditions for brittle fragmentation.*

Fig. 5.1 shows the relationship between water content and Mass flow rate. These values are typical of silicic explosive eruption ($10^5$-$10^7$ kg/s). A quasi-linear relationship between water content and mass flow rate can be observed. For

Green Tuff, Zinedi, and Fastuca, where more than one water content was simulated, we observe that mass flow rates increase with increasing initial water content. This trend can also be extended to all eruptions studied, regardless the chemical composition of the melts and the eruptive style. Generally, therefore, we can state that increasing initial water content leads to a parallel increase of mass flow rate. Taking as reference Zinedi eruption, we can state that a $\Delta H_2O$ = 3 wt% can lead to an increase of ~3 order of magnitude in mass flow rate. Fig. 5.2 shows the relationship between water content and exit velocity. Exit velocities values are typical of silicic explosive eruptions., As for the mass flow rate, a linear relationship between initial water content and exit velocity, regardless of the initial chemical composition, is evident . Generally, therefore, we can state that increasing initial water content leads to a general increase of exit velocities. Taking as reference Zinedi eruption, we can observe that a $\Delta H_2O$ = 3 wt% can lead to an increase of more than 100 m/s. Fig. The initial water content can be considered the first and most important factor influencing the final vent velocities of an eruption. It is in fact known that the energy for the acceleration of the magma is provided by the expansion of the gas which occurs as the gas-magma mixture rises and the pressure on it decreases. During its rise, bubbles expand, getting cooler and releasing energy. This energy raises and accelerates the gas-magma mixture through the conduit. Fig 5.3 shows the relationship between initial water content and fragmentation depth. Unlike the previous cases, the fragmentation depth does not seem to be correlated in any systematic way with water content. A brief consideration should be given to the possible role of volatiles other than $H_2O$ in eruptive dynamics. Several experimental studies have investigated the effect of halogens on melt viscosity (Dingwell et al., 1985, 1998; Metrich and Rutherford, 1992; Baker et al., 1994, 1995; Giordano et al., 2004; Zimowa and Webb, 2006, 2007; Evans et al., 2008; Baasner et al., 2013). However, most of these studies were performed on synthetic glasses composed of a limited number of oxides (typically three to six components, e.g., $Na_2O$–$Al_2O_3$–$SiO_2$–F or Na–Fe–Si–O–F–Cl), rather than on natural, multicomponent magmatic systems. As a result, the effects of Cl and F inferred from simplified compositions may be significantly attenuated or modified in natural melts. Additional uncertainty arises from experimental procedures, as halogens were commonly introduced using compounds such as $AlF_3$, $FeCl_3$, $FeF_3$, NaF, or $AlF_2$. While these are among the few commercially available reagents, they also introduce network-forming cations (e.g., Al and Fe) into the melt, potentially increasing melt polymerization

and viscosity. Moreover, recent studies have shown that elements such as Fe in natural melts may promote nanolite formation (Di Genova et al., 2020; Cáceres et al., 2021; Bamber et al., 2025), further complicating the interpretation of viscosity measurements. Experimental results (Zimowa and Webb, 2006, 2007; Webb et al., 2014) nonetheless indicate that the effect of chlorine on melt viscosity is strongly composition-dependent and closely linked to the presence and redox state of iron. In iron-free or low-Fe systems, chlorine generally increases melt viscosity, whereas in Fe-bearing melts it may reduce viscosity by promoting the conversion of network-forming $Fe^{3+}$ to network-modifying $Fe^{2+}$. In aluminosilicate melts, chlorine tends to increase viscosity in peralkaline compositions but decrease it in peraluminous melts, reflecting differences in melt polymerization and preferred Cl–$Fe^{2+}$ bonding. In contrast, fluorine consistently lowers melt viscosity by depolymerizing the silicate network. When both halogens are present, their combined effect on viscosity is non-linear, with fluorine generally dominating the depolymerizing effect while chlorine may either enhance or partially counteract viscosity reduction, depending on melt composition. Despite these experimental insights, major uncertainties remain. In particular, the influence of redox conditions on the solubility and structural role of Cl and F is still poorly constrained, and no solubility models are currently available for either chlorine or fluorine in peralkaline melts. The absence of solubility laws precludes any robust description of their degassing behaviour during magma ascent and therefore prevents their explicit inclusion in numerical simulations. In addition, the effect of chlorine on melt viscosity remains highly uncertain and strongly composition-dependent. In this study, fluorine is absent from the investigated magmas, whereas chlorine is present in some cases. However, chlorine cannot be explicitly accounted for in the simulations because its solubility behaviour is unknown and its influence on melt viscosity cannot be quantified in a robust manner. Nonetheless, based on available experimental studies, we infer that the effect of chlorine on melt viscosity is likely to be minor compared to that of water. Water therefore remains the dominant volatile controlling magma viscosity and eruptive dynamics in our modelling framework.

Peralkaline melts are known to be enriched in halogens such as chlorine and fluorine (Metrich and Rutherford, 1992; Webster et al., 1993; Lowenstern, 1994; Barclay et al., 1996; White et al., 2009; Neave et al., 2012; Liszewska et al., 2018; Macdonald et al., 2019). For these reasons, we were not been able to directly investigate the effect of Cl and F on the viscosities of our natural melt compositions and extending this to MAMMA numerical simulations.

### 5.2.2 Influence of temperature

Temperature plays a key role in affecting magma properties, such as viscosity and density, and consequently conduit dynamics. In this section we show the MAMMA numerical simulation results for Green Tuff eruption comparing the dynamics for different input temperature values. We choose Green Tuff as a target eruption for MAMMA numerical simulation because is one the most studied and representative eruption among Pantelleria eruptions and can be therefore taken as a reference for peralkaline Plinian eruptions. In this section, we are going to evaluate the effects of temperature (750 °C - 767 °C - 800 °C) on the eruptive dynamics while maintaining depth (4 km), conduit diameter (20 m), pressure (121 MPa), water content (3 wt%) and Log VND (14.4) constant. Tab. 5.8 show numerical simulation output for water content influence. Fig. 5.4 shows MAMMA numerical simulation results. Fig. 5.5-7 show relationship between MAMMA numerical simulation results with different input temperature.

| Eruption | T input (°C) | Porosity (%) | T exit (°C) | Exit velocity (m/s) | Mass flow rate (kg/s) | Frag. depth (m) |
|---|---|---|---|---|---|---|
| Green Tuff | 750 | 99 | 678 | 96 | 5.81E+05 | -470 |
| Green Tuff | 767 | 99 | 721 | 101 | 9.41E+05 | -148 |
| Green Tuff | 800 | 99 | 727 | 100 | 9.82E+05 | -98 |

*Tab. 5.8 Numerical simulation for detecting influence of temperature on eruptive dynamics keeping depth, conduit diameter, pressure, water content and Log VND constant.*

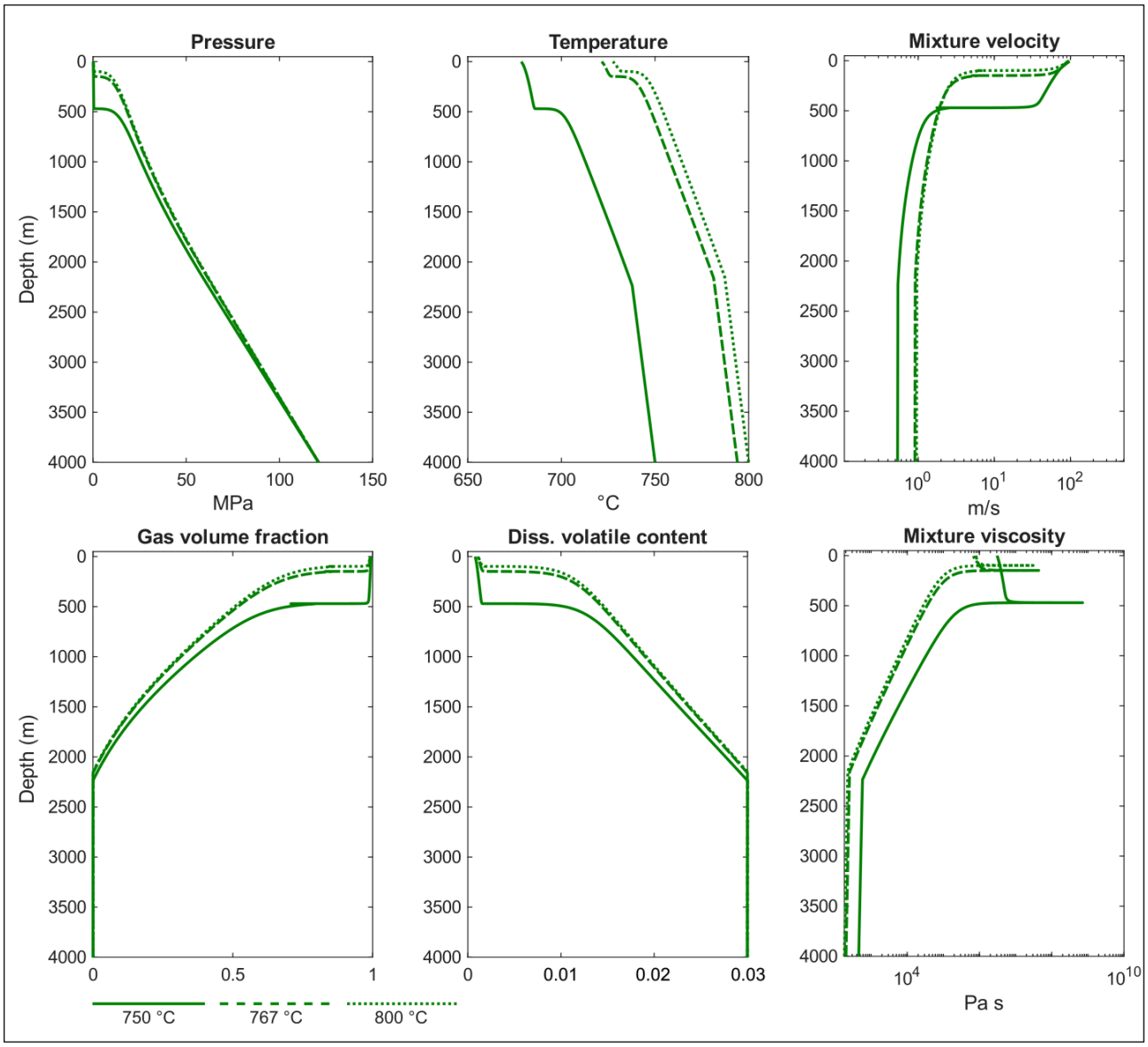


*Fig. 5.4 MAMMA numerical simulation for Green Tuff with different input temperature.*

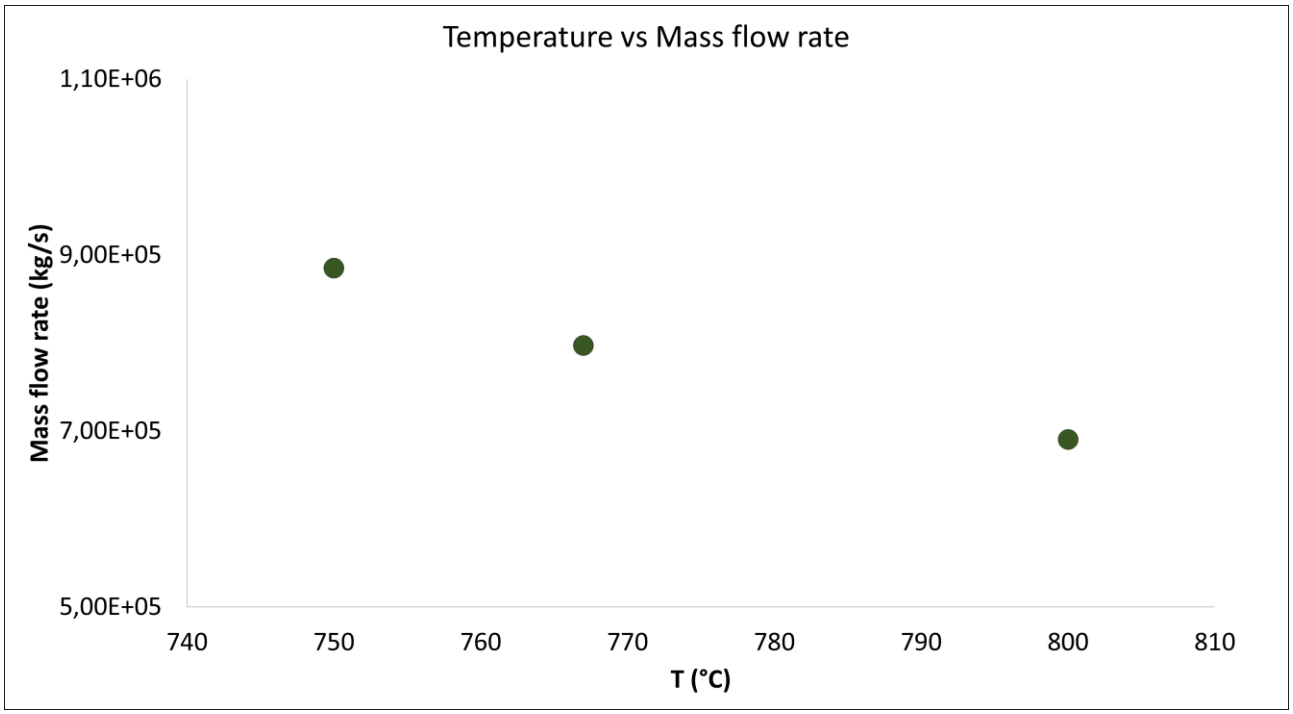


*Fig. 5.5 Temperature vs Mass flow rate relationship for Green Tuff numerical simulations results.*

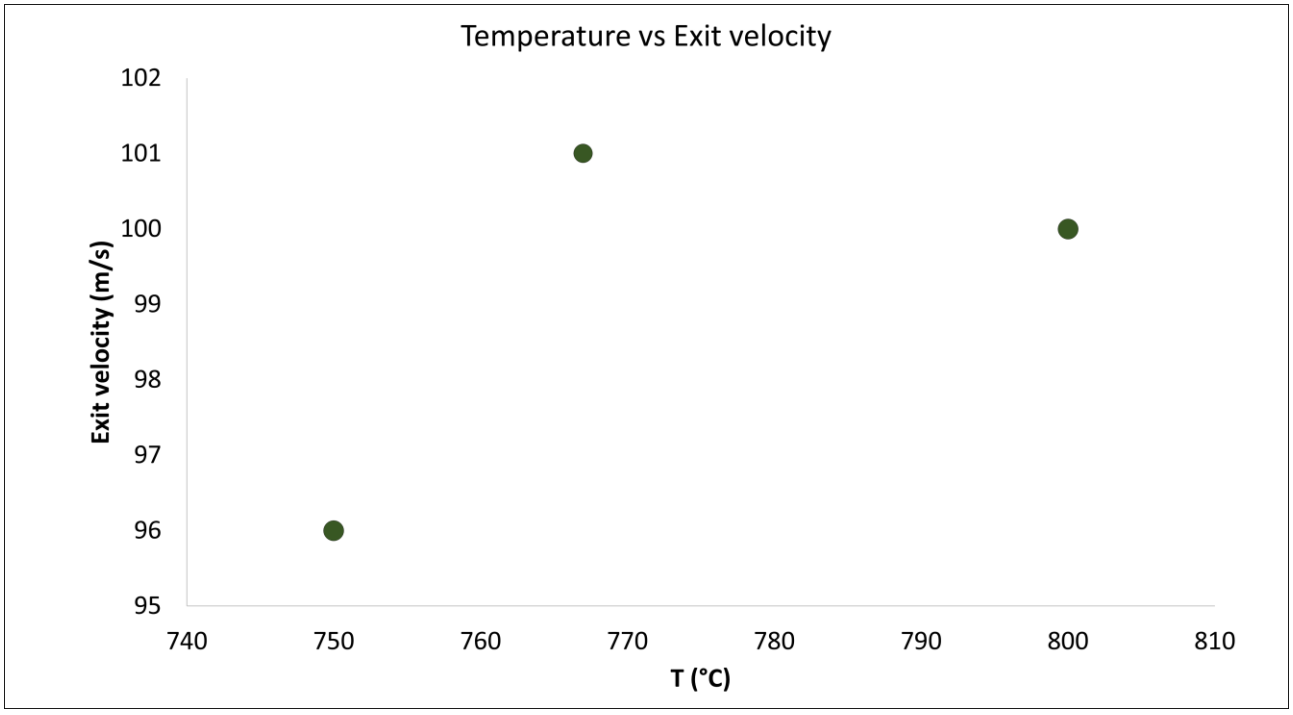


*Fig. 5.6 Temperature vs Exit velocity relationship for Green Tuff numerical simulations results.*

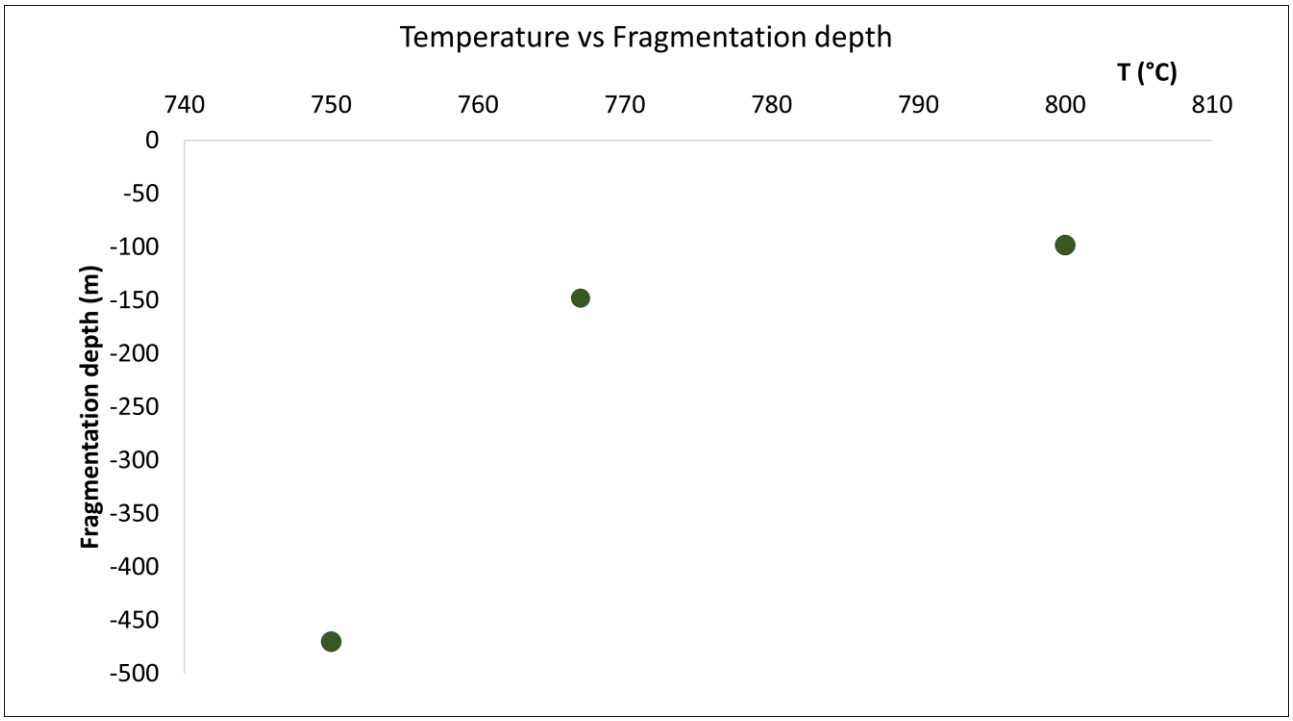


*Fig. 5.7 Temperature vs Fragmentation depth relationship for Green Tuff numerical simulations results.*

For all the three water contents, temperature variation leads to a large variation of the fragmentation depth, correlated to different evolution of water exsolution and porosity along the conduit, while it has rather weak influence on the other output parameters as mass fluxes and velocity at the vent. In general, even though the solubility of water decreases with increasing temperature, so the magma begins to exsolve at a deeper level at higher T, lower viscosities at higher temperature have the opposite effect of decreasing the dP/dz , so decreasing the degree of exsolution. This, and the lower overall viscosities, have the overall effect of delaying the fragmentation at increasing temperature, as evidenced in Fig, 5.7. Variation in exit velocities and mass flow rate are minimal, as due to the complex interplay between the different parameters. Exit velocities increase slightly as a function of temperature, mainly in response to the decrease in viscosities and frictional losses at the wall conduit and lower densities. Mass flow rate also decreases, despite the decrease in viscosities, mainly due to the decrease in density due to the increase in temperature.

### 5.2.3 Influence of conduit diameter

The change in conduit diameter is  very important as it influences the mass flow rate of the magma. In this section we show the MAMMA numerical simulation results for Green Tuff eruption comparing the dynamics for different input conduit values. In particular,, we  evaluate the effects of conduit diameter (30 m – 40 m –

50 m) on the eruptive dynamics keeping depth (4 km), temperature (797 °C), pressure (121 MPa), water content (3 wt% $H_2O$) and Log VND (14.4) constant. Tab. 5.9 shows the numerical simulation outputs for the different scenarios considered. Fig. 5.8 shows MAMMA numerical simulation results. Figures 5.9–5.11 show the output parameters as a function of variations in conduit diameter.

| Eruption | Conduit diameter input (m) | Porosity (%) | T exit (°C) | Exit velocity (m/s) | Mass flow rate (kg/s) | Frag. depth (m) |
|---|---|---|---|---|---|---|
| Green Tuff | 30 | 94 | 727 | 109 | 1.47E+07 | -419 |
| Green Tuff | 40 | 90 | 729 | 113 | 1.79E+08 | -116 |
| Green Tuff | 50 | 89 | 729 | 113 | 3.25E+08 | -74 |

*Tab. 5.9 Numerical simulation for detecting influence of conduit geometry on eruptive dynamics keeping depth, temperature, pressure, water content and Log VND constant.*

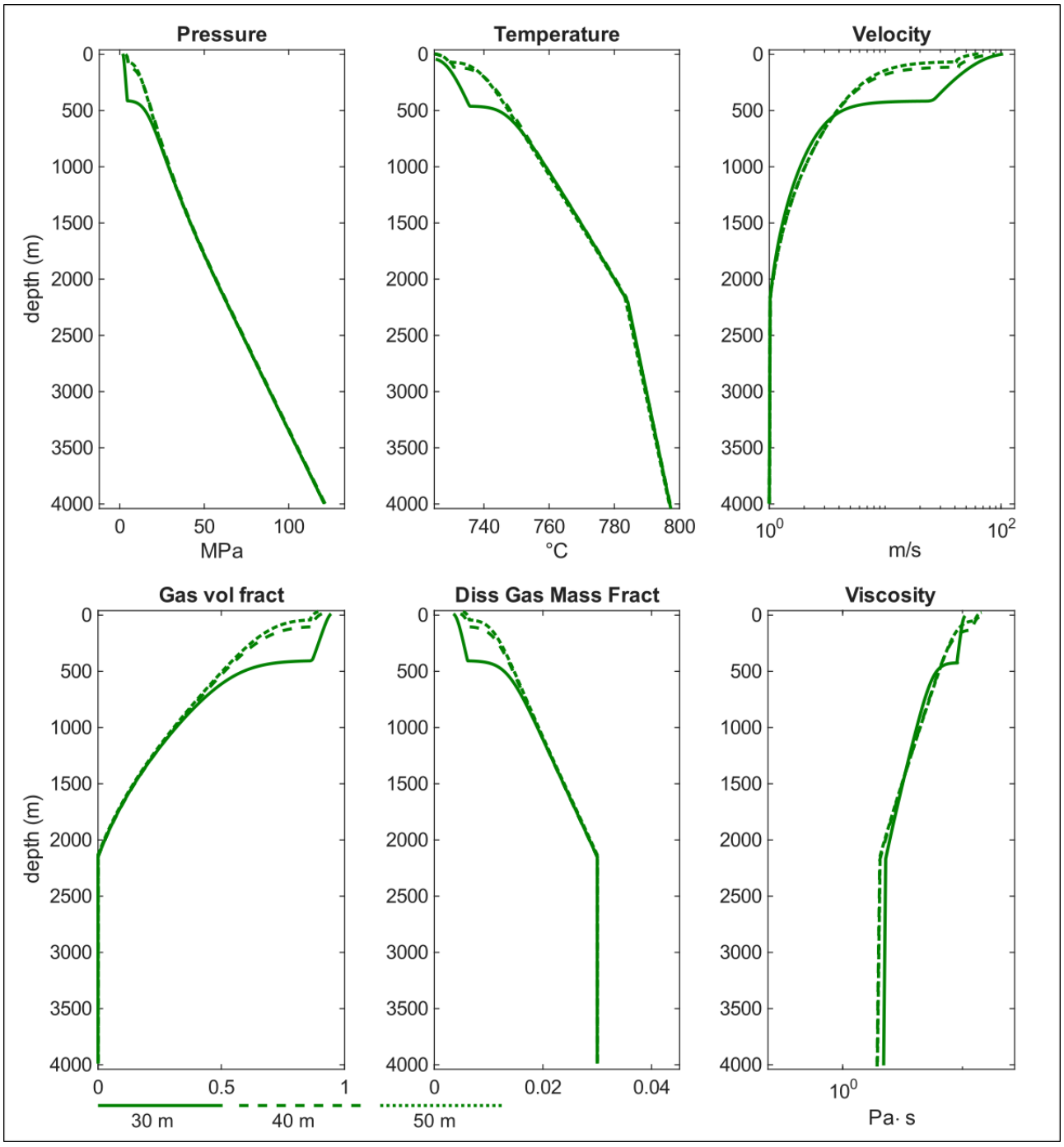


*Fig. 5.8 MAMMA numerical simulation for Green Tuff with different input conduit diameter.*

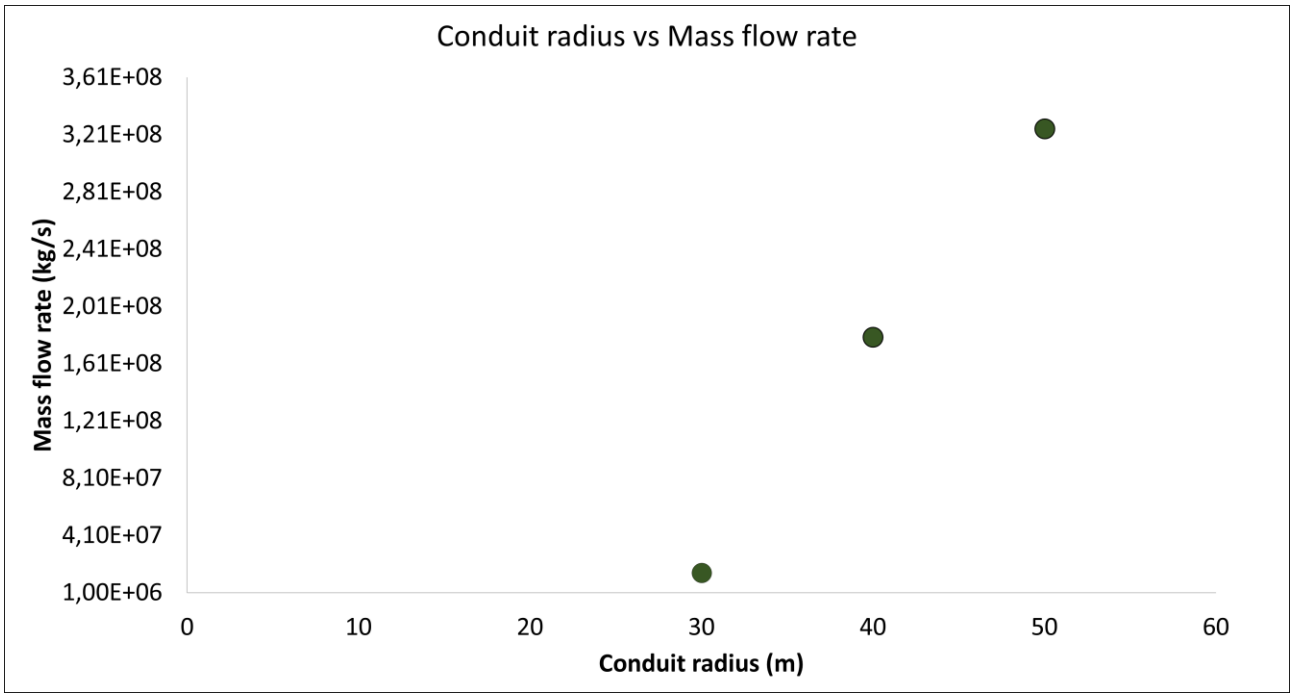


*Fig. 5.9 Conduit diameter vs Mass flow rate relationship for Green Tuff numerical simulations results.*

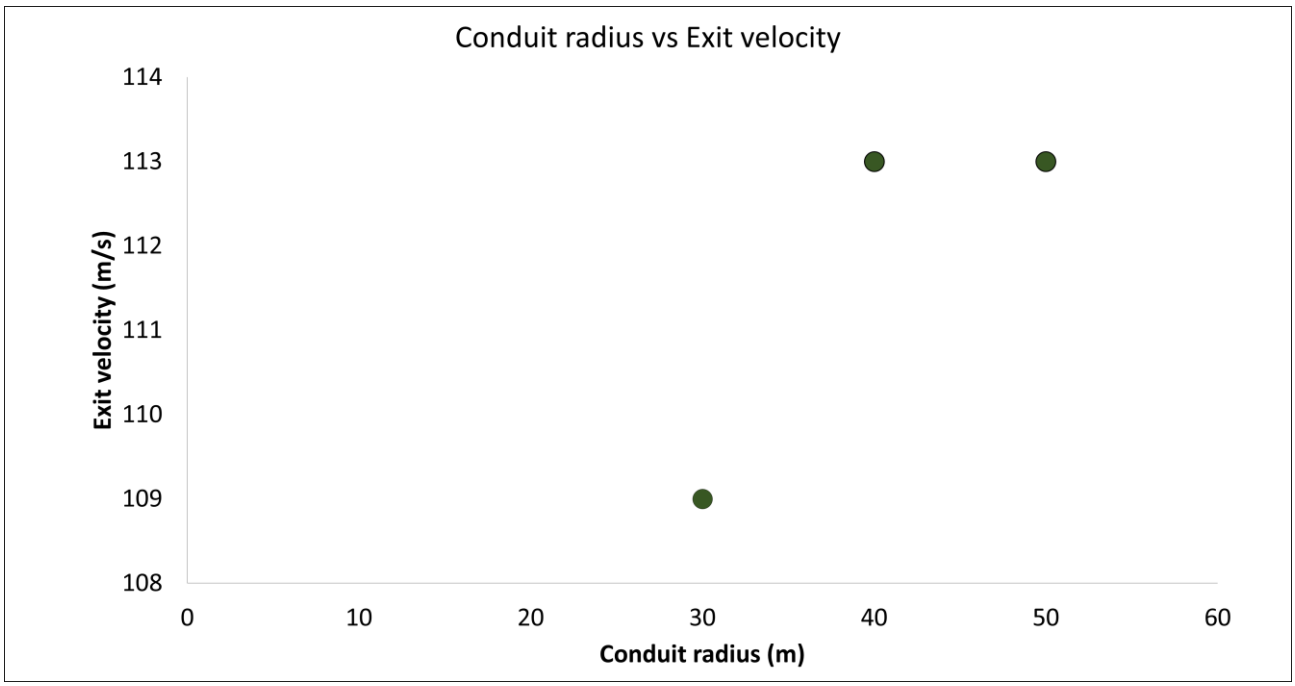


*Fig. 5.10 Conduit diameter vs Exit velocity relationship for Green Tuff numerical simulations results.*

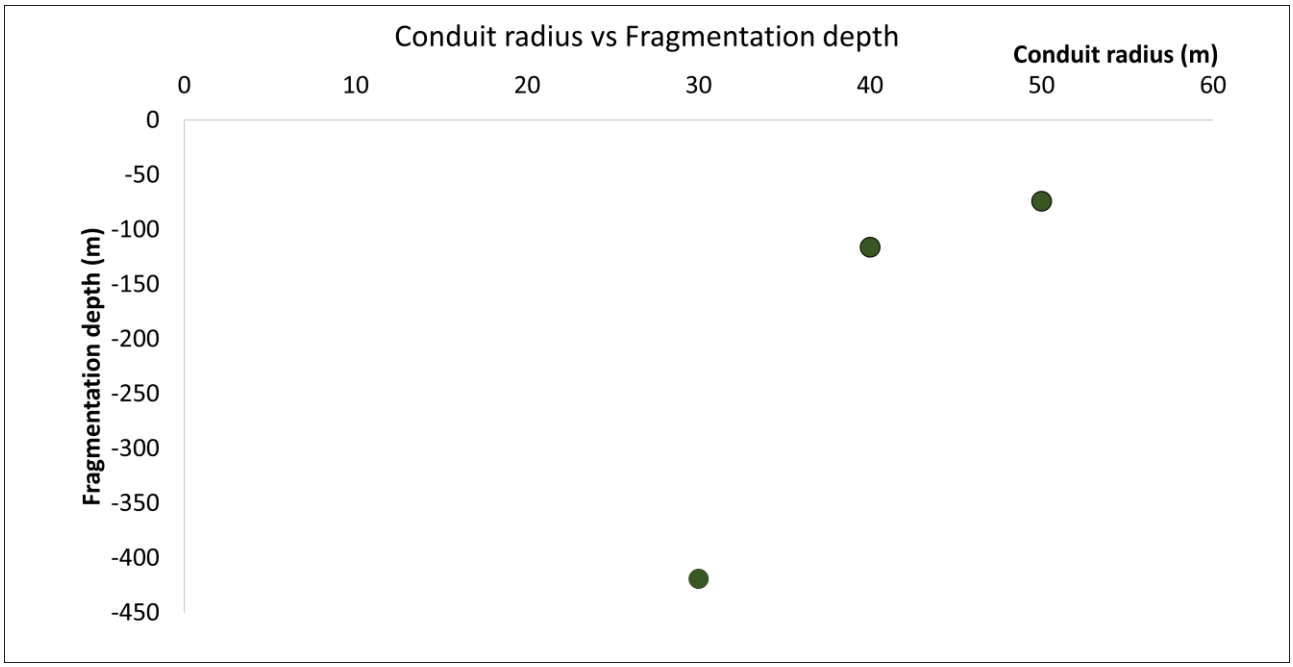


*Fig. 5.11 Conduit diameter vs Fragmentation depth relationship for Green Tuff numerical simulations results.*

Fig 5.9 shows the relationship between conduit diameter and mass flow rate. Conduit diameter strongly affects the mass flow rate of the magmatic mixtures. Mass flow rates range from $1.47 \times 10^7$ to $3.25 \times 10^8$ kg/s, highlighting how a 20 m increase in conduit diameter results in an order-of-magnitude increase in mass flow rate. The dependence of MDR (Mass discharge rate) from conduit diameter is evident by the following:

$$MDR = \rho VA \quad (5.24)$$

where ρ is the bulk density of magma, V is magma velocity and A is the vent cross sectional area. Assuming a circular geometry for the vent, A is equal to:

$$A = \pi r^2 \quad (5.25)$$

Fig 5.10 shows the relationship between conduit diameter and exit velocity. A slight increase in exit velocity as a function of conduit diameter can be observed. As the original water content is identical in all cases, the balance of the final gas volume fraction and mixture density leads to very small variation in exit choked flow velocities. Fig 5.11 shows the relationship between conduit diameter and fragmentation depth. We can observe a linear relationship between conduit diameter and fragmentation depth. In particular, the increase in conduit diameter leads to a decrease in fragmentation depth matching an increase of mass flux along the conduit. This behavior is attributable to an increase of frictional resistance along the conduit walls as the conduit diameter increases, which

results in a reduced magma flow velocity. So, the change in conduit diameter is very important as it enhances the differences in mass discharge rate and fragmentation depth within the eruptions.

### 5.2.4 Influence of VND

Volcanic rocks and magma display a wide range of porosity and vesicle size as a result of their complex genesis. For an equivalent water content, VND can be considered a proxy of ascent velocities and pressure decrease within a magma conduit. In this section we show the MAMMA numerical simulation results for Green Tuff eruption comparing the dynamics for different input Log VND. We evaluate the effects of Log VND (14 – 15 – 16) on the eruptive dynamics keeping depth (4 km), temperature (797 °C), pressure (121 MPa), water content (3 wt%) and conduit diameter (20 m) constant. Log VND values analysed have been chosen in order to investigate the entire display of Log VND for silicic Plinian eruption. Tab. 5.10 shows numerical simulation outputs for VND influence. Fig. 5.12 shows MAMMA numerical simulation results. Figures 5.13–5.15 show the output parameters as a function of variations in Log VND.

| Eruption | Log VND input | Porosity (%) | T exit (°C) | Exit velocity (m/s) | Mass flow rate (kg/s) | Frag. depth (m) |
|---|---|---|---|---|---|---|
| Green Tuff | 14 | 99 | 724 | 101 | 9.20E+05 | -113 |
| Green Tuff | 15 | 95 | 727 | 109 | 5.90E+06 | -589 |
| Green Tuff | 16 | 95 | 727 | 109 | 6.24E+06 | -603 |

*Tab. 5.10 Numerical simulation for detecting influence of VND on eruptive dynamics keeping depth, temperature, pressure, water content and conduit diameter constant.*

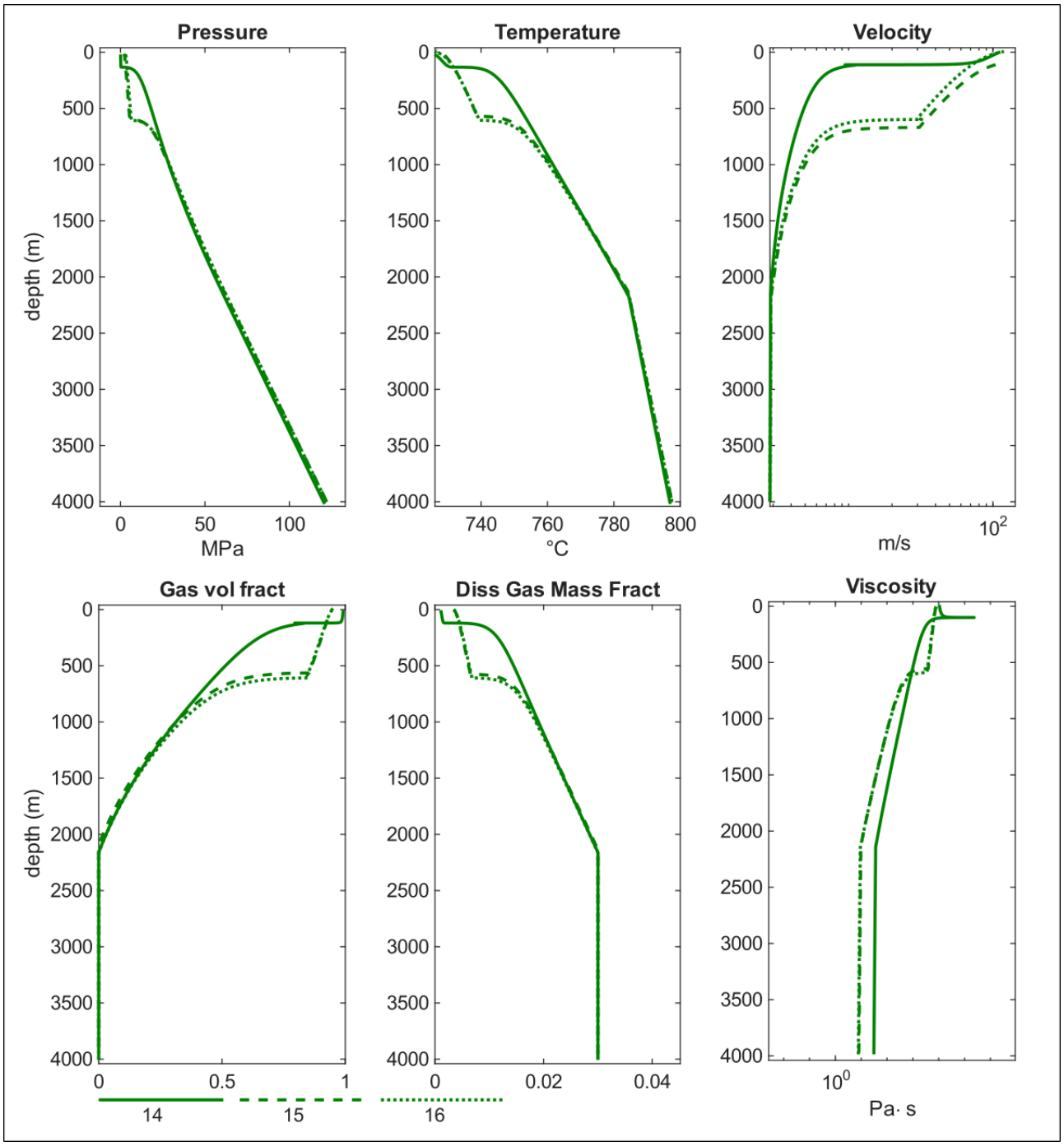


*Fig. 5.12 MAMMA numerical simulation for Green Tuff with different input Log VND.*

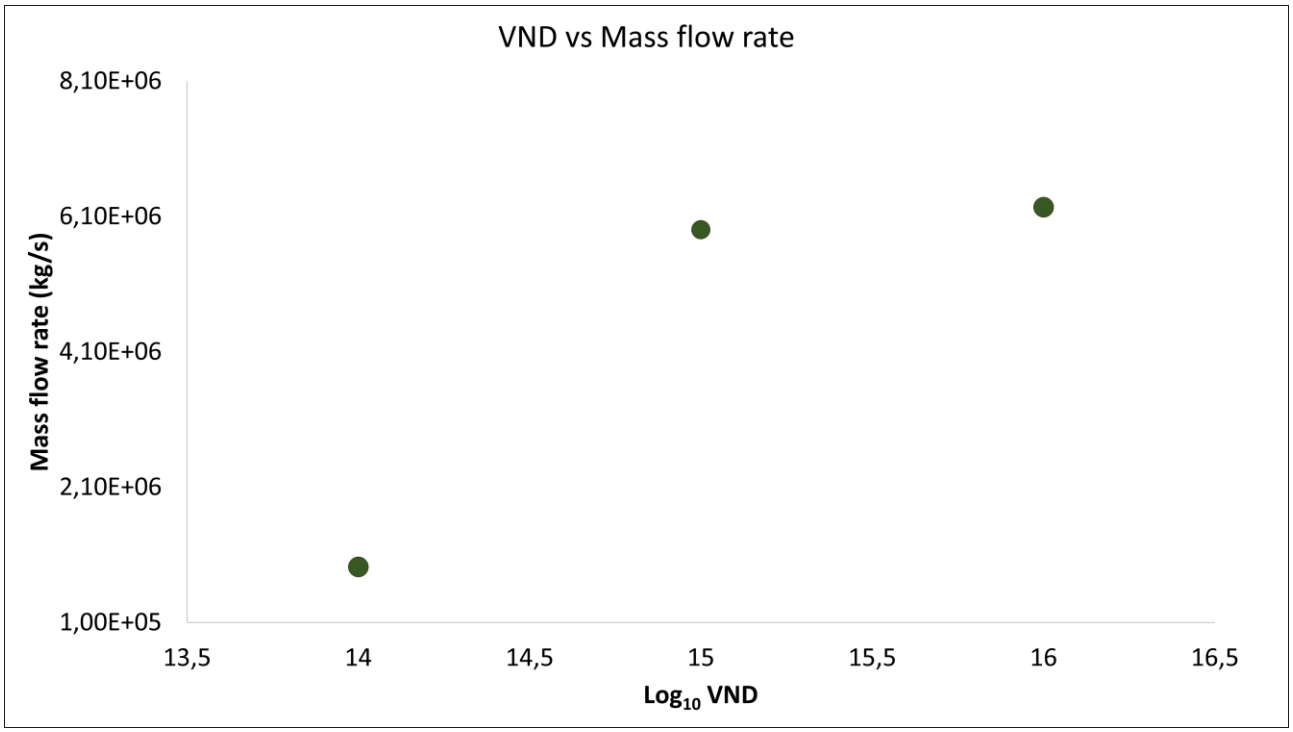


*Fig. 5.13 VND vs Mass flow rate relationship for Green Tuff numerical simulations results.*

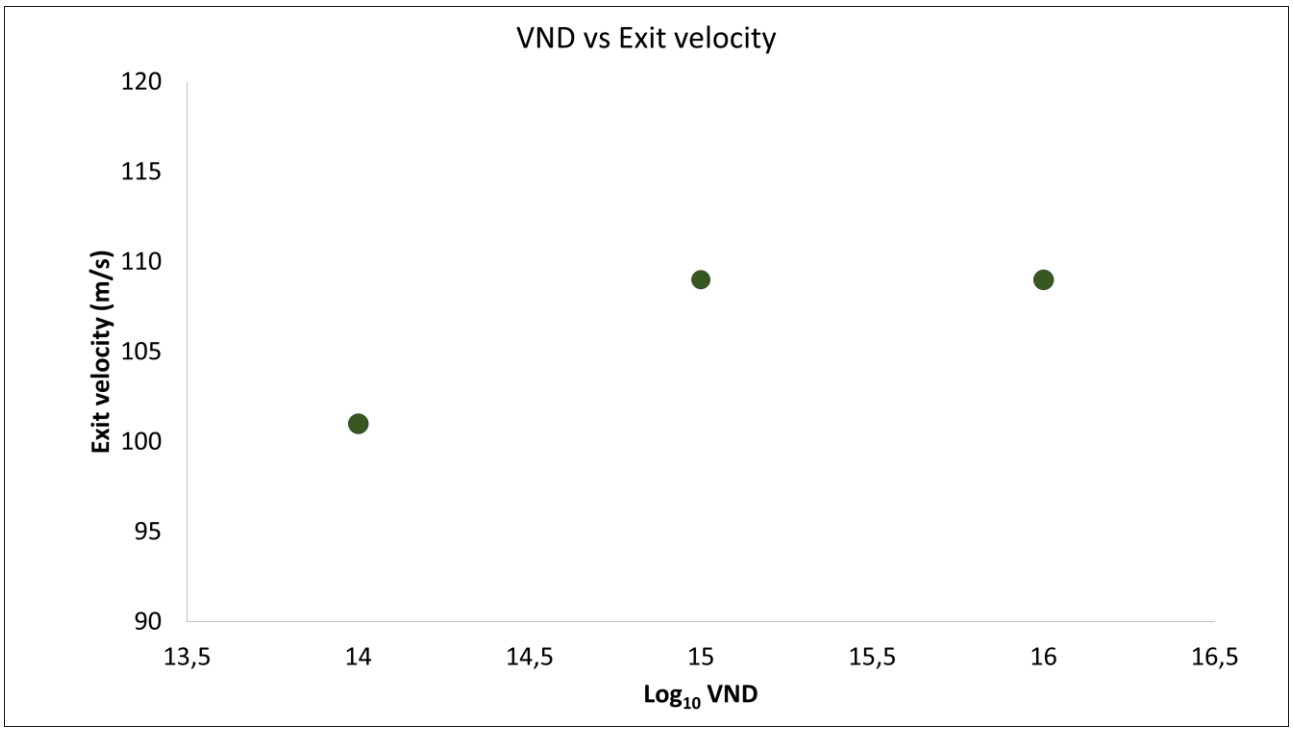


*Fig. 5.14 VND vs Exit velocity rate relationship for Green Tuff numerical simulations results.*

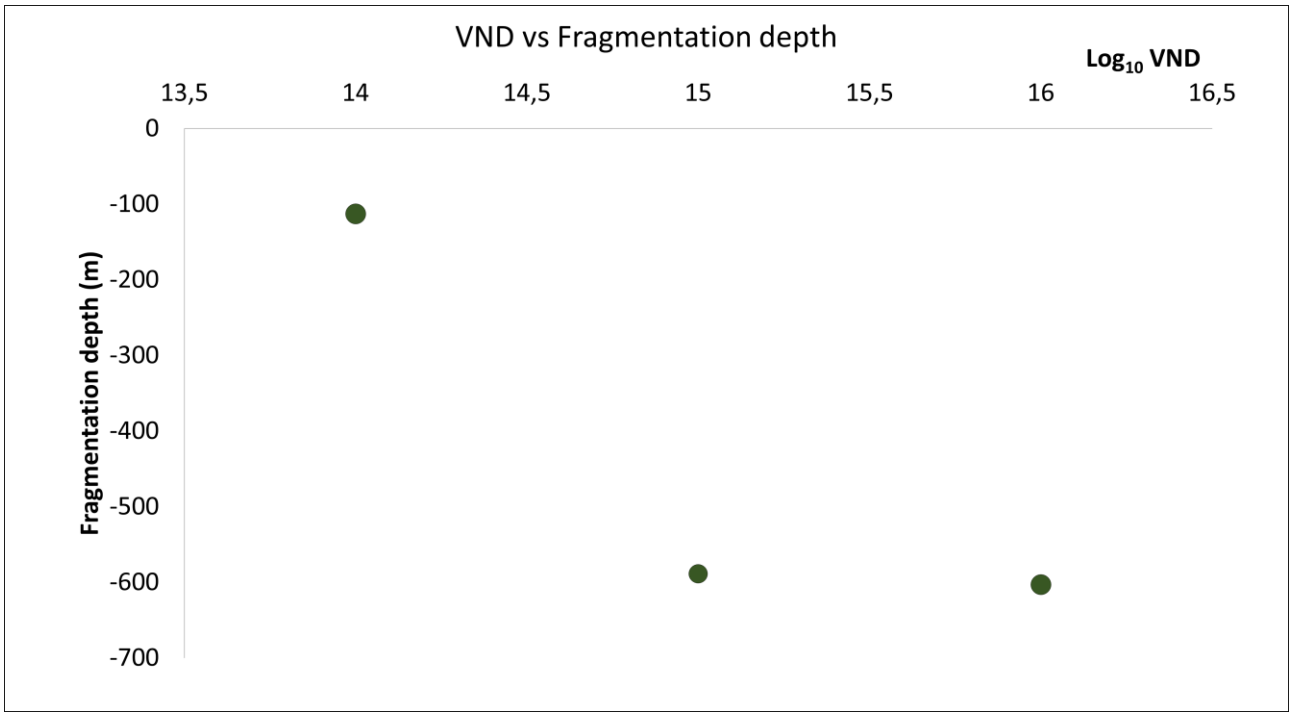


*Fig. 5.15 VND vs Fragmentation depth relationship for Green Tuff numerical simulations results.*

The VND parameter regulates the bubble radius and therefore the porosity of the magma at a given depth, whereas the total gas volume fraction is determined by the solubility law. Higher VND values correspond to higher porosity for the same gas volume fraction, thereby directly affecting both magma viscosity and mechanical strength: higher VNDs lead to lower viscosity and lower mechanical strength. Consequently, higher VNDs are directly correlated with higher exit velocities and mass flow rates, owing to the VND–viscosity relationship. The fragmentation depth increases from VND = 14 to VND = 15 as a result of the weakening of the magma's mechanical resistance. A further increase in VND (VND = 16) does not produce a significant change in fragmentation depth, because the combined effects of decreased mechanical strength and decreased viscosity counterbalance each other.

### 5.2.5 Influence of magmatic chamber depth

In this section, we show the MAMMA numerical simulation results for Green Tuff eruption comparing the dynamics at different magmatic chamber depths. We evaluate the effects of magmatic chamber depth (2 – 3 – 4 km) and, related to it, the pressure (60 – 90 – 121 MPa) on the eruptive dynamics keeping temperature (767 °C), water content (3 wt%), conduit diameter (20 m) and Log VND (14.4) constant. Tab. 5.11 shows numerical simulation outputs whereas Fig. 5.16 shows

MAMMA numerical simulation results. Fig. 5.17-19 show the relationship between MAMMA numerical simulation results and different magmatic chamber depths.

| Eruption | Magmatic chamber depth (m) | Porosity (%) | T exit (°C) | Exit velocity (m/s) | Mass flow rate (kg/s) | Frag. depth (m) |
|---|---|---|---|---|---|---|
| Green Tuff | 2000 | 99 | 709 | 100 | 8.85E+05 | -135 |
| Green Tuff | 3000 | 99 | 701 | 100 | 7.97E+05 | -252 |
| Green Tuff | 4000 | 99 | 695 | 98 | 6.90E+05 | -342 |

*Tab. 5.11 Numerical simulation for detecting influence of magmatic chamber depth on eruptive dynamics keeping temperature, water content, conduit diameter and Log VND constant.*

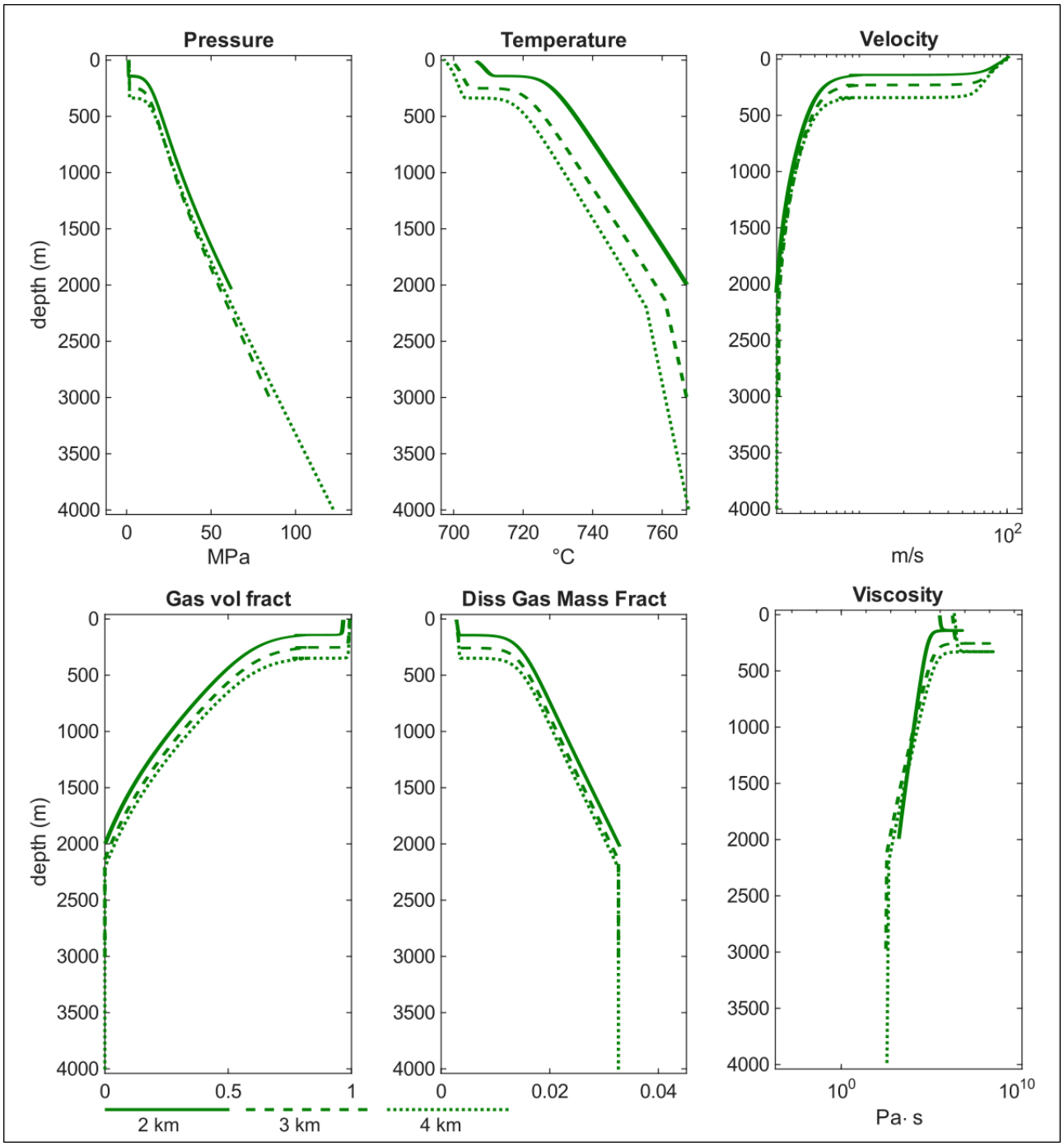


*Fig. 5.16 MAMMA numerical simulation for Green Tuff with different input magmatic chamber depth.*

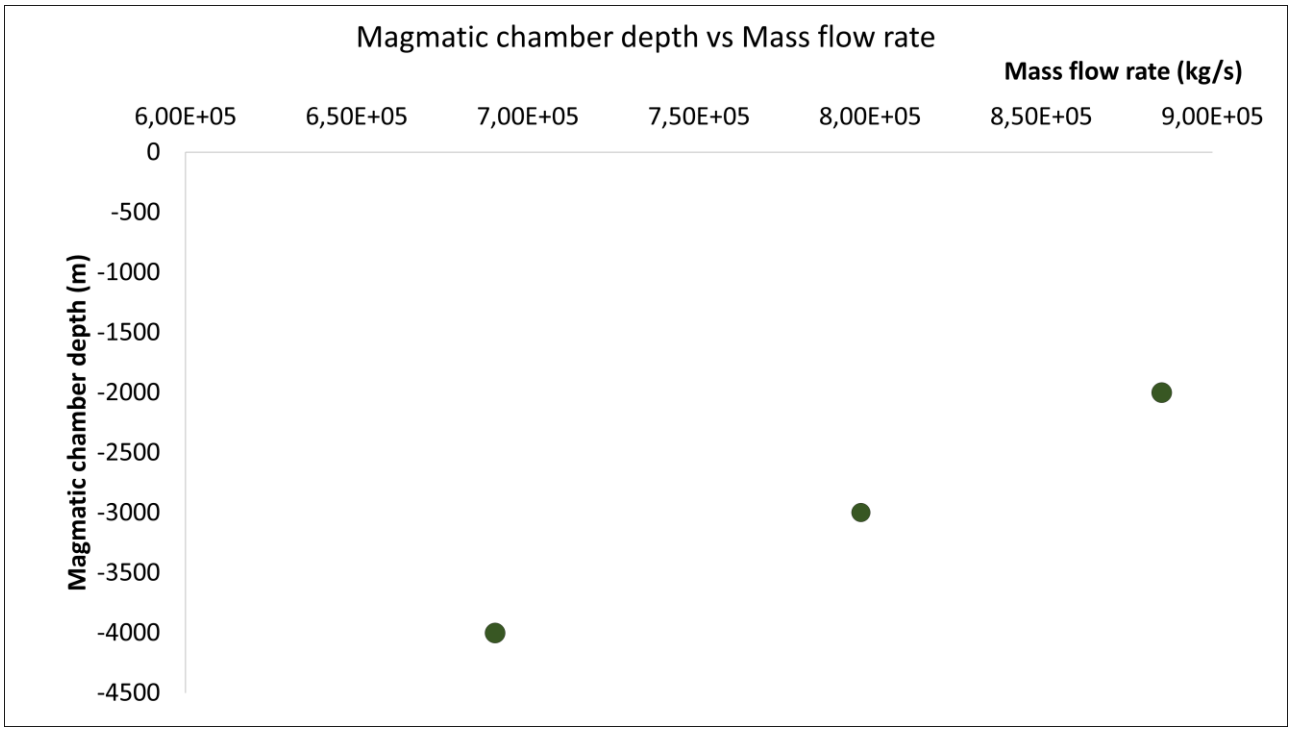


*Fig. 5.17 Magmatic chamber depth vs Mass flow rate relationship for Green Tuff numerical simulations results.*

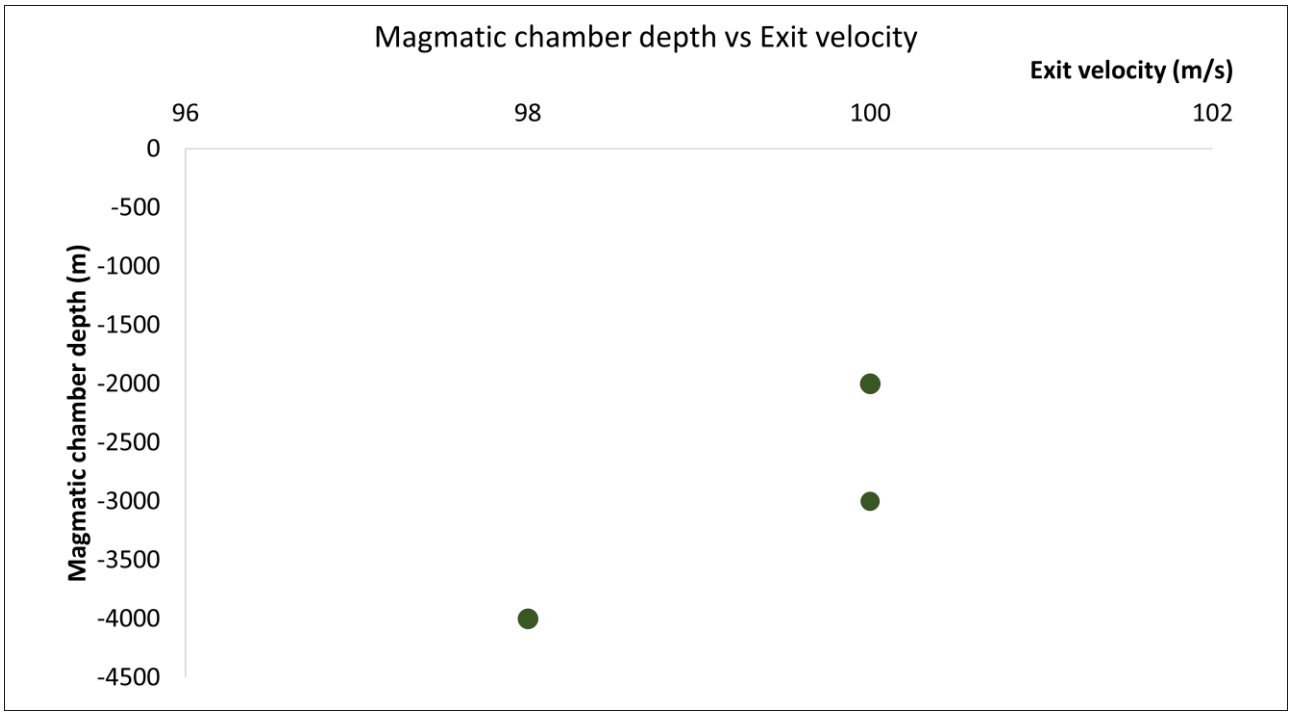


*Fig. 5.18 Magmatic chamber depth vs Exit velocity rate relationship for Green Tuff numerical simulations results.*

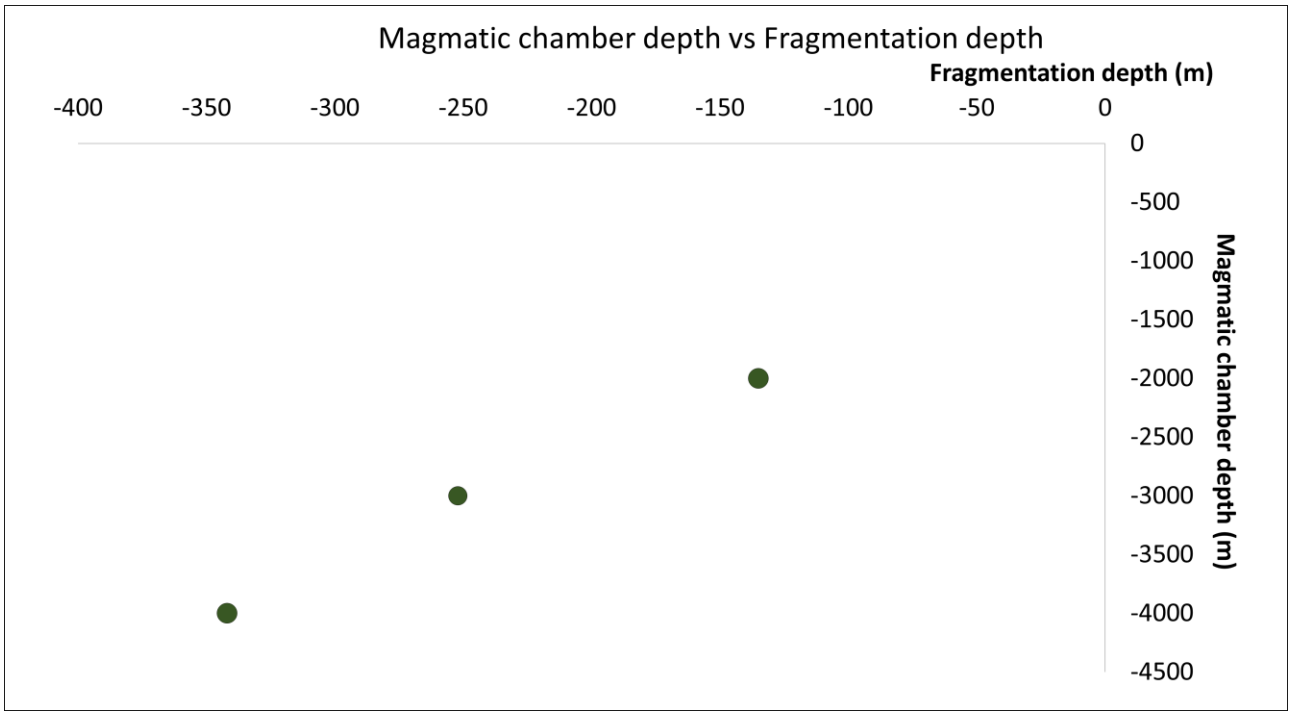


*Fig. 5.19 Magmatic chamber depth vs Fragmentation depth relationship for Green Tuff numerical simulations results.*

As shown in Figs. 5.17 and 5.18, variations in the magmatic chamber depth do not significantly affect the mass flow rate or the exit velocity. This suggests that these parameters are mainly controlled by magma viscosity and volatile content rather than by the initial pressure conditions. Conversely, the depth of the magmatic chamber appears to have a certain influence on the fragmentation depth. Although the 4 km case experiences greater cooling, which would typically inhibit degassing, the earlier onset of exsolution indicates that the pressure conditions in this simulation favour gas release at greater depths, resulting in a deeper fragmentation level. The enhanced gas release in the 4 km case leads to higher conduit velocities and a lower fragmentation threshold, both of which contribute to the onset of fragmentation at greater depths. In contrast, the slightly higher pressures in the 3 km and 2 km cases promote more superficial fragmentation.

### 5.2.5 Influence of chemical composition

In this section, we analyse the effect of chemical composition on the eruptive dynamics. In order to do so, we changed chemical composition keeping all the other parameters constant (depth (4 km), conduit diameter (20 m), temperature (825 °C), pressure (121 MPa), water content (3 wt%) and Log VND (14.92; derived as the mean of the VND values from the analysed eruptions, except for the Green Tuff eruption, which is not considered representative, as explained earlier in this

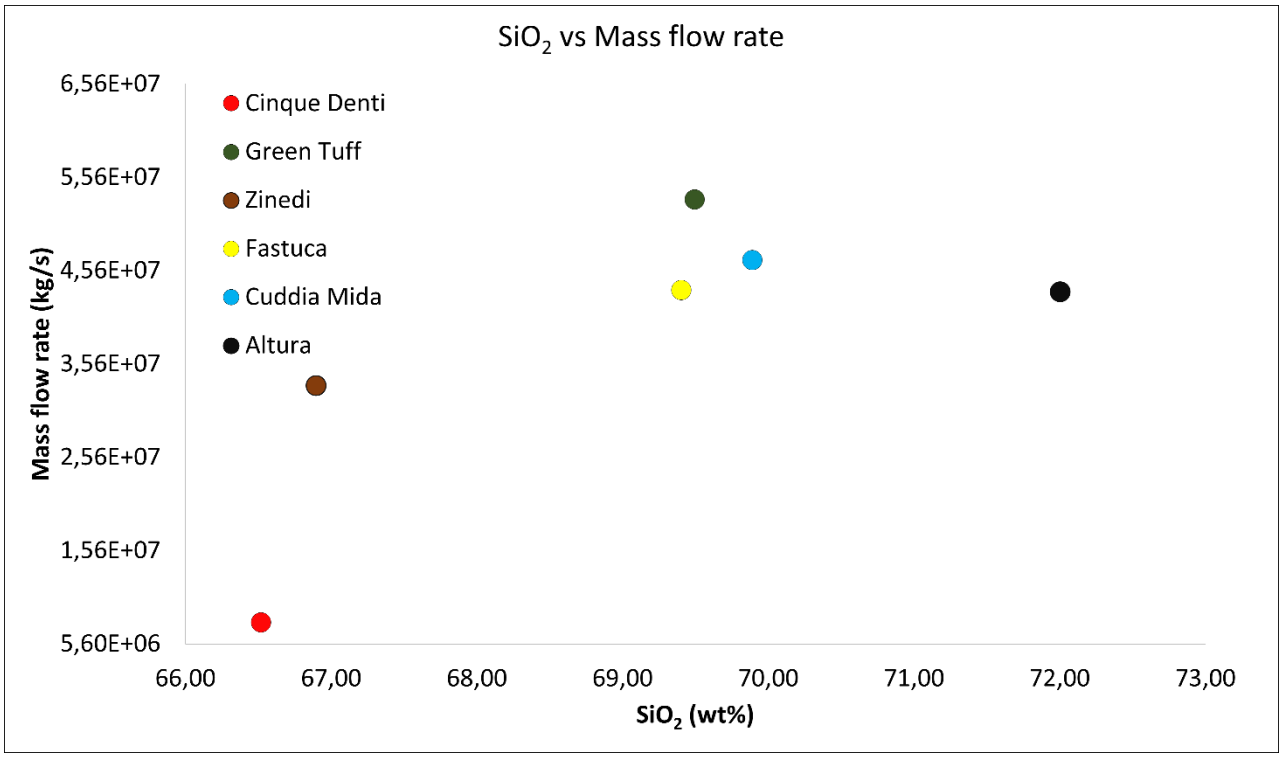


*Fig. 5.20 $SiO_2$ wt% content vs Mass flow rate relationship for the six eruptions studied.*

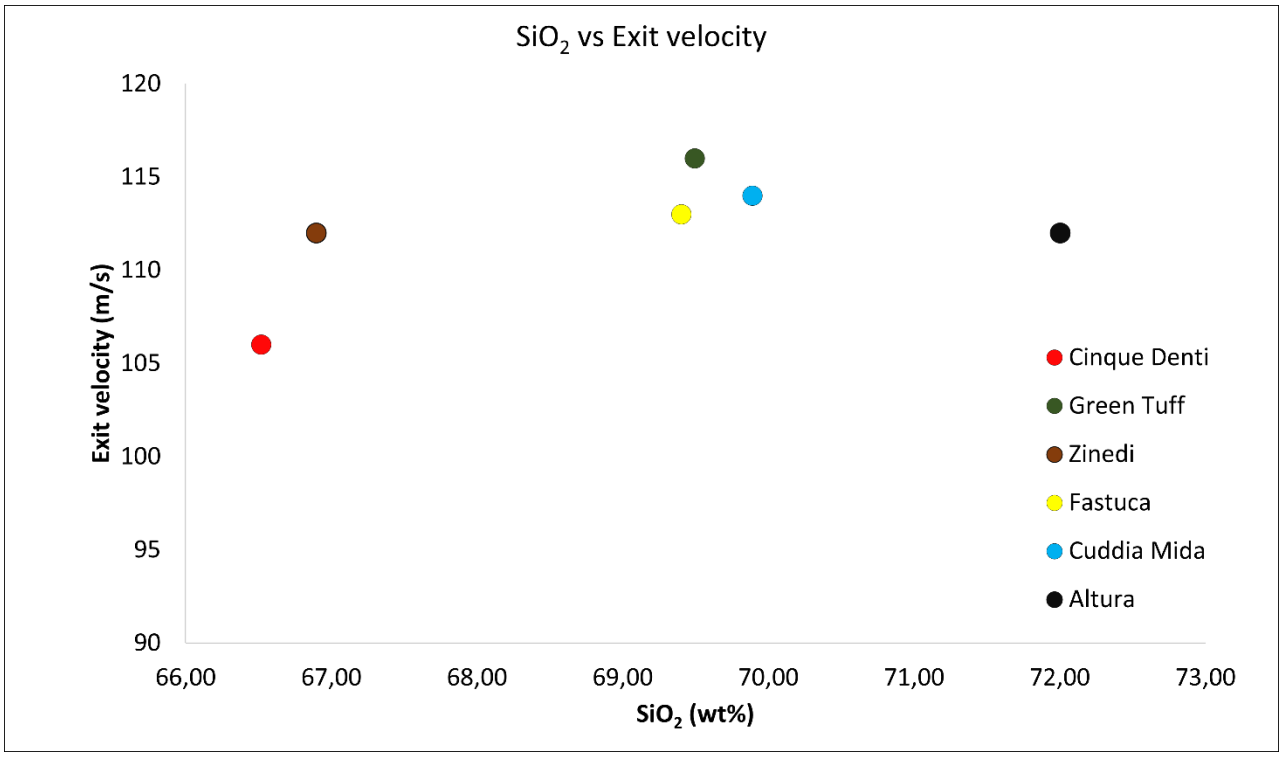


*Fig. 5.21 $SiO_2$ wt% content vs Exit velocity rate relationship for the six eruptions studied.*

modelling conditions. Fig. 5.22 shows the relationship between $SiO_2$ wt% content and fragmentation depth. Cinque Denti shows the deepest fragmentation level (1519 m), representing an outlier compared to the peralkaline eruptions. Among the peralkaline products, Zinedi exhibits a considerably deeper fragmentation depth (900 m) than the others. Green Tuff, Fastuca, Cuddia Mida and Altura all fragment at much shallower depths, ranging from approximately -12 m to -59 m. Fragmentation depth is therefore the parameter most sensitive to variations in magma composition. The shallow fragmentation typical of the peralkaline eruptions likely reflects their rheological characteristics. Zinedi constitutes an intermediate case, combining a relatively low mass flow rate with a significantly deeper fragmentation level. Cinque Denti again stands out as an outlier, reflecting fundamentally different physical conditions associated with its metaluminous character. Fig. 5.23-25 shows relationship between MAMMA numerical simulation results with P.I.

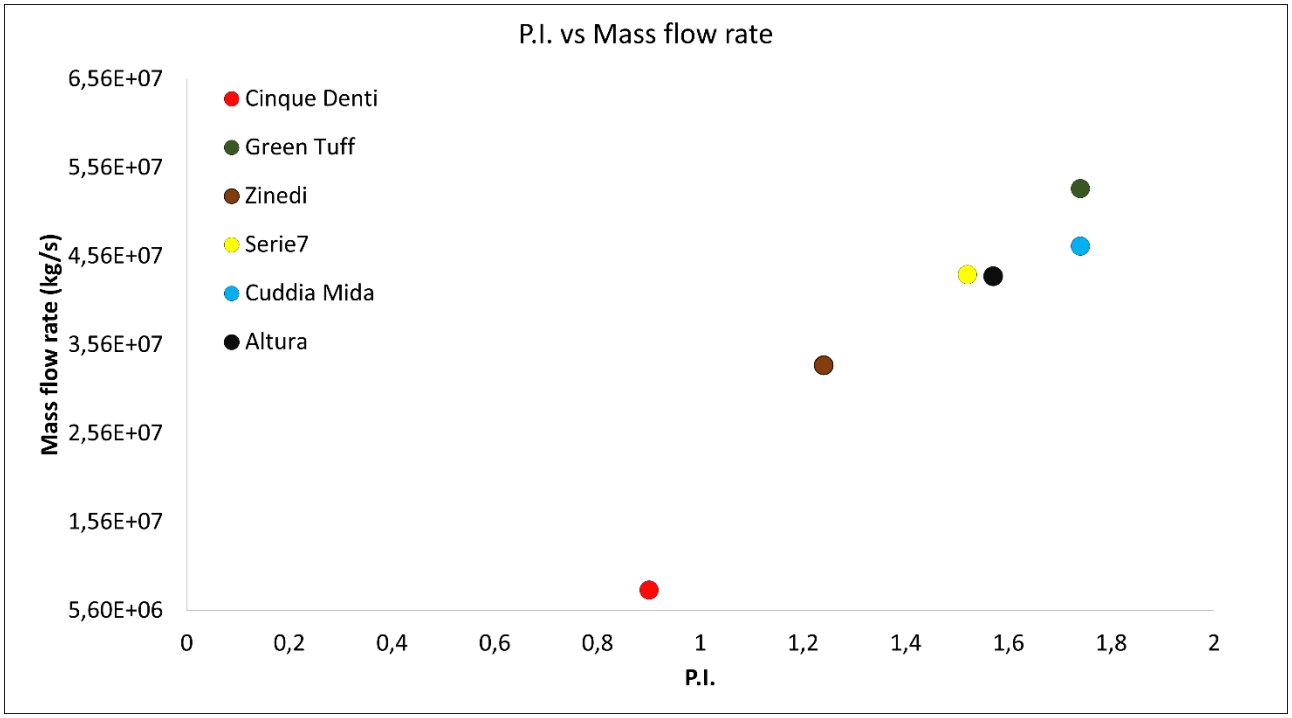


*Fig. 5.23 P.I. vs Mass flow rate relationship for the six eruptions studied.*

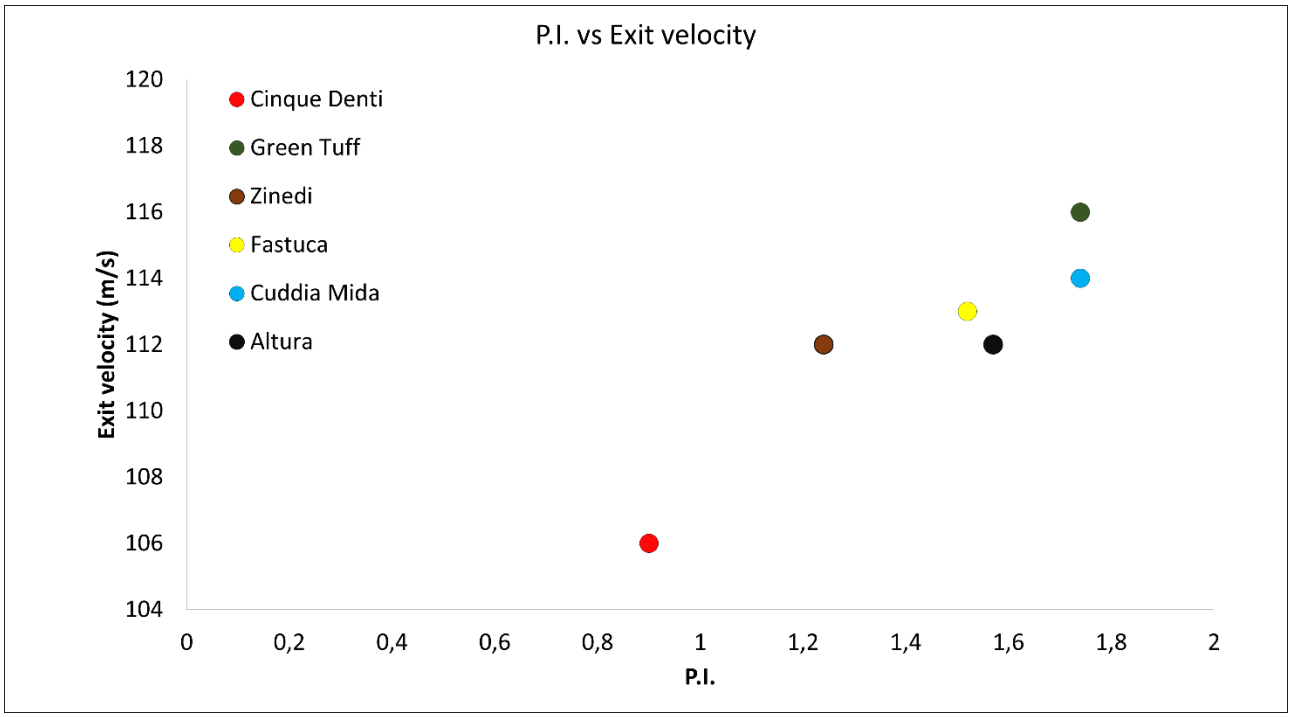


*Fig. 5.24 P.I. vs Exit velocity rate relationship for the six eruptions studied.*

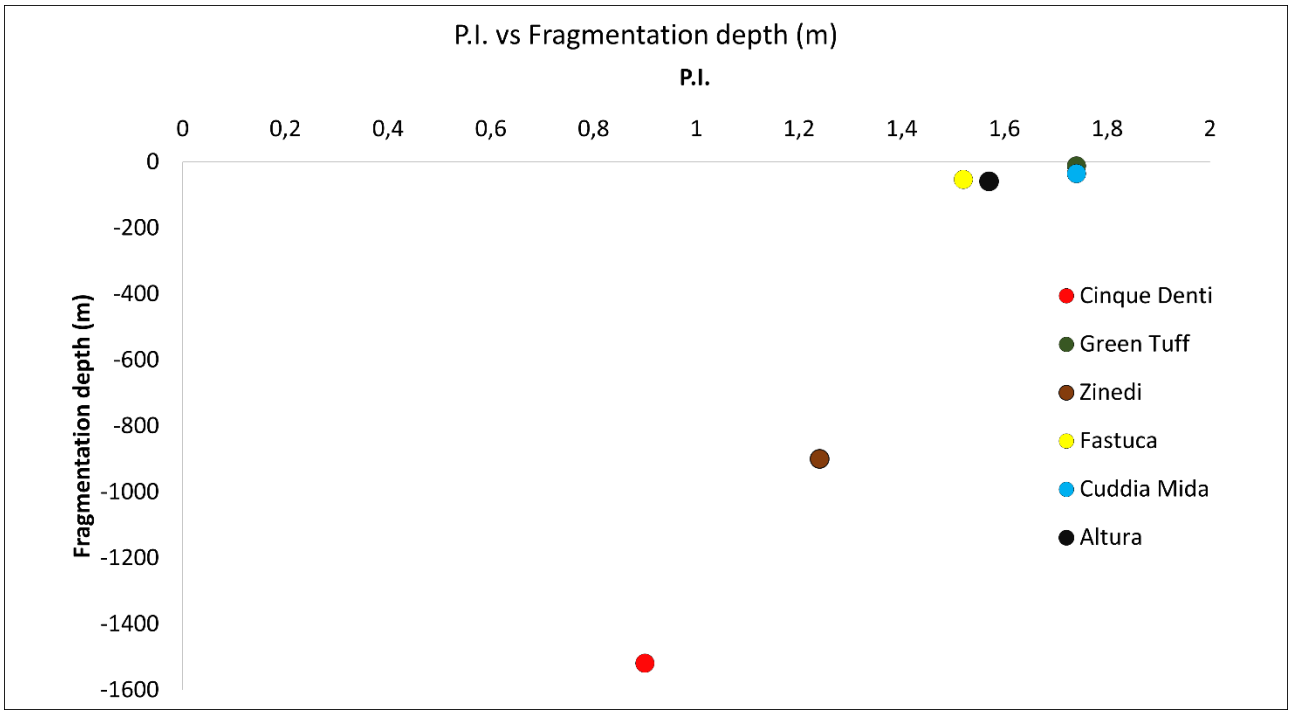


*Fig. 5.25 P.I. vs Fragmentation depth relationship for the six eruptions studied.*

Fig. 5.23 shows the relationship between the Peralkalinity Index (P.I.) and the mass flow rate. As already observed for $SiO_2$, Cinque Denti clearly stands apart from the peralkaline group. With a P.I. lower than 1, it displays by far the lowest mass flow rate ($7.92 \times 10^6$ kg/s), reflecting its metaluminous composition and the distinct physical behaviour associated with it. In contrast, all peralkaline

eruptions (P.I. > 1) exhibit substantially higher mass flow rates, ranging from $3.33 \times 10^7$ to $5.32 \times 10^7$ kg/s. Within this cluster, Zinedi shows the lowest value, whereas Green Tuff, Fastuca, Cuddia Mida, and Altura occupy the upper end of the distribution. Overall, the graph demonstrates that once magmas enter the peralkaline field (P.I. > 1), their mass flow rates vary within a relatively narrow interval and exhibit a roughly linear increase with the degree of peralkalinity. The main control is therefore compositional grouping (metaluminous vs. peralkaline), with Cinque Denti behaving as a clear outlier due to its fundamentally different magma chemistry. The chemistry is related to the different viscosities within this group of magmas, whereby the higher viscosity of the Cinque Denti magma leads to a lower mass flow rate, while the progressively lower viscosities of the more peralkaline compositions result in higher mass flow rates. Fig. 5.24 displays the relationship between P.I. and exit velocity. The peralkaline eruptions show a remarkably narrow velocity range (112–116 m/s). Green Tuff reaches the upper bound (116 m/s), while Zinedi, Fastuca, Cuddia Mida and Altura show slightly lower but comparable values (112–114 m/s). Cinque Denti, with a P.I. lower than 1, exhibits a distinctly lower exit velocity (106 m/s), mirroring the same trend observed for $SiO_2$ and mass flow rate. The slight increase in exit velocity with peralkalinity can be attributed to the decrease in magma viscosity. At 750 °C, more peralkaline compositions are less viscous (as long as no viscosity crossovers occur) and at a constant volatile content, lower viscosity promotes slightly faster magma ascent. This behaviour is consistent with the observed trend, where the metaluminous Cinque Denti, the most viscous composition, shows the lowest velocity. It is noteworthy that Cuddia Mida and Altura, the two Strombolian eruptions in the dataset, display the highest velocities, consistent with their more peralkaline nature. Although volatile content is the primary control on eruptive dynamics, these results highlight that even small anhydrous compositional variations can significantly influence ascent velocity. Fig. 5.25 illustrates the relationship between P.I. and fragmentation depth. Cinque Denti, the only metaluminous eruption, shows the deepest fragmentation level (-1519 m), reinforcing its distinctive behaviour. Within the peralkaline group, Zinedi occupies an intermediate position (-900 m), whereas Green Tuff, Fastuca, Cuddia Mida, and Altura exhibit very shallow fragmentation levels (between -12 m and -59 m). This pattern is controlled primarily by viscosity: more viscous magmas reach the conditions for fragmentation at greater depths, while less viscous (more peralkaline) magmas fragment closer to the surface, where confining pressure is

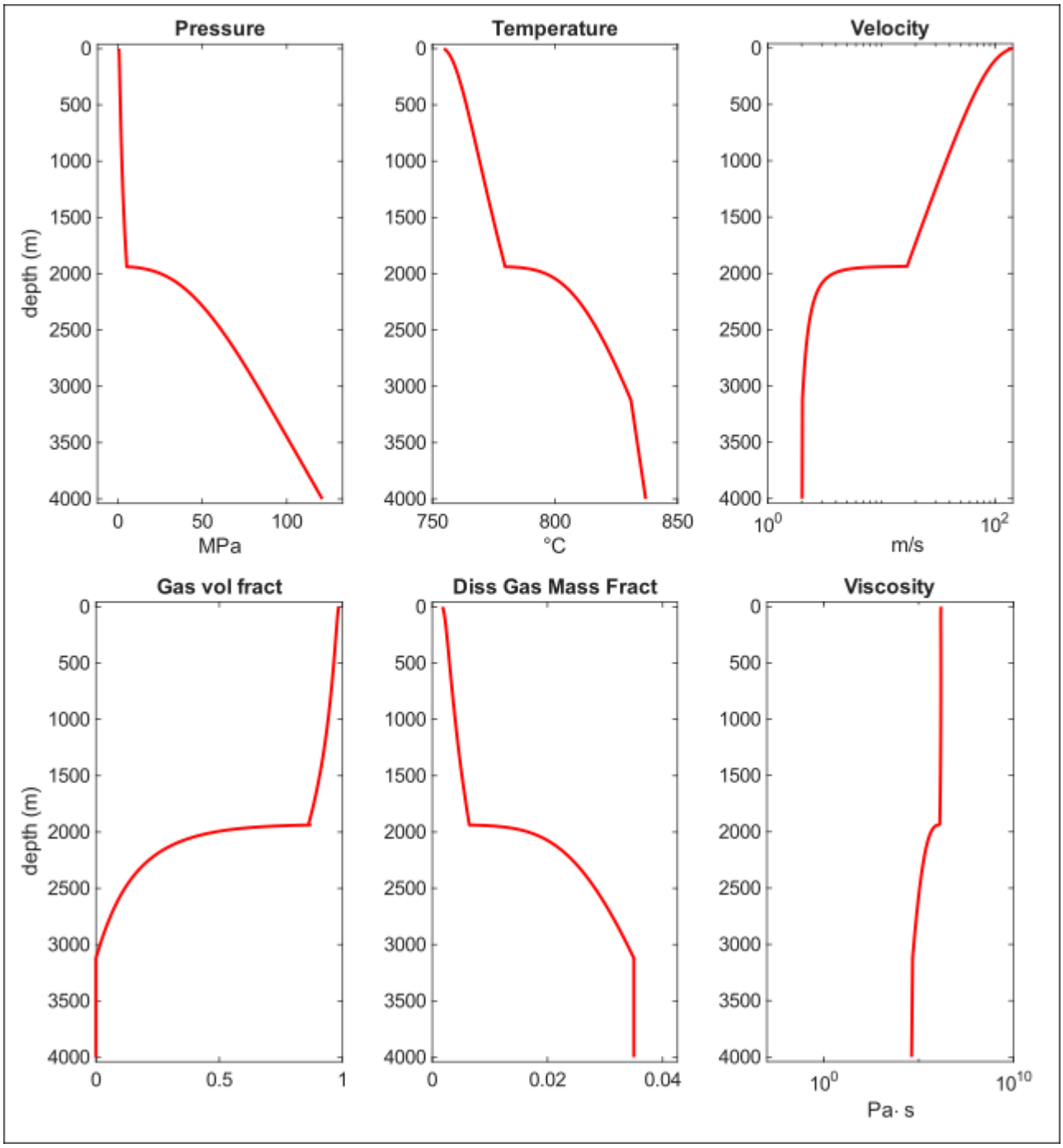


*Fig. 5.26 MAMMA numerical simulation for Cinque Denti for specific eruptive conditions.*

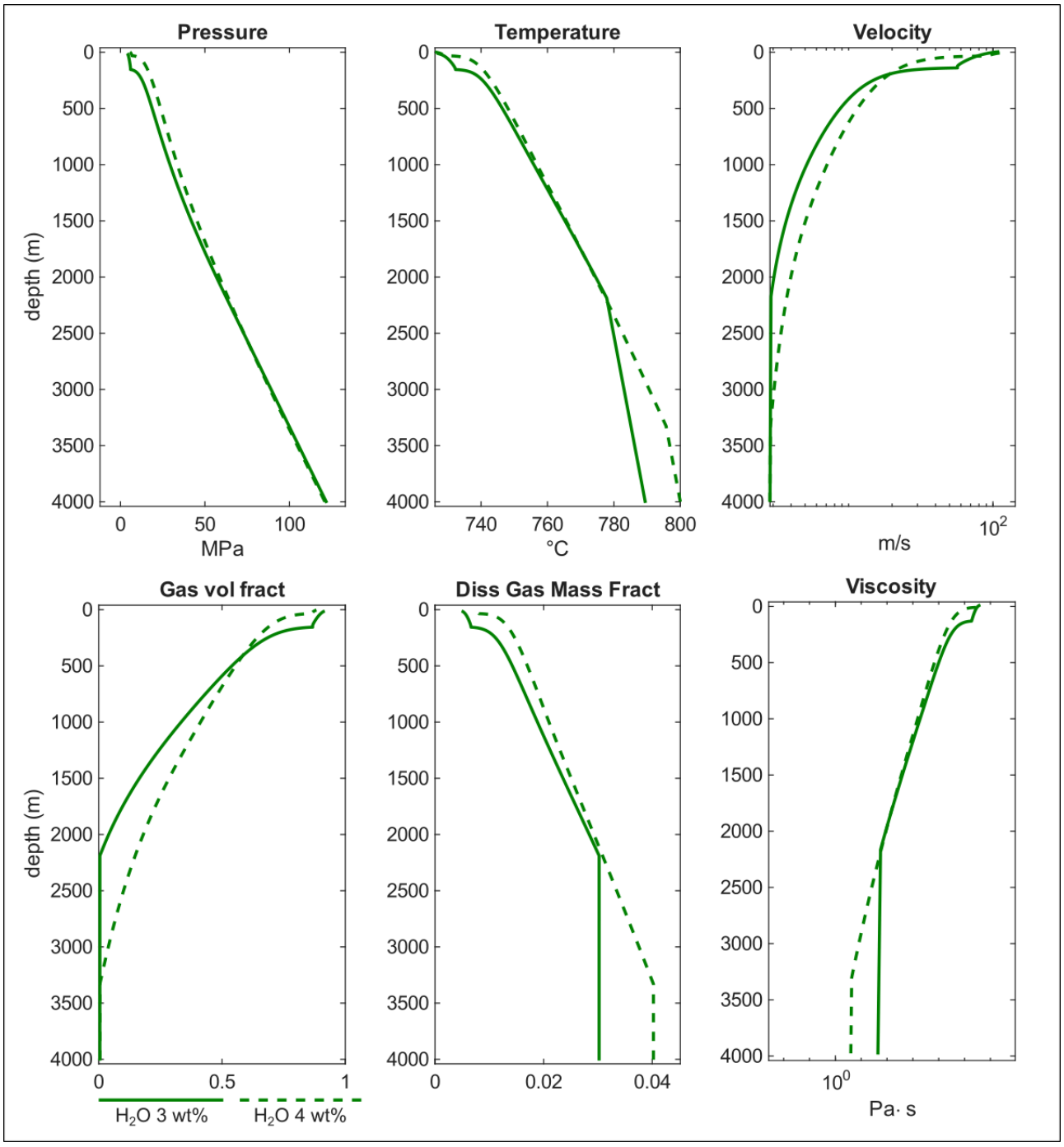


*Fig. 5.27 MAMMA numerical simulation for Green Tuff with different water content for specific eruptive conditions.*

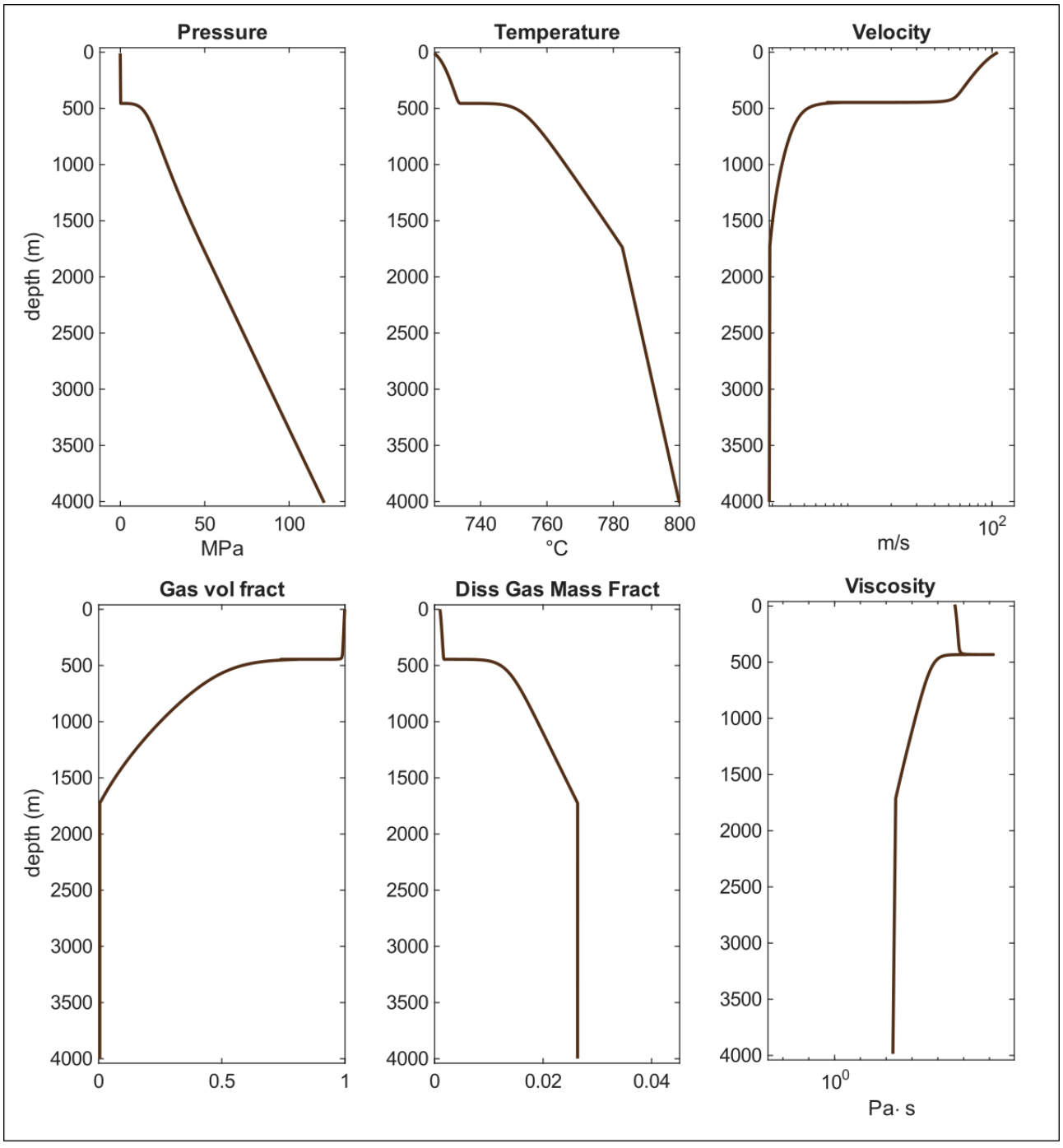


*Fig. 5.28 MAMMA numerical simulation for Zinedi for specific eruptive conditions.*

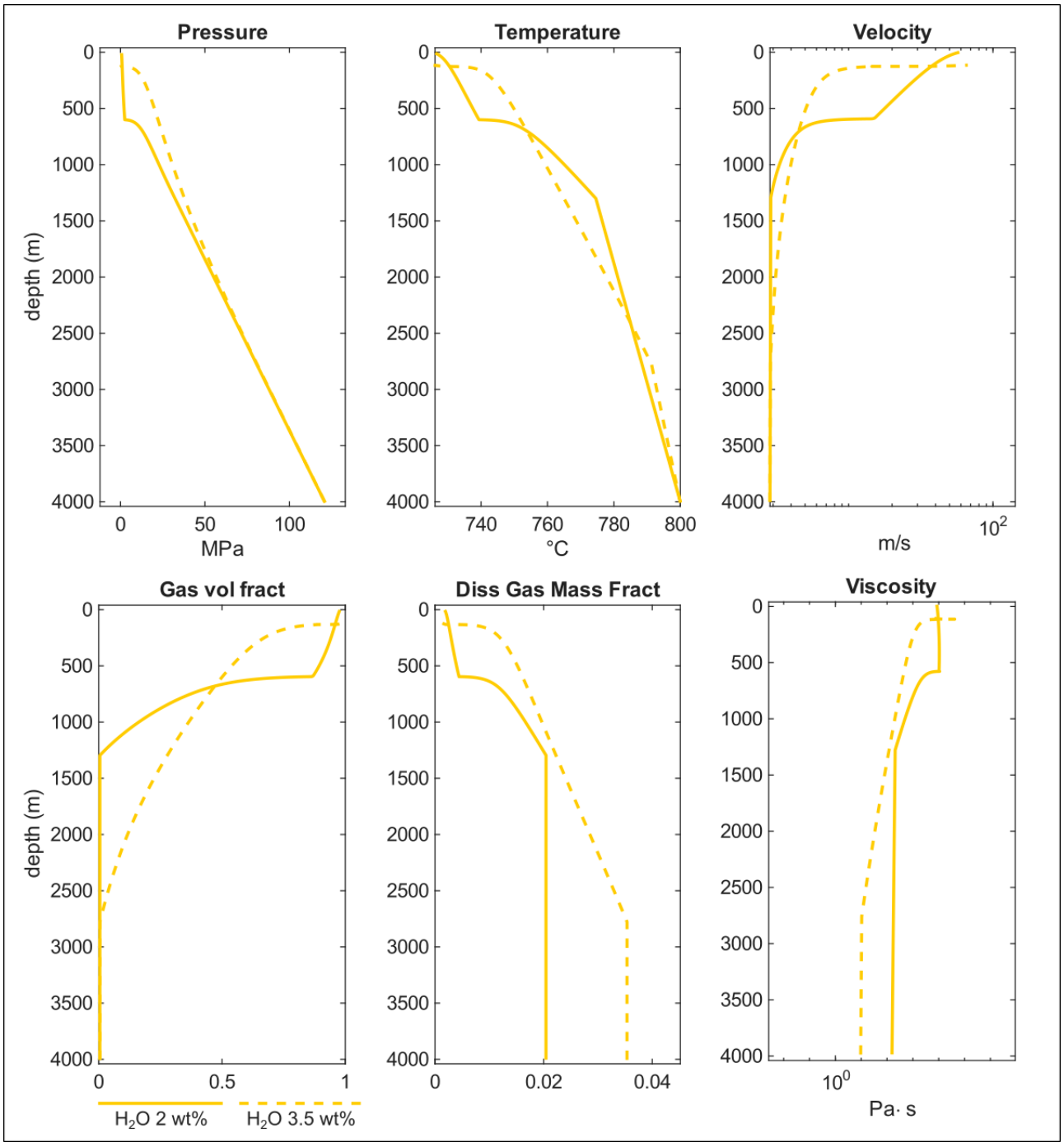


*Fig. 5.29 MAMMA numerical simulation for Fastuca with different water content for specific eruptive conditions.*

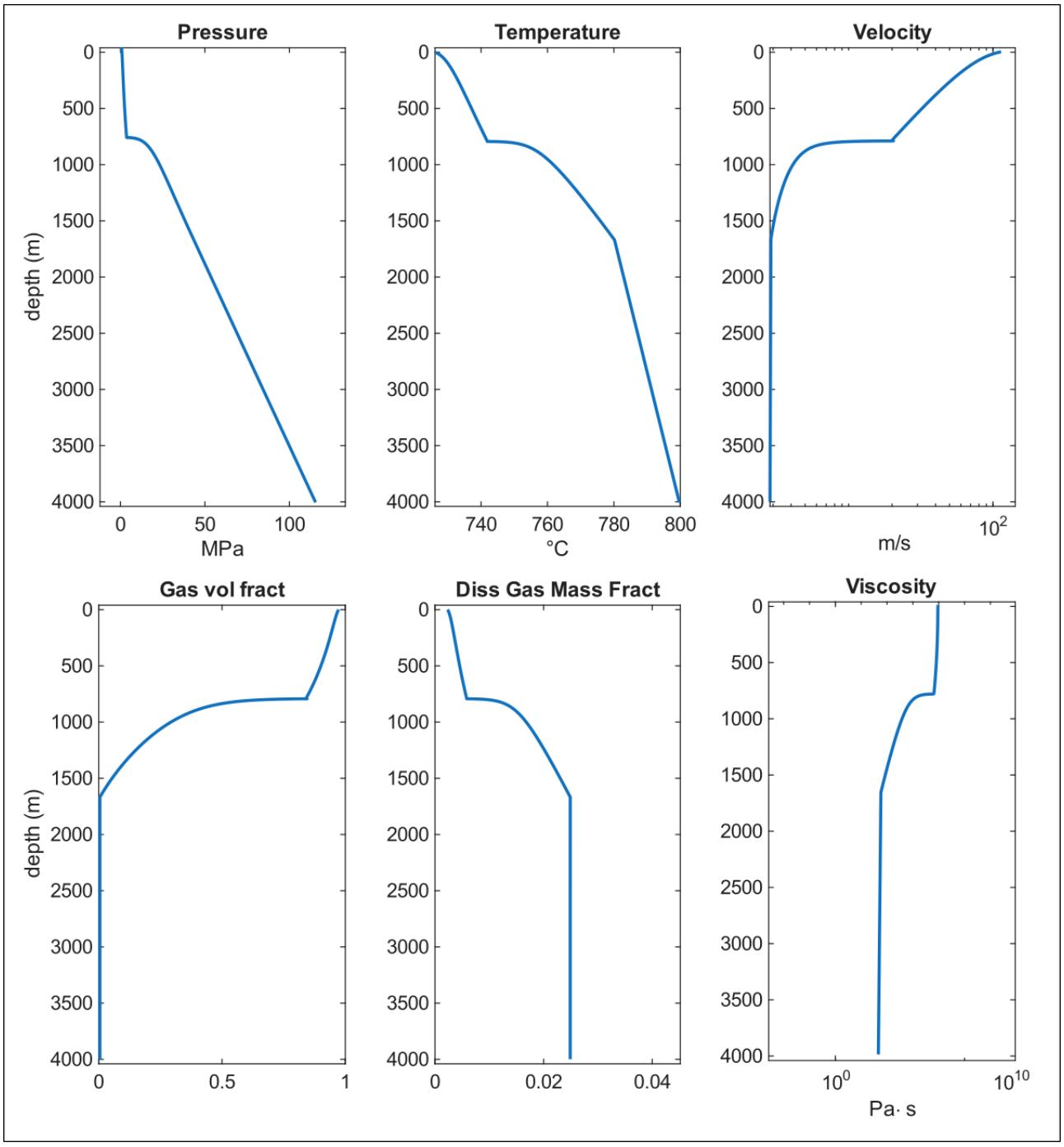


*Fig. 5.30 MAMMA numerical simulation for Cuddia Mida for specific eruptive conditions.*

decompression rate (dP/dt) is related. To reproduce the natural conditions of Green Tuff eruption, numerical simulation have been performed in order to match the MFR estimated by Williams et al. (2010; $2.00\times10^{8}$ kg/s). The viscosity measurements (Cap. 3 and 4) indicate a low viscosity magma, strongly depolymerized due to the combined effect of alkalis and high water content. Achieving brittle fragmentation in such a magma would require high ascent velocities, generating strain rates large enough to overcome viscous relaxation and induce brittle failure. These conditions are attainable only at shallow conduit levels, where magma acceleration is sufficient to reach the necessary strain-rate – viscosity conditions for fragmentation. The shallow fragmentation is attributable to the lower viscosity together with the lower VNDs compared to Cinque Denti magma, which both act to delay fragmentation. The higher mass flow rate is a direct consequence of the large conduit diameter imposed in the simulation and, to a lower extent, to a lower viscosity of GT compared to Cinque Denti eruption. The high exit velocities, fully comparable to the Cinque Denti exit velocities are mainly due to the high water content of this magma, which represents the main driving force for this energetic caldera forming Plinian eruption;

- Zinedi (sub-Plinian eruption): Zinedi eruption was simulated with a 30 m conduit diameter and a water content of 2.5 wt%. The model yields a mass flow rate of $1.33\times10^{6}$ kg/s, an exit velocity of 94 m/s, and an exit temperature of 759 °C, with fragmentation occurring at -445 m depth and a low decompression rate (0.03 MPa/s). Zinedi magma is characterized by the highest anhydrous viscosities and low initial water content. The relatively low VND yields a small conduit diameter, which therefore reflects the modest mass flow rate at the exit conduit, comparable to the values from the other eruptions but significantly lower than Green Tuff eruption values (calculated however on the different basis of MDR from literature data). To a minor degree, the modest mass flow rate is also influenced by the higher anhydrous viscosity of this magma compared to the Green Tuff magma. The depth of fragmentation is relatively high, compared to Green Tuff, as a result of the higher VNDs and therefore lower yield strength of the magma together with the higher anhydrous viscosities. The exit velocity, lower compared to the velocities for Cinque Denti and Green Tuff, is related to the

net effect depends on the combination of all the other parameters, and therefore it is difficult to predict. This is even more clearly visible when compared results performed with different VNDs  with simulations performed with the BAI criteria (Table 5.15) where the VND is not considered at all. Differences with the previous two sets of simulations are, also in this case, minimal.

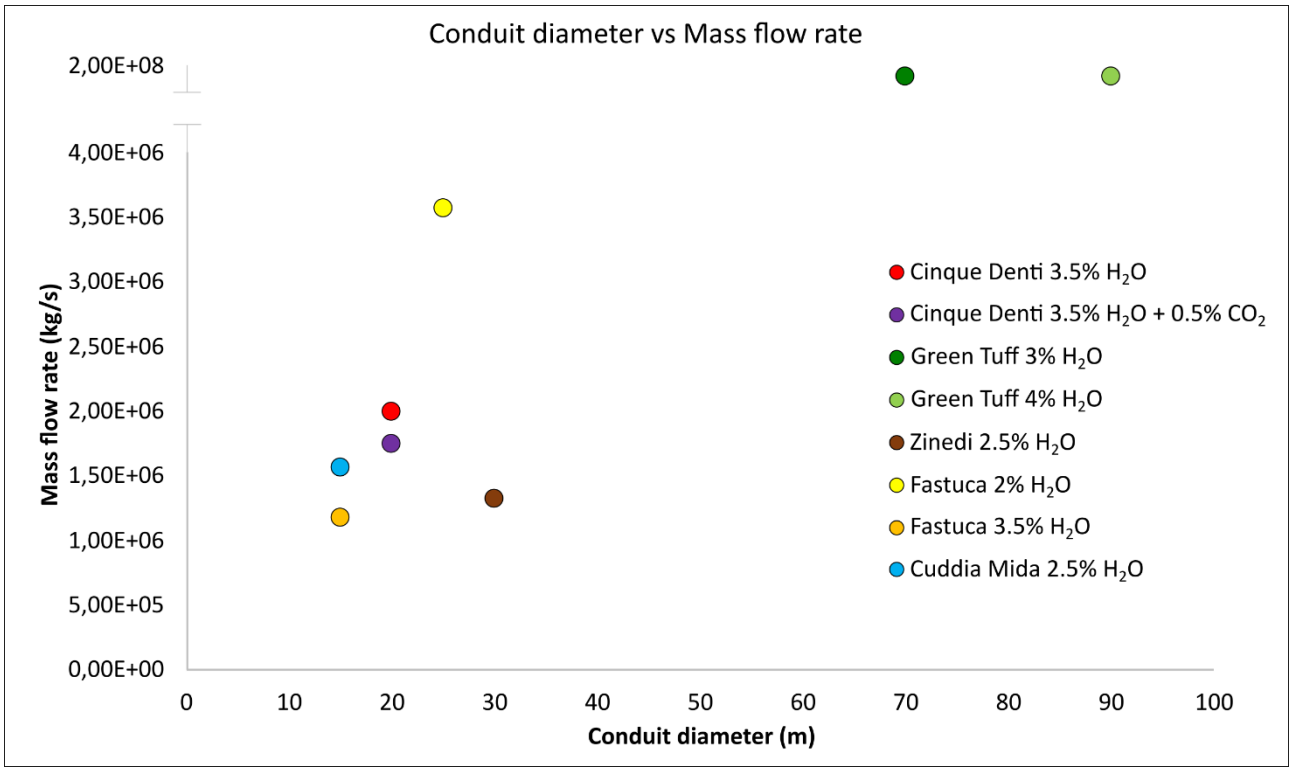


*Fig. 5.31 MAMMA numerical simulation results for Mass flow rate with conduit diameter in order to match dP/dt from Toramaru equation (1995, 2006). Note that the Y-axis is broken to highlight the differences between Green Tuff eruption mass flow rates and other eruptions.*

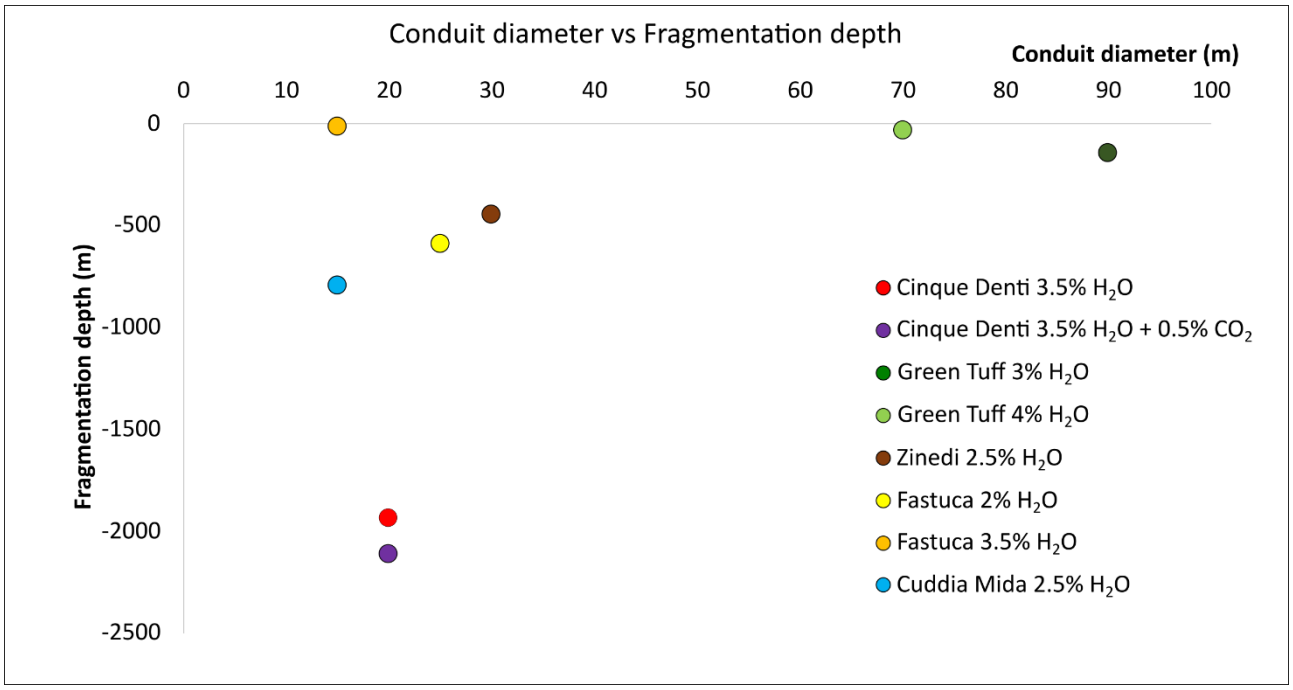


*Fig. 5.32 MAMMA numerical simulation results for Fragmentation depth with conduit diameter in order to match dP/dt from Toramaru equation (1995, 2006).*

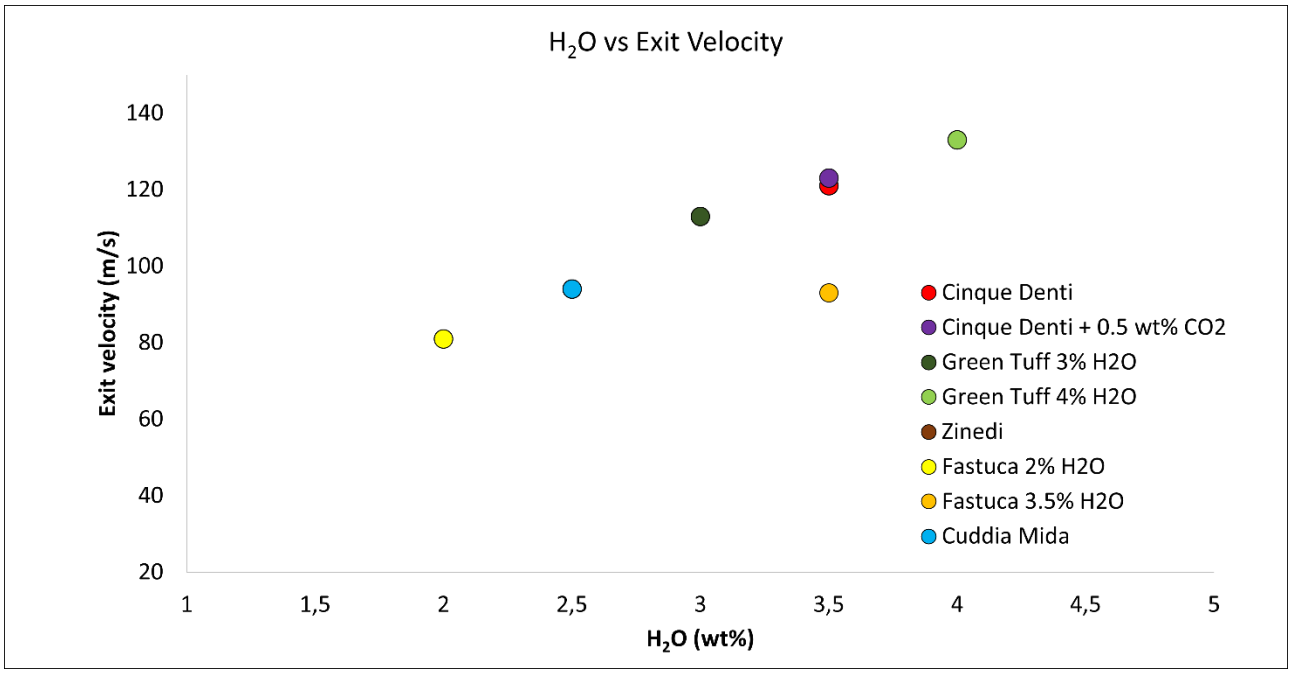


*Fig. 5.33 MAMMA numerical simulation results for water content with exit velocity in order to match dP/dt from Toramaru equation (1995, 2006).*

This research starts with a general overview of peralkaline magmatic systems, underlining their geological relevance and peculiar composition, besides the still open questions on mantle and crustal origins. The introduction underlined the wide range of tectonic settings in which such magmas develop and stressed their relevance for volcanic hazard assessment. In this framework, Pantelleria represents a natural laboratory for the study of peralkaline magma behavior due to its outstanding record of explosive and effusive eruptions of different magnitudes and compositions.

Image-based textural analyses provided critical constraints on vesiculation and degassing processes and led to several key findings: all investigated eruptions produced highly vesicular pumices with modal porosities ranging between 70 and 80%, in agreement with values characteristic of other high-silica explosive products. In spite of large differences in eruptive style, the samples display remarkably similar VNDs, between $10^5$ and $10^6$ $mm^{-3}$, indicating that in peralkaline systems, vesiculation is not directly related to the intensity of the eruption but is mainly controlled by melt rheology and the kinetics of degassing. The Green Tuff differs from other eruptions studied herein for its peculiar textures, consisting of widespread vesicle coalescence, deformation and partial collapse of bubble walls. These features, coupled with polymodal vesicle size distributions, are thought to be the result of post-fragmentation relaxation processes driven by the low viscosity of pantelleritic melts and prolonged high-temperature conditions beneath the overlying ignimbrite. By contrast, the eruptions of Cinque Denti and Zinedi, which represent Plinian and sub-Plinian activity, respectively, are characterized by unimodal vesicle distributions typical of continuous nucleation and growth under the rapid ascent typical of their explosive style. The Strombolian eruption of Cuddia Mida displays more complex and polymodal textures consistent with variable ascent rates and intermittent conduit stagnation.

Rheological experiments, performed using concentric cylinder apparatus (CC), differential scanning calorimetry (DSC) and micropenetration techniques (MP), yielded precise determinations of viscosity across wide temperature intervals. Peralkaline magmas are distinguished from metaluminous and peraluminous counterparts by their exceptionally low viscosities, even at low temperatures, due to their alkali-rich composition. As a consequence, these melts can cross the glass transition multiple times during and after eruption, allowing post

fragmentation degassing, coalescence and welding. The Green Tuff provides a striking example of this rheomorphic behavior, where deformation and bubble collapse likely occurred after deposition, under lithostatic load and prolonged thermal conditions. These observations question the widely held assumption that vesicle textures reflect only conduit processes and show that post-fragmentation modification may be an important component of the peralkaline eruptive systems. An interesting outcome of this study is represented by the evidence that textural analysis did not provide any significant discrimination among all the eruptions investigated in this work, despite the variation in intensity and eruptive style, thus offering limited information on the conditions of brittle fragmentation in such relatively low-viscosity magmas. Prediction of our viscosity measurements made by using available viscosity for general composition (Giordano et al., 2008) and for peralkaline composition (Di Genova et al., 2013) pointed out the limitations of the present models to reproduce the behavior of peralkaline melts. To overcome this issue, a new empirical viscosity model was formulated in this work, able to provide an improved predictive capability for peralkaline magmas.

Numerical simulations carried out with the MAMMA model quantitatively reproduce the control of each chemical and physical parameters in the conduit dynamic and more in general, the ascent dynamics of the six eruptions by incorporating experimentally constrained viscosity, melt compositions, textural analysis, estimated eruptive temperature and water content of the natural products, the simulations allowed to understand the ascent dynamics through the conduit. Results show that fragmentation in peralkaline magmas can occur at relatively low pressures due to their low melt viscosity and high volatile diffusivity for all the investigated eruptions.

From the parametric study conducted in this work, we identified the following relationships:

- The conduit diameter exerts a dominant linear control on the mass flow rate and shows an inverse relationship with the fragmentation depth, likely due to the increase in the friction term in the overall momentum equation.
- An increase in temperature leads to a decrease in fragmentation depth as a result of reduced magma viscosity, which lowers the pressure gradient (dP/dz) and consequently decreases the degree of volatile exsolution.

can be explained by the impossibility of the model to fully take into account the variable nature of the volatile phases ($CO_2$, Cl, $SO_2$) of this magma and the effect of those on its viscosity and degassing behavior. Difficult to explain, but potentially also related to the anomalous volatile phases present in this magma is the high VND retrieved, which can also be partially responsible for the high velocities at the vent resulted from the model simulation. Overall, however, the variations observed among the simulated cases are fully consistent with the corresponding natural eruptive styles. This confirms that the model captures the first-order controls of viscosity, volatile content and conduit geometry on the transition between Strombolian, sub-Plinian and Plinian regimes. In a broader context, this work contributes to refining the conceptual framework of peralkaline volcanic systems by integrating field observations, laboratory data, and numerical modeling. These findings have implications for volcanic hazard assessment in peralkaline provinces globally, such as the East African Rift, the Canary Islands and the Azores, where the potential for rapid switches between explosive and effusive regimes may be underestimated. The role of halogens in peralkaline melts and their effects on viscosity, volatile solubility, and eruption dynamics should be further pursued in future research. This work discussed speculations concerning the effect of halogens but did not find support for such hypotheses in the available literature. In any case, the results of this work offer solid ground for future investigations into the complex, multiscale dynamics of peralkaline magmatism and contribute to a more thorough understanding of one of the most interesting and fascinating volcanic systems on Earth.

# Supplementary Material

## 1. SEM images used for Textural Analysis

## 1.1 Cinque Denti eruption

Pumice ID: 5D23 (High Density clast) 60X magnification

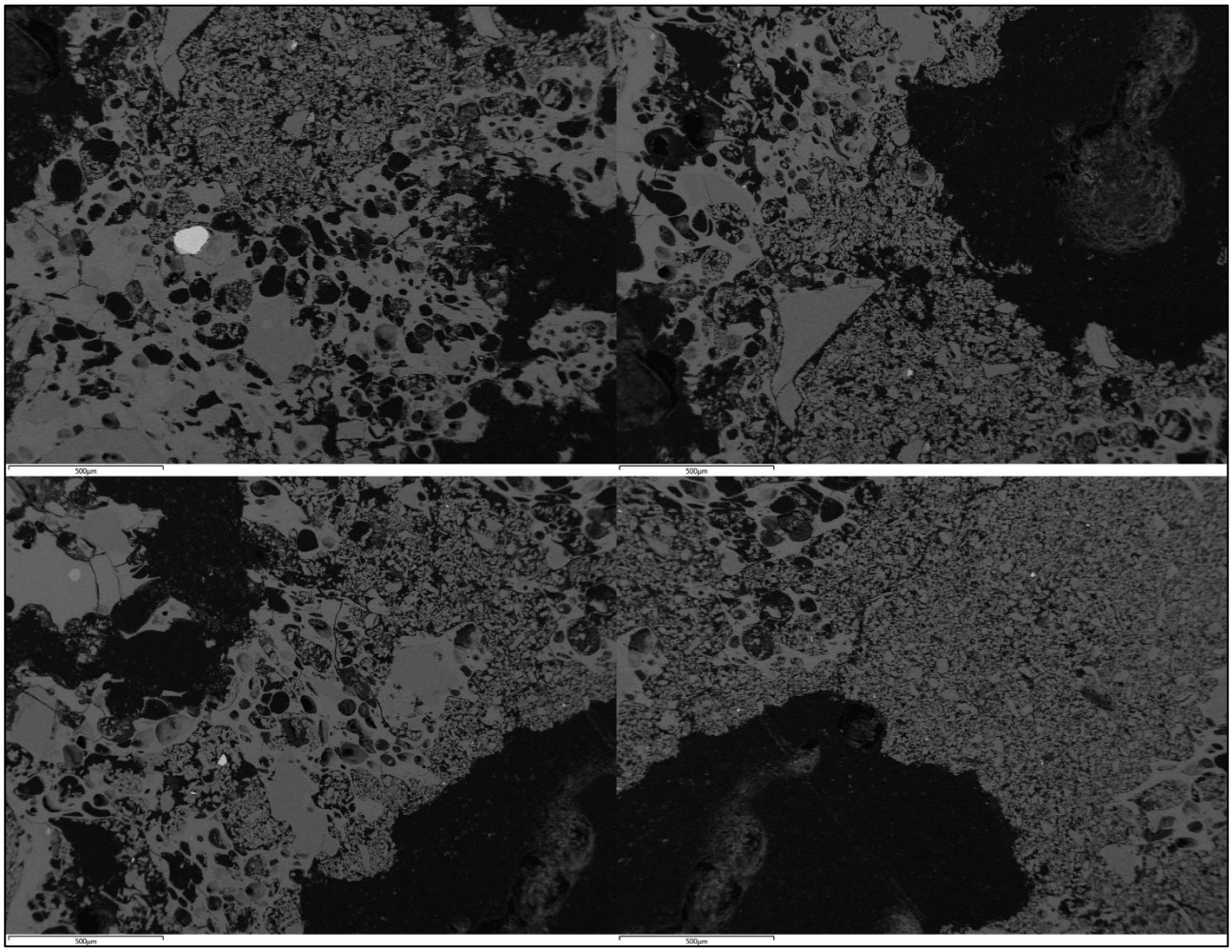

Pumice ID: 5D23 (High Density clast) 300X magnification